The Magnetic Fields of Young Solar-Type Stars

Ian Angus Waite
B. App. Sc. (D.D.I.A.E);
Dip. Ed.; B. Econ. (U.Q.);
M. Phil. (U.S.Q)

University of Southern Queensland

A thesis submitted for the degree of

PhilosophiæDoctor (PhD)

2013, July

Abstract

This thesis describes an investigation aimed at using spectropolarimetric observations of the magnetic fields of young solar-type stars to improve the understanding of the early development of solar and stellar dynamos and activity cycles. The emergence of stellar dynamos is important in understanding the evolution of young stars (and activity effects on any attendant emerging planetary systems). Stars were selected on the basis of their rapid rotation and activity. HD 106506, HD 76298, HD 35256, HD 29613 and EK Draconis formed the primary targets. Spectropolarimetric data were obtained with the Anglo-Australian Telescope, the Canada-France-Hawaii Telescope and the Télescope Bernard Lyot with supporting broadband photometric data from the Mount Kent Observatory. Reduction and analysis of the data were performed to produce magnetic field detections, spot occupancy and magnetic field maps, differential rotation values, chromospheric flux estimates, starspot light curves and other measurements. Several results were obtained, as follows: (1) A distributed dynamo fundamentally different to the modern Sun's interface-layer dynamo appears widespread in young solar-type stars, with all targets displaying significant surface azimuthal fields consistent with the dynamo operating throughout the convection zone. (2) All stars showed significant enhancement in chromospheric activity that appears to be primarily a function of rapid stellar rotation (3) Multi-epoch observations of the young solar analogue EK Draconis demonstrated a rapidly evolving magnetic field that could not be explained due to differential rotation alone, and hints at the presence of temporal variability due to the rapid evolution from a strongly toroidal magnetic field ($\sim$80%) to a more balanced poloidal-toroidal configuration in three months of observations. (4) The differential rotation of HD 29615, with a rotational shear $\delta\Omega = 0.58^{+0.14}_{-0.12}$ rad d^{-1} is one of the largest yet observed through χ^2 minimisation method, making this star a useful test case for the theory and modelling of dynamos in young solar-type stars.

Certification of Dissertation

I certify that this dissertation contains no material accepted for the award of any other degree or diploma in any university. To the best of my knowledge, it contains no material published or written by another person, except where due reference is made in the text.

Signature of Candidate Date

ENDORSEMENT

Signature of Supervisor Date

Acknowledgements

I wish to pay tribute to the late Dr Meir Semel, from Laboratoire d'etudes spatiales et d'instrumentation en astrophysique (LESIA), Observatoire de Paris-Meudon, France.

This work has been supported, either by financial or in-kind support, by the following organisations:

- University of Southern Queensland, including the Australian Centre for Sustainable Catchments
- Mount Kent Observatory,
- University of Louisville,
- Commonwealth of Australia, Department of Industry, Innovation, Science, Research and Tertiary Education under the International Science Linkages programme
- Anglo-Australian Observatory
- L'Institut de Recherche en Astrophysique et Planétologie (IRAP), l'Université Paul Sabatier (PRES Université de Toulouse)
- Laboratoire d'Etudes Spatiales et d'Instrumentation en Astrophysique (LESIA), Observatoire de Paris-Meudon
- Toowoomba Grammar School, Queensland, Australia

This work has been published under the auspices of the Bcool collaboration.

I would like to thank the technical staff at the MKO, including Dr Rhodes Hart & Dr John Kielkopf, AAT, CFHT and TBL for their helpful assistance during the acquisition of data contained in this thesis. This project used the facilities of SIMBAD, HIPPARCOS and IRAF. This research has made

use of NASA's Astrophysics Data System. This research was achieved using the POLLUX database (http://pollux.graal.univ-montp2.fr) operated at LUPM (Universit Montpellier II - CNRS, France) with the support of the PNPS and INSU. In addition, I wish to thank Dr Jean-Françios Donati, from IRAP, for providing ESPRIT, *ZDICAM* and the reduced data on EK Draconis and to Dr Pascal Petit, also from IRAP, for providing the reduced data on HD 35296. I would like to acknowledge the thousands of individuals who have coded for the LaTeX project for free. It is due to their efforts that we can generate professionally typeset PDFs now.

My thanks must go to the three anonymous examiners for taking the time to share their insight and expertise during the examination process and hence has made this thesis a better document.

Special thanks must go to Dr Bradley Carter and Dr Stephen Marsden for their friendship and extensive assistance with this work; from the beginning to the end.

Finally, this work is dedicated to lovely wife Geraldine and three beautiful children: Stephanie, Michaela and Andrew.

List of Publications

After enrolling in the Doctor of Philosophy Programme

The following are a list of papers have been published during my candidature of which I have had some involvement. The papers that relate directly to this thesis, have been highlighted in **bold** font.

1. Alécian, E., Wade, G. A., Catala, C., Grunhut, J. H., Landstreet, J. D., Bagnulo, S., Böhm, T., Folsom, C. P., Marsden, S., **Waite, I. A.**, 2012, *A high-resolution spectropolarimetric survey of Herbig Ae/Be stars - I. Observations and measurements*, MNRAS, 429, 1001

2. Henrichs, H. F., Kolenberg, K., Plaggenborg, B., Marsden, S. C., **Waite, I. A.**, Landstreet, J. D., Wade, G. A., Grunhut, J. H., Oksala, M. E. and Mimes Collaboration, 2012, *σ Lup Stroemgren v differential magnitudes (Henrichs+, 2012), VizieR On-line Data Catalog: J/A+A/545/A119* Originally published in: 2012, A&A, 545, 119

3. Henrichs, H. F., Kolenberg, K., Plaggenborg, B., Marsden, S. C., **Waite, I. A.**, Landstreet, J. D., Wade, G. A., Grunhut, J. H., Oksala, M. E., 2012, *Discovery of a magnetic field in the early B-type star σ Lupi*, A&A, 545, 119

4. Folsom, C. P., Bagnulo, S., Wade, G. A., Alécian, E., Landstreet, J. D., Marsden, S. C., **Waite, I. A.**, 2012, *Chemical abundances of magnetic and non-magnetic Herbig Ae/Be stars*, 2012, MNRAS, 422, 2072

5. **Waite, I. A., Marsden, S. C., Carter, B. D., Alécian, E., Brown, C., Burton, D., & Hart, R., 2011, *High-resolution Spectroscopy and Spectropolarimetry of Some Late F- / Early G-type Sun-like Stars as Targets for Zeeman Doppler Imaging*, PASA, 28, 323.**

6. Henrichs, H. F., Kolenberg, K., Plaggenborg, B., Marsden, S. C., **Waite, I. A.,** Landstreet, J., Grunhut, J., Oksala, M., Wade, G., the MiMeS Collaboration, 2011, *Discovery of the magnetic field of the B1/B2V star σ Lupi*, arXiv1108.4556.

7. Henrichs, Huib F., Kolenberg, Katrien, Plaggenborg, Benjamin, Marsden, Stephen C., **Waite, Ian A.,** Wade, Gregg A., 2011, *The magnetic field of the B1/B2V star σ Lup*, IAUS, 272, 192.

8. **Waite, I. A., Marsden, S. C., Carter, B. D., Hart, R., Donati, J.-F., Ramírez Vélez, J. C., Semel, M., Dunstone, N., 2011, *Magnetic fields and differential rotation on the pre-main sequence - III. The early-G star HD 106506*, MNRAS, 413, 1949.**

9. Marsden, S. C., Jardine, M. M., Ramírez Vélez, J. C., Alécian, E., Brown, C. J., Carter, B. D., Donati, J.-F., Dunstone, N., Hart, R., Semel, M., **Waite, I. A.,** 2011, *Magnetic fields and differential rotation on the pre-main sequence - II. The early-G star HD 141943 - coronal magnetic field, Hα emission and differential rotation*, MNRAS, 413, 1939.

10. Marsden, S. C., Jardine, M. M., Ramírez Vélez, J. C., Alécian, E., Brown, C. J., Carter, B. D., Donati, J.-F., Dunstone, N., Hart, R., Semel, M., **Waite, I. A.,** 2011, *Magnetic fields and differential rotation on the pre-main sequence - I. The early-G star HD 141943 - brightness and magnetic topologies*, MNRAS, 413, 1922.

11. Marsden, Stephen C., Jeffers, Sandra V., Donati, Jean-Francois, Mengel, Matthew W., **Waite, Ian A.,** Carter, Brad D., 2010, *Do young Suns undergo magnetic reversals?* IAUS, 264, 130.

12. Guggenberger, E., Kolenberg, K., Marsden, S. C., **Waite, I. A.,** Henrichs, H. F., Lüftinger, T., 2009, *High-Resolution Magnetic Field Measurements of RR Lyrae Stars with SemPol*, 1170, 278

13. Wood, P. R., Marsden, S., **Waite, I.,** Nicholls, C. P., 2009, *Spectropolarimetric Observations of the Sequence-D Red Giant Variables S Lep and Z Eri.* AIPC, 1170, 173

14. Marsden, S. C., Donati, J.-F., Petit, P., Dunstone, N. J., Jardine, M., Carter, B. D., **Waite, I. A.,** Semel, M., Ramírez Vélez, J., 2009, *Stellar Magnetic Fields in Swollen Convection Zones.* ASPC, 405, 531

15. Marsden, Stephen C., **Waite, Ian A.,** Carter, Bradley D., 2009 *Magnetic fields and differential rotation on the pre-main sequence.* AIPC, 1094, 531.

16. Wilson, I. R. G., Carter, B. D., **Waite, I. A.,** 2008, *Does a Spin-Orbit Coupling Between the Sun and the Jovian Planets Govern the Solar Cycle?* PASA, 25, 85

17. Kielkopf, John F., Carter, B., Brown, C., Hart, R., Hay, J., **Waite, I.,** 2007, *Performance of the Digital Science Partnership Remotely-Operated 0.5-Meter Corrected Dall-Kirkham Telescopes.* AAS, 211, 1130

18. **Waite, Ian,** Marsden, Stephen & The AAT Zeeman Doppler Imaging Team, 2007, *Spectropolarimetry of solar-type stars with the AAT*, Anglo-Australian Newsletter, 112, 3

Prior to enrolling in the Doctor of Philosophy Programme

The following papers have been published prior to my candidature.

1. Budding, E., Bembrick, C., Carter, B. D., Erkan, N., Jardine, M., Marsden, S. C., Osten, R., Petit, P., Semel, M., Slee, O. B., **Waite, I.,** 2006, *Multisite, Multiwavelength Studies of the Active Cool Binary CC Eri.* Ap&SS, 304, 13

2. Marsden, S. C., **Waite, I. A.,** Carter, B. D., Donati, J.-F., 2005, *Doppler imaging and surface differential rotation of young open cluster stars - I. HD 307938 (R58) in IC 2602.* MNRAS, 359, 711

3. **Waite, Ian A.,** Carter, Brad D., Marsden, Stephen C., Mengel, Matthew W., 2005, *High-Resolution Spectroscopy of some Active Southern Stars.* PASA, 22, 29

4. Marsden, S. C., **Waite, I. A.,** Carter, B. D., Donati, J.-F., 2004, *Doppler imaging of G-dwarfs in two young open clusters.* AN, 325, 246

5. Slee, O. B., Budding, E., Carter, B. D., Mengel, M. W., **Waite, I.,** Donati, J.-F., 2004, *A Multiwavelength Study of CC Eridani.* PASA, 21, 72

6. Marsden, Stephen C., **Waite, Ian A.,** Carter, Brad D., Donati, Jean-Françios, 2003, *Doppler Imaging of a G-Dwarf in the Open Cluster IC 2602.* IAUJD, 9, 8

7. **Waite, I.,** 2000, *The active young solar-type star PZ Tel. (Thesis abstract).* PASA, 17, 286

8. **Waite, I. A.,** 1996, *Photometry using an ST-6 camera.* AuJA, 6, 277

Contents

[1]This section is based on the overview presented by Berdyugina, S.V. *Starspots: A key to the Stellar Dynamo*, vol 2, 2005, http://solarphysics.livingreviews.org/refdb/record/22832

List of Figures

List of Tables

Chapter 1

Introduction

The Sun's spots, flares, prominences and coronal mass ejections provide us with graphic demonstrations of the importance of magnetic phenomena in a stellar atmosphere. Some of these solar phenomena are shown in Figure 1.1. This magnetic activity has its origins inside the Sun. At the interface layer between the subsurface convective zone and the zone of radiative energy transport below it, solar differential rotation and convection motion combine to drive a dynamo that continually generates magnetic fields that emerge at the surface. Magnetic fields can thus help our understanding of the solar interior as well as its atmosphere. The variable nature of the magnetic fields on the Sun is a consequence of differential rotation that generates the large-scale toroidal magnetic field from the initial poloidal field. The precise process of regeneration of the poloidal magnetic field is still a matter of debate, with cyclonic convection (Parker, 1955) and meridional circulation (Dikpati et al., 2004) being two possible mechanisms.

1.1 The Sun as a Star

The Sun is a main-sequence G2V dwarf star approximately 4.5 billion years old and is the only dwarf star we can directly resolve to show the full range of photospheric, chromospheric and coronal activity. The Sun is nearly a perfect sphere with an oblateness measured to be $\epsilon = 8.77 \times 10^{-6}$ compared with a rigidly rotating sphere (Godier and Rozelot, 2000), with Kuhn et al. (2012) reporting a difference of only 10km between the equatorial and polar diameters. The basic structure of the Sun is shown in Figure 1.2. This simple model of the Sun's interior shows a core, where the Sun's energy is

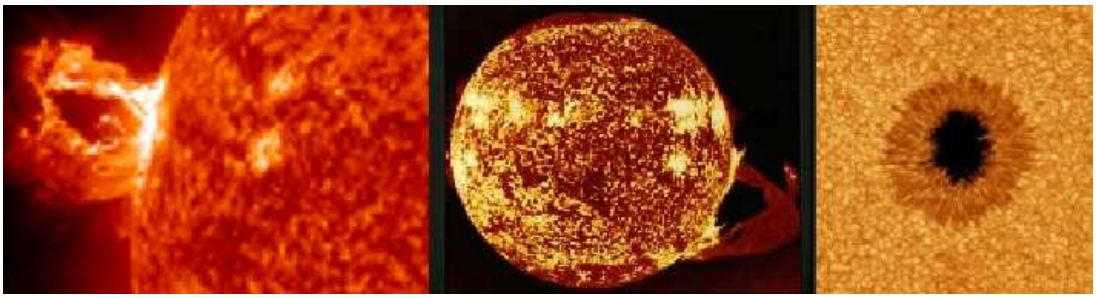

Figure 1.1: The Sun's flares, prominences and spots provide us with graphic demonstrations of the importance of magnetic phenomena in a stellar atmosphere. The solar flare[1] eruption (left) of April 16, 2012 was captured by NASA's Solar Dynamics Observatory at a wavelength of 304 Å. At the centre is a Skylab image of one of the largest eruptive prominences[2] in recorded history, taken December 19, 1973. The image of a sunspot[3] (right) was taken on July 2, 2010 using an TiO filter operating at 706 nm by the New Solar Telescope at Big Bear Solar Observatory. Real-time correction for atmospheric distortion (adaptive optics) was used. The spot is surrounded by the Sun's granular field in which the small individual bright points in intergranular lanes are near the diffraction limit of the telescope.

sources:

[1]http://www.nasa.gov/mission_pages/sunearth/news/News041612-M1.7flare.html *date accessed:* June 11, 2012.

[2]http://antwrp.gsfc.nasa.gov/apod/ap980830.html *date accessed:* June 11, 2012

[3]http://www.bbso.njit.edu/nst_gallery.html *date accessed:* June 11, 2012.

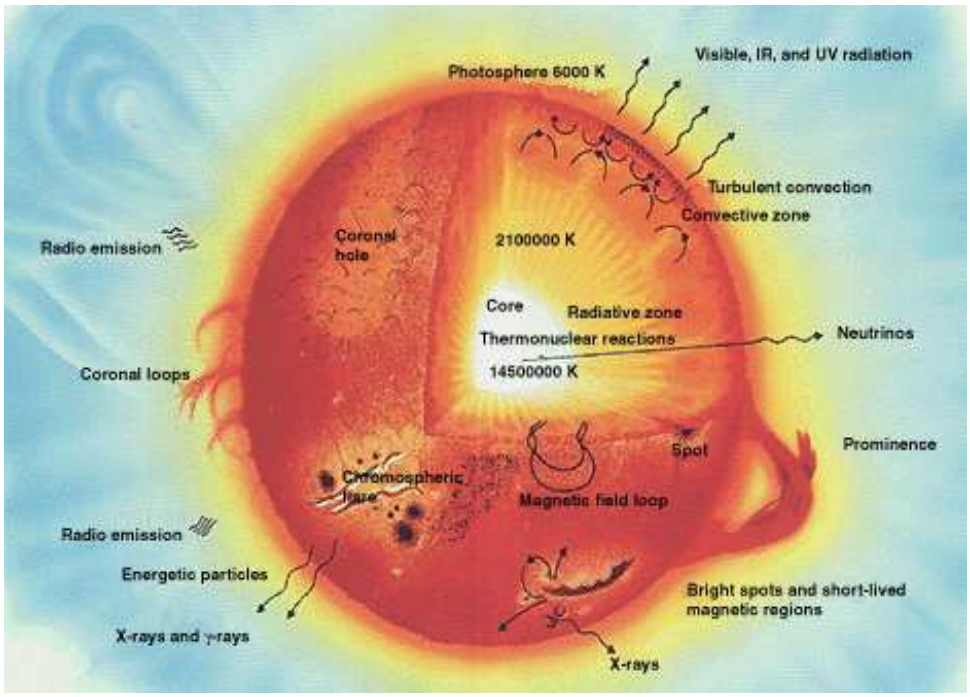

Figure 1.2: A simplified diagram of the internal structure of the Sun showing the core, radiative zone, convection zone and the photosphere.
source : http://imagine.gsfc.nasa.gov/docs/science/know_l2/sun_parts.html *date accessed:* January 11, 2013

produced extending to ∼25% of the solar radius and a radiative zone above it that transfers energy via a radiative diffusion process to the convective zone (CZ) boundary at a radial distance of $(0.713 \pm 0.001)R_{\odot}$ (Basu and Antia, 1997), giving a convective zone depth (CZD) of 0.287 $R_{\odot}$. The basic properties of the Sun are given in Table 1.1.

1.1.1 The Solar Atmosphere

The Sun's atmosphere can be described in terms of variations in temperature with height, with a simplified one-dimensional temperature model shown in Figure 1.3. The solar atmosphere can be divided into five physically distinct parts or regions, and when we move progressively outward from the Sun, these are the: (1) Photosphere; (2) Chromosphere; (3) Transition Region; (4) Corona and (5) Solar Wind. Each will now be considered in turn, as well as the forms of solar activity they display.

Table 1.1: Basic solar data, taken from (Lang, 2000)

Property	Value
Solar Luminosity ($L_\odot$)	3.854 x 10^{26} J s^{-1}
Solar Mass ($M_\odot$)	1.989 x 10^{30} kg
Solar Radius ($R_\odot$)	6.955 x 10^{8} m
Effective Photospheric Temperature ($T_{eff}\odot$)	5 780 K
Spectral Type	G2 V

The photosphere is the visible surface of the Sun, complete with faculae, granulations and sunspots. Faculae are photospheric brightenings that are mainly seen at the limb of the Sun and in the general vicinity of sunspots. Sunspots appear darker against the brighter photosphere and are restricted to the equatorial regions on the Sun. Sunspots are significantly cooler (∼4000 K) than the surrounding photosphere (∼5870 K) (Schrijver and Title, 2001) and their lifetimes range from a few days to several weeks. Granulation is due to the convection currents of plasma operating below the photosphere. Sunspots mark regions of high concentration of magnetic field that inhibit the convective flow of energy to the upper regions of the photosphere and the cooling of that area that results in darkening. Although sunspots are a photospheric phenomenon, they are associated with overlaying chromospheric plages and flares in active regions on the solar disc. The solar chromosphere is immediately above the photosphere and is more tenuous but hotter, and characterised by vertical elongated upwardly moving jets of material known as spicules. Plages are brightenings in the chromosphere and are almost equally well seen regardless of the limb angle. Solar prominences are material suspended above the photosphere into the chromosphere, and may be supported by hydrostatic effects (flare heating), ballistic effects (inertia) or magnetic effects (magnetic flux tubes). The region that separates the chromosphere from the much hotter corona is known as the transition region. The temperature rises rapidly from approximately 20 000 K at the top of the chromosphere to some 1 MK at the corona (Hathaway, 2012b). Here the gases are super-heated to temperatures in excess of 1 MK and extend out at least several solar radii. Due to these extreme temperatures, X-rays are emitted from this region (Hathaway, 2012a). In the corona, hydrogen, helium and other elements such as carbon, nitrogen and oxygen are fully ionized although some atoms such as iron

and calcium can retain some of their electrons. Coronal holes and solar activity are sources of a solar wind, consisting of mostly high-energy electrons and protons, that flows beyond the orbits of the planets to the heliopause, a boundary of sorts between the solar system and inter-stellar space.

The speed of the solar wind during solar minimum, when the wind speed is at a maximum (Pinto et al., 2011), can vary from ∼400 $\mathrm{km\,s^{-1}}$ up to ∼750 $\mathrm{km\,s^{-1}}$, depending on the original source of that wind (e.g. Feldman et al., 2005). Generally, the fast solar wind is associated with high heliographic latitudes (from funnels in the coronal holes) while the slower solar wind is associated with mid-latitudes regions, near the heliomagnetic streamer belt. This belt is a region of closed magnetic field encircling the Sun at the heliomagnetic equator (Phillips et al., 1995). The mass loss due to this low density solar wind $\sim 2 \times 10^{-14}\ M_{\odot}\ \mathrm{yr}^{-1}$ (e.g. Schrijver and Zwaan, 2000) and is dominated by outward flows originating at these low latitudes (Pinto et al., 2010). Pinto et al. (2011) used numerical simulations and found that this mass loss varies from $4.2 \times 10^{-14}\ M_{\odot}\ \mathrm{yr}^{-1}$ to $6.9 \times 10^{-14}\ M_{\odot}\ \mathrm{yr}^{-1}$ during an 11-year solar cycle. It is the solar wind, resulting in mass loss, coupled with the interaction with the magnetic field, that results in the loss of solar angular momentum, with maximum loss occurring on the Sun during periods of solar minimum (Pinto et al., 2010). This is commonly referred to as magnetic braking. Present day observations of the solar wind indicate the average angular momentum flux loss from the Sun is ∼0.2-0.3 $\times\ 10^{23}$ Nm (e.g. Pizzo et al., 1983). The decrease in the Sun's rotation rate throughout its main-sequence lifetime is believed to be due to this magnetic braking.

1.1.2 Solar Differential Rotation

Galileo first observed dark spots, now known as sunspots, on the solar surface and was able to use these sunspots to measure the rotational period of the Sun. However, the rotation of the Sun is not uniform. This means that the Sun's equatorial rotational period (∼25 d) is far different from that of the polar region which rotates at a much slower rate (∼34 d). This is known as surface differential rotation, or simply differential rotation. The differential rotation on the Sun today is modest, with the equator lapping the poles every ∼115 d. Modern techniques, such as that employed with the Global Oscillations Network Group (GONG) (e.g. Wilson et al., 1997) and National Aeronautics and Space Administration's (NASA) Solar and Heliospheric Observatory (SOHO)

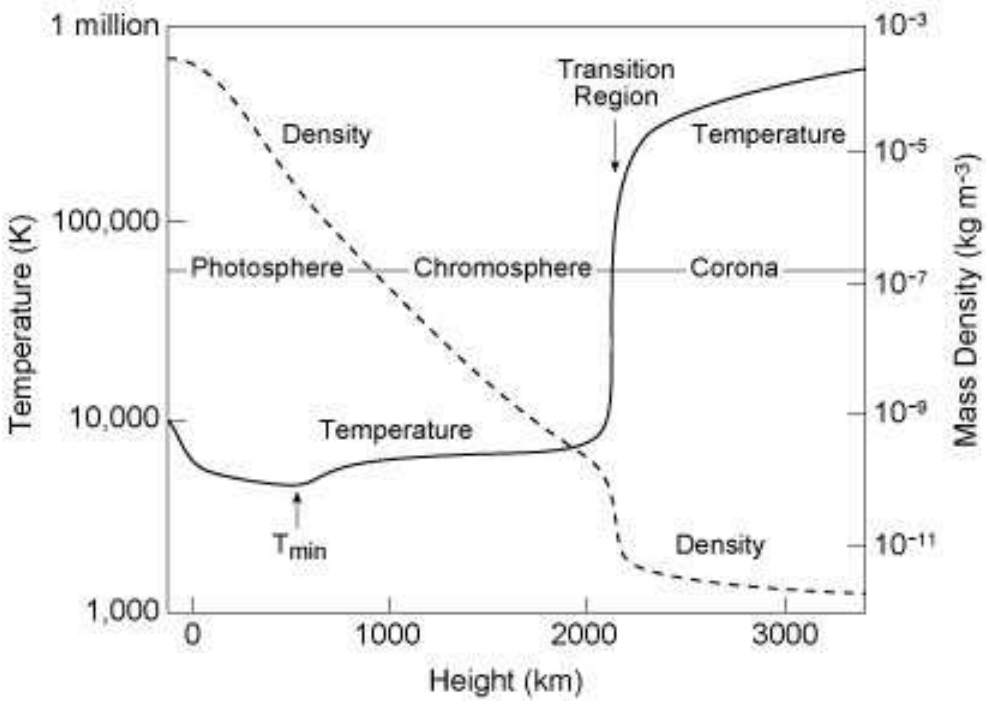

Figure 1.3: A simplified one-dimensional model of the temperature and density variations in the solar atmosphere as a function of height above the solar surface. The diagram has been taken from Lang (2000).

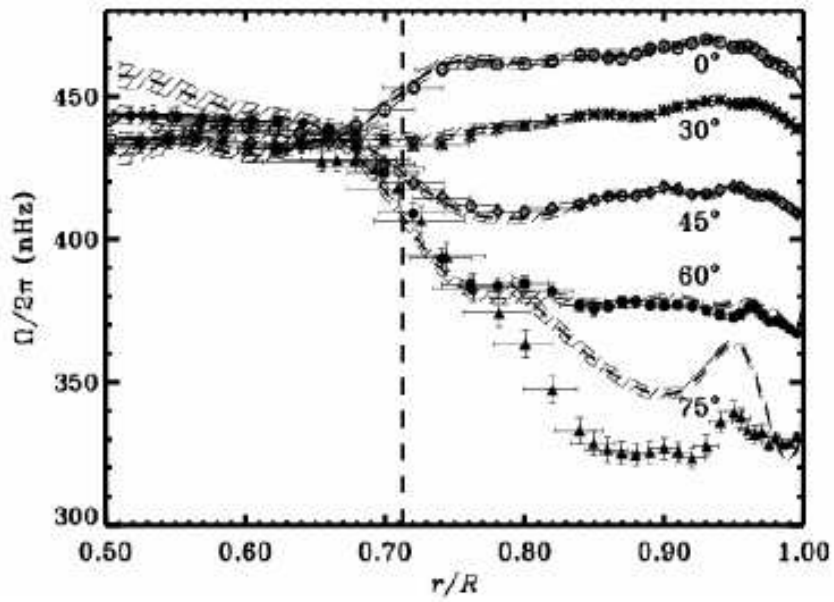

Figure 1.4: Measurements from the Solar and Heliospheric Observatory (SOHO) spacecraft show that differential rotation is maintained through the convective zone. Angular velocity is plotted as a function of radius for several latitudes. The dashed line indicates the base of the convective zone. Based on data from the Michelson Doppler Imager (MDI) instrument aboard the SOHO spacecraft, averaged over 144 days. Note that differential rotation disappears once the radiative zone is reached, supporting a solar model where the radiative zone rotates as a solid body. From Thompson et al. (2003).

(e.g. Schou et al., 1998) spacecraft have used the principles of helioseismology (which is the study of the propagation of wave oscillations, particularly acoustic pressure waves, in the Sun) to probe the outer layers of the Sun. These show that differential rotation occurs throughout the convection zone, whereas the radiative zone rotates as a solid body. Figure 1.4 shows this variation of rotation rate as a function of depth at various latitudes.

Differential rotation is believed to be due to steep temperature gradients from the core outwards and is thought to be generated by convection currents within the Sun (e.g. Kitchatinov and Olemskoy, 2011). Differential rotation, along with north-south meridional flow transporting angular momentum, are the two main components of the global circulation observed, and are thus drivers of the dynamo in the Sun (Kitchatinov,

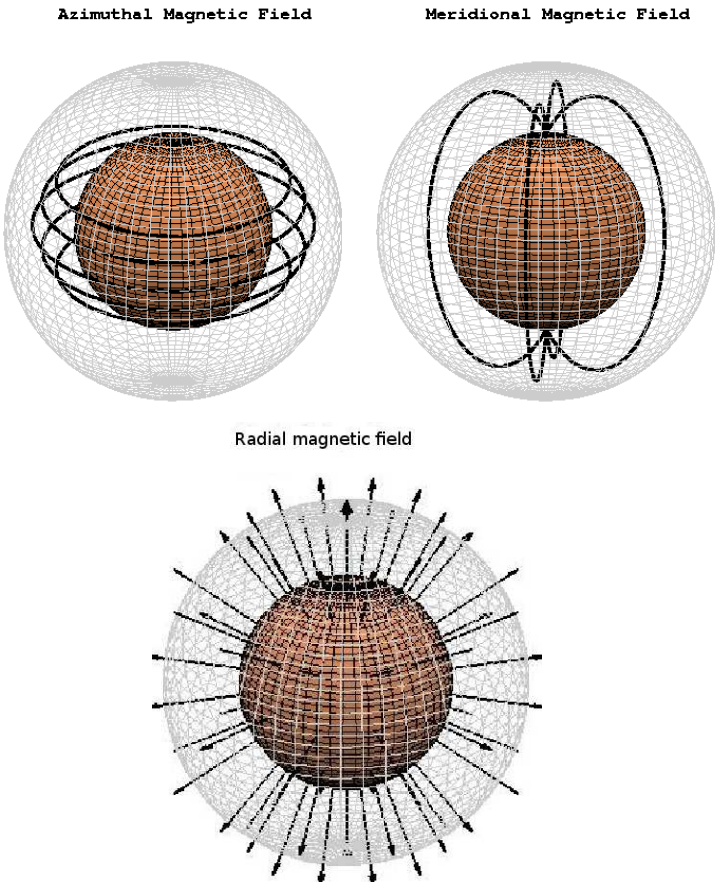

Figure 1.5: Simplified representation of the orientation of magnetic field orientations: Azimuthal (top left), meridional (top right) and radial (bottom) magnetic fields.

2013). As a result, the combination of convective currents, which bring the electrically charged plasma from deep within the Sun to the Sun's surface, and the differential rotation of the outer layers of the Sun strongly influences the Sun's magnetic field.

1.1.3 Magnetic Activity and the Dynamo: The α-Ω model

The solar atmosphere is very complex and displays both spatial and temporal variability that are due, in the most part, to magnetic fields. A simplified representation of the magnetic field orientations are shown in Figure 1.5 to illustrate the geometry of the east-west azimuthal field, the north-south meridional field and the radial magnetic field. Magnetic fields on the Sun were first measured in sunspots by Hale (1908). The Sun's

magnetic fields fundamentally arise from electrical currents generated by the collective contribution of plasma flows, with the fields forming closed loops amplified by the stretching and twisting effects of these flows.

These large-scale magnetic fields on the Sun can be written as the sum of the poloidal and toroidal components (Schrijver and Zwaan, 2000). The poloidal component may be considered a simple dipole field aligned with the rotation axis (i.e. Meridional field or North-South field lines in Figure 1.5) while the toroidal component may be thought of as the Azimuthal, or East-West, field lines. These magnetic fields are generally considered to arise from an α-Ω dynamo (Babcock, 1961) operating in the tachocline, a thin layer at the base of the solar convective zone where solar rotation abruptly changes. Large-scale toroidal magnetic fields are generated at the tachocline from a weak poloidal magnetic field as a result of the strong shear forces occurring between the nearly solid-body radiative zone and the differential rotation of the solar convective zone (MacGregor and Charbonneau, 1997; Charbonneau and MacGregor, 1997). As a result, toroidal magnetic fields upwardly traverse the entire convective zone and emerge at the photosphere, thereby forming active regions. Zwaan (1987) argues that the magnetic fields emerge from the photosphere in the form of discrete flux tubes that carry the magnetic energy from the tachocline through the convective zone and into the solar atmosphere. The magnitude of these magnetic fields is in the order of $\sim 10^3$ Gauss or more. At the surface, there is a subsequent reversal of the global poloidal field occurs the toroidal field is converted into the poloidal field. This is the α-effect. A simplified picture of the generation of the Sun's magnetic field is shown in Figure 1.6.

Whereas it is true that the solar dynamo is often thought to operate in the tachocline, there are alternative views. Brandenburg (2005) has argued that the dynamo is operating in the bulk of the convection zone, known as a distributed dynamo, and may be strongly shaped by the near-surface shear layer. Another view is known as the Babcock-Leighton flux transport model (e.g. Dikpati and Charbonneau, 1999). This is characterised by a solar-like differential rotation profile and a single-cell meridional flow in the convective envelope that is directed poleward at the surface.

This surface activity occurs in bipolar spot magnetic active regions close to the equator (typically within 35 degrees). The magnetic field lines that connect adjacent bipolar active regions thus align roughly East/West, wrapping around the Sun due to solar differential rotation. The leading spot forms slightly closer to the equator than the

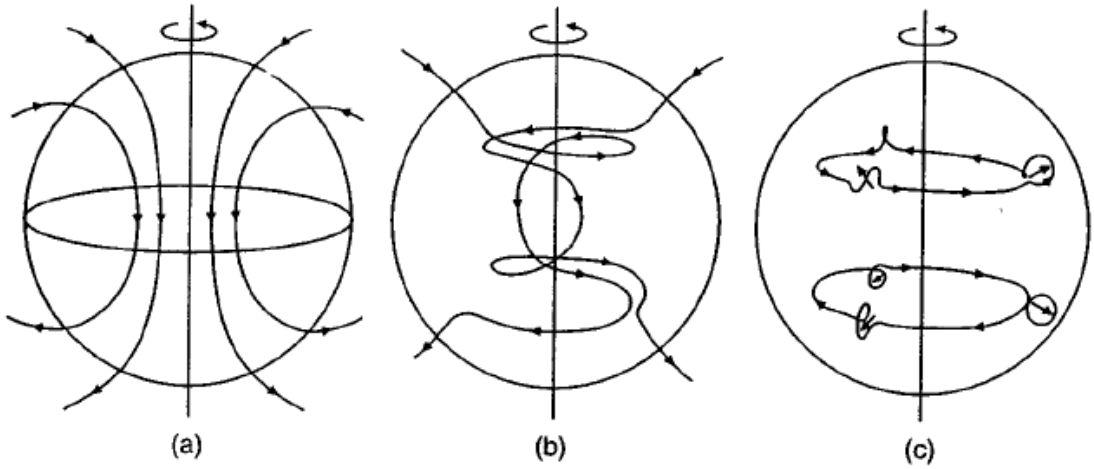

Figure 1.6: The solar dynamo is generally considered to be an α-Ω dynamo. This figure shows the conversion of (a) the initial solar poloidal field into (b) toroidal field (the Ω-effect) and back into (c) poloidal field (the α-effect). Image taken from Russell (1999).

trailing spot, with the tilt, due to the Coriolis effect, progressively larger for groups further from the equator. This effect is known as Joy's law (Hale et al., 1919). The leading spot of nearly all active regions on one hemisphere tend to have the same magnetic polarity, with the other hemisphere simultaneously showing spot pairs led by the opposite polarity.

Every eleven or so years, the polarity of the leading spots reverses as does the Sun's global field (Hale's law: Hale et al., 1919), and signifies the beginning of a new sunspot cycle. After two such spot cycles, the Sun's magnetic field thus repeats, making the magnetic cycle of the modern-day Sun some 22 years in duration. Measurement of sunspot latitudes over time reveals the familiar "butterfly" pattern, showing the cyclic nature of solar activity, first presented by Maunder (1904). Figure 1.7 shows how the typical sunspot latitude decreases during a solar cycle. Total sunspot area for a given hemisphere also follows this cyclic pattern. Babcock (1961) first suggested that differential rotation and convective motion drive these cycles. During a cycle, there is a pronounced migration of spot activity towards the equator. This drift could be due to cyclonic convection (Parker, 1955) as a result of differential rotation and meridional circulation near the base of the convection zone (Küker et al., 2001; Dikpati et al., 2004).

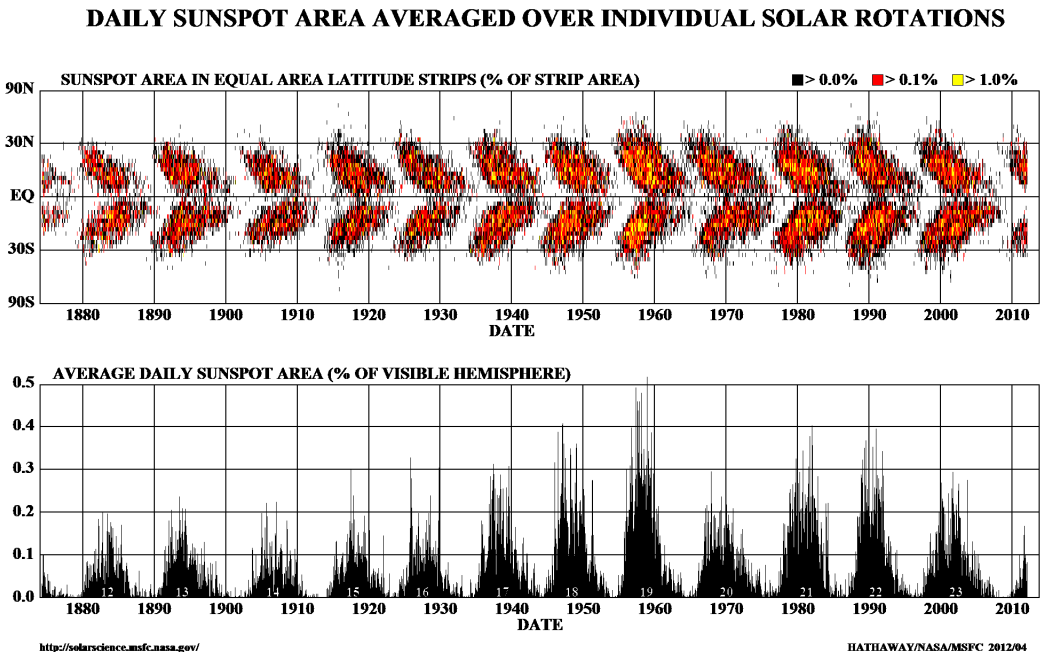

Figure 1.7: Solar butterfly diagram (upper panel) shows how the typical sunspot latitude decreases during a solar cycle. The sunspot coverage (lower panel) shows how the daily sunspot area, as a function of the visible hemisphere of the Sun, changes during the solar cycle. This diagram is based on data from 1874 to March, 2012. This figure was produced by D.H. Hathaway, NASA Marshall Space Flight Centre and was obtained from http://solarscience.msfc.nasa.gov/images/bfly.gif *date accessed:* April 04, 2012.

Thus differential rotation coupled with meridional flows are the two major components of the global circulation responsible for this observed migration of sunspot activity. However, there is still debate as to which of these two physical processes are controlling the magnetic cycle (e.g. Charbonneau, 2005).

1.2 Solar-Stellar Connection

The solar-stellar connection refers both to what can be learned about other stars from the Sun and what can be learned about the Sun from studying other stars. A key question in this respect is: how does the young Sun differ in its internal structure and energy transport systems when compared with the modern-day Sun? An understanding

of the solar-dynamo and resulting magnetic fields of active, young, solar-type stars gives us a window into the Sun's past and gives us clues to the evolution of the Sun from its pre-main sequence (PMS) existence.

1.2.1 Stellar Magnetic Activity across the HR Diagram

Stellar observations remind us of the importance of magnetic fields to stellar astrophysics, by providing evidence of magnetic phenomena in the atmospheres of a wide range of stars (young, old, cool, warm) and stellar systems (binary, single).

Stars that are significantly lighter than the Sun ($M \leq 0.35 M_{\odot}$) are generally completely convective (Chabrier and Baraffe, 1997) in their structure and transport of energy. These low mass stars (M and L spectral types) make up a large proportion of the Galaxy and are of interest due to these strong surface magnetic fields (Johns-Krull and Valenti, 1996). Active M-type red dwarf stars display variability; the stellar equivalent of solar magnetic activity. For instance, strong optical flares, analogous to solar flares, have been observed on stars such as UV Ceti type stars, a class of stars often referred to as flare stars. These stars increase in brightness over a broad wavelength range from X-rays to radio waves on time scales from a few minutes to a few hours. Chromospheric activity varies according to spectral type. Hawley et al. (1996) used the H_{α} spectral line (specifically the ratio of the luminosity emitted in H_{α} to the bolometric luminosity) and found that the activity level increases with spectral type reaching a maximum at approximately M5 before declining again. However, West et al. (2004) used a larger dataset from the Sloan Digital Sky Survey[1] to observe the mean activity strength being constant over the range M0 to M5-type but declining at later spectral types. This progression from early-M to late-M dwarfs is important as it coincides with the mass regime where the transition from partial convection to full convection occurs (Chabrier and Baraffe, 1997) where there is probably no tachocline, hence no differential rotation, to drive the magnetic fields and the associated magnetic activity. While some M-dwarf stars exhibit magnetic related phenomena, a large fraction of M-dwarfs have very limited observable activity and hence are becoming the "targets for the search for Earth-like extrasolar planets" (Reiners et al., 2012).

Stars that have masses larger than $0.35 M_{\odot}$ but less than $1.3 M_{\odot}$ are known as solar-type stars, possessing an internal structure similar to the Sun, as shown in Figure 1.2. As the

[1] www.sdss.org/

mass of the star increases, the depth of the convection zone decreases. Various authors have classified solar-type stars in terms of the B-V colour index. Cayrel de Strobel (1996) defined solar-type stars within the range of 0.48 $\leq$ B-V $\leq$ 0.80. Soderblom (1985) extended this range from 0.50 $\leq$ B-V $\leq$ 1.00, or in terms of spectral type, from ∼F8 V to ∼K2 V. This equates to an effective temperature range of ∼4940 K $\leq$ T_{eff} $\leq$ ∼6170 K (Gray and Corally, 2009). A subset of solar-type stars are solar-analogues (or sun-like) stars. These have similar properties to the Sun, with T_{eff} within 500 K and no close companion (Saxner and Hammarbäck, 1985). Solar-twins are generally indistinguishable from the Sun in terms of its evolutionary state (± ∼1 Gyr), metallicity, T_{eff} (within 10 - 50 K) and have no known stellar companions (Soderblom and King, 2013). By implication, the search for sun-like stars and solar-twins is motivated by the search for Earth-like planets, particularly in habitable zones. This is a region around a star in which it is theoretically possible for a planet, with sufficient atmospheric pressure, to have water in its liquid state. One sun-like star with a potential habitable zone similar to the Sun is HD 70642. This particular star has an extra-solar planet ($\geq$ 1.97 ± 0.18 M_j) orbiting it in a nearly circular orbit (e = 0.034) at 3.23 ± 0.19 Astronomical Units (AU) (Carter et al., 2003). This star is theorised to have a habitable zone of ∼1 AU (Hinse et al., 2008). One possible solar-twin is HR 6060 (18 Scorpii) (Porto de Mello and da Silva, 1997), although as yet, no planets have been found orbiting this star. Currently, the "best candidate" for a solar-twin is HIP 56948 (Meléndez and Ramírez, 2007; Meléndez et al., 2012) as it closely resembles the Sun in almost every respect (size, mass, chemical abundances including lithium abundances). Like HR 6060, no planetary system has yet been found around HIP 56948.

Young, single, solar-type F-, G-, K-type stars (stars they have both a convective zone and a radiative zone) are usually stars that display abundant activity derived from powerful dynamos. These stars are still carrying sufficient angular momentum as to be rotating once every few days or less, giving rise to this abundant activity. T-Tauri type stars are usually F-, G-, K- type PMS stars that are very active with large star spots, prominences and other magnetically induced phenomena. Members of evolved binaries where rapid rotation is preserved and interiors have deep convective zones also display starspots, and are usually chromospherically active. Examples of this type are RS Canum Venaticorum (RS CVn) type stars. RS CVn stars are close detached binaries with a more massive G- or K-giant (or subgiant) and a secondary subgiant (or dwarf),

usually G- to M-type. For example, the RS CVn type star HR 1099 has been observed extensively and was the first star, other than our Sun, to be magnetically mapped using spectropolarimetry (see Chapter 2) (Donati et al., 1992b,a). RS CVn's are characterised by photometric variability, chromospheric emission (activity), fast rotation and orbital period variations. Algol-like systems and W Ursae Majoris-type (W UMa) stars are eclipsing binaries that exhibit rapid rotation and other magnetic induced phenomena. FK Comae-type (FK Com) stars are evolved stars, and are most likely coalesced W UMa binaries, rather than single stars (Bopp and Stencel, 1981). FK Com stars exhibit rotationally modulated photometric variations, due to starspots, strong and variable chromospheric emission and are very rapidly rotating. BY Draconis-type (BY Dra) stars are usually (but not always) K- or M-type dwarf stars that vary in brightness as a result of rotation, usually as a result of spot activity or other chromospheric activity. In short, magnetic activity phenomena have been observed (or inferred) on all these stellar types and is thus appears to be ambiquitious on solar-type stars.

Stars significantly heavier than our Sun ($M \geq 1.3 M_{\odot}$) appear not to possess a convective zone (Schrijver and Zwaan, 2000). Massive stars, such as the PMS Herbig Ae/Be stars, OB stars, neutron stars and magnetars have magnetic fields that have influenced their evolution. Some stars even appear to preserve "fossil" magnetic fields from their formation (Mathys, 2007). Many of these hotter stars appear to have static, uncomplicated magnetic fields (e.g. Berdyugina, 2009). Stars with masses exceeding 10 $M_{\odot}$ tend to be very active with strong (and variable) winds, variations in Hα emission, chemical peculiarities and radio/X-ray emissions. However, surveys such as that conducted by Hubrig et al. (2008) found longitudinal magnetic fields, $< B_z > \leq 200$G and concluded that organised, large-scale magnetic fields are not widespread among these O-type stars.

Thus, the role of magnetic fields in stellar studies is a broad one, occurring across a substantial portion of the H-R diagram. MagIcS[1] (Magnetic Investigation of various classes of Stars) is an international collaboration aimed at studying the origins of magnetic fields and impact on any attendant planetary systems. There are a number of threads associated with MagIcS including Bcool[2] (Magnetic fields of low-mass stars),

[1] http://www.ast.obs-mip.fr/users/donati/magics/v1/

[2] http://bcool.ast.obs-mip.fr/Bcool/Bcool__cool_magnetic_stars.html

MiMeS[1] (magnetism in massive stars), MaPP[2](magnetic protostars and planets) and SPI[3] (star-planet interactions). This work has been completed under the auspices of the Bcool collaboration.

1.2.2 Age, Rotation and Stellar Magnetic Activity

Over the past 40 years, there have been a number of observational surveys to establish a relationship between a star's age, rotation period and magnetic activity such as the Columbia/Cornell/Caltech Palomar Transient Factory (Covey et al., 2010) while others (e.g. Mamajek and Hillenbrand, 2008; Mamajek, 2009) continue to improve age estimations for solar-type dwarf stars using a range of activity-rotation diagnostics such as the Ca II H and K emission index. Thus the age and rotation of a star is linked to this activity for solar-type stars.

Skumanich (1972) first suggested that as stars age, they rotate much more slowly. Skumanich proposed that $v_{rot} \propto t^{0.5}$, as does the level of Ca II emission, a measure of chromospheric activity and proxy for magnetic field strength. A number of authors (e.g. Vilhu, 1984; Noyes et al., 1984; Baliunas et al., 1995; Güdel et al., 1997) show that as the rotation rate decreases, so does the activity seen on the star. The primary driver of this decrease in rotation rate throughout the main-sequence life of the star is a result of the angular momentum loss via magnetic braking (e.g. Weber and Davis Jr, 1967; Mestel, 1992) predominately by the solar wind. As a result, rotation and stellar magnetism are inevitably linked.

The time required for stars to significantly "spin-down" is a function of stellar mass (e.g. Barnes, 2003; West et al., 2004). Scholz (2009) suggest that the main agents for rotational braking are believed to be star-disk interaction and magnetically powered stellar winds. Star-disk interaction involves the angular momentum being removed via the interaction between the star and the disk. This includes "disk-locking" and accretion-powered stellar winds. Disk-locking is believed to operate over relatively short timescales and early in the star's life, from 1 Myr to 10 Myr. This is roughly the same timescale as the disk itself, with Jayawardhana et al. (2006) suggesting that rotational braking by disks extends to ∼8 Myr. However, the time-scales involved with

[1] http://www.physics.queensu.ca/ wade/mimes/MiMeS_Magnetism_in_Massive_Stars.html
[2] http://lamwws.oamp.fr/magics/mapp
[3] http://lamwws.oamp.fr/exo/starplanetinteractions/SPIScience

the stellar winds as a mechanism for mass loss are much longer. Wood et al. (2002) used NASA's Hubble Space Telescope (*HST*) to investigate the mass-loss rates from some solar-like G- and K-dwarfs. When combining with other measurements, they suggested that the mass loss, M, is related to time, t, and developed the power law: $M \propto t^{-2.00 \pm 0.52}$. This indicates that mass loss decreases with time for solar-like stars. Wood et al. (2002) goes on to suggest that the solar wind may have been as much as 1000× stronger in the past.

These age, rotation and stellar magnetic activity relationships are now firmly established for main-sequence stars (MS), including the Sun, and are driven by the magnetic fields that are generated within the star's convective zone with the primary driver of this generation being differential rotation.

1.2.3 Stellar differential rotation

Observations of young stars of late F-/early G-spectral type, as mentioned previously, exhibit abundant magnetically related activity. These solar-type stars have been shown to rotate "differentially", and can have significantly higher levels of surface differential rotation compared to that of the Sun (e.g. see Marsden et al., 2006; Reiners, 2006) by an order of magnitude greater.

Several stars have had their differential rotation measured using a range of techniques (see Section 2.6). For example, PZ Telescopium (Barnes et al., 2000) has a photospheric shear ∼1-2 times the solar value, meaning that the equator laps the polar regions (otherwise known as the *laptime*, see Section 2.17) in ∼86 ± 14 days. LQ Lupus (Donati et al., 2000) has a photospheric shear ∼2-3 times the solar value, meaning its *laptime* is ∼50 ± 10 days. Possibly the star with the highest photospheric shear, as measured using techniques consistent with this thesis, is V889 Her (HD 171488). Jeffers and Donati (2008) measured a *laptime* of only 12.1 ± 1 days. This is compared with the Sun's *laptime* of ∼115 days. With ongoing monitoring, it has been observed that some stars have undergone variations in their level of differential rotation. AB Doradus, for example, (Donati and Collier Cameron, 1997; Collier Cameron and Donati, 2002; Collier Cameron et al., 2002; Donati et al., 2003a) has undergone temporal fluctuations (Collier Cameron and Donati, 2002) with observed lap times of ∼70 to 140 days while Donati et al. (2003a) measured between ∼108 to ∼136 days. The variation in

LQ Hydrae's *laptime* is even more remarkable. Donati et al. (2003a) observed variation in LQ Hydrae's *laptime* from ∼32 days to ∼436 days, in only one year! With the increasing sample size, one can note that the majority of stars do undergo "solar-like" differential rotation where the equatorial regions rotate faster than the polar regions. Alternatively, there are some stars such as DX Leo (SpType: K0V[1]) and LQ Hydra (SpType: K0V[1]) where the high-latitude spots appear to rotate faster than lower-latitude spots (Messina and Guinan, 2003).

Barnes et al. (2005a) have investigated the link between differential rotation and effective temperature, and hence convective turnover time, and were able to fit an empirical power law to recent observations of a small sample of stars. As stellar temperature increases, so does the rotational shear. Kitchatinov (2013) has proposed that differential rotation of a main-sequence star varies "mildly" with rotation rate but increase strongly with stellar surface temperature. Marsden et al. (2011b) and Jeffers et al. (2011) investigated differential rotation as a function of convective zone depth (CZD), demonstrating that differential rotation increases with decreasing CZD, i.e. the thinner the convective zone, the greater the rotational shear. As differential rotation is responsible for winding the magnetic field around the star's stellar rotation axis, and thus magnetic reconnection and reversal, the level of differential rotation could be linked to the star's magnetic cycle.

1.2.4 Stellar magnetic cycles

Do other stars show magnetic cycles? Stellar magnetic cycles have been inferred using a number of indirect approaches. The Mount Wilson HK project (Baliunas et al., 1995) use chromospheric Ca II H (396.85 nm) & K (396.37 nm) line fluxes and found that many cool stars exhibit cyclic changes. They also found some stars appear to have no cycles while very active stars tend to have irregular cycles. Messina and Guinan (2002) used photometry to track starspots and found that starspot cycles ranged from 2.1 to 13.1 years. Messina and Guinan (2003) further deduced that relative differential rotation, (specifically $\delta\Omega/\Omega$: see Section 1.1.2), is a key parameter controlling the length of the activity cycle, with the Ω value (the rotation) possibly being the dominant influence. Alternatively Donati et al. (2008b) suggest that the absolute differential rotation ($\delta\Omega$) could be the primary influence and that stars with higher levels of differential rotation

[1] Montes et al. (2001)

should have significantly shorter cycles (potentially as short as a few years) due to the more rapid winding of the magnetic fields around the rotation axis. Thus the role of differential rotation in cycle length is still uncertain.

1.2.5 The Stellar dynamo

To improve our understanding of the evolution of the solar dynamo, young solar-type F, G, and K stars provide proxies for the Sun's early history and insight into its intense pre-main sequence and zero-age main sequence magnetic activity including angular momentum loss. In this regard, observations of starspots and surface magnetic fields are important, as they provide the empirical basis for understanding the star's magnetic dynamo and its internal structure. On the Sun, a "shell-like" dynamo, based on the $\alpha - \Omega$ mechanism to amplify the fields as explained in section 1.1.3, can be used to explain the majority of the magnetic features observed, including the 11-year sunspot cycle. With this model, the α-effect is the sole source of the poloidal component whereas the Ω-effect (rotational shear) is the sole source of the toroidal component.

Spectroscopic and spectropolarimetric observations of solar-like stars in recent years show low-, mid- and high latitude spots, and even polar spots. These features cannot be explained by this $\alpha\Omega$ mechanism. One explanation of these features is that the magnetic dynamo is operating throughout the entire convective zone. This is known as a distributed $\alpha^2\Omega$ dynamo (Brandenburg et al., 1989; Moss et al., 1995), where both the α-effect **and** differential rotation shear contribute to the production of the toroidal field. Charbonneau (2009) suggests that this type of dynamo would operate in a star if the level of differential rotation is relatively weak, and/or if the dynamo occurs in a very thin layer.

A distributed dynamo in rapidly rotating stars should lead to flux tubes emerging at high latitudes almost parallel, due to the Coriolis effect, to the star's rotation axis, consistent with the observed high-latitude activity (Calibari et al., 1995). Studies by Donati et al. (2003b) of K-dwarf stars and by Marsden et al. (2011a,b) of PMS G-type stars (with temperatures commensurate with that of the Sun) show regions of near-surface azimuthal fields. Donati et al. (2003b) interpret this in terms of a dynamo being distributed throughout the entire convection zone and close to the surface of the star itself.

A distributed dynamo is one explanation for mid- to high latitude features observed on young solar-type stars. However, Schüssler and Solanki (1992); Schüssler et al. (1996); DeLuca et al. (1997) argue that these mid- to high latitude features result from the Coriolis force, leading to the strong poleward deflection of the flux tubes rising through the convective zone of a rapidly rotating cool star. This is supported by the numerical studies of Granzer et al. (2000) in their study of PMS and Zero Age Main Sequence (ZAMS) stars between 0.4 $M_{\odot}$ and 1.7 $M_{\odot}$. Their stellar models showed a strong increase in emergence latitude with increasing rotation rate with flux emergence both at low latitudes and polar regions in the early stages of stellar evolution. An alternative hypothesis (Kitchatinov and Rüdiger, 1999; Schrijver and Title, 2001) involves the transport of flux through the process of meridional flow to produce high latitude and even polar spot features. Kitchatinov and Olemskoy (2011) proposes that the meridional flow in slow rotators is distributed throughout the convection zone but with increasing rotation rate is more confined to the boundaries, both lower and upper, of the convection zone.

The strength of the dynamo is related to the star's rotation speed. Below a certain projected rotational velocity, $v\sin i \lesssim 20$ km s^{-1}, the strength of the star's magnetic dynamo is believed to be related to the star's rotation rate but above this speed, it is thought that dynamo saturation is occurring where the strength of the star's magnetic dynamo is no longer dependent upon stellar rotation. This plateau occurs at the $v\sin i \sim 20$ km s^{-1}. One empirical measure of this saturation in young solar-type stars is coronal X-ray emission. Pallavicini et al. (1981) found that X-ray luminosity increases as rotation increases according to the relationship $L_x \approx (v\sin i)^2$. However, Micela et al. (1985) found that this relationship didn't hold for more rapid rotation, placing a limit on the emission, defined as the ratio of the star's X-ray luminosity (L_x) to that of the star's bolometric luminosity L_{bol} (Vilhu, 1984), at $L_x/L_{bol} \sim 10^{-3}$. Stauffer et al. (1997) theorised that this is consistent with dynamo saturation. Upon reaching a projected rotation velocity of $\sim$ 100km s^{-1} the X-ray luminosity decreases below the saturated level (Randich, 1998), an effect that Prosser et al. (1996) called supersaturation. Supersaturation occurring in the fastest rotators has been investigated in more detail by Wright et al. (2011, 2013). They found that late F-type stars should never pass through the saturated regime, but simply moving straight from the unsaturated to supersaturated X-ray emission. They also theorise that a different dynamo configuration is

operating with stars with saturated coronal emission, hinting at a "correlation between empirical saturation threshold and the time when stars transition between convective (distributed) dynamos and interface (like operating on the Sun) sequences in rotational spin-down models". However, supersaturation remains controversial as Marsden et al. (2009) showed that there was no supersaturation for chromospheric emission in their study of IC 2602 and IC 2391.

As mentioned previously in Section 1.2.1, stars after spectral type of ∼M3 ($M \leq 0.35 M_{\odot}$) become fully convective. Late-M dwarfs most likely possess global magnetic dynamos very different from those in more massive stars. It is clear that self-sustained dynamos in fully convective stars are possible, but these dynamos are not $\alpha - \Omega$ but perhaps more α^2-type dynamo processes. For example, Rüdiger et al. (2003) has investigated cyclic dynamos solely based on the α-effect (α^2-dynamo). Whereas the link between the dynamo and stellar rotation in F- and G-type stars is compelling, it begins to break down in late-K and M stars. Pizzolato et al. (2003) observed the coronal X-ray emissions of late-type dwarfs (∼F8 to ∼M8: 0.5 ≤ B-V ≤ 2.0) and found that the "saturation" level of $L_x/L_{bol} \sim 10^{-3.3}$ in all stars with rotation periods shorter than ∼ 10 days. In addition, Stelzer et al. (2013) observed a similar "saturation" level of $L_x/L_{bol} \sim 10^{-3}$ for young M-dwarfs in the TW Hydra association (∼10 Myr). Like solar-type stars, Mohanty and Basri (2003) argue that there is a "saturation-type" rotation-activity relationship existing in early M-dwarfs ($v \sin i \leq 4$ km s^{-1}) with late-M dwarfs (M5.5 - M8.5) having a significantly higher saturation velocity ($v \sin i \sim 10$ km s^{-1}). Overall, this could indicate that this "saturation" level is independent of rotation period in fully convective stars. However, Reiners et al. (2012) found there was no evidence "for a transition from a rotationally dominated dynamo in partially convective stars to a rotation-independent turbulent dynamo in fully convective stars; turbulent dynamos in fully convective stars of spectral types around M4 are still driven by rotation". These conflicting views demonstrate that the understanding of the global magnetic field generation in M-dwarfs is still in its infancy.

Recently, Ligniéres et al. (2009) and Petit et al. (2010) have reported weak surface magnetic fields on the intermediate-mass star Vega. Dynamos can operate in the fully convective interior of more massive stars with buoyancy bringing the flux tubes to the surface (e.g. Charbonneau and MacGregor, 2001). Alternatively, MacDonald and

Mullen (2004) argue that this does not occur and offer an alternative transport mechanism based on the dynamo operating in shear-unstable gas in the radiative stellar envelope. Cantiello and Braithwaite (2011) have theorised the occurrence of subsurface magnetic fields on massive stars with thin convective layers. Yet again, these views demonstrate the uncertainty still remaining in this field.

The Sun today undergoes activity cycles in the form of magnetic reversals, but at what stage do these cycles begin during the early evolution of the star? Recent theoretical work by Brown et al. (2010) has suggested that young stars can undergo "attempted" field reversals, where the magnetic field begins to break-up, a signature of an impending reversal, only to reinforce again in the original direction. Brown et al. (2010) also showed that magnetic cycles can exist without the need of an "interface" layer like that observed on the Sun. Resolving the origin of the solar dynamo should help address the more general question of how stellar magnetic cycles develop in young stars, and affect any attendant emerging planetary systems. The search for targets is thus motivated by the need to study a sample of young Suns to test modern dynamo theory for these stars.

1.3 Selection of suitable targets

The investigation of young solar-type late-F, early-G stars provide proxies for the Sun's early evolution and insight into its intense pre-main sequence and zero-age main sequence magnetic activity. Five stars were selected on the basis of their observed activity, rapid rotation and apparent youthful evolutionary status. As discussed in Section 1.2.5, the strength of the star's magnetic dynamo is believed to be related to the star's rotation rate if $v \sin i \lesssim 20$ km s^{-1}, but above this speed, it is thought that dynamo saturation is occurring where the strength of the star's magnetic dynamo is no longer dependent upon stellar rotation. HD 35296, HD 29615 and EK Draconis are stars that the magnetic dynamo is still dependent on the star's rotation rate. The rotational behaviour of stars is often quoted using the projected rotational velocity, $v \sin i$, as the inclination angle of the star, as shown in Figure 1.8 is usually not known. The inclination angle has a large effect on the $v \sin i$. Therefore $v \sin i$ can only be used as a statistical measure of rotation, especially where low values are often observed. The true rotational velocity,

Table 1.2: Selected targets for this thesis.

Star	Spectral Type	$v \sin i$ ($\mathrm{km\,s^{-1}}$)	Age (Myr)	Mass ($M_\odot$)	Radius ($R_\odot$)
HD 106506	G0V[1]	≈80 [3]	≤ 10 [3]	1.5 [3]	2.15 [3]
HD 76298	G1V[1]	≈38 [3]	∼10 (?) [12]	1.6 [12]	2.20 [12]
HD 35296	F8V[2]	15.9 [4]	20-50 [7]	1.1 [8]	1.2 [9]
HD 29615	G3V[1]	≈18 [5]	20-30 [10]	0.95 [11]	0.96 [12]
EK Draconis	G1.5V[1]	16.8 [6]	30-50 [13]	1.06 [9]	0.99 [9]

[1]Torres et al. (2006); [2]Montes et al. (2001); [3]Waite et al. (2005); [4]Reiners and Schmitt (2003); [5]da Silva et al. (2009); [6]Valenti and Fischer (2005); [7]Li and Hu (1998); [8]Casagrande et al. (2011); [9]Wright et al. (2011); [10]Zuckerman and Song (2004); [11]Allende Prieto and Lambert (1999); [12]Waite et al. (2011a); [13]Järvinen et al. (2007)

v, could vary greatly depending on the inclination angle. The five targets are listed in Table 1.2.

1.4 Conclusions

The evolutionary origins of the solar dynamo remain unclear. However, young and rapidly rotating Sun-like stars display differential rotation and magnetic fields that can be used to empirically test modern dynamo models. This thesis investigates the nature of the underlying dynamo processes operating in young cool-dwarf solar-type stars by using the techniques of Doppler imaging (DI) and Zeeman Doppler imaging (ZDI) (Semel, 1989; Donati et al., 1992b, 1997) to test a number of hypotheses:

1. that distributed dynamos are operating on young, active, rapidly-rotating stars,
2. that strong but varying differential rotation, consistent with emerging activity cycles, is dependent on convective zone depth and rotation rate,
3. that young stars undergo rapid temporal variations of surface magnetic topologies.

Chapter 2 reviews the tools that will be employed in this study. These include the techniques of DI and ZDI using Least Squares Deconvolution (LSD) to extract the various signatures from the high-resolution spectropolarimetric spectra obtained from

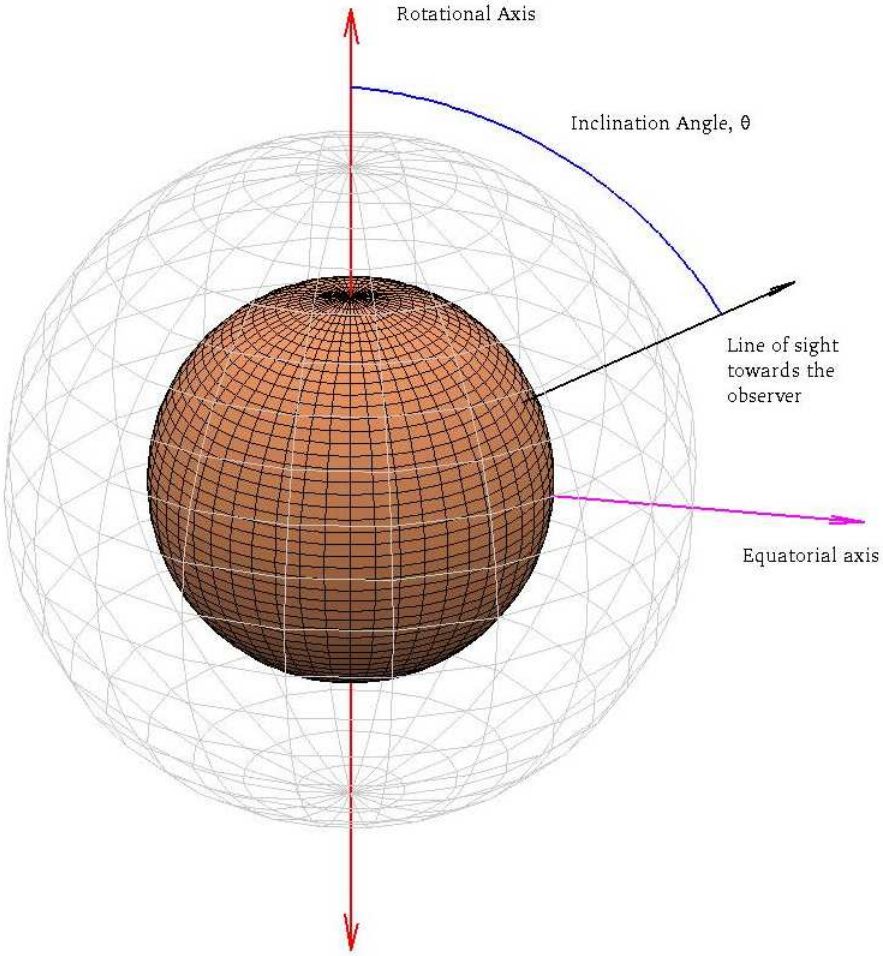

Figure 1.8: An illustration defining the inclination angle of a star

the Anglo-Australian Telescope (AAT), Canada-France-Hawaii Telescope (CFHT) and Télescope Bernard Lyot (TBL).

Chapter 3 focuses on the rapidly rotating, PMS star HD 106506 (SpType = G1V; Age $\approx$ 10Myr). Brightness and magnetic maps are presented and the magnitude of differential rotation using both the brightness and magnetic tracers is determined. Evidence is presented that this star has a substantial azimuthal magnetic field, indicative of a dynamo operating on this star this is fundamentally different from that operating on the sun today.

Chapter 4 investigates another solar-type star HD 76298 (SpType = G1V). Its rotational velocity, $v\sin i$, is approximately half that of HD 106506. However, HD 76298 provides a conundrum: Is it a pre-main or post-main sequence star. Evidence is provided that this star is a PMS star; however, it could be an evolved FK Comae star.

Chapters 5 and 6 focuses on two moderately rotating, young suns HD 35296 (SpType = F8V; Age $\approx$ 20-50Myr) and HD 29615 (HIP 21632; SpType = G3V; Age $\approx$ 30Myr). Both of these stars are approximately similar in size, photospheric temperature and rotational velocities. Both appear to have a dynamo that is operating entirely throughout the convective zone. The differential rotation measured on HIP 21632 has the largest rotational shear yet measured using the principles of ZDI.

Chapter 7 focuses on another moderately rotating star, EK Draconis (HD 129333; SpType = G1.5V; Age $\approx$ 30-50Myr) - the infant Sun. This star has previously been studied extensively via multi-wavelength studies using an array of telescopes and techniques. This investigation uses ZDI for the first time to add to the knowledge surrounding this important young Sun.

Chapter 8 presents the overall conclusions that can be drawn from this work, the questions that this work has raised and suggestions for extending this work in the future.

Chapter 2

Surface Imaging of Rapidly Rotating Solar Type Stars

2.1 Introduction

The study of young sun-like stars provides a window onto the Sun's intensely active past and an understanding of early solar evolution. In particular, the observations of starspots and associated magnetic activity gives clues to the underlying dynamo processes operating in young sun-like stars. Thus, the study of magnetic fields helps us understand the stellar interior as well as its atmosphere. This chapter broadly reviews the observational techniques used to observe, both directly and indirectly, the magnetic fields of solar-type stars. More specifically, the techniques that are employed in this thesis including Broadband Photometry (Section 2.3), Doppler imaging (DI: Section 2.4) and Zeeman Doppler imaging (ZDI: Section 2.5) are reviewed. A major step in the analysis of the data is the utilisation of Least Squares Deconvolution (LSD) (Section 2.5.1) that is employed to extract the magnetic signatures from the polarised light thereby permitting ZDI to map the surfaces of stars and determining the magnetic field and surface differential rotation (Section 2.6). The key instrumentation used in this thesis will also be reviewed.

2.2 Overview of observational techniques

2.2.1 Photometry

There are several techniques that have been employed to study the surface features of stars. Photometry is the most common technique for studying stellar activity, specifically starspots. There are a diversity of approaches, ranging from space-based missions such as the European Space Agency's (ESA) *HIPPARCOS* mission[1], an ever increasing number of Automatic Photometric Telescopes (APTs) and a large band of amateur astronomers providing data for a large sample of stars. The accuracy of these various programmes permit studies in a range of astrophysical problems including the study of stellar activity cycles.

Ground-based observatories, such as APTs, are being used to provide a vast amount of data. Many of these APTs have apertures from 20 cm to 1.2 m around the world and attain an accuracy of $\sim$ 2-5 mmag (milli-magnitude). With the advent of relatively cheap CCD cameras, amateur astronomers across the world have provided an enormous amount of data, both in terms of supporting larger programmes or simply conducting photometric observations of a range of stars across the HR diagram. Amateur astronomers are particularly adept in studying long period variables such as Mira-type stars as they have one advantage over the majority of "professional" observatories - time. The American Association of Variable Star Observers (AAVSO)[2] is one such organisation that co-ordinates the observations made largely by amateur astronomers so as to make them freely available to all astronomers, including professionals.

In recent years, space-based missions have contributed large amounts of high quality data on stars, including solar-type stars. The *HIPPARCOS* mission attained a photometric accuracy of 1 mmag. *HIPPARCOS* was launched in 1989 to measure, to unprecedented accuracy, the parallax and proper motions of over 120 000 stars. A by-product of this effort was the 2-colour photometry for more than 2.5 million stars. At the time, *HIPPARCOS* revolutionised the number of variable stars that it was able to find. More recent space missions such as *CoRoT*[3] from the Centre National d'Etudes

[1] http://www.rssd.esa.int/index.php?project=HIPPARCOS
[2] http://www.aavso.org
[3] http://smsc.cnes.fr/COROT/

Spatiales (CNES) (Baglin et al., 2001) and National Aeronautics and Space Administration's (NASA) Kepler[1] spacecraft use high-precision photometry to find exo-planets, particularly earth-size exo-planets, and to study the interior of stars through asteroseismology (stellar oscillations). Whereas *HIPPARCOS* was revolutionary in 1989, Kepler is proving equally revolutionary since its launch in 2009 with its precision and ability to detect earth-like planets, as well as observing solar-like oscillations (e.g. Chaplin et al., 2010; Stello et al., 2010), photometric variability due to magnetic-related activity (e.g. Basri et al., 2010) including various types of variable stars such as RR Lyrae stars (Kolenberg et al., 2010) and differential rotation (Fröhlich et al., 2012) to an unprecedented level of accuracy.

2.2.2 Spectroscopy and Spectropolarimetry

Although photometry continues to provide large amounts of data, spectroscopy has provided a wealth of interesting discoveries in recent years. Almost all major astronomical facilities provide high-resolution spectrographs ($\Delta\lambda/\lambda$ in excess of 50 000 or more). Many facilities, such as the 3.9 m Anglo-Australian Telescope (AAT), use a cross-dispersed Échelle spectrograph to provide a wide range of wavelengths in a single exposure. From these high-resolution spectra comes the bulk of our knowledge of the physical properties of stars. Spectroscopy permits the characterisation of a star, such as its kinematics (U,V,W) and radial velocity, age (using the Li-I 670.78 nm), chromospheric activity (using a range of spectral lines from Ca II H (396.85 nm) & K (396.37 nm) to Ca II Infrared Triplet (849.8, 854.2 and 866.2 nm)), stellar parameters (including rotational velocities ($v \sin i$), T_{eff}, log g, and metallicity such as [Fe/H]) and absolute and differential abundances (for example chemical tagging) just to highlight a few areas of investigation.

A specialised branch of high-resolution spectroscopy has been spectropolarimetry. This is used to directly map stellar magnetic fields. There are only a few observatories around the world that support spectropolarimetry. These include the AAT (SEMPOL) (Semel, 1989; Donati et al., 1997), the Canadian-France-Hawaii Telescope (CFHT, 4 m) at Hawaii (ESPaDOnS - an **É**chelle **S**pectro**P**ol**a**rimetric **D**evice for the **O**bservatio**n**

[1] http://kepler.nasa.gov/

of **S**tars) (Donati et al., 2006a), the Télescope Bernard Lyot (TBL, 2.2 m) at Pic-du-Midi (NARVAL - the twin of ESPaDOnS), Telescopio Nazionale Galileo (TNG, 3.6 m) at Tenerife (SARG SP), the Nordic Optical Telescope (NOT, 2.5 m) at the Spanish Observatorio del Roque de los Muchachos, La Palma, Canarias, Spain (SOFIN, Pettersson et al., 1998) and recently the European Southern Observatory (ESO) 3.6 m telescope at La Silla, Chile (HARPS-Pol - **H**igh **A**ccuracy **R**adial velocity **P**lanet **S**earcher **Pol**arimeter: Snik et al., 2011).

2.2.3 Interferometry and Microlensing[1]

Two further techniques such as optical interferometry and microlensing have been suggested as possible techniques to image stellar surfaces. In particular, interferometry has the potential to provide images with a high degree of accuracy. Wittkowski et al. (2002) have conducted a feasibility study into the mapping of starspots on magnetically active late-type stars using the Very Large Telescope Interferometer (VLTI) while Jankov et al. (2003) have showed that with interferometric Doppler imaging, it is possible to map the stellar surface abundances of chemically peculiar (CP) stars using the VLTI and the interferometer at the Keck telescopes. Numerical simulations by Rousselet-Perraut et al. (2004) have been undertaken to show that the study of stellar activity and magnetism by optical interferometry is a possibility. Likewise, de Souza et al. (2004) have used numerical simulations to demonstrate the feasibility of measuring stellar differential rotation and inclination from spectro-interferometry. Recently Domiciano de Souza et al. (2012) have reported the equatorial radius, rotational velocity and inclination axis and position angle of Achernar (SpType: B6Vep[2]) using the VLTI while Weigelt et al. (2011) have used the VLTI/AMBER to investigate the disk surrounding the Herbig Be star MWC 297. In addition, Parks et al. (2011) has used the CHARA (Center for High Angular Resolution Astronomy) array at Mount Wilson to generate an interferometric image of the chromospherically active RS CVn giant λ Andromedae (SpType: G8III[3]).

[1] This section is based on the overview presented by Berdyugina, S.V. *Starspots: A key to the Stellar Dynamo*, vol 2, 2005, http://solarphysics.livingreviews.org/refdb/record/22832

[2] Nazé (2009)

[3] van Leeuwen (2007)

Theoretical studies using gravitational imaging as a tool for studying starspots have been undertaken by Heyrovský and Sasselov (2000) and Hendry et al. (2002) using single-lens events while Han et al. (2000) discussed the detections of starspots using binary-lens gravitational microlensing events. Heyrovský and Sasselov (2000) found that the spots can cause deviations in amplification of at least 2%, thus detectable. However, Hendry et al. (2002) found that starspots give a clear signature only in transit events. Recently, Hwang and Han (2010) revisited the use of microlensing and suggested that, given high-cadence lensing surveys, the size and location of starspots on the stellar surface should be achievable although the shape and surface brightness contrast may not be easily constrained. In summary, both interferometry and microlensing techniques are still in their infancy, particularly interferometry, but perhaps have the potential to provide more detailed images of the stellar surface, particularly of slow-rotating stars that are beyond DI and ZDI. At this present time, DI and ZDI give the best information regarding starspot distribution and hence information on the underlying dynamo.

This project uses photometry (Section 2.3), high-resolution spectroscopy (Section 2.4) and high-resolution spectropolarimetry (Section 2.5) to study the surface features of solar-type stars.

2.3 Photometry

Optical photometry is concerned with the measurement of the brightness of a star and its changes in this brightness level over time. For solar-type stars, a photometric lightcurve can be used to determine the rotational period assuming the light modulation is due to starspots. Closely related to brightness is colour which is a measure of the difference in brightness of a star observed at two specific wavelength bands. From detailed colour measurements, the effective surface temperature of the stellar surface can be obtained. Soderblom et al. (1993b) developed a relationship between (B-V)$_o$ and effective temperature, and is shown in equation 2.1.

$$T_{eff} = 1808(B-V)_o^2 - 6103(B-V)_o + 8899 \tag{2.1}$$

Bessell, Castelli, and Plez (1998) used the (V-I) colour index to determine the effective temperature. This relationship, as shown in equation 2.2, is valid for A- to K-dwarfs.

$$T_{eff} = 9581.1 - 14264(V-I) + 40759(V-I)^2 - 74141(V-I)^3 + 60932(V-I)^4 - 18021(V-I)^5 \quad (2.2)$$

Bessell et al. (1998) argue that temperatures obtained from (B-V) colour do not agree well between theory and observation for cool stars and suggest that (V-I) produces good agreement for A- to M-dwarfs.

2.3.1 Telescopes at Mount Kent Observatory

Broadband photometry for this thesis has been conducted at the University of Southern Queensland's Mount Kent Observatory (MKO[1]). MKO is located in Southern Queensland, approximately 160km south-west of Brisbane, Australia. There are two telescopes with photometric capabilities. The O'Mara telescope comprises a 35 cm Schmidt-Cassegrain optical tube, an SBIG[2] STL-1301E CCD camera with 1280 × 1014 16 μm square pixels, and a Paramount ME mount. This system has a plate scale of approximately 0.3 arc seconds per pixel. The second telescope is the University of Louisville 50 cm telescope at MKO, a Corrected Dall-Kirkham design manufactured by Planewave Instruments[3]. The imaging camera uses a SBIG STL-630E with a Kodak KAP-6303E CCD chip that has an array size of 3060 x 2040, 9 μm square pixels giving a plate scale of approximately 0.54 arc seconds per pixel (MKO, 2010). Both telescopes use standard Johnson-Cousins U, B, V, R and I filters.

2.3.2 Data Reduction

The Image Reduction and Analysis Facility (*IRAF*) package was used for the reduction and analysis of the photometry data. The CCD frames had the dark current removed (that also contained the bias information) and were flat fielded using a nightly master flat field, which were usually a combination of 9 dome flat fields. Dome flats were used due to the high signal-to-noise (S/N) obtained from this technique. Sky flats alone

[1] http://orion.mko.usq.edu.au
[2] http://www.sbig.com/
[3] http://www.planewave.com/

are problematical due to the brief time-frame which all filters can be completed. Sky-corrected dome flats were also tested with no improvement in the accuracy of the photometry. To produce each data point, three images were averaged, using *IMCOMBINE*, to produce an image with improved S/N from which the magnitude of all the program stars were measured. The stars in the frame were found using *DAOFIND* and simple aperture photometry was done using *DAOPHOT*. The sky background was determined and removed using the mode of an annulus of 10 pixel radius around the star. The curves of growth method (Stetson, 1990) was used to determine the aperture size that would be used to determine the magnitude of each of the stars in the field. To standardise the stars, standard stars were observed using Graham's E-regions (Graham, 1982). The routines found in the *PHOTCAL* package in *IRAF* were used to determine both the transformation coefficients and the magnitude of the stars. More details are given in Chapter 3.

2.4 Doppler Imaging: DI

DI was first proposed by Deutsch (1958) with Goncharskii et al. (1977) being the first to use an inversion technique to map the chemical peculiarities of the surface of Ap stars. Vogt and Penrod (1983) developed DI as a way of deriving a map of the surface of the star. That star was HR 1099 (SpType = K2:Vnk[1], an RS Canum Venaticorum (RS CVn) type star. Since then, several authors have developed different algorithms utilising essentially the same concept; that starspots deform the spectral line profiles and these deformations move through the profiles due to the star's rotation. DI has been very successful in producing maps of many different stellar systems that rotate rapidly. Vogt and Penrod (1983) specify the minimum projected rotational velocity ($v \sin i$) for this technique to be roughly 25-30 $\mathrm{km\,s^{-1}}$ with a S/N of approximately 200+. Nevertheless, Strassmeier and Rice (1998) have used DI to produce a map of the surface of EK Draconis, a star with a $v \sin i$ of only 17.3 $\mathrm{km\,s^{-1}}$ (although this project measures the $v \sin i$ to be 16.8 $\mathrm{km\,s^{-1}}$, see Chapter 6).

Figure 2.1 explains the basic principle of DI. On a typical star, the individual spectral lines are broadened due to a number of both local (natural broadening, due to the

[1] Gray et al. (2006)

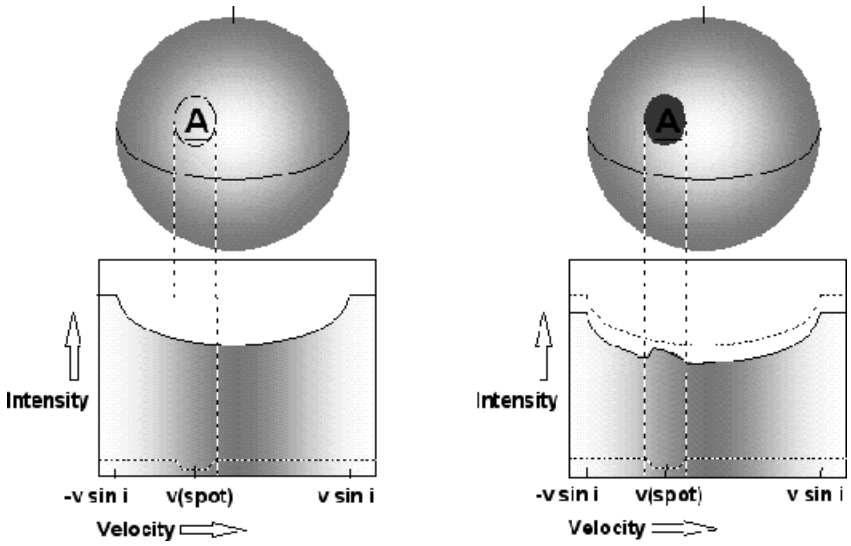

Figure 2.1: The basic concept of Doppler imaging. This illustrates the effect a starspot on the surface of the star has on the observed line profile. Taken from http://star-www.st-and.ac.uk/ acc4/coolpages/dopreviews/sld003.htm. *date accessed:* December 19, 2011

uncertainty principle, thermal Doppler broadening and pressure broadening) and non-local (opacity and Doppler broadening) effects. On rapidly rotating stars, the dominant mechanism is Doppler broadening. The presence of a dark spot on the surface results in a "bump" in the observed spectral line profile of the star, as shown in Figure 2.1: right panel. In addition, because the light is "missing" from the dark spot, a slight reduction in the overall intensity of the spectral line is also observed. As the star rotates, the dark spot moves across the stellar disc, while the "bump" in the line profile changes its Doppler shifted position relative to the stellar rotation axis. To put it simply, the "bump" moves across the line profile. Each profile is a representation of light from the complete stellar surface. Figure 2.2 demonstrates how the "spot" affects the overall profile. As the star rotates, the position of the spot in the profile will vary according to its longitude on the stellar surface thereby providing information about the spot's location. The principles of DI are described in more depth in Vogt and Penrod (1983) and Rice et al. (1989).

In practice, achieving such a high S/N of 200+ is very difficult, and particularly on rapid rotators where there needs to be a trade-off between S/N and the fraction of the

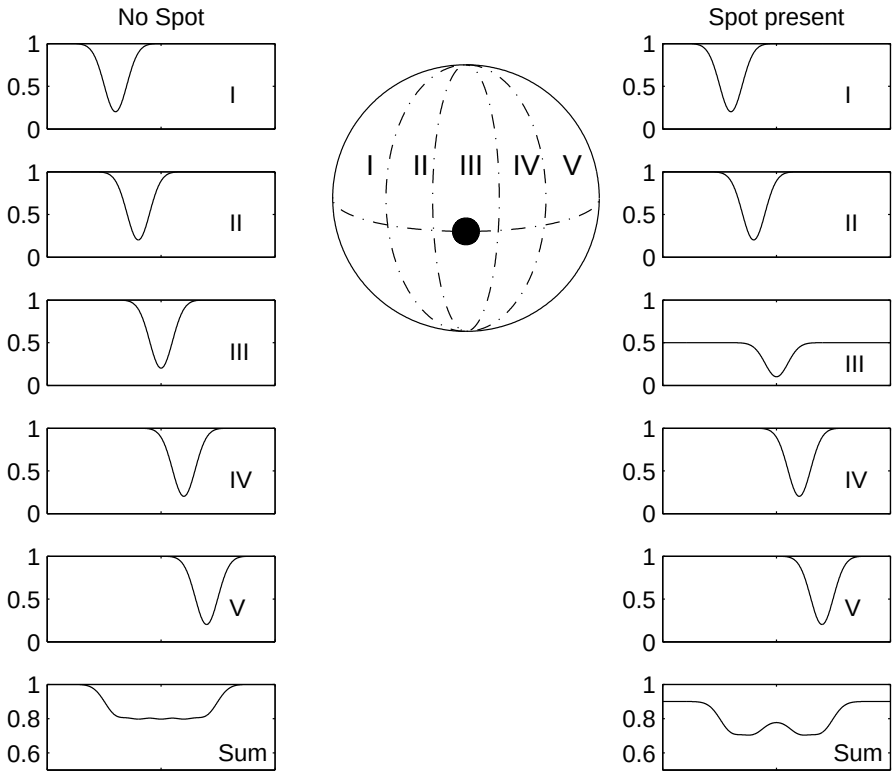

Figure 2.2: An illustration of the technique of Doppler imaging showing the formation of a spectral line profile that is formed by light across the visible disk of the star. This figure has been *adapted* from Vogt and Penrod (1983)

rotation of the star during a typical exposure, known as phase smearing. To improve the desired S/N, a technique known as Least-Squares Deconvolution (LSD) was developed by Donati et al. (1997) whereby a single line profile is synthesised from several thousand photospheric weak absorption lines. This has the advantage that an LSD profile has significantly increased S/N over that of a single-line data. LSD is discussed in more detail in Section 2.5.1.

Brightness (and magnetic) topologies are generated by the time series analysis of spectral line (or LSD) profiles. This inversion process is an ill-posed problem, meaning that there are an infinite number of solutions that can be found that fit the data to the noise level. Hence a regularisation scheme is introduced to determine this unique solution desired. There are several regularisation schemes that have been utilised by various authors when producing maps through DI and ZDI. Several authors (e.g. Vogt and Penrod, 1983; Rice et al., 1989; Brown et al., 1991; Collier Cameron, 1992; Rice and Strassmeier, 2000) have developed algorithms based on the maximum-entropy minimisation (MEM) regularisation of Skilling and Bryan (1984). MEM searches for the solution with the largest entropy. Alternatively, other authors (e.g. Goncharskii et al., 1977; Piskunov et al., 1990; Kochukhov et al., 2010) use the Tikhonov regularisation method (TRM) that develops a solution with the least gradient of the parameters across the map. Rice (2002) notes that TRM is the best choice for Ap stars while MEM is best choice for cool stars, such as those that are investigated in this thesis.

An alternative way to address the inverse problem associated with DI has been developed by Berdyugina (1998), known as the Occamian approach (OA). The solution is based on the analysis of the information content of the data (Berdyugina, 2005). It uses no artificial constraints or assumptions to the solution, except its non-negativity, as a way of producing DI maps. An extension of this method is the Principle Component Analysis (PCA) (Semel et al., 2006; Martínez González et al., 2006; Kopf, 2008; Ramírez Vélez et al., 2010). PCA is designed to extract the polarised signature using cross correlation methods between the stellar spectra and functions containing the polarisation properties of each line based on the principal components of a database of synthetic spectra. Both OA and its extension PCA have the potential to revolutionise DI and ZDI over the next few years. This thesis adopts the MEM approach to regularisation as PCA was still in its infancy when this thesis commenced and follows the algorithms developed by Donati and Brown (1997) and Donati et al. (1997, 2003b).

Even with its limitations, MEM does provide robust global brightness and magnetic maps.

2.4.1 Mapping the Stellar Surface: Doppler Imaging Code

The imaging code used to perform brightness imaging on the stellar surface is based on that developed by Brown et al. (1991) and further enhanced by Donati and Brown (1997). This code, known as *ZDICAM*, implements the maximum entropy optimisation algorithm of Skilling and Bryan (1984). This technique produces images with the minimal amount of information (surface features) required to produce the observed photometric and spectroscopic intensity variations to within the noise level. The code uses a two-component brightness model (Collier Cameron, 1992), one for the photosphere and one for the spots implying that there are no temperature gradients between the two. The initial assumption is that the star is unspotted with synthetic gaussian profiles used to represent both the spot temperature and the quiet photosphere temperature. The local relative area for each image pixel occupied by cool spots is then reconstructed by adding "spots" to match the observed profiles to the noise level. Unruh and Collier Cameron (1995) showed that there is little difference in the resulting maps when using synthetic gaussian profiles when compared with using profiles that were taken of slowly rotating standard stars. A number of authors have followed this formulation such as Petit et al. (2002, 2004b) and Marsden et al. (2005, 2006), as does this thesis.

In the image reconstruction, a spot occupancy is produced by maximising the entropy function, S, which is given in Equation 2.3.

$$S = \sum_i \left(-f_i \, ln \frac{f_i}{m_i} - (1 - f_i) \, ln \frac{(1 - f_i)}{(1 - m_i)} \right) \tag{2.3}$$

where f_i is the spot filling factor ($0 \leq \mathrm{f} \leq 1$), (1-f_i) is the photospheric filling factor and m_i is the default model where the value that a pixel, i, will assume in the absence of any other constraints. The default unspotted filling factor, m_i is usually set to 0.9999. The filling factors are then interactively adjusted accordingly to maximise Equation 2.4 by minimizing the χ^2 value, as shown in Equation 2.5.

$$Q = S - \lambda \chi^2 \tag{2.4}$$

where λ is the Lagrangian multiplier and χ^2 is the measure of the accuracy of the fit. Q is a difference function and is "maximising the entropy, S, along the intersection of the constraint surfaces for the spectral and photospheric data" (Barnes, 1999).

$$\chi^2 = \sum_k \left(\frac{D_k - F_k}{\sigma_k} \right)^2 \tag{2.5}$$

where k is the steps over the entire LSD profile and σ_k, known as the standard error, is calculated from an estimate of the error in the LSD profiles. In addition, D is the observed data and F is the modelled data. The data are fitted to within a desired accuracy of $\chi^2 = \chi^2_{aim}$. In theory, if the data is fitted to the noise level of that data, $\chi^2 = 1$. However, this is dependent on the error, σ_k, being correctly estimated. Frequently these errors are over-estimated and $\chi^2 < 1$ is often achieved. Alternatively, if $\chi^2 > 1$, it means that the fit accuracy never reaches the noise level. This is usually the case when there has been spot emergence or evolution of the spot(s).

In order to produce a self-consistent map, several stellar parameters are required. The imaging code can be used to establish the values of a number of basic parameters, including the star's inclination angle (as shown in Figure 1.8), i, $v\sin i$ and radial velocity, v_{rad}. These can be found by systematically varying each parameter in order to minimise the χ^2 value (e.g. Marsden et al., 2005; Jeffers and Donati, 2008). These key stellar parameters are determined sequentially, first v_{rad}, then $v\sin i$ and finally the inclination angle of the star. However, the $v\sin i$ of the star must be determined at the same time as the equivalent width of the input LSD profiles. These two parameters were found by simultaneously varying the $v\sin i$ and the equivalent width for the LSD profiles and finding the optimum combination of values. The sequence of defining the parameter set was repeated each time additional parameters were modified as a result of the imaging process. The χ^2 is calculated as shown in Equation 2.5.

2.5 Zeeman Doppler Imaging: ZDI

ZDI (Semel, 1989; Donati et al., 1989, 1997, 2003b) is an extension of DI and follows many of the same principles discussed in Section 2.4. ZDI enables the study of stellar magnetic fields using spectropolarimetry and offers an insight into the underlying magnetic dynamo. In the presence of a magnetic field, light is polarised and spectral lines split through the Zeeman effect. Figure 2.3 shows a brief explanation of the Zeeman

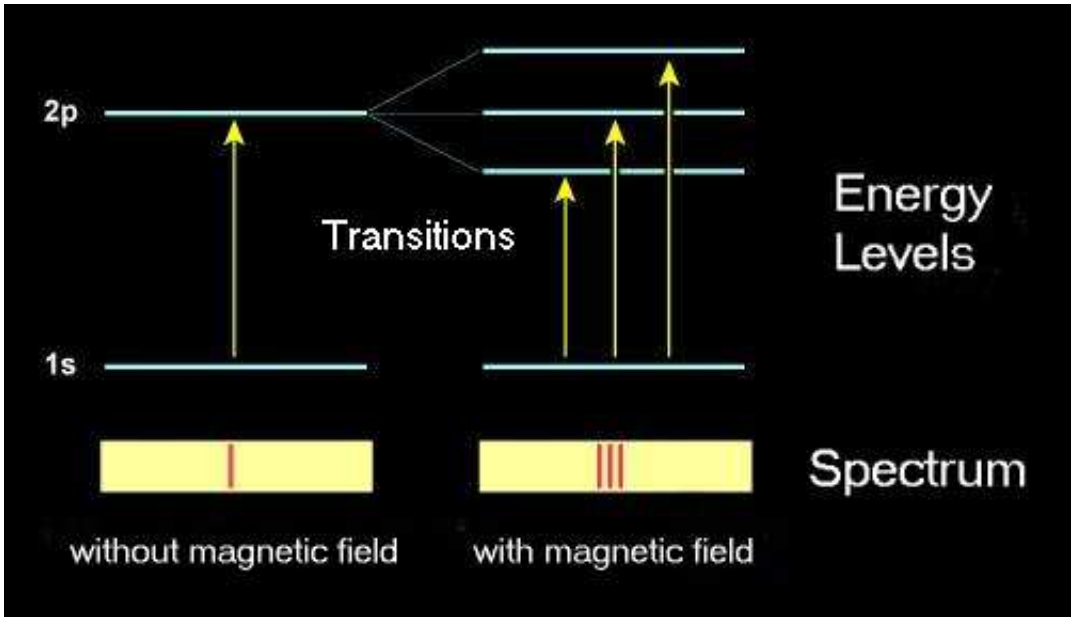

Figure 2.3: The Zeeman effect is the splitting of spectral lines due to the presence of a magnetic field. Source: http://csep10.phys.utk.edu/astr162/lect/light/zeeman-split.html *date accessed:* June 23, 2012

effect, named after Dutch physicist, Pieter Zeeman. The characteristic splitting of the Zeeman components of a particular spectral line can be represented by Equation 2.6.

$$\Delta\lambda_B = \frac{\lambda_c^2 e_o B}{4\pi m_e c^2} \tag{2.6}$$

where $\Delta\lambda_B$ is the change in the wavelength due to the presence of the local magnetic field of strength, B, λ_c is the wavelength of the unperturbed spectral line, m_e is the mass of an electron with a charge of e_o and c is the velocity of light.

Polarised light is split into three components: two symmetric oppositely circularly polarised components and a centrally linearly-polarised components. The parameters associated with each are expressed in terms of the Stokes parameters, where the Stokes I parameter is a measure of the total power (light intensity), Stokes Q and U represent the linearly polarised components and Stokes V represents the circularly polarised component. The Stokes vector, $\vec{S}$, is a combination of different polarisation states. A commonly used system are the components I, Q, U and V. As Harrington (2008)

succinctly noted, the Stokes vector ($\vec{S}$) can be represented by Equation 2.7.

$$\vec{S} = \begin{bmatrix} I \\ Q \\ U \\ V \end{bmatrix} = \begin{bmatrix} \text{Intensity} \\ \updownarrow - \leftrightarrow \\ \nearrow - \searrow \\ \circlearrowleft - \circlearrowright \end{bmatrix} \tag{2.7}$$

where I is the total intensity (unpolarised light), Q and U are the differences in between two linearly polarised states with Q being the difference in intensity between 0^o ($\updownarrow$) and 90^o ($\leftrightarrow$) and U being the difference between 45^o ($\nearrow$) and 135^o ($\searrow$) polarisation states with respect to the components measured in Stokes Q. The Stokes V is the difference between the left- ($\circlearrowleft$) and right-handed ($\circlearrowright$) circular polarisation states.

ZDI is particularly challenging requiring high S/N data as the polarisation signatures are typically less than 0.1% of the total light intensity (Donati et al., 1997). Figure 2.4 shows the principles of ZDI based on the left- and right-hand circular polarisation states. Consider two magnetic "spots" of opposite polarity, labelled X_1 and X_2. The resulting intensity spectrum (I) would show two absorption lines, centred on the positions X_1 and X_2, in wavelength space. Through the Zeeman effect, each magnetic "spot" induces a small yet opposite spectral shift of the corresponding absorption profile in the right- and left-hand circularly polarised spectra. For example, in the right-hand polarised state, the absorption spectrum would be $I + V$ while the left-hand polarised state would produce a $I - V$ polarised spectra. Each of the respective line profiles are subtracted, with the difference being V, as shown in Equation 2.8. This variation with wavelength, $V(\lambda)$, has a characteristic shape thereby producing a "signature" of the surface magnetic fields.

$$V(\lambda) = (I + V) - (I - V) \tag{2.8}$$

The linear polarisation state (Stokes U and Q parameters) are significantly weaker than the circular (Stokes V) state. This is due to the transverse (or perpendicular) Zeeman effect. Linear polarisation has been used to map stellar magnetic topologies on strongly magnetic Ap stars (Wade et al., 2000; Kochukhov et al., 2004); however, it has been very difficult to observe these weak signatures on active cool stars. Recently, Kochukhov et al. (2011) measured all four Stokes parameters, including Stokes U and Q, of the RS CVn binary HR 1099 and the moderately active K-dwarf ϵ Eridani (SpType: K2Vk[1]). They used the 3.6 m ESO telescope (with HARPS-Pol) and found

[1] Gray et al. (2006)

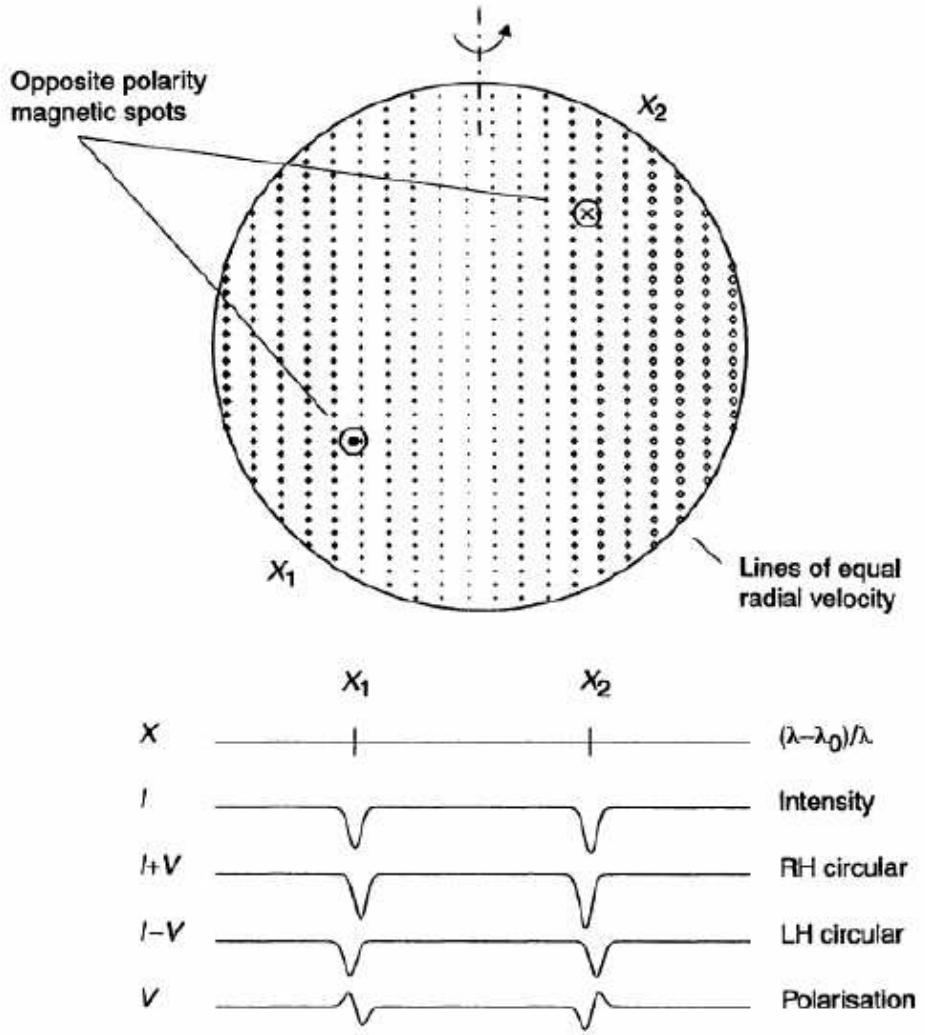

Figure 2.4: The concept of Zeeman Doppler imaging, taken from Carter et al. (1996). This figure shows how the Stokes V (circularly polarised) signature is shifted (and opposite for opposite polarity) for the two spots on the stellar surface due to the Doppler effect.

that the Stokes U and Q were about a factor of 10 lower than the amplitude of the circular polarization signal. They also noted that very high resolution, $\lambda/\Delta\lambda \sim 10^5$, was required to "secure detection" of all four parameters. Subsequent to this measurement, Kochukhov et al. (2013) has used HARPS-Pol to map the magnetic field topology of the RS CVn star II Pegasi; the first map of a cool star produced using the full set of Stokes parameters.

Large scale stellar magnetic fields are usually considered as the sum of the toroidal (i.e., azimuthal) component, poloidal component and a meridional component. Simplified diagrams of these components are shown in Figure 1.5. In order to recover the magnetic field topology, a spherical harmonic expansion is utilised (Donati et al., 2006b). This allows certain constraints on the modelling such as assuming that the field is purely potential, or toroidal, or a combination of both. The surface magnetic field, B, is defined such that $B = -\nabla\psi$ where ψ is a flux function. The condition for a potential field, a current-free field, is thus $-\nabla \times B = 0$. Each of the field components, $\mathrm{B}_r(\theta,\phi)$, $\mathrm{B}_\theta(\theta,\phi)$ and $\mathrm{B}_\phi(\theta,\phi)$, can be expressed as a spherical harmonic expansion as shown below (this is a summary of the formalisation found in Donati et al., 2006b):

$$B_r(\theta,\phi) = -\sum_{\ell,m} \alpha_{\ell,m} Y_{\ell,m}(\theta,\phi) \tag{2.9a}$$

$$B_\theta(\theta,\phi) = \sum_{\ell,m} [\beta_{\ell,m} Z_{l,m}(\theta,\phi) + \gamma_{\ell,m} X_{\ell,m}(\theta,\phi)] \tag{2.9b}$$

$$B_\phi(\theta,\phi) = \sum_{\ell,m} [\beta_{\ell,m} X_{\ell,m}(\theta,\phi) + \gamma_{\ell,m} Z_{\ell,m}(\theta,\phi)] \tag{2.9c}$$

where

$$Y_{\ell,m}(\theta,\phi) = c_{\ell,m} P_{\ell,m}(\theta) e^{\mathrm{i}m\phi} \tag{2.10a}$$

$$Z_{\ell,m}(\theta,\phi) = \frac{c_{\ell,m}}{\ell+1} \frac{\partial P_{\ell,m}(\theta)}{\partial\theta} e^{\mathrm{i}m\phi} \tag{2.10b}$$

$$X_{\ell,m}(\theta,\phi) = \frac{c_{\ell,m}}{\ell+1} \frac{\partial P_{\ell,m}(\theta)}{sin\theta} \mathrm{i}m e^{\mathrm{i}m\phi} \tag{2.10c}$$

$$c_{\ell,m} = \sqrt[2]{\frac{2\ell+1}{4\pi} \frac{(\ell-m)!}{(\ell+m)!}} \tag{2.10d}$$

where ℓ and m denote the degree and order of the spherical-harmonic mode $Y_{\ell,m}(\theta,\phi)$ (sometimes referred to as Laplace spherical harmonics), with θ and ϕ being the co-latitude ($0 \leq \theta \leq \pi$) longitude ($0 \leq \phi \leq 2\,\pi$) at the surface of the star. $P_{\ell,m}(\theta)$ is the associated Legendre polynomial. The complex coefficients: $\alpha_{\ell,m}$ represents the radial field component, $\beta_{\ell,m}$ represents azimuthal and meridional components of the potential field term while $\gamma_{\ell,m}$ represents azimuthal and meridional components of the toroidal field term. Fitting a pure potential field to the data is equivalent to fitting $\alpha_{\ell,m}$ and $\beta_{\ell,m}$ while setting $\gamma_{\ell,m}$ to zero. Using all three sets of coefficients produces the more general magnetic topology with a non-zero toroidal field. The degree of the spherical harmonic expansion determines the represented field distribution on the surface of the star: $\ell = 1$ dipole; $\ell = 2$ quadrupole; $\ell = 3$ octupole leading to higher-order terms (e.g. Gerth and Glagolevskij, 2004). The order of the spherical harmonic expansion, m, relates to the symmetry with $m \leq \ell/2$ for axisymetric modes. The simplest model is a dipole field aligned with the rotation axis: $\ell = 1$ and $m = 0$. Thus for a given set of complex coefficients, one can derive an associated magnetic map of the surface of the star. This thesis, when using ZDI to map the magnetic field topologies, assumes a combination of both potential and toroidal components.

This reconstruction process begins with the assumption that there is no magnetic field and iteratively improves the magnetic model by comparing the synthetic Stokes V profiles with the observed Stokes V profiles until the model reproduces the data at a given χ^2 level (i.e. $\chi^2 = 1$). This inversion process is partly ill-posed so the entropy function is used to select the magnetic field with the minimum amount of information among all those reproducing the data equally well. The MEM reconstruction is applied to the coefficients listed above as opposed to the image pixels used in DI.

There is one limitation in that ZDI only measures the large-scale magnetic fields as small-scale magnetic fields cannot be recovered as the positive and negative magnetic fields are likely to be cancelled out within the resolution element of the observations, $\sim 11^o$ in longitude at the stellar equator (Marsden et al., 2011a). However, this limit does vary with spectral resolution and $v \sin i$. Nevertheless, ZDI has been achieved on a small sample of single, G-type stars such as HD 171488 (V889 Her) (Marsden et al., 2006; Jeffers and Donati, 2008; Jeffers et al., 2011) and HD 141943 (Marsden et al., 2011a,b), and the sample is growing all the time to include slower rotating solar-type stars (Petit et al., 2008, 2009), planet-hosting stars (e.g. Donati et al., 2008b; Fares

et al., 2009) and M-dwarf stars (fully convective stars) (e.g. Donati et al., 2008a). In summary, ZDI can produce maps of the radial, meridional and azimuthal magnetic field of solar-type stars.

A key assumption in ZDI is that the splitting of the spectral line due to the magnetic field, $\Delta\lambda_B$, is much smaller than the intrinsic width due to thermal Doppler broadening, $\Delta\lambda_D$. This is known as the *weak-field limit* and is a basic assumption in ZDI. Jefferies et al. (1989) used simple classical oscillator theory to calculate that for a 500 nm line with a Doppler width of 4 mÅ, the field strengths of the order of 1000 G would hold up "reasonably well" under this *weak-field* approximation and was consistent with the conclusion reached by Landi Degl'Innocenti and Landi Degl'Innocenti (1972) using a quantum mechanical approach. Donati and Brown (1997) suggest that the weak-field approximation is valid, in principle, to strengths below 1.2 kG.

2.5.1 Least Squares Deconvolution: LSD[1]

As the magnetic signatures within in a stellar spectrum are extremely small, the detection of a magnetic field on solar-type stars would be limited to only the very brightest of stars enabling a very high S/N to be achieved in each spectral line. A technique known as Least Squares Deconvolution (LSD) overcomes this limitation and opens a path to the investigation of a wider range of stellar objects.

The LSD process assumes that each line in the intensity (Stokes I) or polarisation (Stokes V) spectrum of a star has the same line shape, with each line scaled by a certain factor to match the local line depth. A second assumption is that overlapping line profiles are linearly added. Hence the entire spectrum can be described as a sum of scaled, and shifted, identical profiles, as shown in Equation 2.11:

$$Y(v) = \sum_i w_i \delta(v - v_i) Z(v_i) \tag{2.11}$$

where Y is the model residual intensity, either I - I/I_c, or the normalized polarisation spectrum V/I_c. The position, in velocity space, v_i, is $c\Delta\lambda_i/\lambda_i$ and is associated with the wavelength shift, $\Delta\lambda_i$ from the central wavelength of the i^{th} line. The relative contribution of each of the spectral lines is given by the weight, $w_i = g\lambda d$ where g is magnetic

[1]This section, in part, is a summary of the overview presented by Kochukhov, O., Makaganiuk, V. & Piskunov, N. *Least-squares deconvolution of the stellar intensity and polarization spectra*, A&A, vol 524, ID A5, 2010

sensitivity (Landé factor), λ is the wavelength and d is the local line central depth. The Landé factor is a combination of $J, LandS$ quantum numbers corresponding to the total angular momentum, orbital angular momentum and spin angular momentum, as shown in Equation 2.12.

$$g = 1 + \frac{J(J+1) - L(L+1) + S(S+1)}{2J(J+1)} \tag{2.12}$$

Equation 2.11 can be considered a convolution of the line profile pattern, $M(v)$, and the mean profile $Z(v)$, leading to Equation 2.13.

$$Y = M * Z \tag{2.13}$$

The main function of LSD is to solve the inverse problem corresponding to Equation 2.13 in order to estimate the mean line profile, Z, for a given line pattern, M and the observed spectrum, Y coupled with an associated statistical uncertainty, σ. This is achieved by finding the least-squares solution using Equation 2.14.

$$Z = ({}^tM \cdot S^2 \cdot M)^{-1} \quad {}^tM \cdot S^2 \cdot V \tag{2.14}$$

where S is a square diagonal matrix whose elements, S_{jj} contains the inverse error bar $1/\sigma_i$ of spectral pixel i, obtained from the extraction of the spectrum. The ${}^tM \cdot S^2 \cdot V$ term, from Equation 2.14, is a cross-correlation of the observed spectrum V with a line pattern M, a weighted mean of all the lines selected.

So why not produce an average line profile by directly adding all the weighted lines and averaging the total sum? This would be a simpler approach if all the spectral lines are free of blends. In reality, the absorption lines in the spectra of solar-type stars are rarely isolated. Hence the resulting "average" line would be distorted by all the blended lines. Hence the need to undertake this deconvolution method. The respective locations and relative strengths of various lines of the stellar spectrum are found using a template, or line mask, of the same, or similar, spectral type. All the line masks used in this thesis were kindly generated by Dr Jean-Françios Donati, from L'Institut de Recherche en Astrophysique et Planétologie (IRAP) at the Observatoire Midi-Pyrénées and were created from the Kurucz atomic database and ATLAS9 atmospheric models (Kurucz, 1993).

There are limitations to the LSD technique. Most studies (including this thesis) assume that the identical shape assumption of the LSD Stokes I profiles LSD is appropriate for lines weaker than $\sim$ 40%. However, Kochukhov et al. (2010) expresses a concern with this value, arguing that the identical line shape and linear addition of blends assumptions of the LSD of Stokes I is appropriate only for lines weaker than $\sim$20% of the continuum. Kochukhov et al. (2010) also concluded that the LSD assumptions are appropriate for the Stokes V signatures for weak and moderately strong magnetic fields, with $B \leq 2$ kG. All of our targets in this work have global magnetic fields less than 2 kG. For more detailed information regarding LSD, see Donati et al. (1997) and Kochukhov et al. (2010).

2.5.2 Zeeman Doppler imaging at the Anglo-Australian Telescope

The direct study of stellar magnetic fields is a worthwhile but technically challenging effort. ZDI is employed at the AAT to detect and in some cases map stellar magnetic fields, to understand stellar dynamos and the role of magnetism in stellar structure, energy balance and evolution. ZDI can also simultaneously provide the brightness maps of active regions as in conventional Doppler imaging.

ZDI observations at the AAT began in 1989, with the first magnetic field detected for the RS CVn evolved binary HR 1099 (Donati et al., 1992a). Since then ZDI at the AAT has been used to produce a wealth of scientific results. Some examples are:

- Measurement of magnetic fields on a range of stars (young, old, cool, warm, single, binary). For example, Donati et al. (1992b).

- Mapping of the magnetic fields and spot features of active young and evolved objects. For example, Donati and Collier-Cameron (1997), Marsden et al. (2011a).

- Measurement of stellar surface differential rotation apparent in both spot features and fields. For example, Collier Cameron et al. (2002), Donati et al. (2000), Marsden et al. (2011b), Waite et al. (2011b).

- Monitoring of the changing magnetic features on stars undergoing stellar cycles. For example, the late F-type star HR 1817 (Marsden et al. *in preparation*).

- Evidence that young stars possess distributed dynamos different to the solar dynamo. For example, Donati and Collier-Cameron (1997), Marsden et al. (2011b), Waite et al. (2011b).

- Support for international multi-wavelength campaigns. For example, the investigation into the activity of the UV Ceti-like star CC Eridani (SpType: K7V[1]) involving NASA's Chandra (X-ray) spacecraft, National Radio Astronomy Observatory (NRAO) Very Large Array (VLA), Commonwealth Scientific and Industrial Research Organisation (CSIRO) Australia Telescope Compact Array (ATCA), MKO and Mt Tarana Observatory, in central western New South Wales (Broadband B optical photometry). (Slee et al., 2004; Budding et al., 2006)

The AAT uses a visitor instrument known as SEMPOL (or SEMELPOL), named after its designer, the late Meir Semel (Semel, 1989; Donati et al., 1992b, 1997). SEMPOL is used with a wavelength coverage from 437.71 nm to 681.56 nm simultaneously with a mean pixel resolution of $\sim$1.7 km s^{-1}pixel^{-1} at a resolution of $\sim$70 000. The polarimetry module (see Figure 2.5, left panel), consisting of the half-wave Fresnel Rhomb, is attached to the Cassegrain focus of the AAT. Observations in the circular polarisation signature (Stokes V) consist of a sequence of four exposures. After each of the exposures, the half-wave Fresnel Rhomb of the SEMPOL polarimeter is rotated between $+45^o$ and -45^o. This sequence of exposures ($+45^o \rightarrow -45^o \rightarrow -45^o \rightarrow +45^o$), removes most of the systematic effects in the measurements due to spatial and spectral variations in the optical throughput, CCD inhomogeneities, terrestrial and stellar rotation, temporal variability as well as instrumental polarisation signals from the telescope and the polarimeter (Semel et al., 1993; Carter et al., 1996; Donati et al., 2003b). The signal is carried by twin optic fibres into the University College of London Échelle Spectrograph (UCLES) via a beam-splitter (see Figure 2.5, middle panel), housed at the slit

[1] Torres et al. (2006)

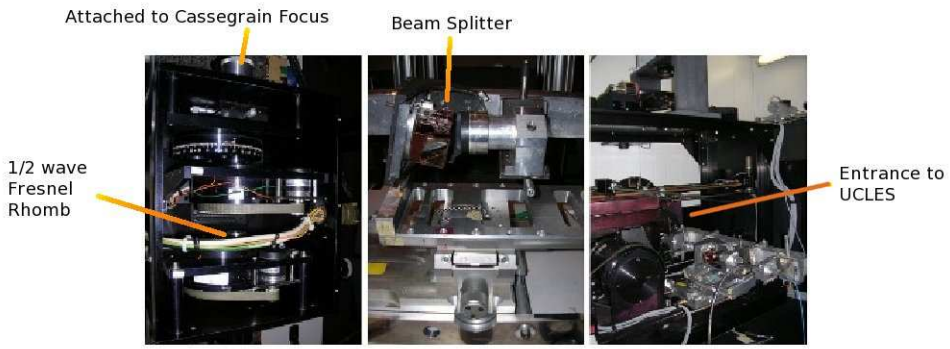

Figure 2.5: These pictures are of the instrumentation setup at the AAT. The left panel shows the polarimetry module that is attached at the Cassegrain focus. It consists of the half-wave Fresnel Rhomb that rotates between $+45^o$ and -45^o so as to remove instrumental polarisation signals from the telescope. The middle panel shows the beam-splitter while the right panel shows the complete assembly that is placed at the entrance of UCLES.

entrance to the spectrograph (see Figure 2.5,right panel) (Semel et al., 1993; Donati et al., 2003b).

As mentioned in Section 2.5.1, LSD combines several thousand extracted intensity weak photospheric absorption lines within the spectrum to produce a single, high S/N line profile, thereby providing an enormous multiplex gain in the S/N (Donati et al., 1997). For example, consider data taken on the April 07, 2007 (of the pre-main sequence star HD 106506 - Chapter 3) at the AAT using SEMPOL. A typical sequence consists of 4 exposures, the average S/N of a single exposure in order 106 ($\sim$ central order) was 84, the resulting Stokes I LSD profile for that single exposure had an average S/N $\sim$1006 while the corresponding Stokes V profile (combining all four exposures) had a S/N $\sim$ 5170.

2.5.3 ESPaDOnS and NARVAL

NARVAL[1], at the TBL, and ESPaDOnS[2], at the CFHT, have been developed as a result of SEMPOL, which is described in Section 2.5.2, and use essentially the same

[1]http://www.ast.obs-mip.fr/projets/narval/v1/
[2]http://www.ast.obs-mip.fr/projets/espadons/espadons.html

principles but with greater through-put and wavelength coverage. Whereas SEMPOL is operated with a wavelength coverage from 437.71 nm to 681.56 nm, NARVAL and ESPaDOnS cover $\sim$ 370 nm to 1048 nm. This extends into the blue region of the electromagnetic spectrum, enabling coverage of the Ca II H & K lines and also into the near infra-red region to include the Ca II Infrared Triplet (IRT) lines. NARVAL and ESPaDOnS are bench mounted, cross-dispersed Échelle spectrographs, fibre-fed from a Cassegrain-mounted polarimeter unit that consists of one fixed quarter-wave retarder sandwiched between 2 rotating half-wave retarders. This is coupled to a Wollaston beamsplitter. They are very similar in their operation with SEMPOL. NARVAL and ESPaDOnS have a mean pixel resolution of 1.8 $\mathrm{km\,s^{-1}}$ per pixel with a resolution was $\sim$65000 spanning 40 grating orders (orders #61 to #22).

2.6 Differential Rotation

Differential rotation was first observed on the Sun when it was recognised that the equatorial rotational period ($\sim$25 d) was far different from that of the polar regions which rotate at a much slower rate ($\sim$34 d), as stated in Section 1.1.2. Differential rotation has also been observed on a number of solar-type stars, as explained in Section 1.2.3.

Solar-like differential rotation may be defined as in Equation 2.15.

$$\Omega(\theta) = \Omega_{eq} - \delta\Omega sin^2\theta \tag{2.15}$$

where $\Omega(\theta)$ is the rotation rate at latitude θ in $\mathrm{rad\,d^{-1}}$, Ω_{eq} is equatorial rotation rate, and $\delta\Omega$ is the rotational shear between the equator and the pole, as shown in Equation 2.16.

$$\delta\Omega = \Omega_{eq} - \Omega_{pole} \tag{2.16}$$

Often, the strength of the rotational shear ($\delta\Omega$) is sometimes quoted as the *lap time*, and is found using Equation 2.17.

$$lap\ time = \frac{2\pi}{\delta\Omega} \tag{2.17}$$

There are a number of different ways in which differential rotation has been measured on solar-type stars. High precision photometry has been used to infer differential rotation. Messina and Guinan (2003) used long-term photometry to infer differential rotation occurring on 6 solar-type stars. They observed short-, medium- and long-term variations in period, shape and amplitude of the light curves. In addition, they observed antisolar-like differential rotation on some stars including DX Leo (SpType: K0V[1]) and LQ Hydra (SpType: K0V[1]) where the high-latitude spots rotate faster than lower-latitude spots. Fröhlich et al. (2012) has used photometric data from the Kepler spacecraft to measure the differential rotation of two young (100 to 200 Myr), sun-like stars KIC7985370 and KIC7765135 with the high-latitude spots rotating slower than the low-latitude ones, observing a shear of $\delta\Omega \sim 0.18$ rad d^{-1}thereby giving a *laptime* of $\sim$ 35 days. Spectroscopy has provided a wealth of information on the differential rotation of stars. For example, Baliunas et al. (1985) used spectroscopy, in particular the relative strength of the chromospheric Ca II emission cores, over several seasons to infer the presence of differential rotation in a number of late-type stars. The limitation with this study was that it merely placed a lower limit on the magnitude and sign (solar-like versus antisolar-like) of the differential rotation.

Reiners (2006); Reiners and Schmitt (2003) and Ammler-von Eiff and Reiners (2012) used a Fourier transform method to derive the parameters for rapidly rotating F-type / early G-type inactive stars. They produce a deconvolved line profile from the stellar spectra and then determine the ratio of the second and first zero of the resulting Fourier transform. This ratio is a measure of the differential rotation on the star. However, for active young stars with significant asymmetry within the line profiles, this technique is not as effective. Doppler imaging (DI) uses the evolution of the star spots to determine the magnitude of the differential rotation. One technique is to use cross-correlation of Doppler images taken several days apart (Donati and Collier-Cameron, 1997; Petit et al., 2002, 2004a; Barnes et al., 2005a). With this technique, successive stellar Doppler images are compared by tracking the spot features at different latitudes on the surface of the star. LQ Lupi (RX J1508.6-4423) (Donati et al., 2000) is one star that has had its differential rotation determined using this cross-correlation technique. Donati et al. (2000) also used another method to determine the differential rotation on LQ Lupi by incorporating a solar-like differential rotation law, as defined in Equation 2.15, into the

[1] Montes et al. (2001)

imaging process and use χ^2 minimization techniques to determine the magnitude of differential rotation. They found reasonable agreement, to within the respective error bars, between this χ^2 minimisation technique, and the estimates obtained from both the visual fit and the cross-correlation image.

The application of the χ^2 minimization is a powerful technique that assumes a solar-like differential rotation profile. This is a limitation as by its nature, it cannot detect non-solar-like behaviour. As mentioned previously, there have been stars found to have antisolar differential rotation. Apart from the study by Messina and Guinan (2003), Vogt et al. (1999) used DI of the RS CVn star HR 1099 over several years to observe antisolar-like differential rotation. Kővári et al. (2007) used cross-correlation techniques to measure antisolar differential rotation on the active K-giant σ Geminorum. Brown (2011) also found tentative evidence of antisolar differential rotation on the early G-type star RX J0850.1-7554.

In this thesis the differential rotation of targets is measured using this χ^2 minimisation technique that systematically adjusts the differential rotation parameters, $\Omega_{\rm eq}$ and $\delta\Omega$ and determines the best fit to the data, by minimising the difference between the data and the model fits using χ^2 minimisation techniques. A paraboloid is fitted to the grid of reduced-χ^2 landscape to determine the differential rotation parameters. χ^2 minimisation has been successfully applied to a small number of late F-/early-G stars (e.g. Petit et al., 2002, 2004b; Barnes et al., 2005a; Marsden et al., 2006). HD 171488 (V889 Her: $\delta\Omega$ $\sim$0.36-0.52 rad d^{-1}) (Marsden et al., 2006; Jeffers and Donati, 2008; Jeffers et al., 2011), HD 307938 (R58 in IC 2602: $\delta\Omega$ $\sim$0.08-0.195 rad d^{-1}) (Marsden et al., 2005; Brown, 2011), HR 1817 ($\delta\Omega$ $\sim$0.256 rad d^{-1}) (Mengel, 2005), LQ Lupi ($\delta\Omega$ $\sim$0.097-0.12 rad d^{-1}) (Donati et al., 2000; Brown, 2011) and RX J0850.1-7554 ($\delta\Omega$ $\sim$0.034 rad d^{-1}) (Brown, 2011) are some of these stars that have had their differential rotation measured using this χ^2 minimisation technique. There appears to be a change in the level of differential rotation with spectral type, and will be explored in more detail throughout this thesis. A more complete list of stars that have had their differential rotation measuring using DI and ZDI is shown in Appendix D.1.

2.7 Conclusions

This project utilises the tools of photometry, spectroscopy and spectropolarimetry to study solar-type stars. In addition, LSD will be used as it combines the information from many spectral lines to produce a single line profile, thereby providing an enormous multiplex gain in the S/N ratio (Donati et al., 1997). For example, a typical AAT spectra has an average S/N for a typical Stokes I LSD profile of $\sim$1006 and a Stokes V LSD profile of $\sim$5170 whereas the maximum S/N for the central order was only $\sim$84. It is through LSD that the spot and magnetic features can be extracted from the spectra and subsequently map the star thereby probing the interior of that star. Thus DI and ZDI provide unique information on the dynamo of solar-type stars. This is a comprehensive research thesis on the magnetic configurations of young solar-type stars hence is timely and relevant as it widens our understanding of magnetic activity across a range of solar-type stars with five more stars, of which three may be considered as sun-like stars, added to the growing sample and gives crucial clues on the possible magnetic behaviour of the young Sun.

Chapter 3

The young G-type star: HD 106506[1]

3.1 Introduction

HD 106506 is a rapidly rotating, intermediate mass, solar-type star in the constellation of Crux. It has a Right Ascension $12^h15^m18.55504^s$ and Declination $^-63^o25'30.3376''$ (J2000.0 van Leeuwen, 2007). HD 106506 is a suitable target for DI and ZDI. Henry et al. (1996) used Ca II H and K spectral lines and measured a $\log R'_{\rm HK} = ^-3.95$. Soderblom et al. (1998) suggested HD 106506 might be a spectroscopic binary (SB2). Mason et al. (1998) and Cutispoto et al. (2002) searched for a companion star as an explanation for the associated activity but deduced this star as being single. de Zeeuw et al. (1999) identified this star as a member of the Lower Centaurus Crux association. The high resolution spectroscopic survey for southern DI and ZDI targets by Waite et al. (2005) confirmed this star to be young, active and rapidly rotating. They measured a rotation rate of $v \sin i \sim 80$ km s^{-1}, strong Hα chromospheric activity ($\log R'_{\rm H\alpha} \sim ^-4.2$), and deformation of the spectral line profiles indicating the presence of large starspots, with perhaps a large polar spot.

The aim of this investigation is to map starspots on the surface of this star with a view to measuring the rotational shear on its surface and to measure and map the magnetic field structure on the surface of this star. Spectropolarimetry of HD 106506

[1]This chapter is based on the published work: Waite, I. A., Marsden, S. C., Carter, B. D., Hart, R., Donati, J.-F., Ramrez Vélez, J. C., Semel, M., Dunstone, N., 2011, *Magnetic fields and differential rotation on the pre-main sequence - III. The early-G star HD 106506*, MNRAS, 413, 1949.

was obtained using the 3.9 m Anglo-Australian Telescope (AAT) over an 11 night period from March 30 to April 09, 2007. Near-simultaneous BVR photometric data were obtained using the University of Louisville's 50cm telescope at the University of Southern Queensland's Mount Kent Observatory (MKO).

3.2 Fundamental Parameters of HD 106506

HD 106506 is a G1V star (Torres et al., 2006) with a median visual magnitude of 8.5617 (van Leeuwen, 2007), a B-V value of 0.605 and a V-I value of 0.67, based on the transformed *HIPPARCOS* and *TYCHO* data, (ESA, 1997). It has a trigonometric parallax of 7.96 ± 0.88 milliarcseconds (mas) (Perryman et al., 1997) giving a distance of 126 ± 14 parsecs (pc) or 410 ± 46 light years (lyr). Using this V-I value, the temperature of HD 106506 is approximately 5870 ± 45 K. This was determined using the formulation of Bessell, Castelli & Plez (1998). The absolute magnitude is 3.053 ± 0.244. Using the bolometric corrections listed in Bessell et al. (1998) and the formulation contained within that paper, HD 106506 is estimated to be 2.15 ± 0.26 $R_{\odot}$. The resulting luminosity of HD 106506 is 4.81 ± 1.2 $L_{\odot}$. Figure 3.1 shows the theoretical tracks of Siess et al. (2000), from which it may be deduced that the star is ≈10 Myr of age and has a mass of between 1.4 and 1.6 $M_{\odot}$.

3.3 Observations and Analysis

3.3.1 BVR Photometry at MKO

Broadband photometry was conducted on HD 106506 at Mount Kent Observatory (MKO) during 2005 and again in 2007. In 2005, the O'Mara telescope, using 35 cm Schmidt-Cassegrain optics, was used to place HD 106506 and associated nearby stars onto the standard Johnson-Cousins photometric system. In 2007, the newly commissioned University of Louisville telescope, consisting of a 50 cm corrected Dall-Kirkham design optics, was used to determine the photometric period. In each case, *IRAF* was used for the reduction and analysis of the data.

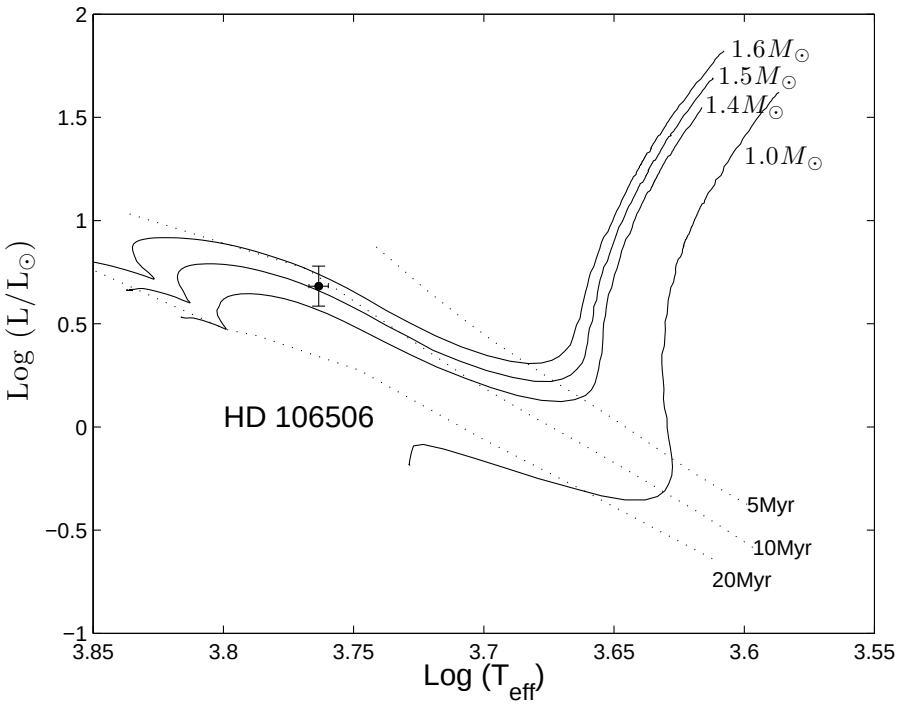

Figure 3.1: The evolutionary status of HD 106506, based on the theoretical models of Siess et al. (2000)

3.3.1.1 Standardisation of Comparison Stars: July 25, 2005

Several BVR photometric observations were taken of a number of standard stars located in Graham's E-regions (Graham, 1982). These stars, at declination close to -45^o make suitable standards for Southern Hemisphere observing programmes. The three regions used were: E-5 (Stars: A,O,U,S,V,Y,c), E-6 (Stars: 98,M.P,X,W) and E-7 (Stars: M and S). Synthetic aperture photometry, using *DAOPHOT*, was used with an aperture radius of 15 pixels ($\sim$ 4.5 arc seconds), based on the curves of growth (Stetson, 1990). The annulus from which the sky contribution was estimated has a size of 10 pixels. The relative sizes of these apertures used on the target star and the five comparison stars are shown in Figure 3.2. These observations were made under photometric conditions, with calm conditions and no detectable cloud. MKO has a Boltwood cloud detector[1] and a Davis weather centre[2] to enable real-time monitoring of sky conditions.

The routines found in the *PHOTCAL* package in *IRAF* were used to determine both the transformation coefficients and the magnitude of the stars, including HD 106506. As explained in Section 2.3.2, there were three images taken through each filter of the star fields and then averaged using *IMCOMBINE*, to produce a single image from which the magnitude of all the standard stars and the program stars were measured. The following transformation equations were solved using the *FITPARAM* task in *IRAF*:

$$m_{\rm b} = B + b_0 + b_1 X_{\rm b} + b_2(B - V) \tag{3.1}$$

$$m_{\rm v} = V + v_0 + v_1 X_{\rm v} + v_2(B - V) \tag{3.2}$$

$$m_{\rm r} = R + r_0 + r_1 X_{\rm r} + r_2(V - R) \tag{3.3}$$

where B, V and R are listed magnitudes of the standard stars in Graham (1982). The instrumental magnitudes, as measured by DAOPHOT were $m_{\rm b}, m_{\rm v}$ and $m_{\rm r}$. The zero points are b_0, v_0 and r_0; while b_1, v_1 and r_1 are the extinction coefficients and b_2, v_2 and r_2 are the colour correction coefficients. The values determined for the coefficients are given in Table 3.1 and the magnitudes are shown in Table 3.2.

[1] http://cyanogen.com/cloud_main.php
[2] http://www.davisnet.com/weather/

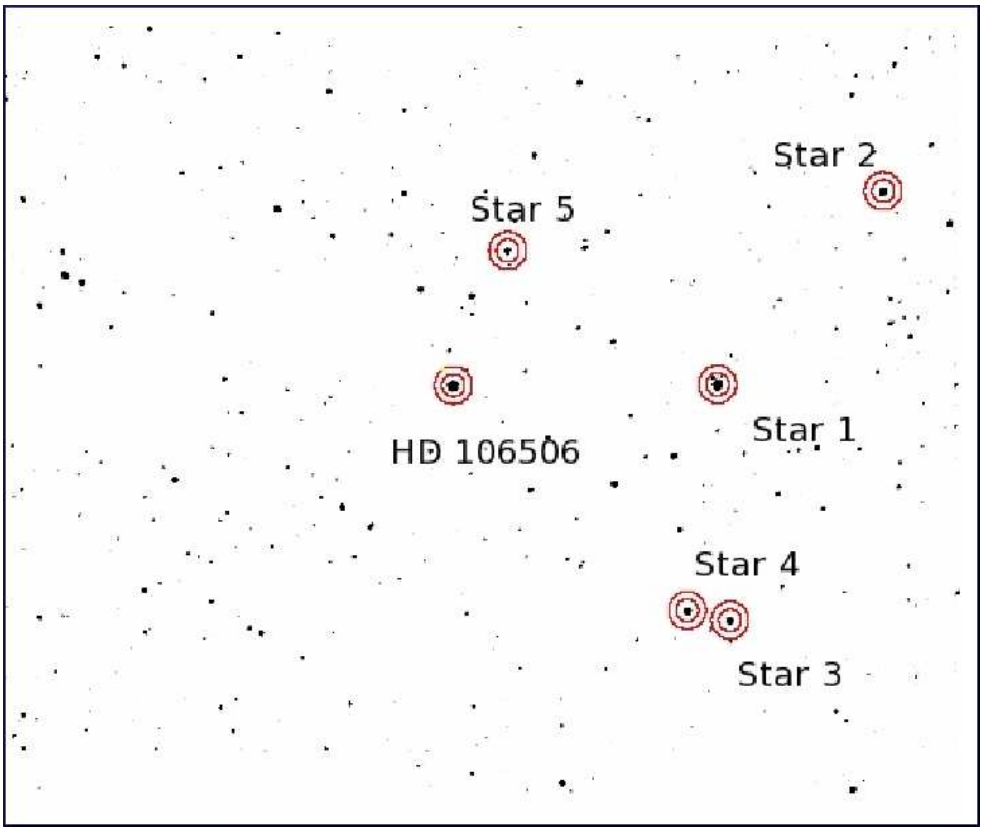

Figure 3.2: The star field surrounding HD 106506, showing five of the brighter stars that were used in the determination of the period. The stars' names are shown in Table 3.2. This image was taken using the O'Mara telescope. This was an 8 second image taken through the V-filter with a field of view of approximately 6.4 × 5.1 arc minutes. The concentric circles indicate the size of the aperture (radius ∼ 4.5 arc seconds) used in the photometry and the annulus indicates the area were the sky contribution was estimated.

Table 3.1: Transformation coefficients for July 25, 2005 photometry at MKO. The associated errors, rms fit and χ^2 value for each filter have been included

n	b_n	v_n	r_n
0	-3.217	-3.506	-3.709
	±0.14	±0.13	±0.12
1	0.311	0.144	0.134
	±0.11	±0.09	±0.10
2	-0.154	0.065	0.020
	±0.12	±0.06	±0.14
χ^2	0.103	0.060	0.023
rms fit	0.021	0.019	0.011

Table 3.2: The BVR information for HD 106506 and the comparison stars used to determine the period of HD 106506. Graham (1982) E-Regions, E5, E6 and E7, were used to standardise these stars. The data was processed using the routines in *PHOTCAL* found in *IRAF*. The data were taken on July 25, 2005 and a sample image, with the star number included, is shown in Figure 3.2.

Star	Star's Name	V	B-V	V-R
Target	HD 106506	8.463	0.594	0.356
Star 1	HD 106507	9.152	-0.024	0.044
Star 2	TYC 8979-979-1	10.108	0.100	0.101
Star 3	TYC 8978-1180-1	10.003	1.083	0.584
Star 4	HD 106417	10.133	1.015	0.558
Star 5	TYC 8978-5479-1	10.948	0.203	0.165

Table 3.3: The Journal of photometric observations of HD 106506 during 2007 showing the date and filters used. The E5-Region (Graham, 1982) was observed on April 11, 2007. The University of Louisville telescope was used for this run.

UT Date	Filters Used	UT begin	UT end
2007 April 01	B,V,R	09:12:11	19:03:53
2007 April 02	B,V,R	11:09:03	17:57:21
2007 April 03	B,V,R	09:48:02	18:10:43
2007 April 04	B,V,R	14:33:42	17:59:18
2007 April 05	B,V,R	11:06:02	17:14:08
2007 April 06	B,V,R	09:16:22	18:19:50
2007 April 07	B,V,R	09:13:45	18:13:12
2007 April 08	B,V,R	09:06:57	18:17:01
2007 April 11	B,V,R	10:10:43	13:26:59

3.3.1.2 BVR broadband photometric observations from MKO: 2007

The newly commissioned University of Louisville 50 cm telescope was used to provide supporting photometry to the ZDI run at the AAT. The raw data were taken by Dr Rhodes Hart and Mr Roger McQueen (while the author conducted all the reduction and analysis of that data). Table 3.3 shows a log of data taken during the observation run in 2007. *IRAF* was used to reduce and analyse the data, as explained in Section 2.3.2. Synthetic aperture photometry, using *DAOPHOT*, was used with an aperture radius of 15 pixels ($\sim$ 8 arc seconds), based on the curves of growth (Stetson, 1990). The annulus from which the sky contribution was estimated has a size of 10 pixels. On April 11, 2007, several observations were taken of the standard stars in Graham's E5-regions (Graham, 1982) so as to place HD 106506 on the standard magnitude scale. The stars used were A, O, U and S. *PHOTCAL* again was used to determine both the transformation coefficients to the magnitude of the stars (listed in Table 3.2), including HD 106506.

3.3.1.3 Period Determination in 2007

Five brighter stars, as shown in Figure 3.2, were selected as possible comparison stars. The instrumental magnitude of each of the five comparison stars was checked against

each other (Comparison - Check) in order to validate the consistency of the apparent brightness of each star during the observing run. Once that criteria was satisfied, the instrumental magnitude of each star was converted to intensity units, co-added and converted into a single instrumental magnitude for each image. This had the effect of improving the S/N of the five comparison stars as if it were a single star. Differential photometry was this applied to HD 106506 with the synthetic instrumental magnitude as the comparison "star". Discrete Fourier transforms (DFT), based on the algorithm as explained by Belserene (1988), was used on the time-series differential photometry data. The period of HD 106506 was determined in B, V and R bands. Figure 3.3 shows the phased folded light curve for the V- band as well as the B-V and V-R colour indices. The power spectrum is also shown as generated by the DFT algorithm. Graham's E5 Region, coupled with the five stars previously standardised, were used to place HD 106506 onto the Cousins magnitude system. The average period was determined to be 1.416 ± 0.133 days, and was consistent across all the comparison stars and in all observed photometry bands. The error was determined by finding the full width half maximum of the DFT line profile.

3.3.2 High Resolution Spectropolarimetric Observations from the AAT

High resolution spectropolarimetric data were obtained from the AAT using the University College of London Échelle Spectrograph (UCLES) and the Semel Polarimeter (SEMPOL) (Semel, 1989; Semel et al., 1993; Donati et al., 2003b). The detector used was the deep depletion English Electric Valve (EEV2) charge coupled device (CCD) with 2048 x 4096 13.5μm square pixels. UCLES was used with a 31.6 gr/mm grating covering 46 orders (orders # 84 to # 129). The central wavelength was 522.002 nm with full wavelength coverage from 437.71 nm to 681.56 nm. The dispersion of ∼0.004958 nm at order # 129 gave a resolution of approximately 71000. See Section 2.5.2 for more details regarding SEMPOL. A journal of the observations is shown in Tables 3.4 and 3.5.

The Stokes V profile is the result of constructively adding the individual spectra from the four exposures by "pair-processing" sub-exposures corresponding to the opposite orientations of the half-wave Fresnel Rhomb. To determine the reliability of the process, a "null" profile is produced as a measure of the noise within the LSD process. This null profile is found by "pair-processing" sub-exposures corresponding to the identical

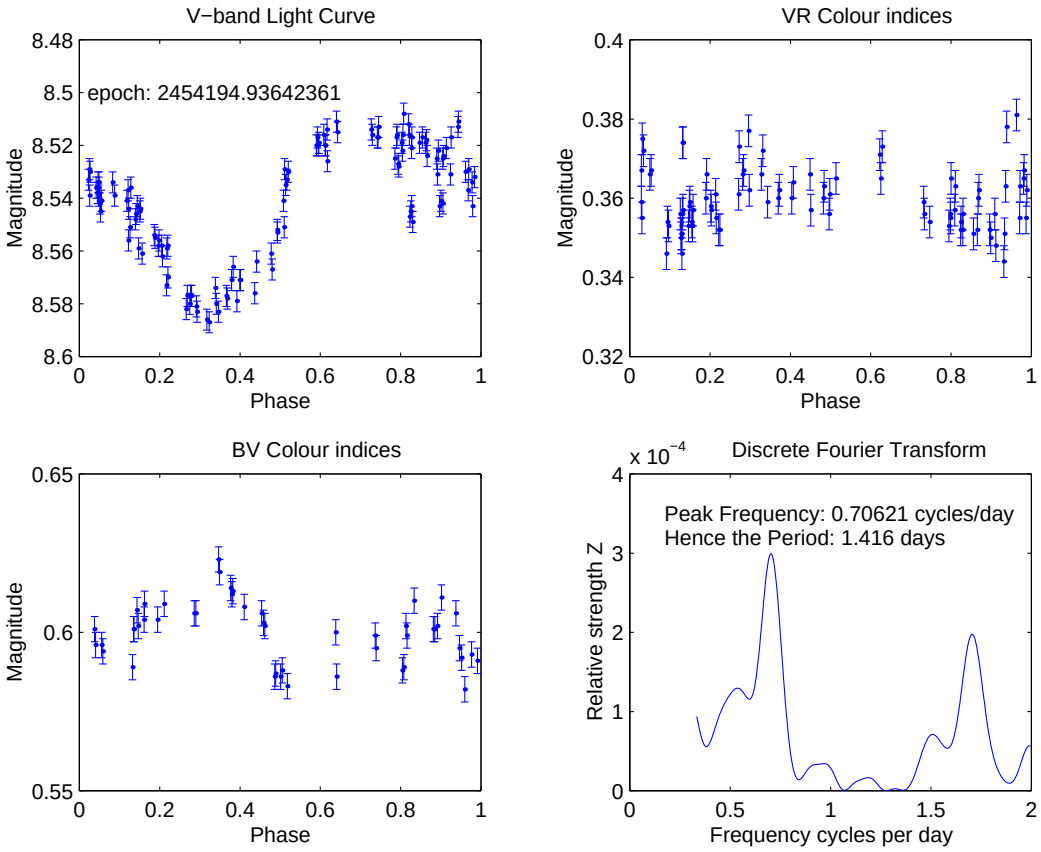

Figure 3.3: The top left panel shows the V-band light curve for HD 106506, with the phase referenced to epoch = 2453543.93642361 d which coincided approximately with the middle of the AAT observing run on the star. The BV and VR colour light curves are also shown. The bottom right panel shows the Discrete Fourier transform, which is interpreted in terms of the photometric rotation period of 1.416 days.

Table 3.4: Journal of spectropolarimetric observations of HD 106506 using the 3.9 m AAT.

UT Date	UT middle	Exp. Time[1] (sec)	Stokes V Mean S/N[2]	FAP[3]	Detection?
2007 March 30	09:25:08	4×600	3653	8.501×10^{-2}	no detection
2007 March 30	10:11:13	4×600	3866	3.890×10^{-3}	marginal
2007 March 30	10:57:10	4×600	3443	5.022×10^{-2}	no detection
2007 March 30	11:43:08	4×600	3361	5.921×10^{-3}	marginal
2007 March 30	13:19:04	4×600	4284	2.213×10^{-1}	marginal
2007 March 31	09:15:44	4×600	3273	2.138×10^{-4}	marginal
2007 March 31	10:01:41	4×600	3081	1.648×10^{-1}	no detection
2007 March 31	10:47:39	4×600	3473	6.316×10^{-2}	no detection
2007 March 31	11:33:37	4×600	4241	5.021×10^{-4}	marginal
2007 March 31	13:07:52	4×600	4725	1.043×10^{-2}	no detection
2007 April 01	09:13:49	4×600	2949	1.455×10^{-1}	no detection
2007 April 01	10:05:32	4×600	3156	7.558×10^{-1}	no detection
2007 April 01	10:51:30	4×600	3296	4.358×10^{-2}	no detection
2007 April 01	11:37:28	4×600	4182	3.769×10^{-1}	no detection
2007 April 01	13:13:53	4×600	3506	8.019×10^{-1}	no detection
2007 April 02	09:17:42	4×600	3799	6.824×10^{-2}	no detection
2007 April 02	10:03:40	4×600	3987	9.068×10^{-3}	marginal
2007 April 02	10:49:38	4×600	4891	2.828×10^{-4}	marginal
2007 April 02	11:35:35	4×600	5190	5.523×10^{-3}	marginal
2007 April 02	13:15:55	4×600	5353	9.738×10^{-9}	definite
2007 April 03	09:48:13	4×600	2425	4.810×10^{-1}	no detection
2007 April 03	10:34:11	4×600	2483	8.305×10^{-1}	no detection
2007 April 04	09:19:19	4×600	3924	4.995×10^{-2}	no detection
2007 April 04	12:20:28	4×600	5433	3.150×10^{-2}	no detection
2007 April 05	10:35:37	4×600	4749	1.023×10^{-8}	definite
2007 April 05	11:21:35	4×600	5382	5.633×10^{-7}	definite
2007 April 05	12:58:03	4×600	3938	3.882×10^{-1}	no detection
2007 April 05	13:44:01	4×600	3536	2.102×10^{-2}	no detection

continued next page....

[1] Each sequence of 4×600=2400 seconds exposures. After each exposure, the "rotating half-wave retarder" of the polarimeter is rotated between $+45^o$ and -45^o so as to remove instrumental polarization signals from the telescope and the polarimeter.

[2] Signal-to-noise (S/N) of the resulting Stokes V profile.

[3] FAP: False Alarm Probability. See Section 3.3.2 for more details.

Table 3.5: Journal of spectropolarimetric observations of HD 106506 using the 3.9 m AAT cont.

UT Date	UT middle	Exp. Time[1] (sec)	Stokes V Mean S/N[2]	FAP[3]	Detection?
2007 April 06	09:31:05	4×600	2408	1.023×10^{-8}	definite
2007 April 06	11:45:16	4×600	2989	5.633×10^{-7}	definite
2007 April 07	09:12:06	4×600	5171	1.274×10^{-3}	marginal
2007 April 07	09:58:10	4×600	4827	3.857×10^{-3}	marginal
2007 April 07	10:44:08	4×600	4530	4.484×10^{-2}	no detection
2007 April 07	11:30:11	4×600	5611	7.793×10^{-5}	definite
2007 April 07	13:05:60	4×600	5688	3.775×10^{-15}	definite
2007 April 08	10:53:32	4×600	4909	4.278×10^{-2}	no detection
2007 April 09	09:09:42	4×600	4995	2.436×10^{-6}	definite
2007 April 09	09:57:26	4×600	4799	7.649×10^{-6}	definite

[1] Each sequence of 4×600=2400 seconds exposures. After each exposure, the "rotating half-wave retarder" of the polarimeter is rotated between $+45^o$ and -45^o so as to remove instrumental polarization signals from the telescope and the polarimeter.

[2] Signal-to-noise (S/N) of the resulting Stokes V profile.

[3] FAP: False Alarm Probability. See Section 3.3.2 for more details.

positions of the half-wave Fresnel Rhomb of the SEMPOL polarimeter during each sequence of 4 sub-exposures. For each observation a false-alarm probability (FAP) of magnetic field detection was determined. FAP is a measure of the chance of the signal found in the Stokes V profile being a result of noise fluctuations rather than a real magnetic detection. The FAP is based on a χ^2 probability function (Donati et al., 1992b) and is estimated by considering the reduced χ^2 statistics both inside and outside the spectral lines, as defined by the position of the unpolarised LSD profiles, for both the Stokes V and the null profiles (Donati et al., 1997). The FAP for each observation is listed in Tables 3.4 and 3.5. A definite magnetic detection in the Stokes V was considered if the associated FAP was smaller than 10^{-5} (i.e. χ^2 probability was larger than 99.999 %) while a marginal detection was observed if the FAP was less than 10^{-3} but greater than 10^{-5}. In addition to this, the signal must only have been detected in the Stokes V profile and not within the null profile, and be within the line profile velocity interval, from (v_{rad} - $v\sin i$) to (v_{rad} + $v\sin i$). This criteria is consistent with the limits used by Donati et al. (1997).

3.3.3 Spectropolarimetric Analysis

The initial data reduction was completed using the ESpRIT (Échelle Spectra Reduction: an Interactive Tool) software package (Donati et al., 1997, 2003b). Preliminary processing involved removing the bias and using a nightly master flat combining typically 20 flat field exposures. Each stellar spectrum was extracted and wavelength calibrated against a Thorium-Argon lamp. The mean pixel resolution for the AAT spectra was determined to be 1.689 $\mathrm{km\,s^{-1}pixel^{-1}}$. In order to correct for the minor instrumental shifts in wavelength space due to atmospheric temperature or pressure fluctuations, each spectrum was shifted to match the centre of the Stokes I LSD profile of the telluric lines contained in the spectra, as was done by Donati et al. (2003b) and Marsden et al. (2006). After using ESpRIT, LSD was applied to the reduced spectra. A G2 line mask created from the Kurucz atomic database and ATLAS9 atmospheric models (Kurucz, 1993) was used during the LSD process.

Table 3.6 shows the initial parameters that were used in the analysis and the production of the Stokes I (intensity) and Stokes V (magnetic) maps.

Table 3.6: The parameters used to produce the maximum-entropy image reconstruction of HD 106506, including those associated with surface differential rotation.

Parameter	Value
Spectral Type [1]	G0V
Photometric Period	1.416 ± 0.133 days
Equatorial Period (Using Stokes I)	1.39 ± 0.01 days
Inclination Angle	65 ± 5^o
Projected Rotational Velocity, $v\sin i$	79.5 ± 0.5 km s^{-1}
Unspotted Apparent Visual magnitude	8.38
Photospheric Temperature, T$_{phot}$	5900 ± 50 K
Spot Temperature, T$_{spot}$	4000 ± 50 K
Radial Velocity, v$_{rad}$	13.1 ± 0.1 km s^{-1}
Stellar Radius[2]	2.15 ± 0.26 $R_\odot$
Convection Zone Depth[4]	0.137 ± 0.006 $R_\star$
	0.284±0.043 $R_\odot$
Age[3]	≈10 Myr
Mass[2]	1.5 ± 0.1 $M_\odot$
Stokes I: Ω_{eq}	4.54 ± 0.01 rad d^{-1}
Stokes I: $\delta\Omega$	$0.21^{+0.02}_{-0.03}$ rad d^{-1}
Stokes V: Ω_{eq}	4.51 ± 0.01 rad d^{-1}
Stokes V: $\delta\Omega$	0.24 ± 0.03 rad d^{-1}
Epoch used (HJD)	2454194.93642361

[1] Torres et al. (2006)

[2] based on the formulation contained in Bessell et al. (1998)

[3] based on the theoretical isochrones from Siess et al. (2000)

[4] based on the formulation contained in Noyes et al. (1984); see Section 5.4.5 in Chapter 5 for more details

3.4 Photospheric and Chromospheric Features of HD 106506

The brightness and magnetic images of HD 106506 were created using *ZDICAM* (Brown et al., 1991; Donati and Brown, 1997). This utilizes the time-series Stokes I and V LSD profiles as inputs for the inversion process to produce the brightness and magnetic images, as explained in Section 2.4.1.

3.4.1 Image Reconstruction: Stokes I Doppler imaging and surface differential rotation

In order to produce the brightness image of HD 106506, a two-temperature model was used (Collier Cameron, 1992), assuming one temperature was for the quiet photosphere, T_{phot}, while the other temperature is for the cooler spots, T_{spot}. Synthetic gaussian profiles were used to represent both the spot temperature and the quiet photosphere temperature.

The imaging code was used to establish the values of a number of basic parameters, including the star's inclination angle, projected rotational velocity, $v\sin i$, and radial velocity, v_{rad}, as explained in Section 2.4.1. The full set of parameters that gave the minimum χ^2 value are shown in Table 3.6 and were adopted when producing the final Doppler imaging map in Figure 3.4(left panel). By incorporating the photometry from MKO into the imaging process, T_{phot} and T_{spot} were determined by minimising the deviations between the measured and modelled data in both the V- and R-bands. The effective photospheric temperature was determined to be 5900 $\pm$ 50K, which is consistent with that calculated based on the photometric colours of the star and using the bolometric corrections of Bessell et al. (1998) within the error bars of both determinations. The spot temperature was determined to be 4000 $\pm$ 50K. This photospheric-spot temperature difference of 1900K for this early G-dwarf is consistent with measurements made by other authors such as Marsden et al. (2005, 2011a,b) and supports the relationship between photospheric and spot temperatures found by Berdyugina (2005) (Figure 7 on page 27 of that work). The intensity map with the photometry included is shown in Figure 3.4(b). The incorporation of the photometry is simply an extension of the DI process with the photometry data being fitted simultaneously with the spectroscopy data. The emphasis placed on the photometric data is determined by the weighting assigned to it. For the HD 106506 images in Figure 3.4(right panel), a weighting of

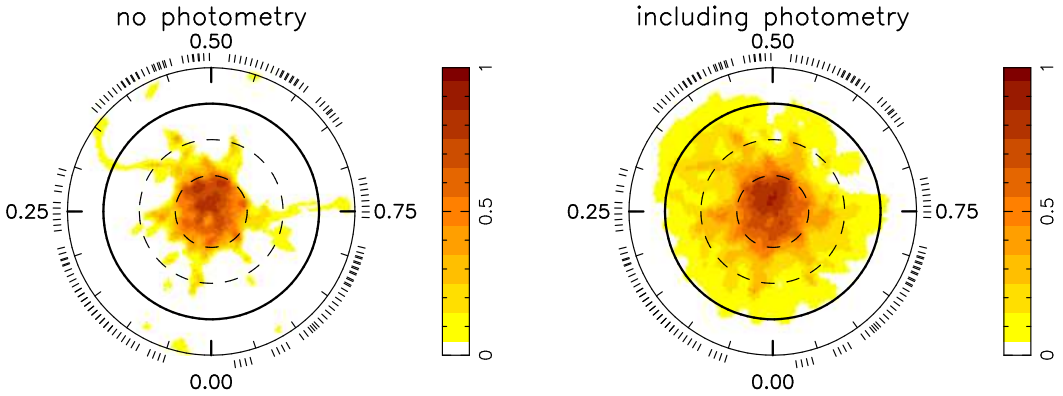

Figure 3.4: (a) The figure on the left is the maximum entropy map that was generated entirely from the AAT data, with a spot filling factor (the level of spot coverage over the entire stellar surface) of 0.062 (or 6.2%). (b) The figure on the right is a similar map but including near simultaneous photometry from the MKO. The spot filling factor was 0.127 (or 12.7%). The χ^2 value was set to 0.5 in the modelling process. The images are polar projections extending down to a latitude of -30^o. The bold line denotes the equator and the dashed lines are +30^o and +60^o latitude parallels. The radial ticks indicate the phases at which this star was observed spectroscopically.

1 was assigned to the photometric data. A weighting of 1.0 on both data sets means that the relative weighting for each spectroscopic and photometric data point is equal to $1/\sigma_i^2$, where σ_i is the error bar associated with point i (Marsden et al., 2005). A weighting of 0.0 means that the photometric data is ignored in the analysis (Figure 3.4: left panel). Changing the weighting of the photometric data had a very minor impact on the resulting maps with lower latitude features still being enhanced. Various maps produced using different weightings are presented in Appendix A.

Surface differential rotation was determined using the χ^2 minimisation technique, as explained in Chapter 2. This technique incorporates a solar-like differential rotation law, as defined in Equation 2.15 (see Section 2.6), by systematically adjusting the differential rotation parameters, Ω_{eq} and $\delta\Omega$, and determining the best fit to the data. Initially, a fixed spot filling factor (the level of spot coverage over the entire stellar surface) of 0.062 (or 6.2%), as determined from the reconstructed map assuming solid-body rotation, was used and Ω_{eq} and $\delta\Omega$ were considered to be free parameters. The magnitude of the differential rotation was then determined by fitting a paraboloid to the reduced χ^2 values. The optimum value for Ω_{eq} was determined to be 4.54 $\pm$ 0.01

rad d^{-1}and $\delta\Omega$ was $0.21^{+0.02}_{-0.03}$ rad d^{-1}. These optimum values are listed in Table 3.6. The errors for the value of the differential rotation were established by varying both the spot filling factor and the inclination angle by $\pm$ 10% and determining Ω_{eq} and $\delta\Omega$ respectively. When varying the inclination angle, the associated multiplication factors were redetermined and the resulting spot filling factor was found to match the new angle by minimising the χ^2 value. Figure 3.5 shows each datapoint obtained from the variation in the parameter set, as explained above, with the actual data listed in Section C.2 of Appendix C. The error bar on each data point is the result of paraboloid fit of the reduced-χ^2 landscape for each individual differential rotation value when varying the spot filling factor and inclination angle of the star. The error bar on each datapoint being 1-σ errors in the paraboloid fit. The reduced χ^2 landscape for the various Ω_{eq} and $\delta\Omega$, assuming the best set of parameters, is shown in Figure 3.6 with the associated error ellipse been superimposed on that figure.

Incorporating the differential rotation into the maximum-entropy image reconstruction of the AAT spectroscopic data produces the map shown in Figure 3.4 (left panel). This map shows a large polar spot with some mid- to high-latitude features. The dynamic spectrum of the residuals between the observed and modelled profiles is shown in Figure 3.7. It appears that the Doppler imaging process, along with incorporating the differential rotation parameters, has removed the majority of the large scale features with only a small amount of structure still apparent in this dynamic spectrum.

With the inclusion of the near-simultaneous photometry data taken at MKO, the map produces features extending to the lower latitudes. This is clearly seen in Figure 3.4 (right panel). The photometric data has been able to enhance the lower-latitude features. In each map, an equatorial period of 1.39 d has been used, which was established during the differential rotation analysis. The zero-phase epoch was set to HJD = 2454194.93642361, which was the middle of the observation run. To determine the effectiveness of the modelling strategy, the model fits to the LSD profiles are shown in Figure 3.9. These modelled fits have the differential rotation and simultaneous photometry included in the modelling strategy. Whereas the modelling process has been able to recover most of the features, there appears to be some features that were not. For example, from phase, ϕ, 0.470 to 0.488 (i.e. the number of rotations, 1.470 to 1.488 on Figure 3.9), there appears to be an absorption feature that has not been recovered in the modelled line profiles. Donati et al. (2003b) observed similar features on the LSD

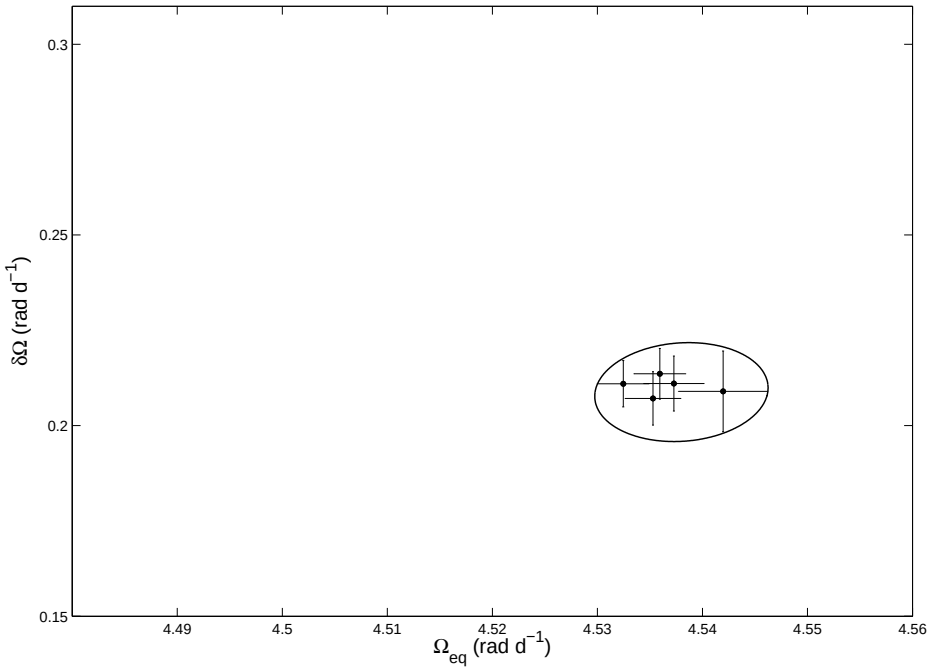

Figure 3.5: The determination of the overall error estimate for differential rotation of HD 106506 using the Stokes I data. Each datapoint is the result of paraboloid fit of the reduced-χ^2 landscape for each individual differential rotation value, given a specific change in a particular parameter such as inclination and spot size across a physically reasonable range. The error bar on each datapoint being 1-σ errors in the paraboloid fit.

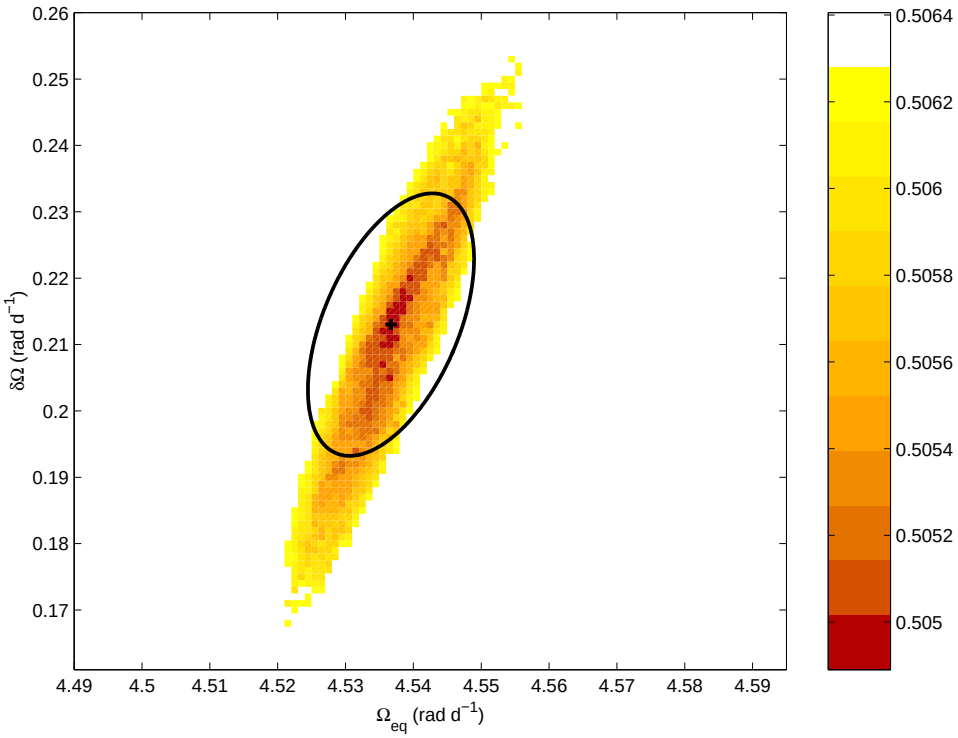

Figure 3.6: Surface differential rotation χ^2 minimisation for HD 106506. The image shows the reduced χ^2 values from the maximum-entropy Doppler imaging code for a fixed spot coverage of 0.062 and an inclination angle of 65^o. The darker regions correspond to lower χ^2 values. The image scale projects $\pm$ 7σ on to the axes in both $\Omega_{\rm eq}$ and $\delta\Omega$. The ellipse superimposed demonstrates the error for the value of the differential rotation and was determined by varying both the star's inclination and spot filling factors by $\pm$ 10% and determining $\Omega_{\rm eq}$ and $\delta\Omega$, as shown in Figure 3.5.

profiles of AB Doradus. They argued that only bright features (e.g. faculae) located on the surface of that star would produce such transient features on the observed line profiles. Given that the modelling strategy is optimised to reconstruct cool features (starspots), the code fails to fit these brighter features. Considering that there are very few of these type of features on HD 106506 at any given epoch, it is not a significant limitation for the present study. In addition, other features such as those observed from $\phi = 0.959$ to 0.976 (number of rotations from -0.041 to -0.024) may be the result of spot evolution. This is not an uncommon occurrence on stars, including our own Sun. Donati et al. (2003a), observed "mediocre fit" at some phase of the RS CVn-type star HR 1099 (SpType: K2:Vnk[1]) and concluded that temporal variability was the likely reason and that this "could be occurring on time-scales as short as a fortnight". Barnes (1999) also observed such variability on G-dwarf stars in the α Persei cluster on time-scales less than a month. So it is not unreasonable to suggest that some of the misfitting of the data could be a result of both faculae and starspot emergence and evolution.

As mentioned previously, the addition of photometry has extracted more lower-latitude features. Figure 3.8 shows the V and R light curves that were used to produce the final DI map, as shown in Figure 3.6 (right panel). Figure 3.9 shows the model profiles superimposed on the measured LSD profiles. The model profiles include the differential rotation parameters. As with the spectroscopy, the modelling strategy has not been able to fit all the data points. This is easily observed in Figure 3.8 with $\phi = \sim$0.35 not being able to extend to the fainter magnitude when HD 106506 was at its faintest in terms of apparent magnitude. Likewise at $\phi = \sim$0.65 where there appears to be a brightening of HD 106506 yet when the spectroscopy was added, there might have been a cooler feature (i.e. starspot) present. The Observed-Calculated (O-C) information in Figure 3.8 (bottom panels) show some structure remaining after modelling. This may indicate that the accuracy of the data may be at the limit required for simultaneous spectroscopy/photometry to be of significant value.

[1] Montes et al. (2001)

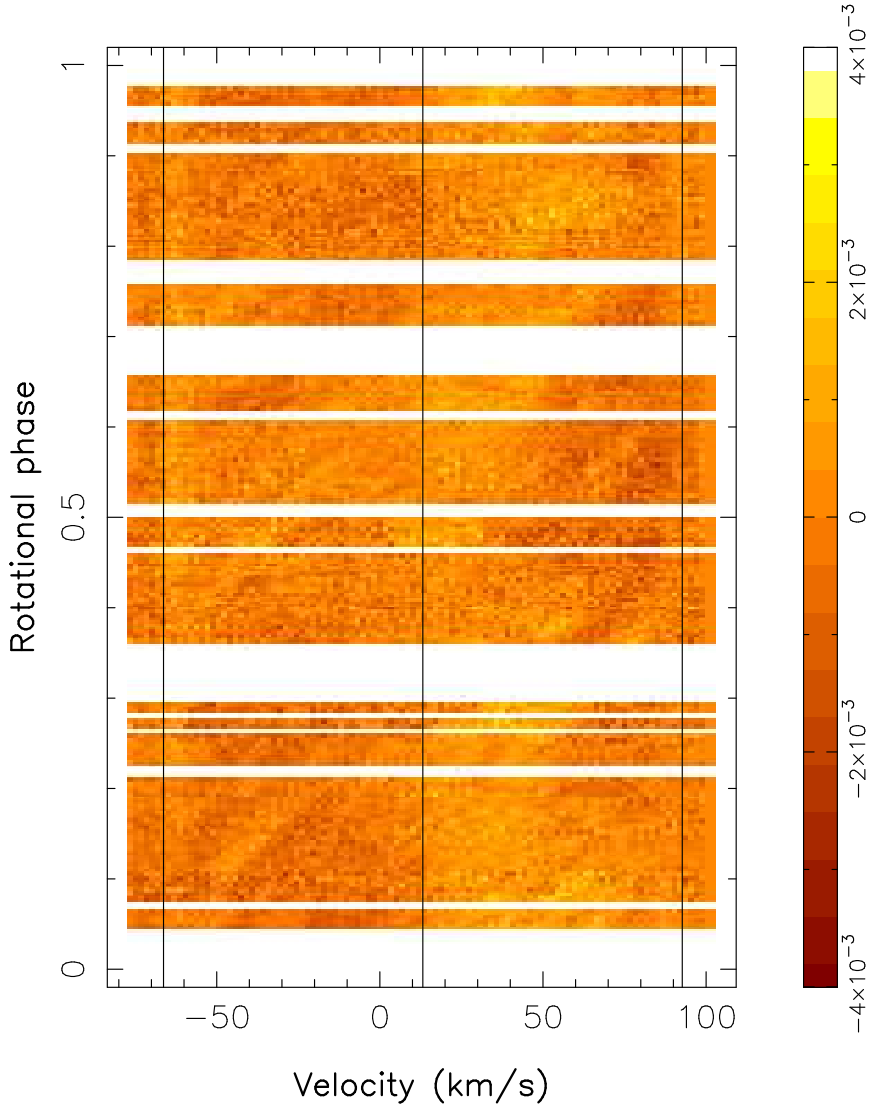

Figure 3.7: Dynamic spectra of the residuals between the observed-modelled LSD profiles, including differential rotation. The spectra is centred on the radial velocity of HD 106506. The three lines on the image shows the centre of the line profile (centre line) and the rotational broadening of the line profile (outer lines), which is 79.5 $\mathrm{km\,s^{-1}}$.

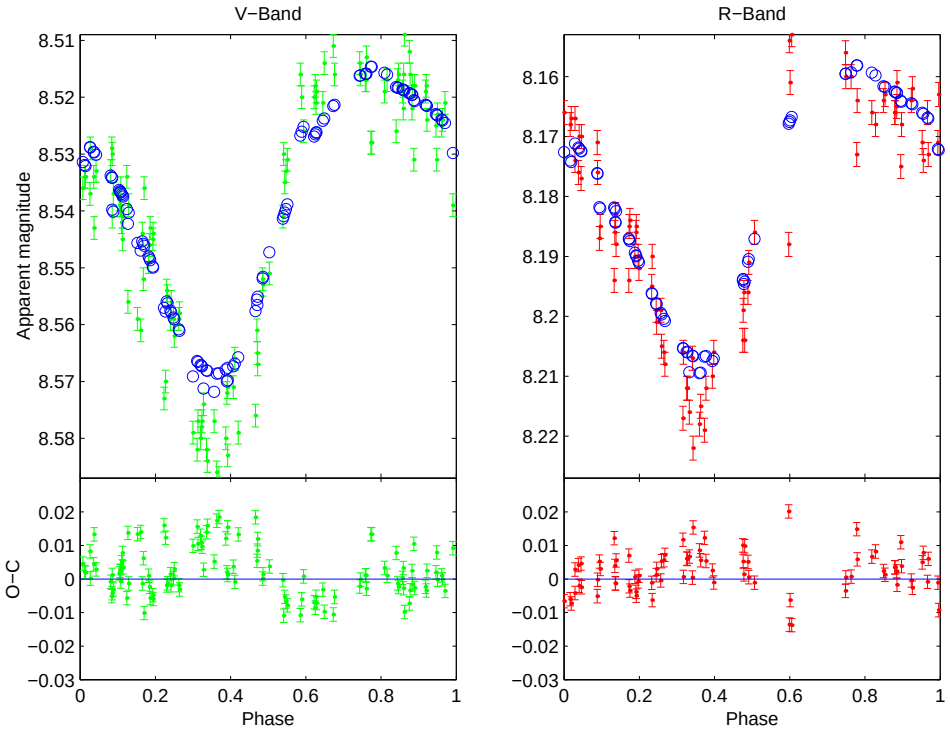

Figure 3.8: The photometric light curves for both the V filter and R filter (the points with error bars) coupled with the maximum-entropy fits (circles) for HD 106506. The bottom graph in each panel shows the Observed-Calculated values.

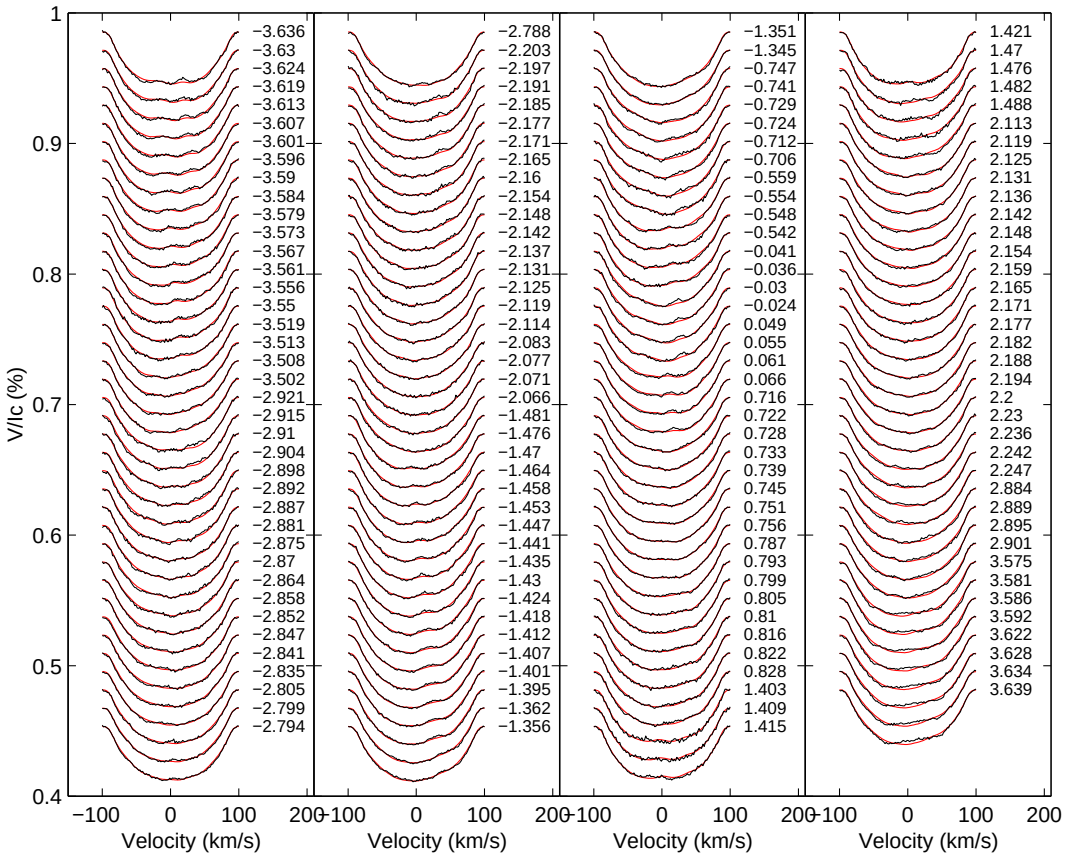

Figure 3.9: The maximum-entropy fits to the LSD profiles for HD 106506 with both photometry and surface differential rotation incorporated into the analysis. The red lines represent the modelled lines produced by the Doppler imaging process whereas the black lines represent the actual observed LSD profiles. Each successive profile has been shifted down by 0.014 for graphical purposes. The rotational phases at which the observations took place are indicated to the right of each profile.

3.4.2 Zeeman Doppler imaging: magnetic features on the surface of HD 106506

The modelling strategy of Donati and Brown (1997) was used to construct the magnetic field topology on HD 106506. This involved utilising the spherical harmonic expansions of the surface magnetic field as implemented by Donati et al. (2006b) (see Section 2.5 for more details). The maximum spherical harmonic expansion of $l_{max} = 40$ was selected as this was the minimum value where any further increase resulted in no further changes in the magnetic topologies.

A poloidal plus toroidal field was assumed in the reconstructed imaging and the images were created by fitting the data to within the noise level and resulted in a mean field strength of 69 G. A similar approach to measuring the differential rotation parameters, including the estimate of the error, was used as done for the Stokes I (brightness) features. Figure 3.10 shows each datapoint obtained from the variation in the parameter set, as explained in Section 3.4.1. Again, the error bar on each data point is the result of paraboloid fit of the reduced-χ^2 landscape for each individual differential rotation value. The error bar on each datapoint being 1-σ errors in the paraboloid fit. The actual data used to generate the final error ellipse is listed in Section C.2 in Appendix C. When considering these magnetic features, the equatorial rotation rate $\Omega_{\rm eq}$ was 4.51 $\pm$ 0.01 rad d^{-1}, with a photospheric shear $\delta\Omega$ of 0.24 $\pm$ 0.03 rad d^{-1}. This implies that the equatorial rotation period was 1.38 days with a shear approximately 4 times that of the solar value. The final reconstructed magnetic fields, incorporating differential rotation, are shown in Figure 3.11 with the associated fits to the Stokes V LSD profiles given in Figure 3.12.

3.4.3 Chromospheric Features: Prominences

The Hα line has been extensively used as an indicator of chromospheric activity (e.g. Thatcher and Robinson, 1993; Montes et al., 2004). A mean Hα spectral line for HD 106506 was generated from all the Hα profiles obtained during the observing run. Each individual spectrum was then subtracted from the mean Hα line, and a dynamic spectrum was then produced. Chromospheric features were observed at phases $\sim$0.15 and $\sim$0.75. Figure 3.13 shows this dynamic spectrum with a "bright" spot in this dynamic profile at $\sim$0.15 phase. This is where the chromosphere is much denser as a

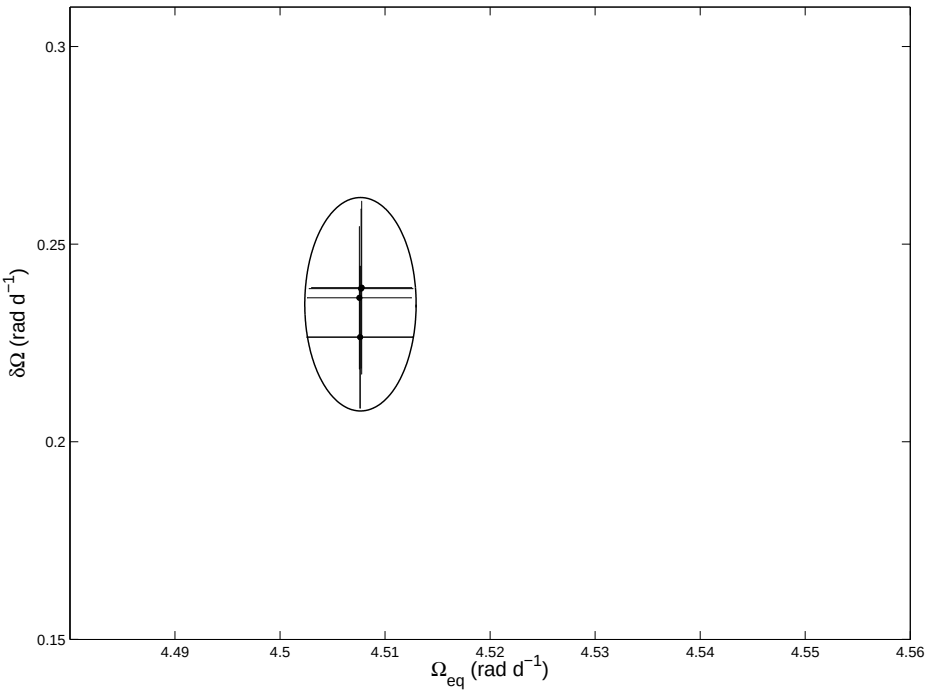

Figure 3.10: The determination of the overall error estimate for differential rotation of HD 106506 using the Stokes V data. Each datapoint is the result of paraboloid fit of the reduced-χ^2 landscape for each individual differential rotation value, given a specific change in a particular parameter such as inclination and global magnetic field strength across a physically reasonable range. The error bar on each datapoint being 1-σ errors in the paraboloid fit.

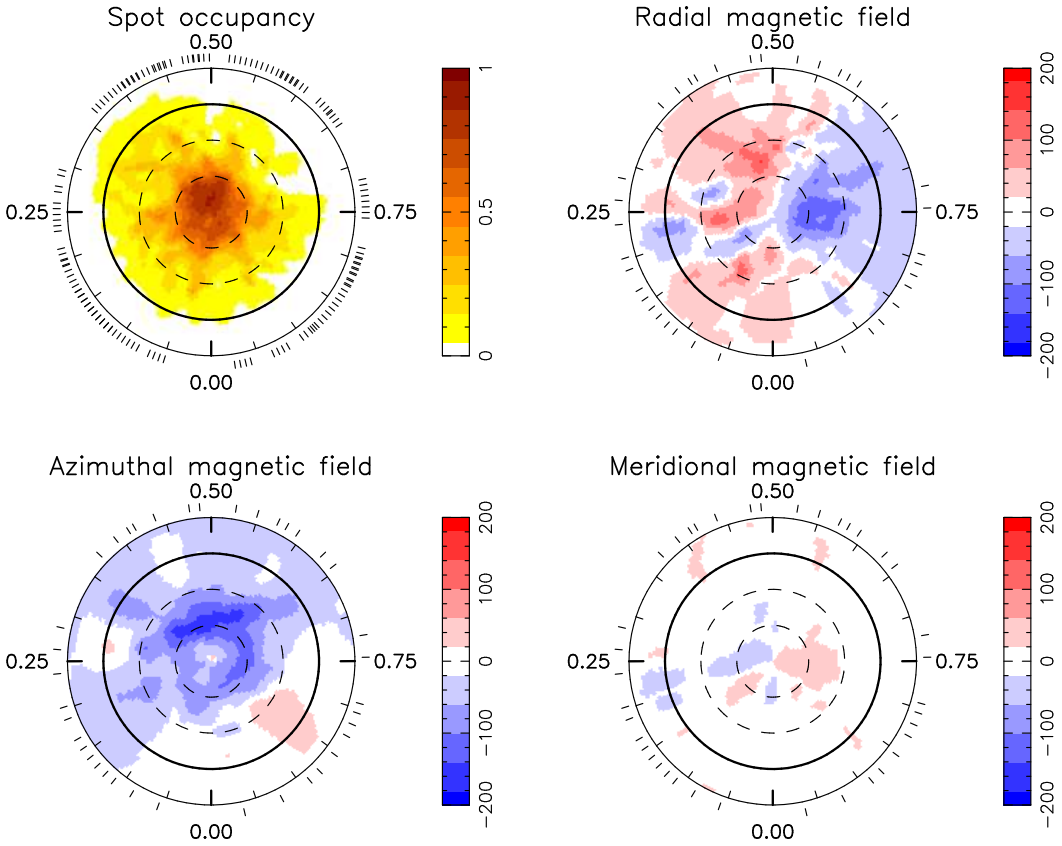

Figure 3.11: The maximum-entropy brightness and magnetic image reconstructions for HD 106506. These maps are polar projections extending down to -30^o. The bold lines denote the equator and the dashed lines are +30^o and +60^o latitude parallels. The radial ticks indicate the phases at which this star was observed spectroscopically. The scale of the magnetic images are in Gauss. The brightness image (top left-hand image) has a spot filling factor of ∼0.127 (or 12.7%) and is a combination of both the spectroscopic and photometric data. The magnetic images have a field modulus of 69 G. Differential rotation, as measured using the Stokes V profiles, has been incorporated into the analysis.

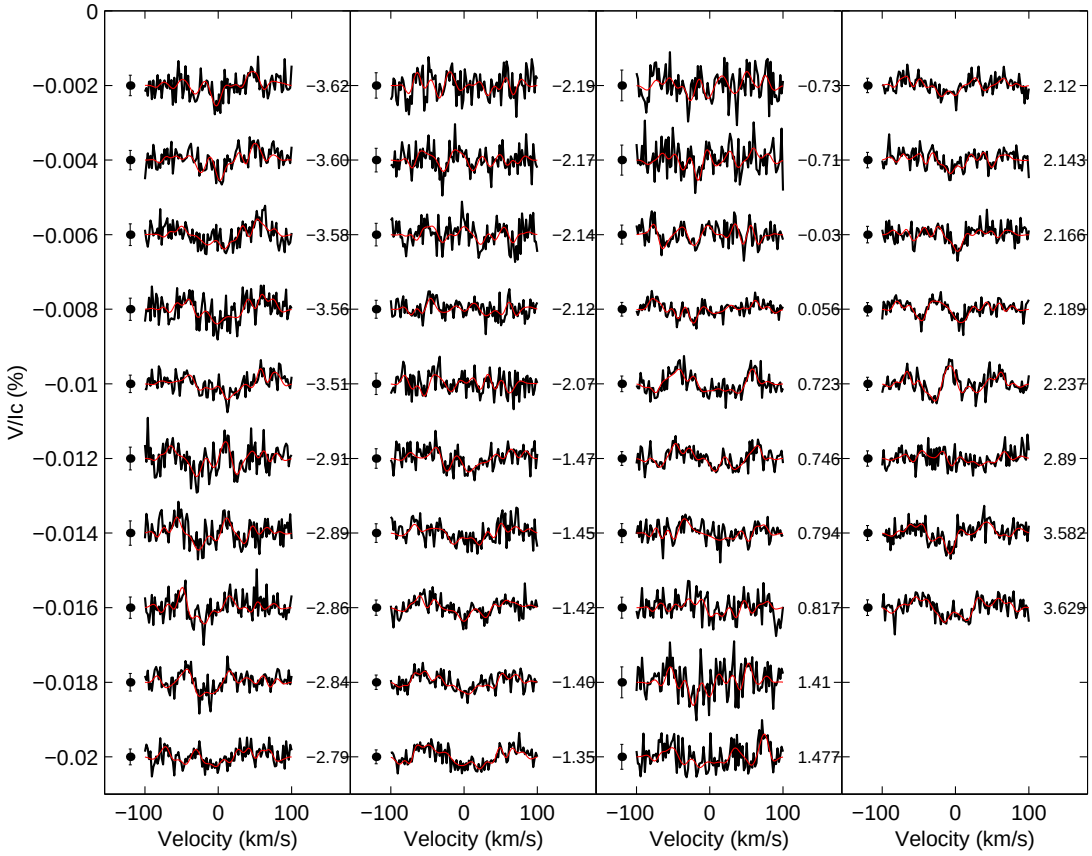

Figure 3.12: The maximum-entropy fits to the Stokes V LSD profiles for HD 106506 with surface differential rotation, as measured using the Stokes V profiles, incorporated into the analysis. The red lines represent the modelled lines produced by the Zeeman Doppler imaging process whereas the black lines represent the actual observed LSD profiles. Each successive profile has been shifted down by 0.002 for graphical purposes. The error bar on the left of each profile is plotted to $\pm$ 0.5 σ. The rotational phases, in terms of the number of rotational cycles, at which the observations took place are indicated to the right of each profile.

result of an increase in temperature in that local region. There appears to be a reduced emission at ∼0.75 phase as well. These variations in Hα emission lie within the stellar velocity profile and hence most likely arise from regions close to the stellar surface. These Hα variations can be interpreted in terms of prominences more akin to solar prominences than the more extended features knows to exist at the co-rotation radius of other active solar-type stars, such as LQ Lupus (Donati et al., 2000). Alternatively, plages, which are brigthenings in the chromosphere, may be an explanation to this observation. Plages are often associated with faculae that are located in the photosphere below.

Many authors (e.g. Zarro and Rodgers, 1983; Young et al., 1989; Thatcher and Robinson, 1993; Soderblom et al., 1993b; Montes et al., 2004; Waite et al., 2005) determine the emission component of the Hα line by subtracting the stellar spectrum from a radial velocity-corrected, inactive star that has been rotationally broadened to match the $v \sin i$ of the target. An example of this process is shown in Figure 4.14 in Chapter 4. As this technique is temperature dependent, the inactive star has to be close in spectral type. α-Centaurus A (SpType=G2V[1]) was used as this inactive star that was rotationally broadened to the $v \sin i$ = 79.5 km s^{-1}. The maximum emission equivalent width (EEW) was 551 ± 34 mÅ. This value was an average of 10 measurements taken on April 05, 2007 with the error estimate being the minimum and maximum for that series. Using the effective temperature for HD 106506, the surface flux per Ångstrom was determined by interpolating between model spectra obtained from the Pollux database[2]. This surface flux was then multiplied by the star's EEW to give the flux in the emission component of the H$_\alpha$ line. In order to remove the dependence upon the star's photosphere component, the chromospheric emission ratio, R$'_{H\alpha}$, was calculated using Equation 3.4.

$$R'_{H\alpha} = \frac{F'_{H\alpha}}{\sigma T_{eff}^4} \tag{3.4}$$

where F$'_{\mathrm{H}\alpha}$ is the surface flux emitted by the Hα line, σ is Stefan-Boltzmann constant (5.670373×10^{+8} Wm^{-2}K^{-4}) and T$_{eff}$ is the effective temperature of the star. The maximum chromospheric activity for HD 106506 was measured to be log R$'_{H\alpha}$ = $^{-}$4.21 ± 0.02. This value is similar to that observed by Waite et al. (2005) in April 2002.

[1] Torres et al. (2006)

[2] http://pollux.graal.univ-montp2.fr/

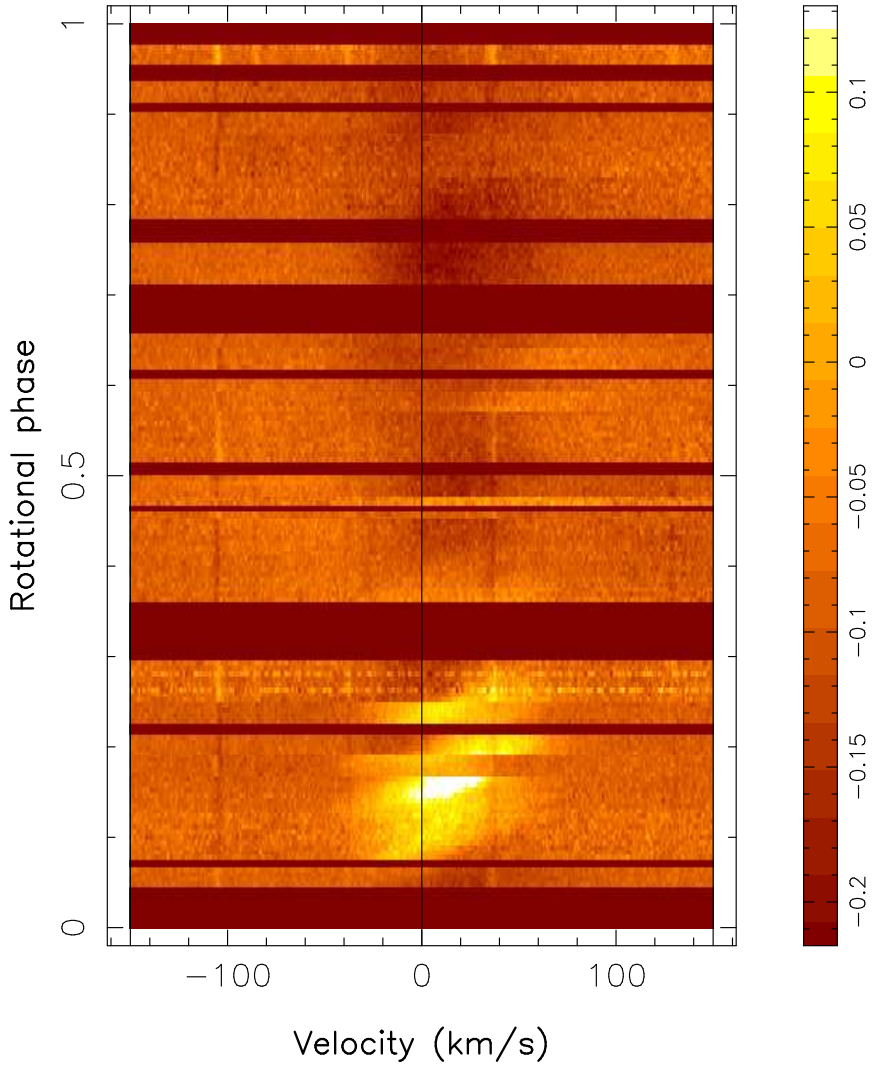

Figure 3.13: This figure shows a chromospheric features observed on HD 106506. The chromosphere is more dense at phase of ~ 0.15. There also appears to be an area at ~ 0.75 where the chromosphere is less dense than average.

3.5 Discussion

3.5.1 Spot Features and Surface Differential Rotation

Spectroscopic and photometric observations were used to produce the spot occupancy map shown in Figure 3.4. Photometry is very useful at extracting out the lower latitude features (Jeffers et al., 2002) but is not sensitive to the high-latitude features as these are always in view, whereas the spectroscopy extracts the higher latitude features (Unruh and Collier Cameron, 1997) but cannot discriminate lower latitude features at latitudes $\lesssim$ 30 degrees. Hence to get a more complete picture of the stellar image, both photometric and spectroscopic data need to be incorporated into the imaging process. Using the Stokes I spectroscopic information coupled with the photometry, the spot occupancy map, as shown in Figure 3.4 shows low-latitude to mid-latitude spots, and a predominant polar spot. These reconstructed images are consistent with those obtained in other Doppler images produced for young, single, rapidly rotating solar-type stars. The photometry enabled more of the low-latitude features to be recovered, as was done for the star R58 (in IC 2602) by Marsden et al. (2005). However, how reliable are these maps that include photometry? The photometric data has been able to enhance the lower-latitude features. This is not surprising as photometry, by its nature, is more sensitive to the features that are close to the visible stellar disc (that depends on the star's inclination). Alternatively, photometry contains limited information regarding the latitude of the spot features. Hence, features that are at higher (or lower) latitudes (and thus are not visible all of the time) may be interpreted as being at the centre of the visible stellar disk. HD 106506 has an inclination angle of $\sim 65 \pm 5^o$, meaning that the the visible disk would then be centred at a latitude of approximately 25^o. As seen in Figure 3.4 (right panel), the photometry that was added appears to have enhanced the features at approximately 25^o latitude. As stated in Section 3.4.1, the relative weight between the spectroscopic and photometric data had limited effect on the resulting maps.

This variation of spot occupancy with stellar latitude using spectroscopy alone and inclusive of the photometry is shown in Figure 3.14. The fractional spottedness is defined in Equation 3.5.

$$F(\theta) = \frac{S(\theta)cos(\theta)\delta\theta}{2} \tag{3.5}$$

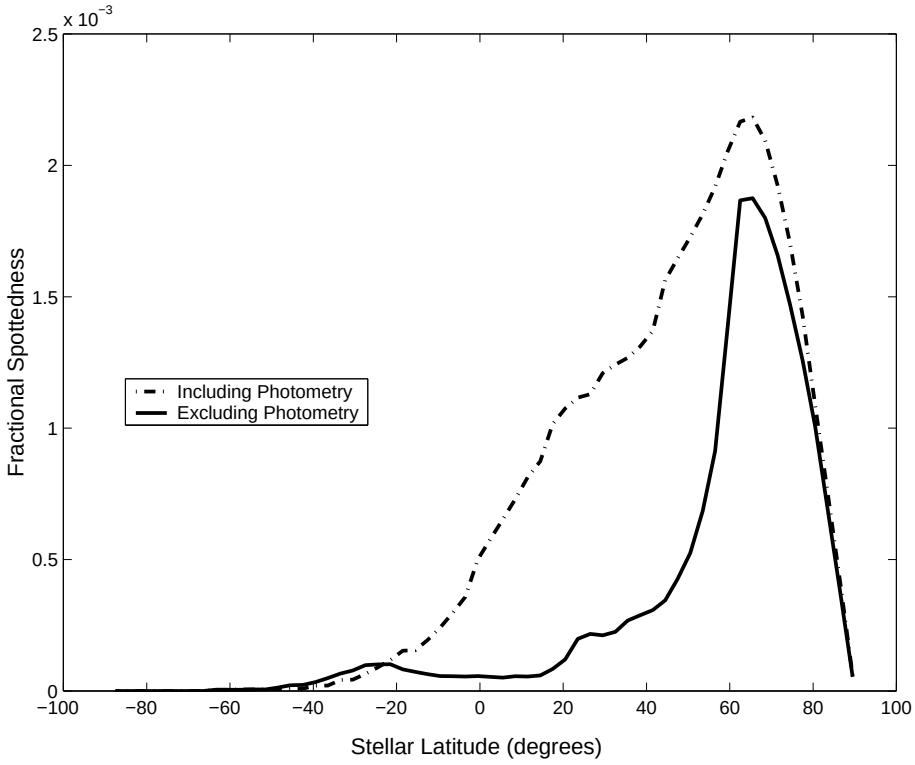

Figure 3.14: The fractional spottedness versus stellar latitude for HD106506 with and without photometry included in the imaging process. The fractional spottedness is based on the average spot occupancy at each longitude and is defined in Equation 3.5. The photometry is very useful at extracting out the lower latitude features whereas the spectroscopy extracts the higher latitude features.

where $F(\theta)$ is the fractional spottedness at latitude θ, $S(\theta)$ is the average spot occupancy at latitude θ, and $\delta\theta$ is the latitude width of each latitude ring. This clearly shows how the enhanced lower latitude features when incorporating the photometry data. Given the limited latitude information contained in that photometric data, one must treat this plot with caution.

The exact reasons why rapidly rotating stars have polar spots are still not fully understood. One theory (Schüssler et al., 1996; Buzasi, 1997; DeLuca et al., 1997) postulates that high-latitude, but not truly polar, spots are a result of the increased Coriolis effect, due to the rapid rotation, which may have the effect of deflecting the spot features to higher latitudes as they erupt through the star's convection zone. An additional hypothesis involves the transport of flux through the process of meridional flow (Schrijver and Title, 2001; Kitchatinov and Rüdiger, 1999). It is yet to be determined whether the polar spots on young solar-type stars are formed at high latitudes by the strong Coriolis effect in these rapidly rotating stars, or formed at low latitudes and pushed poleward by subsurface meridional flows. Nevertheless, the issue can be clarified by long-term monitoring of the spot topology of these stars, because meridional flows should be detectable as a poleward drifts in starspot features over time. Weber et al. (2005) have reported tentative evidence for large poleward meridional flows on early-K giants, but such an effect has yet to be detected for young solar-type stars.

When using the Stokes I information HD 106506 was found to have a photospheric shear of $0.21^{+0.02}_{-0.03}$ rad d^{-1} with the equator lapping the poles every $\sim 30^{+5}_{-3}$ days. When compared with the Sun's value for $\delta\Omega$=0.055 rad d^{-1}, with a *laptime* of 115 days, this young pre-main sequence solar-type star has a shear of roughly 4 times greater than the Sun. This result is consistent with the relationship determined by Barnes et al. (2005a) for young stars in that differential rotation is dependent on spectral class (surface temperature), with M-dwarfs rotating almost as a solid body through to early-G dwarfs exhibiting a strong rotational shear. Marsden et al. (2006) and Jeffers and Donati (2008) have found that the early G-dwarf, HD 171488 (V889 Her) has a photospheric shear up to seven times the solar value. So why do these two stars that exhibit similar surface temperature properties have vastly different photospheric shears? One possible reason is that HD 106506 younger with a larger convective zone when compared with HD 171488. Being a younger star, it is probably still contracting down to the main sequence. But it is still unclear why HD 171488 should have such

a large $\delta\Omega$ and perhaps it is convective zone depth and the rate at which that zone is turned over that is more important than surface temperature (hence spectral type).

3.5.2 Magnetic Topology

The reconstructed magnetic fields are shown in Figure 3.11 and the fits to the Stokes V LSD profiles are given in Figure 3.12. Magnetic features in both the azimuthal and radial magnetic fields extend from low-latitude to high-latitude features. As discussed by Donati et al. (2003b), the radial component may be interpreted to be representative of the poloidal component while the azimuthal component may be considered as representative of the toroidal component of the large-scale dynamo field. The strong azimuthal ring of negative field around the star is similar to those observed on other stars such as HD 171488 (Jeffers and Donati, 2008). However, the azimuthal ring on HD 106506 is of different polarity to those observed on other stars, such as HD 141943 (SpType: G2[1]) (Marsden et al., 2011a). This is unlikely to be due to instrumental orientation as the data for HD 106506 were taken with the same instrumental setup and at the same time as HD 141943.

Clearly, the azimuthal ring of magnetic field (toroidal component) is visible at the photospheric level and not buried deep within the star, unlike the Sun. (Donati et al., 2003b) proposes that this could indicate that the dynamo operating in active solar-type stars and is capable of generating fields directly in the subsurface region (e.g Dikpati et al., 2002) and could be distributed throughout the whole convective zone (e.g. Lanza et al., 1998). This concept is consistent with the wreathes of azimuthal magnetic fields theorised by Brown et al. (2010), except at a much higher latitude. Their 3-dimensional magnetohydrodynamics (MHD) models found that stars with increased rotation rate (up to three times that of the Sun) could produce self-generating wreathes of azimuthal field without the need for an interface layer. One can speculate that the increased rotation rate of HD 106506 could be deflecting the wreathes of magnetic fields to much higher latitudes. Alternatively, Solanki (2002) argues that these azimuthal rings may represent large penumbral regions with a predominantly horizontal magnetic field although Donati et al. (2003b) argues against this these horizontal field structures being able to be produced deep within the star and rising, through buoyancy forces, to the photospheric surface and still maintain "their integrity".

[1] Torres et al. (2006)

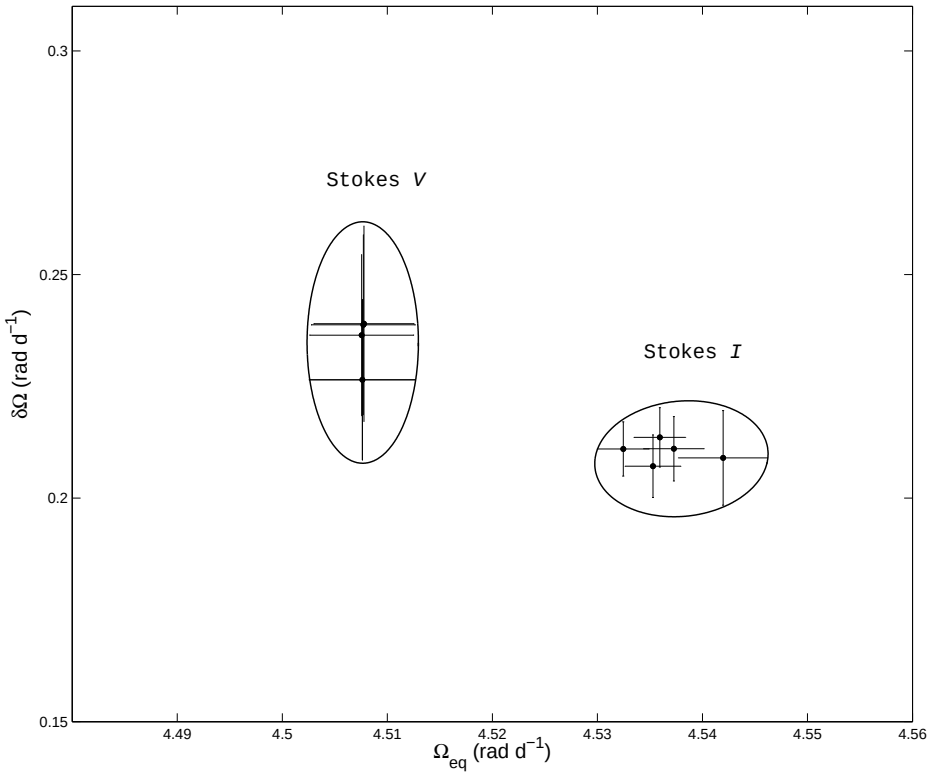

Figure 3.15: This shows a graph of the error ellipses for the differential rotation measurements for both the Stokes I (on the right) and the Stokes V (left). These error ellipses were generated by varying some of the stellar parameters, including the star's inclination ($\pm$ 10^o) and the Stokes I spot coverage or the Stokes V global magnetic field ($\pm$ 10%). The individual data points, as explained in Figures 3.5 and 3.10, are also shown.

Petit et al. (2008) found that with increasing rotation rate of a star, the toroidal component of the surface magnetic field dominates over the poloidal component of that field. They inferred that a rotation period $\lesssim$12 d is necessary for the toroidal component to dominate over the poloidal component. The magnetic field on HD 106506 is predominantly toroidal with approximately 70 $\pm$ 3% of the magnetic energy being toroidal magnetic energy. This is similar to other solar-type stars, with the toroidal field being the dominant field of HD 171488 (Marsden et al., 2006; Jeffers and Donati, 2008), AB Doradus and LQ Hydrae (Donati et al., 2003b). Like HD 171488, this field is quite complex and much more so than that operating the Sun. Considering only the toroidal component, an octupole field ($\ell = 3$ mode) dominates with approximately 37 $\pm$ 9% of the magnetic energy whereas the simple dipole field ($\ell = 1$) contains only 18 $\pm$ 5% and a quadrupole field ($\ell = 2$ mode) containing approximately 16 $\pm$ 7% of the magnetic energy. This is in contrast to the poloidal field were the respective components are roughly equal between a dipole (10 $\pm$ 2%), quadruple (11 $\pm$ 2%) and octupole field (10 $\pm$ 1%). This would indicate that a complex dynamo is operating on HD 106506 and is similar to that on other young, solar-type stars. In addition, the reconstructed toroidal field was predominantly axisymmetric ($m < \ell/2$) with respect to the rotation axis (95 $\pm$ 2%) whereas the reconstructed poloidal field tended to be more non-axisymmetric (with $m > \ell/2$) with 65 $\pm$ 7% of the poloidal field energy held in that mode. This is consistent with the observations of Donati and Landstreet (2009) and Marsden et al. (2011a) where stars with significant toroidal fields often have non-axisymmetic poloidal fields. The error estimates on these measures were obtained by varying a range of stellar parameters such as inclination, radial velocity, Ω_{eq}, $\delta\Omega$, period and $v \sin i$. Hence these may be referred to as a *variation* bar, which is analogous to an error bar except that the measurement indicates the variation found by this method. Tables 3.7 gives a full listing of the various components for this star.

When measuring the differential rotation using the magnetic features, the equatorial rotation rate Ω_{eq} was 4.51 $\pm$ 0.01 rad d^{-1}, with a photospheric shear $\delta\Omega$ of 0.24 $\pm$ 0.03 rad d^{-1}. The comparison with those parameters found using the Stokes I information is shown in Figure 3.15. The difference in the $\delta\Omega$ values are within the error bars of the two measurements. When compared with the differences observed on other stars of similar spectral type such as HD 141943 (Marsden et al., 2011b), these features may be anchored at similar depths in the convective zone, unlike HD 141943 which may be

Table 3.7: Magnetic quantities derived from the set of magnetic maps for HD 106506. Both the poloidal and toroidal components are listed along with the relative weightings in each geometry.

B_{mean} (G)	geometry	Energy[1] (% tot)	dipole[2] (%)	quad.[2] (%)	oct.[2] (%)	higher[2,3] order (%)	axi.[2] (%)	axi.[1] (%)
69	poloidal	30±3	10±2	11±1.5	10±1	68±3	28±2	8±1
	toroidal	70±3	18±5	16±7	37±9	29±7	94±2	65±4

[1] this is a % of the total magnetic energy available. [2] this is a % of the respective poloidal or toroidal field geometry. Listed also is the fraction of the poloidal or toroidal magnetic energy in the dipolar ($\ell = 1$), quadrupolar ($\ell = 2$), octupolar ($\ell = 3$) and [3] higher order ($\ell \geq 4$) components as well as the fraction of energy of each component stored in the axisymmetric component ($m < \ell/2$) and the fraction of the total energy stored in each component ($m = 0$).

anchored at different depths of the convective zone. However, the error ellipses of the measured equatorial rotational rates, Ω_{eq}, do not overlap. Hence this conclusion must be treated with caution until further data is obtained for this star.

3.6 Conclusions

In this chapter, reconstructed brightness and magnetic images of the young solar-type star HD 106506 have been presented. The brightness image shows low- to mid-latitude features coupled with a predominant polar spot. This is very similar to many of rapidly rotating solar-type stars. The magnetic images reveal regions of azimuthal field near the stellar surface that suggest that the dynamo mechanism may be occurring entirely in the convective zone and close to the surface of the star itself. The photospheric shear for HD 106506 supports the findings of Barnes et al. (2005a), that effective temperature is the dominant factor in the level of surface differential rotation. The reason why such a relation exists remains unclear.

Chapter 4

The G-type star: HD 76298

4.1 Introduction

HD 76298 (HIP 43720) is a rapidly rotating, intermediate mass, solar-type star in the constellation of Pyxis. It has a Right Ascension $08^h54^m14.05803^s$ and Declination $^-31^o53'06.4958''$ (J2000.0 van Leeuwen, 2007). Koen and Eyer (2002) identified HD 76298 as being an unresolved variable star based on *HIPPARCOS* data. Torres et al. (2006) observed the star's spectral type as G1V. HD 76298 was detected at X-ray wavelengths by the ROSAT survey with a count rate of 0.176 ± 0.021 counts second^{-1} (Voges et al., 1986). HD 76298 was observed by the Two Micron All Sky Survey (2MASS) showing significant infrared excess: J_{mag} = 7.804 ± 0.027, H_{mag} = 7.472 ± 0.057 and K_{mag} = 7.350 ± 0.024 (Skrutskie et al., 2006). There is evidence of an active chromosphere with an emission equivalent width for the Hα line of ∼400 ± 28 mÅ and strong emission in the magnesium triplet lines (Waite et al., 2011a). Waite et al. (2011a) detected magnetic fields on this star, although no mapping was done due to the survey nature of that project. The aim, as was for HD 106506, is to map the magnetic field topologies of HD 76298 and to measure the differential rotation using brightness and magnetic tracers.

4.2 Fundamental parameters of HD 76298

HD 76298 is a particularly active, G1V star (Torres et al., 2006). It has a trigonometric parallax of 5.38 ± 0.94 mas (van Leeuwen, 2007) giving a distance of 186^{+39}_{-28} pc or 606^{+128}_{-90} ly. Using the star's V-I value and the formulation in Bessell et al. (1998), the

star's temperature was estimated to be 5700 ± 40 K. However, this is slightly lower than that determined by this investigation. Using DI, it was estimated that the star's temperature is 6000 ± 30 K (see Section 4.4.1). Using this value, and placing HD 76298 onto the theoretical isochrones of Siess et al. (2000), as shown in Figure 4.1, this star has a stellar radius of $2.2^{+0.6}_{-0.4} R_{\odot}$ and has a mass of $1.6^{+2}_{-2} M_{\odot}$ making it slightly larger than HD 106506.

Figure 4.1 also indicates that this star's age is $\sim 10^{+4}_{-3}$ Myr years[1]. However, this age estimate is not supported by the depth of the Li I line, with an equivalent width of <5 mÅ. Generally, the Li I 670.8 nm line has been used to place constraints on the age of a star. For example, Montes et al. (2001) produced a relationship between the equivalent width of that line versus spectral type for members of well-known young open clusters of different ages. da Silva et al. (2009) found that Lithium depletion is a function of age for young stars with temperatures between 3500 K to 5000 K. They did note that Lithium depletion is inhibited in stars with rotational velocities in excess of 20 $\mathrm{km\,s^{-1}}$. There are red giant branch (RGB) asymptotic giant branch (AGB) stars that are so-called "Lithium-rich" stars (Abia et al., 1999; Charbonnel and Balachandran, 2000). This would indicate that using the Li I 670.8 nm spectral line alone as an age indicator needs to be treated with caution. There are a number of plausible reasons for the lack of the Li I 670.8 nm spectral line. Using the assumption of its PMS status, one can theorise that the lithium has already been depleted. Guillout et al. (2009) suggest that stars with deep convective envelopes, such as M-dwarfs, are very efficient at depleting their Lithium concentration. Although HD 76298 is larger than a typical M-dwarf, it still might have a deep convective zone as it is still contracting down onto the main sequence. However, this is unlikely; the star is clearly following a Henyey radiative track (Henyey et al., 1955) where PMS stars can remain in radiative equilibrium throughout some period of its contraction to the main sequence. It is entirely probable that this star had depleted its Lithium during its earlier Hayashi track phase (Hayashi, 1961). Bouvier (2008) suggest that this depletion may be due to a large velocity shear at the base of the convective zone as a result of star-disk interaction. Alternatively, this star may be a post-main sequence (post-MS) star as the PMS and post-MS tracks overlap. An alternative, and intriguing hypothesis, is that this star could be an FK Comae-type

[1] This is slightly older than the estimate by Waite et al. (2011a) (see Appendix C) as they used an effective temperature of 5700 K

star. FK Comae-type stars are most likely coalesced W Ursae Majoris-type (W UMa) binaries, rather than single stars (Bopp and Stencel, 1981). This class of stars are rapidly rotating with photometric modulation with strong and variable chromospheric emission in the Ca II H & K lines. The evolutionary status of HD 75298 remains unclear.

4.3 Observations and Analysis

4.3.1 High Resolution Spectropolarimetric Observations from the AAT

Spectropolarimetry of HD 76298 was obtained using the 3.9 m AAT over a 10 night period from March 25 to April 05, 2010 and again from January 15 to 17, 2011. The experimental setup of this SEMPOL/AAT combination was identical (as close as possible) to that described in Section 3.3.2. This was necessary so that long-term analysis of data could be undertaken in the search for activity cycles that may be occurring on our group's primary targets (such as HR 1817, which is not part of this thesis). For this observation run, the central wavelength was 522.002 nm with full wavelength coverage from 437.71 nm to 681.56 nm. The dispersion of ∼0.004958 nm at order # 129 was achieved giving an approximate resolution across the detector of ∼71000. A journal of observations for the March/April 2010 and January 2011 runs are shown in Tables 4.1 and 4.2 respectively.

4.3.2 Spectropolarimetric Analysis

The initial data reduction was completed using ESpRIT. The preliminary processing was the same as that explained in Section 3.3.3. The mean pixel resolution for the AAT spectra was determined to be 1.689 $\mathrm{km\,s^{-1}\ pixel^{-1}}$ and was the same as for other AAT observing runs, as explained in Section 3.3.2. After using ESpRIT, LSD was applied to the reduced spectra. A G2 line mask created from the Kurucz atomic database and ATLAS9 atmospheric models (Kurucz, 1993) was used during the LSD process.

Table 4.1: The Journal of spectropolarimetric observations of HD 76298 using the 3.9 m AAT in 2010.

UT Date	UT middle	Exp. Time[1] (sec)	Stokes V Mean S/N[2]	FAP[3]	Detection?
2010 March 25	10:46:51	4×800	6200	7.772×10^{-16}	definite
2010 March 26	09:47:20	4×800	4868	1.300×10^{-10}	definite
2010 March 26	13:05:25	4×800	5327	3.226×10^{-2}	no detection
2010 March 27	09:14:08	4×800	609	6.093×10^{-2}	no detection
2010 March 27	10:13:31	4×800	536	8.771×10^{-1}	no detection
2010 March 27	11:43:33	4×800	5168	3.382×10^{-5}	definite
2010 March 27	13:50:49	4×800	4197	1.520×10^{-2}	no detection
2010 March 28	09:03:34	4×800	3693	1.098×10^{-1}	no detection
2010 March 28	10:02:56	4×800	2296	8.395×10^{-2}	no detection
2010 March 28	11:02:19	4×800	2686	2.065×10^{-1}	no detection
2010 March 28	12:01:44	4×800	3077	7.875×10^{-3}	marginal
2010 March 28	12:46:19	2×800	2777	1.614×10^{-2}	no detection
2010 March 28	13:31:00	4×800	4029	1.504×10^{-5}	definite
2010 March 29	09:16:51	2×800	4052	3.352×10^{-4}	marginal
2010 March 29	11:11:11	4×800	1027	0.000	definite
2010 March 31	11:05:59	4×800	3608	9.397×10^{-2}	no detection
2010 March 31	12:05:24	4×800	4050	8.884×10^{-2}	no detection
2010 April 1	09:26:52	4×800	5374	2.220×10^{-16}	definite
2010 April 2	09:07:59	4×800	5023	1.397×10^{-6}	definite
2010 April 2	10:58:10	4×800	1046	3.666×10^{-5}	definite
2010 April 2	13:50:46	2×800	4061	6.250×10^{-1}	no detection
2010 April 3	09:19:50	4×800	4255	6.361×10^{-1}	no detection
2010 April 3	12:11:42	4×800	3783	6.727×10^{-1}	no detection
2010 April 4	09:35:24	4×800	566	7.333×10^{-1}	no detection
2010 April 4	12:15:48	4×800	1204	8.394×10^{-1}	no detection
2010 April 4	13:15:13	4×800	3257	1.311×10^{-6}	definite
2010 April 5	09:00:21	4×800	5285	0.000	definite

[1] Each sequence of 4×800=3200 seconds exposures. After each exposure, the "rotating half-wave retarder" of the polarimeter is rotated between $+45^o$ and -45^o so as to remove instrumental polarization signals from the telescope and the polarimeter.

[2] Signal-to-noise (S/N) of the resulting Stokes V profile.

[3] FAP: False Alarm Probability. See Section 3.3.2 for more details.

Table 4.2: The Journal of spectropolarimetric observations of HD 76298 using the 3.9 m AAT in 2011.

UT Date	UT middle	Exp. Time[1] (sec)	Stokes V Mean S/N[2]	FAP[3]	Detection?
2011 January 15	13:14:36	4×800	2326	9.455×10^{-2}	no detection
2011 January 15	17:01:55	2×800	309[4]	2.274×10^{-1}	no detection
2011 January 16	11:34:07	4×800	3403	1.258×10^{-1}	no detection
2011 January 16	14:48:45	4×800	5548	9.426×10^{-6}	definite
2011 January 16	17:57:28	4×800	4127	4.462×10^{-4}	marginal
2011 January 17	14:31:30	4×800	2752	2.231×10^{-4}	marginal
2011 January 17	17:39:41	4×800	2936	2.722×10^{-2}	no detection

[1] Each sequence of 4×800=3200 seconds exposures. After each exposure, the "rotating half-wave retarder" of the polarimeter is rotated between $+45^o$ and -45^o so as to remove instrumental polarization signals from the telescope and the polarimeter.

[2] Signal-to-noise (S/N) of the resulting Stokes V profile.

[3] FAP: False Alarm Probability. See Section 3.3.2 for more details.

[4] Profile not used as there was a marginal magnetic detection in the Null profile.

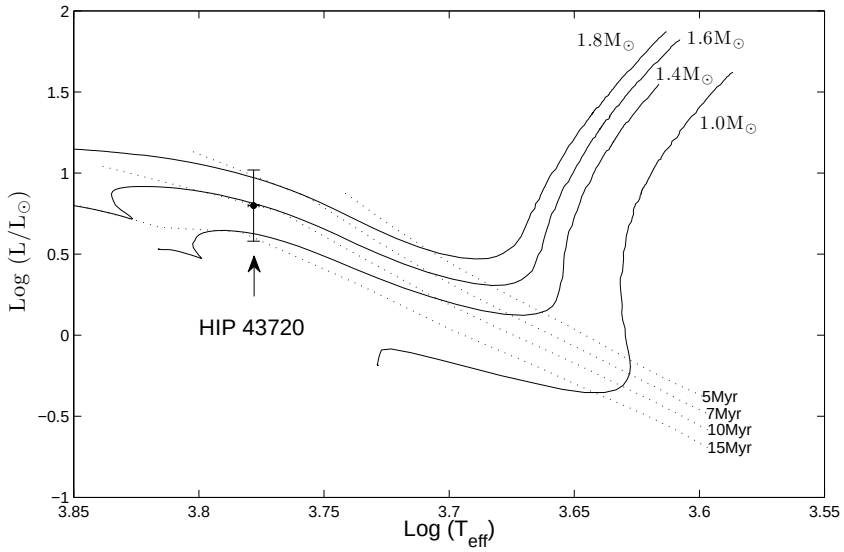

Figure 4.1: The possible evolutionary status of HD 76298, as placed on the theoretical isochrones of Siess et al. (2000). This assumes a pre-main sequence age for this star.

4.4 Photospheric and Chromospheric Features

4.4.1 Image reconstruction: Stokes *I* Doppler imaging and surface differential rotation

ZDICAM was used to establish the values of a number of basic parameters, including the star's equatorial period, axial inclination angle, projected rotational velocity, $v \sin i$, radial velocity, $\mathrm{v_{rad}}$, photosphere and spot temperature, T_{phot} and T_{spot}. This was achieved by systematically varying each parameter in order to minimise the χ^2 value (e.g. Marsden et al., 2005; Jeffers and Donati, 2008; Waite et al., 2011b). These key stellar parameters were determined sequentially, first $\mathrm{v_{rad}}$, then $v \sin i$ and inclination angle. The minimisation of χ^2 against the radial velocity and the inclination angle is shown in Figure 4.2.

The radial velocity, found using χ^2 minimisation mapping techniques, appeared to vary from the 2010 to 2011 data sets. The 2010 dataset was optimised to a radial velocity of 2.4 ± 0.1 km s^{-1} whereas the 2011 dataset was found to have a radial velocity of 2.2 ± 0.1 km s^{-1}. Torres et al. (2006) reported a heliocentric radial velocity of 0.5

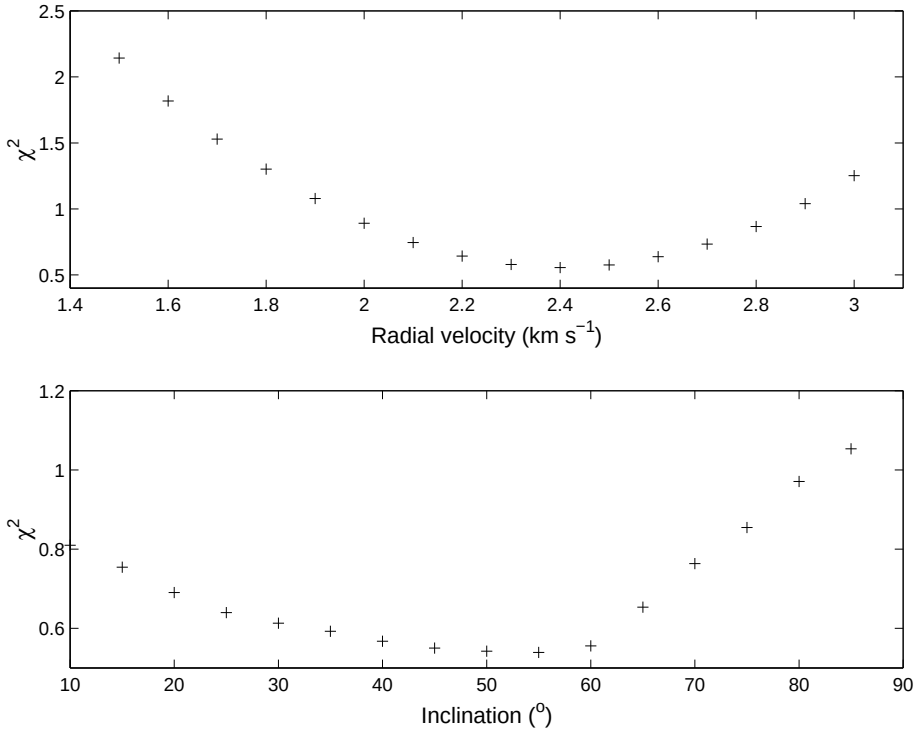

Figure 4.2: The determination of the radial velocity and the inclination angle of HD 76298 using the data from the 2010 observation run. The top panel shows the variation in the χ^2 when the radial velocity was varied while the lower panel shows the variation in the χ^2 with respect to varying the inclination angle.

km s^{-1} while Waite et al. (2011a) reported a value of 2.2 ± 1 km s^{-1}. This variation, if real, may be explained by the presence of a companion star such as an M-dwarf. When applying an early M-dwarf line mask, that was created from the Kurucz atomic database and ATLAS9 atmospheric models (Kurucz, 1993), to the Doppler-corrected spectra during the LSD process, there was no evidence of any variations in the size, shape or position of any distortions that may be attributed to a fainter companion star. Further data on this star would need to be taken in order to verify the presence, or absence, of a companion star.

The initial equatorial period was estimated using the maximum-entropy Doppler imaging code, with the assumption of solid body rotation, with the rotational period being systematically changed and determining the minimum χ^2 value for each period. Figure 4.3 shows the results of this process with the minimum χ^2 occurring with an equatorial

rotation period of approximately 3.2 days. This result is consistent with that found by Kiraga (2012) who measured a period of 3.189 d.

The photospheric and spot temperatures of the star were determined by developing a grid of T_{phot} and T_{spot} and determining the best-fit model by minimising χ^2. For each new temperature pair, the multiplication factors were re-determined. The photospheric temperature, T_{phot}, was determined to be 6000 K with the spot temperature, T_{spot}, determined as 4100 K. The photospheric-spot temperature difference of 1900K for this early G-dwarf is consistent with measurements of other solar-type stars made by authors such as Marsden et al. (2005, 2011a) and supports the relationship found by Berdyugina (2005) (see Figure 7, page 27 of that work). Finally, the differential rotation of HD 76298 was determined. As done previously in this thesis, the χ^2 minimisation technique was used, as explained in Section 2.6. The minimum value for $\Omega_{\rm eq}$ was determined to be $\Omega_{eq} = 2.01^{+0.10}_{-0.03}$ rad d^{-1}and $\delta\Omega = 0.09^{+0.03}_{-0.04}$ rad d^{-1}. The errors for the value of the differential rotation were established by varying both the spot size ($\pm$ 10%), the inclination angle ($\pm$ 10%) and $v\sin i$ ($\pm$ 0.5 km s^{-1}) and determining $\Omega_{\rm eq}$ and $\delta\Omega$ respectively. When varying the inclination angle and $v\sin i$, the associated multiplication factors were redetermined and the resulting spot filling factor was found to match the new angle and $v\sin i$ by minimising the χ^2 value. The reduced χ^2 values for the various $\Omega_{\rm eq}$ and $\delta\Omega$ values, along with the associated error ellipse, are shown in Figure 4.4 while Section C.3 in Appendix C lists the full set of results used in the determination of this error. This error ellipse was generated so as to encompass all the various $\Omega_{\rm eq}$ and $\delta\Omega$ pairs as a result of varying the different parameters (see Section 3.4.1). With limited phase coverage during the 2011 run, no differential rotation measurement was found on that data set. The full set of parameters that gave the minimum χ^2 value are shown in Table 4.3. Incorporating differential rotation into the maximum-entropy image reconstruction, the resulting map is shown in Figure 4.5 (left panel), along with the model fits to the LSD profiles in Figure 4.6. Using the differential rotation parameters found for the 2010 data, the resulting Stokes I map for the 2011 data is shown in Figure 4.5 (right panel) while the associated fits between the data and the modelled profiles are shown in Figure 4.7.

The residuals for the 2010 data are plotted as a dynamic spectrum and is shown in Figure 4.8. This shows that the mapping process was able to extract most, but not all, of the brightness features evident on the surface of this star. Donati et al. (2003b)

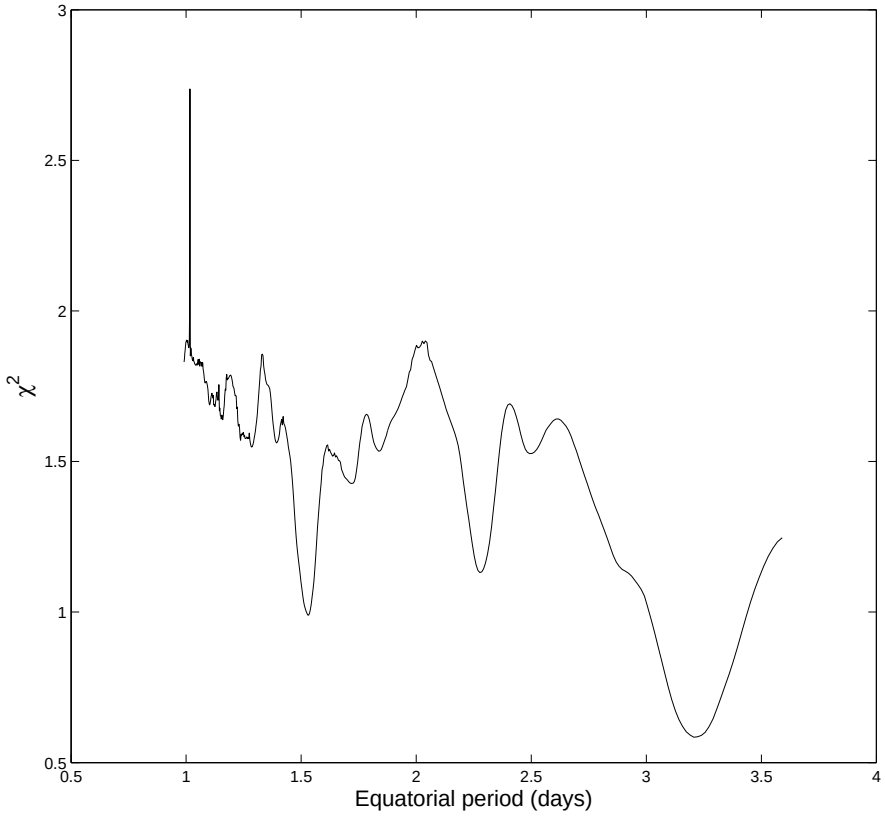

Figure 4.3: The initial equatorial period was determined with the assumption of solid body rotation. The minimum χ^2 value was determined to be approximately 3.2 day rotation period.

Table 4.3: The parameters used to produce the maximum-entropy image reconstruction of HD 76298, including those associated with surface differential rotation.

Parameter	Value
Spectral Type[1]	G1V
Photometric Period[2]	3.189 days
Equatorial Period[3]	3.14 ± 0.1 days
Inclination Angle	55 $\pm 5^o$
Projected Rotational Velocity, $v \sin i$	39.5 ± 0.5 $\mathrm{km\,s^{-1}}$
Photospheric Temperature, T_{phot}	6000 ± 30 K
Spot Temperature, T_{spot}	4100 ± 30 K
Radial Velocity, v_{rad}[4]	2.4 ± 0.1 km s^{-1}(2010)
	2.2 ± 0.1 km s^{-1}(2011)
Stellar radius[5]	$2.2^{+0.6}_{-0.4} R_\odot$
Convection Zone depth[6]	0.206 $\pm$0.019 $R_\star$
	$0.445^{+0.049}_{-0.042}$ $R_\odot$
Age	Uncertain[7]
Mass	$\sim$1.6 $M_\odot$
Stokes I: Ω_{eq}	$2.01^{+0.10}_{-0.03}$ rad d^{-1}
Stokes I: $\delta\Omega$	$0.09^{+0.03}_{-0.04}$ rad d^{-1}
Stokes V: Ω_{eq}	$2.15^{+0.10}_{-0.11}$ rad d^{-1}
Stokes V: $\delta\Omega$	$0.34^{+0.01}_{-0.16}$ rad d^{-1}
Epoch used (HJD)	2455286.52407306 (2010)
	2455578.153426805 (2011)

[1] Torres et al. (2006)

[2] Kiraga (2012)

[3] Using Stokes I data.

[4] Both radial velocity estimates are reported here. These are discussed in Section 4.4.1

[5] based on the formulation contained in Bessell et al. (1998)

[6] based on the formulation contained in Noyes et al. (1984); see Section 5.4.5 in Chapter 5 for more details

[7] See Section 4.5.2 for a discussion on the age of this star.

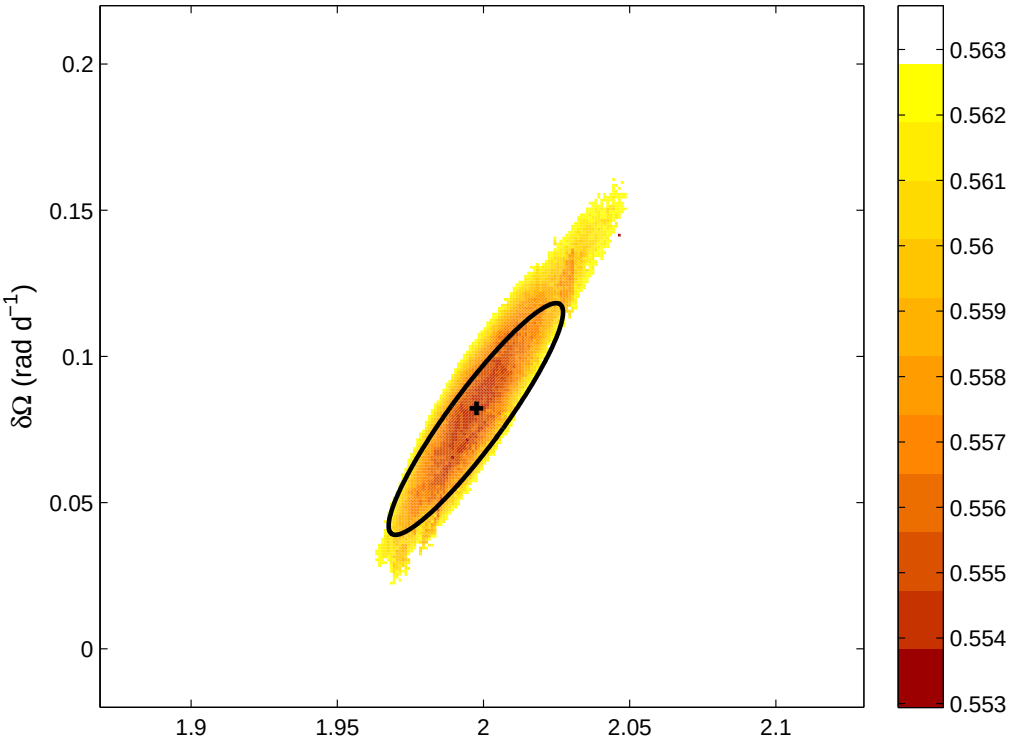

Figure 4.4: Surface differential rotation χ^2 minimisation for HD 76298 using data obtained in 2010. The image shows the reduced χ^2 values from the maximum-entropy Doppler imaging code for a fixed spot coverage of 0.067 and an inclination angle of 55^o. The darker regions correspond to lower χ^2 values. The image scale projects $\pm$ 10σ on to the axes in both $\Omega_{\rm eq}$ and $\delta\Omega$. The ellipse superimposed demonstrates the error for the value of the differential rotation and was determined by varying both the star's inclination, $v\sin i$ and spot filling factors by $\pm$ 10% and determining $\Omega_{\rm eq}$ and $\delta\Omega$.

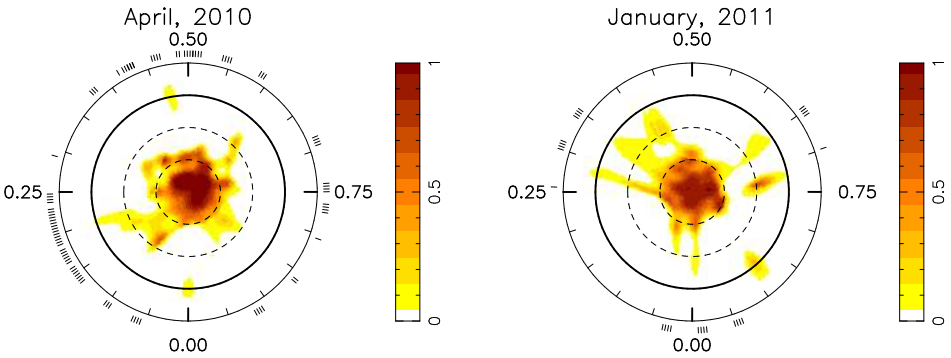

Figure 4.5: The maximum-entropy brightness and magnetic image reconstructions for HD 76298 using 2010 (left panel) and 2011 (right panel). These maps are polar projections extending down to -30^o. The bold lines denote the equator and the dashed lines are +30^o and +60^o latitude parallels. The radial ticks indicate the phases at which this star was observed. Differential rotation, as measured using the Stokes I profiles for the 2010 data, has been incorporated into the analysis of both maps. The April 2010 data has a spot coverage of 6.6% while the January 2011 data has a spot coverage of 6.2%.

noted that some absorption features in the LSD profiles are not well modelled using our DI techniques. Therefore, one may conclude that the remaining features observed in the dynamic spectrum (in Figure 4.8) could be the result of plages (bright spots) in the chromosphere or faculae (bright spots) in the photosphere. A dynamic spectrum was not produced for 2011 due to the limited amount of data.

The fractional spottedness of the star with respect to latitude is shown in Figure 4.9. The solid line shows the fraction of spots at each latitude using the parameters from Table 4.3. The dotted lines in Figure 4.9 shows the error limits. The error estimates at each latitude were based on varying each of the parameters with the stated errors (as stated in Table 4.3). The specific parameters that were varied are: $v\sin i$, inclination angle, photospheric temperature, spot-to-photosphere temperature and the differential rotation parameters Ω_{eq} and $\delta\Omega$.

4.4.2 Zeeman Doppler imaging: magnetic features on the surface of HD 76298

As with HD 106506, *ZDICAM* was used to construct the magnetic field topology on HD 76298. The spherical harmonic expansion $l_{max} = 30$ was selected as this was the

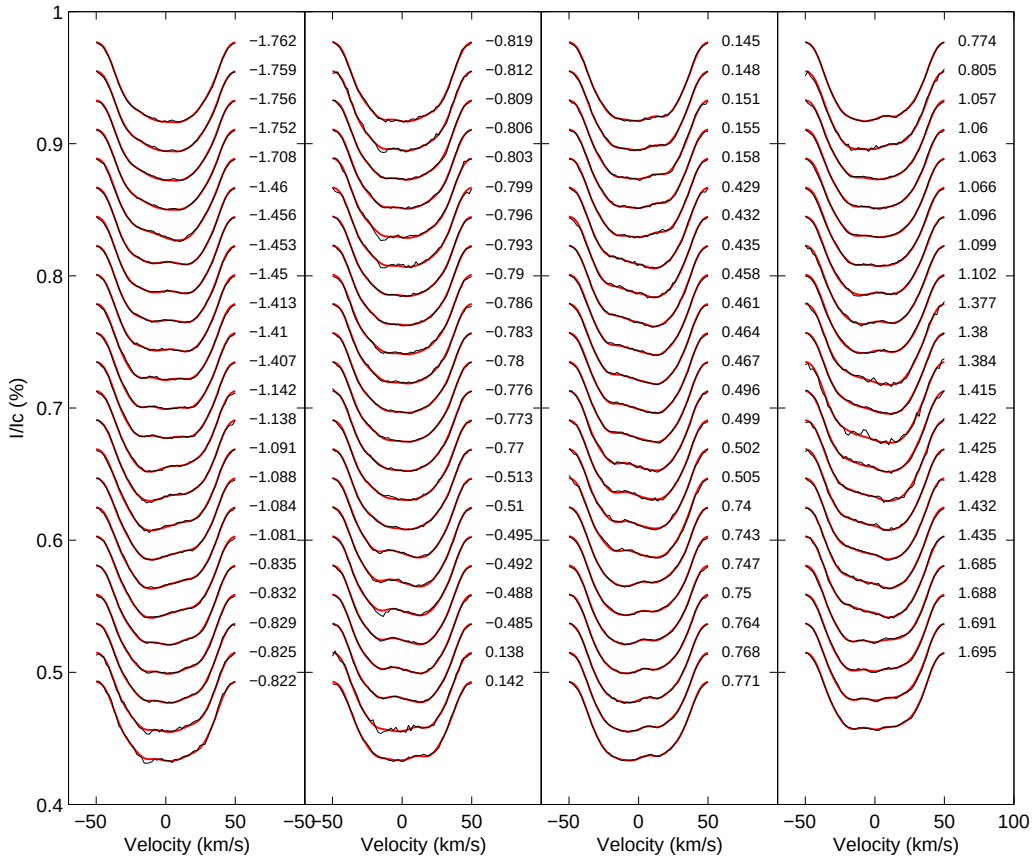

Figure 4.6: The maximum-entropy fits to the LSD profiles for HD 76298 with surface differential rotation incorporated into the analysis of the 2010 dataset. The red lines represent the modelled lines produced by the Doppler imaging process whereas the black lines represent the actual observed LSD profiles. Each successive profile has been shifted down by 0.022 for graphical purposes. The rotational phases at which the observations took place are indicated to the right of each profile. The mis-fitting of the data observed from phase $\sim$ -0.825 to phase $\sim$ -0.799 and again at phase $\sim$ -0.495 could be the result of plages (bright spots) in the chromosphere or faculae (bright spots) in the photosphere.

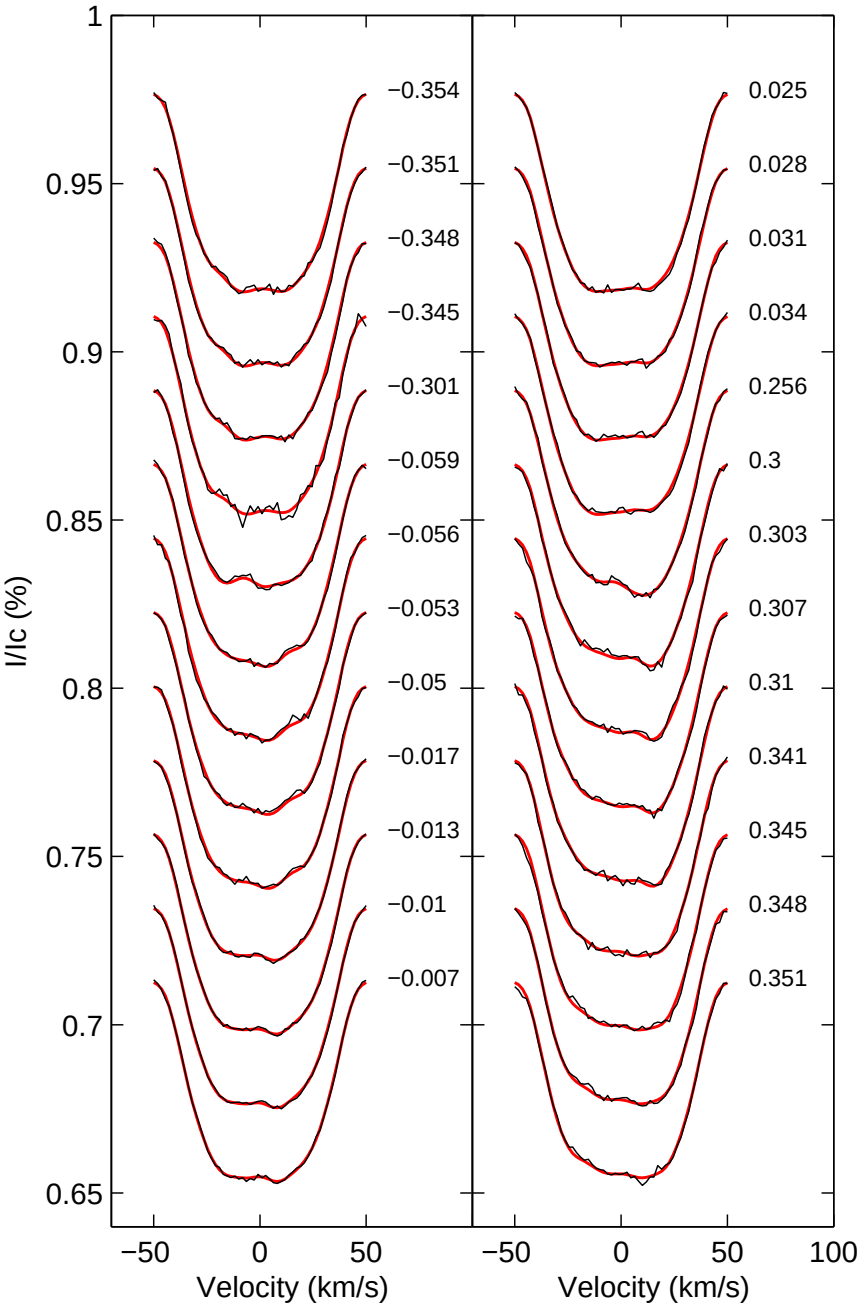

Figure 4.7: The maximum-entropy fits to the LSD profiles for HD 76298 with the 2010 surface differential rotation incorporated into the analysis for the 2011 dataset. The red lines represent the modelled lines produced by the Doppler imaging process whereas the black lines represent the actual observed LSD profiles. Each successive profile has been shifted down by 0.022 for graphical purposes. The rotational phases at which the observations took place are indicated to the right of each profile.

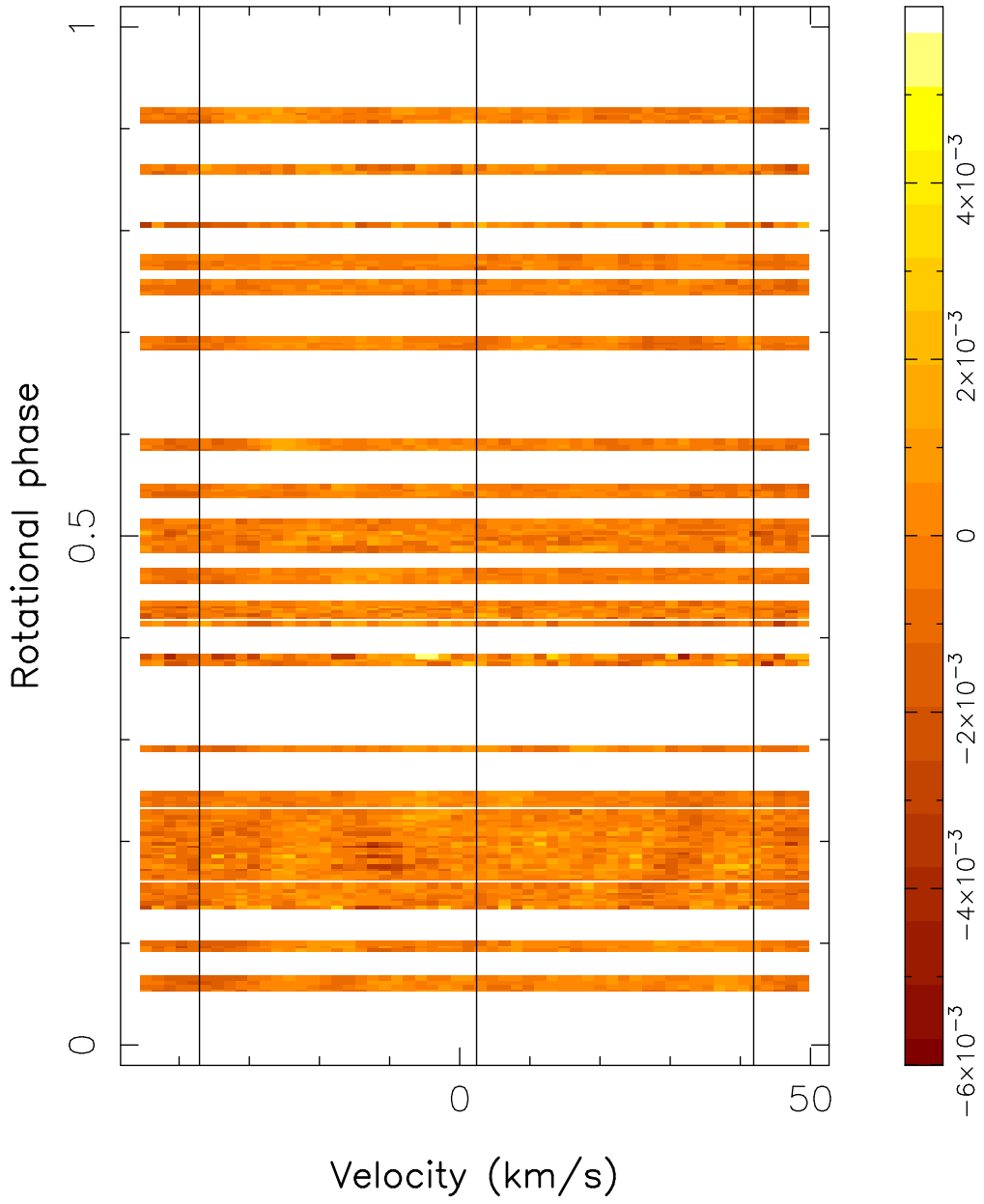

Figure 4.8: The residual fits for the Stoke I brightness maps plotted as a dynamic spectrum for the 2010 observation run.

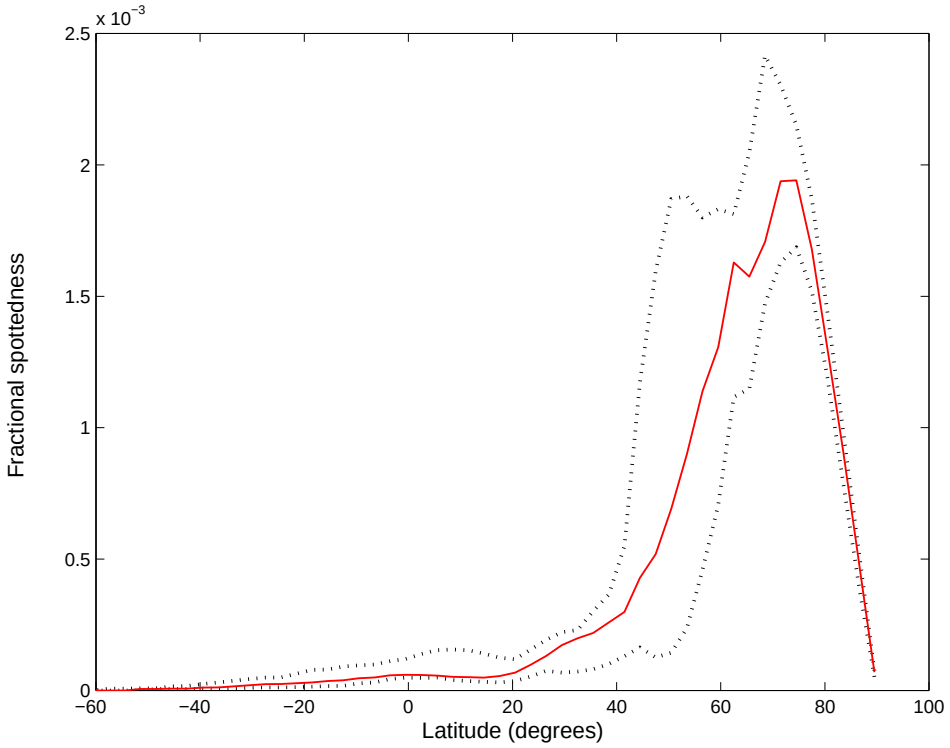

Figure 4.9: The fractional spottedness of HD 76298 at various latitudes. The solid line is that fraction using the parameters from Table 4.3 while the dotted lines show the respective error limits at each latitude.

minimum value where any further increase resulted in no further changes in the magnetic topologies. This implies that the star was resolved into 30 equatorial elements in order to reproduce the observations and give adequate surface sampling. This corresponds to mapping a total of 464 modes at the surface of the star, implying that a total of 1856 image parameters were used in the case of a potential field, and 2784 in the case of a potential- plus toroidal field configuration.

Initially, a poloidal plus toroidal field was assumed, and the images were created by fitting the data to within the noise level and resulted in a mean field strength of 41 G for the 2010 data. A similar approach to measuring the differential rotation parameters was used as that for the Stokes I (brightness) features. When considering these magnetic features, the equatorial rotation rate ($\Omega_{\rm eq}$) was $2.15^{+0.10}_{-0.11}$ rad d^{-1}, with a photospheric shear ($\delta\Omega$) of $0.34^{+0.01}_{-0.16}$ rad d^{-1}. This translates to an equatorial rotation period of 2.92 days with a *laptime* of $\sim 18.5^{+16.4}_{-0.5}$ days. The χ^2 minimisation landscape for the optimum parameter set is shown in Figure 4.10. The error ellipse is substantially larger than that found using Stokes I information and the error ellipse is "off-set" due to the larger errors obtained when varying the parameters. This large error is the result of varying both the inclination angle and $v\sin i$. Marsden et al. (2006) suggested that this is the most difficult parameter to define using Doppler imaging techniques. Also increasing the global magnetic field strength by 10% produced smaller differential rotation parameters thereby increasing the error in the $\Omega_{\rm eq}$ and $\delta\Omega$ values. Section C.3 in Appendix C lists the actual values found for each specific differential rotation measurement.

The reconstructed magnetic fields for the 2010 and 2011 data are shown in Figure 4.11. The fits to the Stokes V LSD profiles are given in Figure 4.12. The 2011 data set revealed that the azimuthal magnetic field continues to be in the same direction as the 2010 data set. The associated fits for this 2011 dataset are shown in Figure 4.13.

4.4.3 Chromospheric Features: Circumstellar material

The core of the Hα spectral line is formed in the middle of the chromosphere (Montes et al., 2004) and is often associated with plages and prominences. A typical HD 76298 Hα spectra is shown in Figure 4.14 compared with a rotationally broadened solar spectrum. The difference spectra (lower profile in Figure 4.14) is a measure of the emission

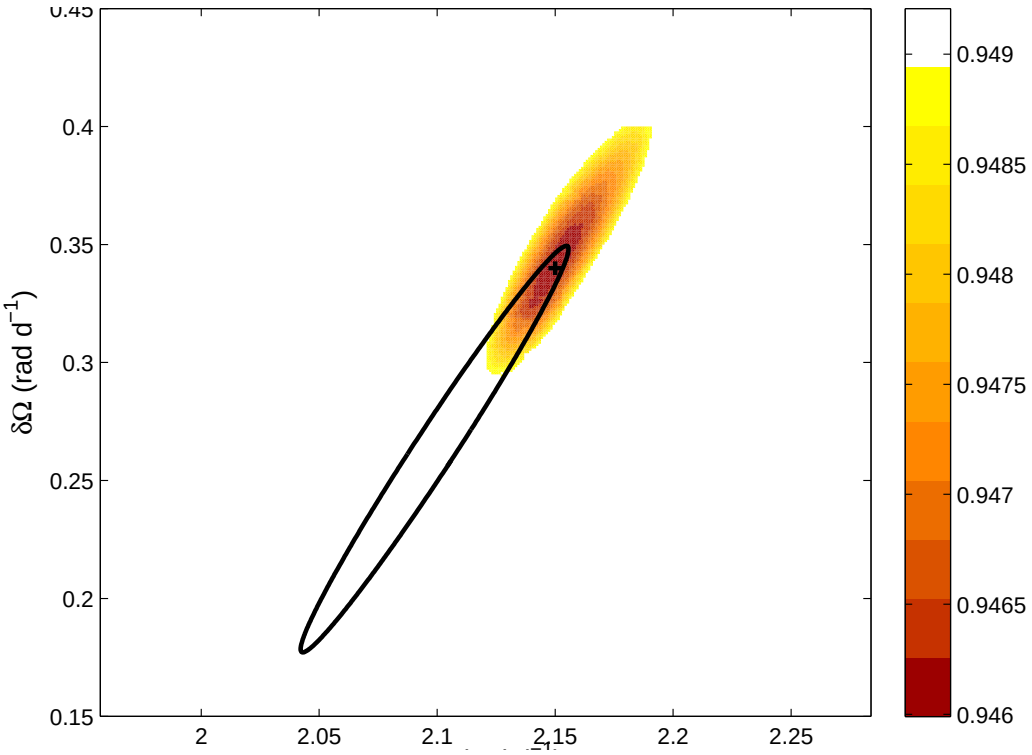

Figure 4.10: The surface differential rotation, using χ^2 minimisation, for HD 76298 using 2010 Stokes V data. The reduced χ^2 values from the maximum-entropy Zeeman Doppler imaging code for a fixed global magnetic field strength of 47 G and an inclination angle of 55^o. The darker regions correspond to lower χ^2 values. The image scale projects $\pm$ 3 σ on to the axes in both $\Omega_{\rm eq}$ and $\delta\Omega$. The ellipse superimposed demonstrates the error for the value of the differential rotation and was determined by varying both the $v\sin i$ and spot filling factors by $\pm$ 10% and determining $\Omega_{\rm eq}$ and $\delta\Omega$.

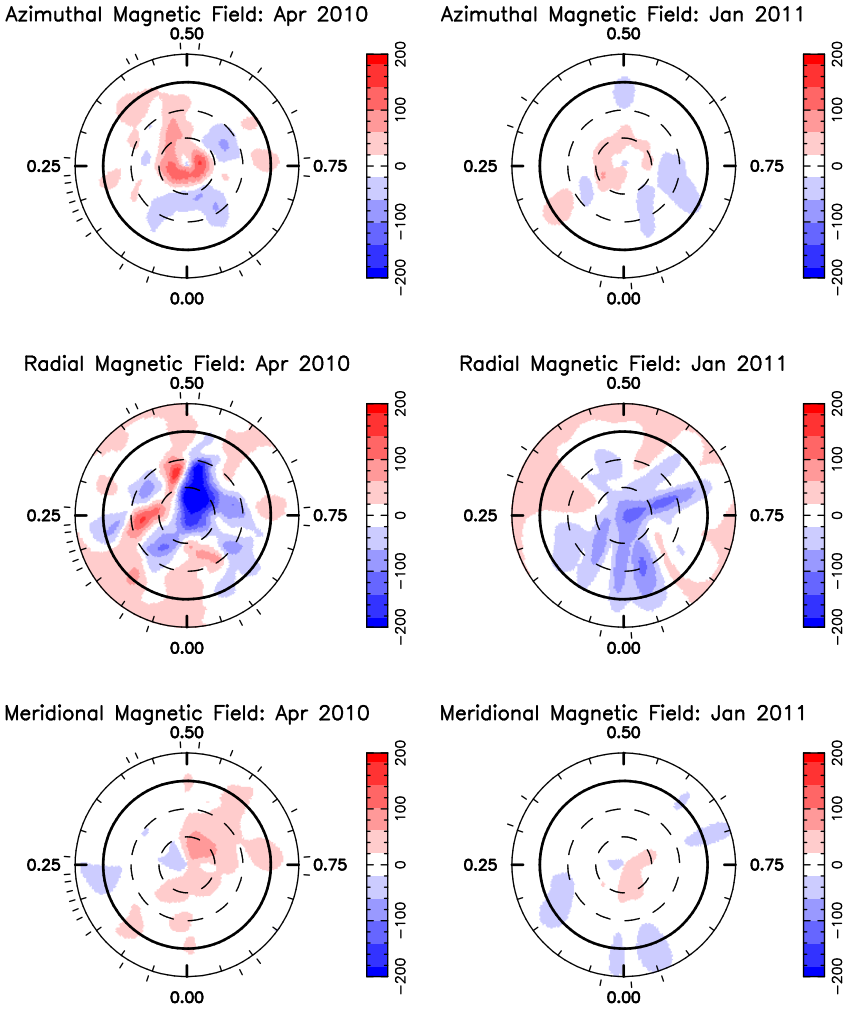

Figure 4.11: The maximum-entropy magnetic image reconstructions for HD 76298. Differential rotation, as measured using the Stokes V profiles for the 2010 data, has been incorporated into the analysis of the maps. The April 2010 data had a global magnetic field strength of 41G while the January 2011 data had a global magnetic field of 33G. These maps are polar projections extending down to -30^o. The bold lines denote the equator and the dashed lines are +30^o and +60^o latitude parallels. The radial ticks indicate the phases at which this star was observed.

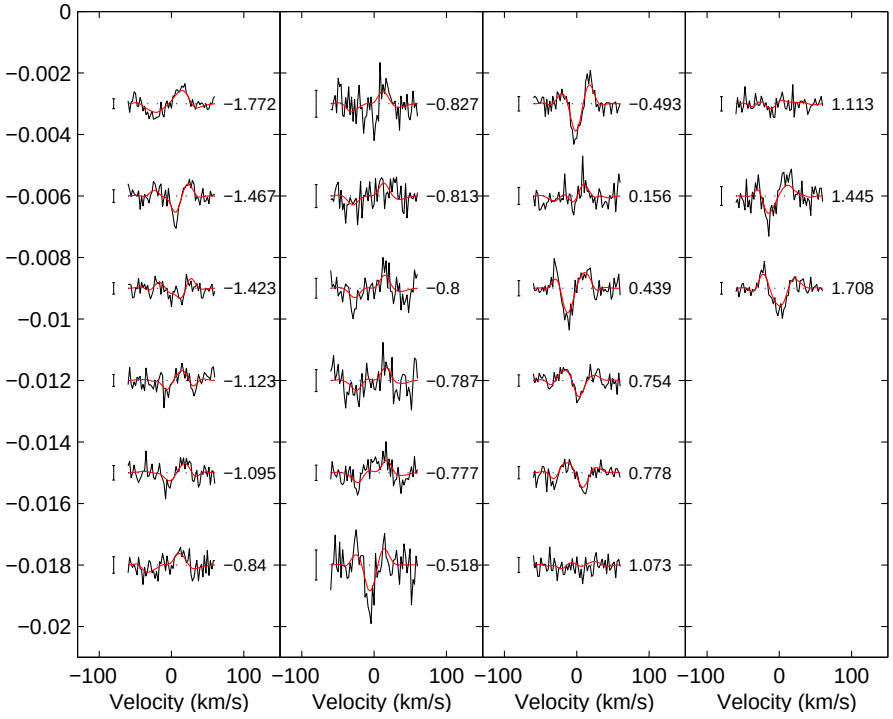

Figure 4.12: The maximum-entropy fits to the Stokes V LSD profiles for HD 76298 with surface differential rotation, as measured using the Stokes V profiles, incorporated into the analysis for the 2010 dataset. The red lines represent the modelled lines produced by the Zeeman Doppler imaging process whereas the thin lines represent the actual observed LSD profiles. Each successive profile has been shifted down by 0.003 for graphical purposes. The error bar on the left of each profile is plotted to $\pm$ 0.5σ. The rotational phases, in terms of the number of rotational cycles, at which the observations took place are indicated to the right of each profile.

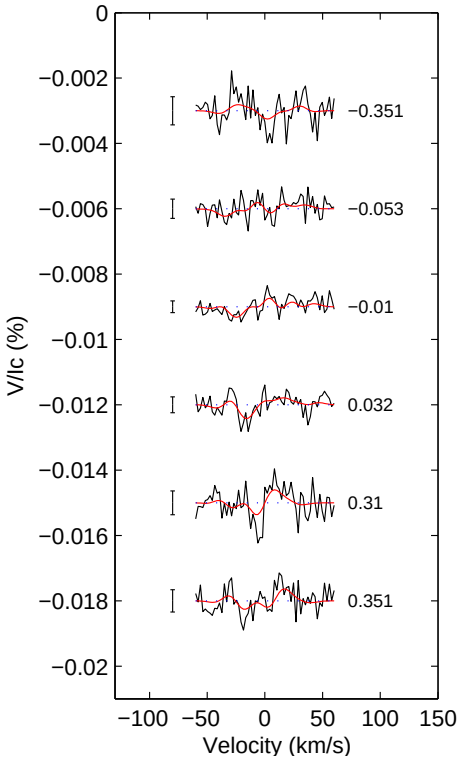

Figure 4.13: The maximum-entropy fits to the Stokes V LSD profiles for HD 76298 with surface differential rotation, as measured using the Stokes V profiles from the 2010 data, incorporated into the analysis for the 2011 dataset. The red lines represent the modelled lines produced by the Zeeman Doppler imaging process whereas the thin lines represent the actual observed LSD profiles. Each successive profile has been shifted down by 0.18 for graphical purposes. The error bar on the left of each profile is plotted to $\pm$ 0.5σ. The rotational phases, in terms of the number of rotational cycles, at which the observations took place are indicated to the right of each profile.

component of the Hα line. There is strong core emission, indicative of a dense, and active, chromosphere. The maximum chromospheric activity for HD 76298 was measured to be $\log R'_{H\alpha} = {}^{-}4.18 \pm 0.01$ in 2010 while $\log R'_{H\alpha} = {}^{-}4.26 \pm 0.015$ in 2011. This was measured using the same procedure as explained in Section 3.4.3. There is evidence of transit features within the Hα profile in the 2010 data. However, when attempting to produce a dynamic spectrum like that produced for HD 106506 in Chapter 3, these features were not recoverable above the noise level when considering the whole run. Nevertheless, the depth of the mean profile indicates that HD 76298 has a very dense chromosphere.

In addition to this activity, there appears to be "filling in" of the wings of the Hα line, where the line profile differs significantly from a rotationally broadened profile, not seen in other active stars in this project. However, this is not seen at all phases. One interpretation that this could be due to incorrect continuum normalisation. After careful consideration of other spectral lines in that section of the spectra, this explanation is unlikely. Another interpretation, as suggested by Skelly et al. (2008, 2009), is the presence of circumstellar material or even prominences co-rotating with the star. Co-rotating prominences are not uncommon and have been observed on other stars such as AB Doradus (Donati et al., 1999) and the post T-Tauri star RX J1508.6-4423 (Donati et al., 2000). Two gaussian curves were fitted to this emission component, one to match the core of the emission line and the other to fit the wings of the line, as shown in Figure 4.15. This is similar to the approach adopted by Skelly et al. (2008, 2009). The first gaussian profile has a full width at half maximum (FWHM) of 40 $\mathrm{km\,s^{-1}}$ (which matches the $v \sin i$ of the star) while the second gaussian profile had a FWHM of 156 $\mathrm{km\,s^{-1}}$. This second value is interpreted as being due to the circumstellar material around this young star.

4.5 Discussion

4.5.1 Spot features and surface differential rotation

Like many young, rapidly rotating solar-type stars, HD 76298 has a large polar spot, with some mid- latitude spot features. The polar spot extends to latitude $+60^o$ in both 2010 and 2011. There are some mid-latitude spots extending to latitude $+30^o$ although limited phase coverage in 2011 placed significant constraints on the ability to adequately

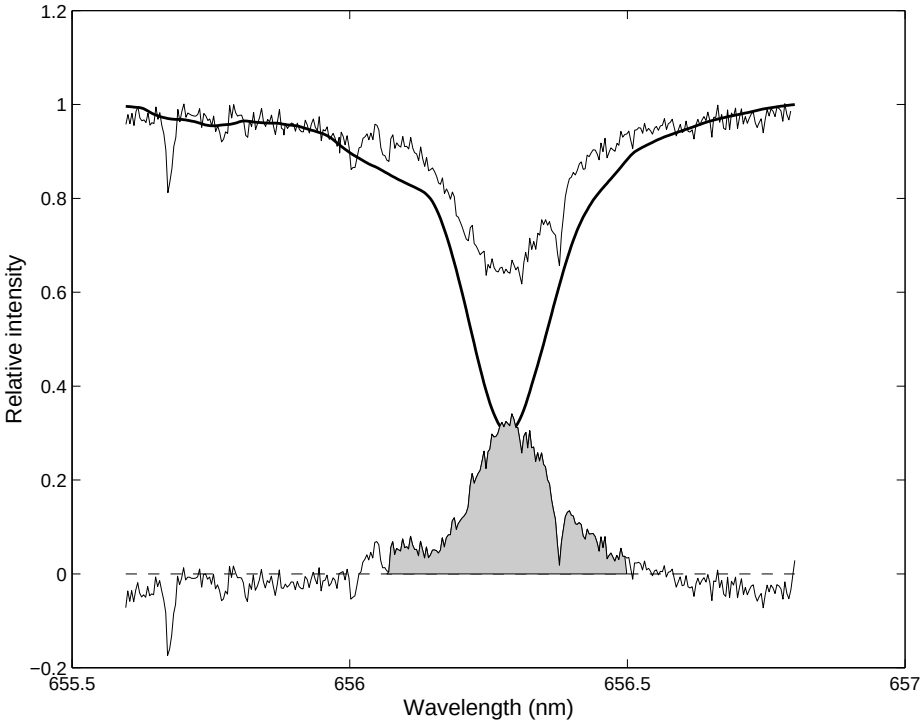

Figure 4.14: The core emission component (bottom line) of the Hα spectral line is produced by subtracting a rotationally broadened solar spectrum from that of HD 76298.

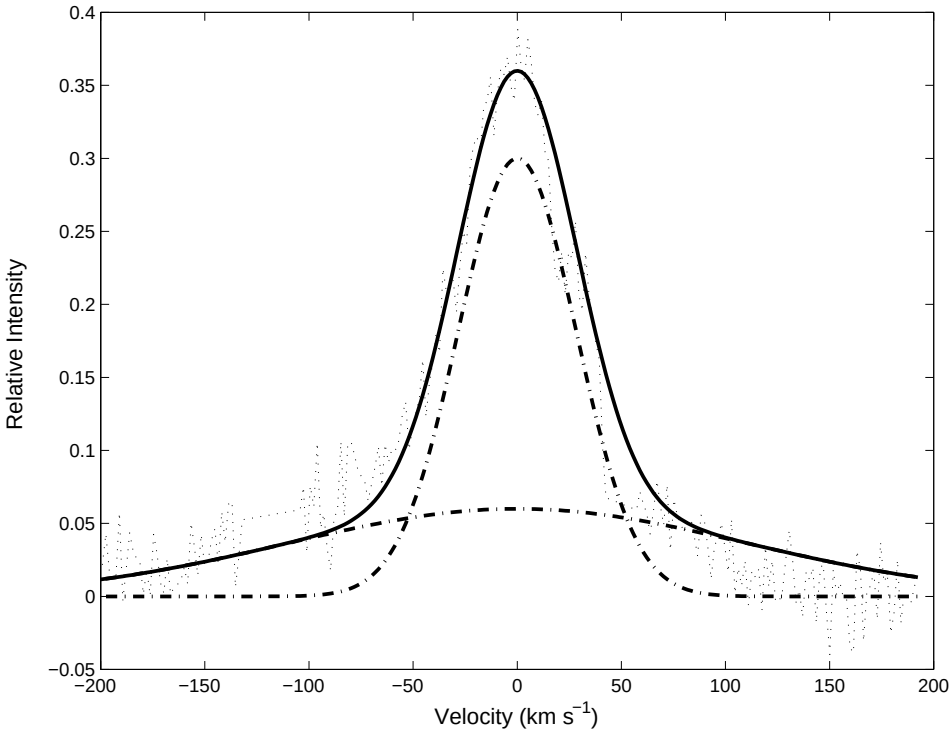

Figure 4.15: The emission component of the Hα line is shown, along with the two gaussian profiles that were used to fit the data. The two profiles have $v\sin i$ of 40 km s^{-1} and 156 km s^{-1} respectively. The solid line is the resultant of the two gaussian profiles while the individual gaussian profiles are the dot-dashed (-·-) lines. The actual raw data is the dotted profile.

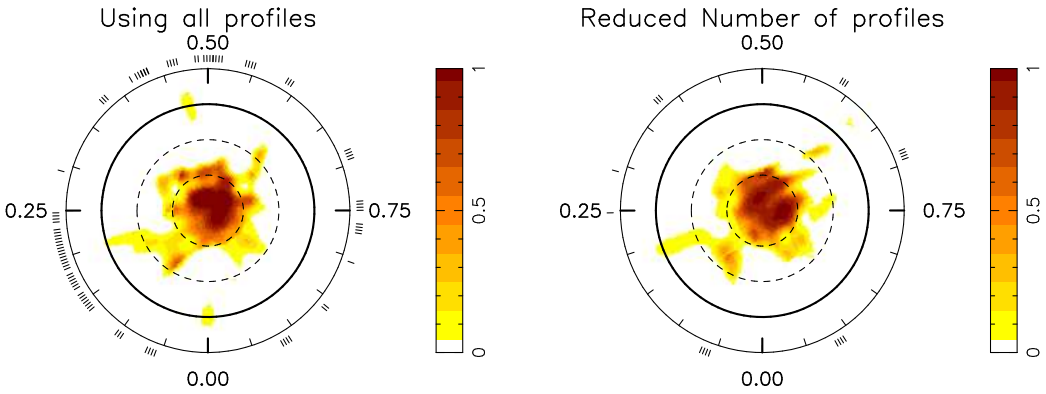

Figure 4.16: A comparison of the 2010 HD 76298 Stokes I map (left panel) with a map constructed with fewer profiles (right panel). The reduced number of profiles approximates the phase from those phases with the 2011 map. These maps are polar projections extending down to -30^o. The bold lines denote the equator and the dashed lines are +30^o and +60^o latitude parallels. The radial ticks indicate the phases at which this star was observed. Differential rotation has been incorporated into the analysis of both maps. The map using the full dataset (left panel) has a spot coverage of 6.6% while the map using the reduced number of profiles (right panel) has a spot coverage of 6.2%.

determine the latitude of each spot, as seen in Figure 4.5 (right panel). The 2011 map exhibits this inability of the code to accurately determine the latitude hence the spots appear to cover from 0^o to 60^o at phase 0.30 to 0.40 (for example). The reduced number of profiles also reduces the size of the spot coverage that is recoverable. Figure 4.16 (right panel) shows the 2010 Stokes I map with a reduced number of profiles. The profiles were selected on the basis of the approximate phase of the 2011 data, with the minimum amount of profiles to match that phase. A total of twelve profiles were used to generate this map. The spot coverage with the reduced number of profiles was 6.2% while the spot coverage with the full number of profiles was 6.6%. When compared with the full map, reproduced in Figure 4.16 for comparison purposes, the mapping process was able to recover most of the large scale spot features. However, fewer profiles do not constrain the location of some of the features as effectively as using data that have higher cadence. In addition, data that is taken at approximately the same phase at different epochs, otherwise known as overlapping data, constrains the maps and is very important when determining the differential rotation occurring on a star.

These spot features were used to determine the differential rotation occurring on this

star. The χ^2-landscape is shown in Figure 4.4 for Stokes I. The relatively large error ellipse, was due to the variation in the $v\sin i$. This was the dominant error in Stokes I, with lower $v\sin i$ producing more spot features at the mid-latitudes while the greater $v\sin i$ produced fewer number of spot features at these mid-latitudes. This is shown in Figure 4.9, the fractional spottedness of the star with respect to latitude. The projected rotational velocity was the dominant error in the mid-latitude features (from 40^o to 60^o). For this young, rapidly rotating star, the rotational shear was found to be $\delta\Omega = 0.09^{+0.03}_{-0.04}$ rad d^{-1}when using the brightness features. This equates to a *laptime*, using Equation 2.17, of 70^{+56}_{-17} days.

4.5.2 Magnetic topology and surface differential rotation

The reconstructed magnetic fields are shown in Figure 4.11 for both the 2010 and 2011 datasets. The fits to the Stokes V LSD profiles are given in Figure 4.12 for the 2010 dataset and in Figure 4.13 for the 2011 dataset. Magnetic features on both the azimuthal and radial magnetic maps extend from low-latitude to high-latitude features. As discussed by Donati et al. (2003b), the radial component may be interpreted to be representative of the poloidal component while the azimuthal component may be considered as representative of the toroidal component of the large-scale dynamo field. The strong, predominantly positive, azimuthal ring around the star is similar to those observed on other late F-/early G-type stars. This could indicate that the dynamo is operating throughout the convection zone as outlined in Section 1.2.5. This distributed $\alpha^2\Omega$ dynamo (Brandenburg et al., 1989; Moss et al., 1995) is where the α-effect **and** differential rotation shear contribute to the production of the toroidal field, manifested as the strong azimuthal field observed on this star.

The magnetic field on HD 76298 is predominantly poloidal with approximately 78^{+4}_{-10} % of the magnetic energy being poloidal magnetic energy and only 22^{+10}_{-4} % being toroidal magnetic energy during the 2010 observing season. The 2011 observing season had limited data and whereas it does show that the star continues to be strongly poloidal in configuration. This strongly poloidal field is dissimilar to the toroidal field being the dominant field of HD 106506 (Chapter 3), AB Doradus and LQ Hydra (Donati et al., 2003b) which are more rapidly rotating. Donati and Landstreet (2009) found that increasing rotation rate of a star, the toroidal component of the surface magnetic field dominates over the poloidal component of that field. Table 4.4 shows the relative size

Table 4.4: A comparison between the two geometries: poloidal and toroidal magnetic fields.

	2010 data		2011 data	
Parameter	Poloidal (%)	Toroidal (%)	Poloidal (%)	Toroidal (%)
Total Energy[1]	78^{+4}_{-10}	22^{+10}_{-4}	93^{+1}_{-3}	8^{+3}_{-2}
dipole[2]	20^{+11}_{-10}	6^{+6}_{-7}	74^{+4}_{-6}	7^{+3}_{-3}
quadrupole[2]	12^{+3}_{-4}	9^{+6}_{-5}	2^{+1}_{-1}	3^{+3}_{-2}
octupole[2]	13^{+4}_{-2}	7^{+3}_{-5}	4^{+1}_{-1}	2^{+2}_{-1}
higher order[2,3]	54^{+14}_{-11}	78^{+12}_{-9}	21^{+5}_{-4}	89^{+4}_{-5}
with respect to the total energy				
axisymetric	32^{+8}_{-14}	13^{+6}_{-2}	80^{+3}_{-5}	4^{+1}_{-1}
non-axisymetric	28^{+8}_{-14}	8^{+5}_{-2}	11^{+3}_{-2}	3^{+2}_{-1}
with respect to the energy held in that configuration				
axisymetric	41^{+11}_{-17}	59^{+6}_{-4}	86^{+3}_{-3}	57^{+7}_{-6}
non-axisymetric	37^{+17}_{-11}	35^{+6}_{-4}	12^{+3}_{-2}	43^{+6}_{-7}

[1] this is a % of the total magnetic energy available.

[2] this is a % of that particular field geometry.

[3] higher order multipole magnetic fields ($\ell \geq 4$)

of the various components. Like other stars observed in this thesis, this field is quite complex and much more so than that operating the Sun. Unlike other stars, it was more difficult to extract the symmetry of the configurations in 2010. Hence one cannot make any conclusions regarding the axisymmetry or otherwise in both the poloidal or toroidal fields. Considering the poloidal component, 54^{+14}_{-11} % of the magnetic energy in 2010 was spread across higher order terms ($\ell \geq 4$). Again, the toroidal field is dominated by the $\ell \geq 4$ components with 78^{+12}_{-9} %. The error estimates on these measures were obtained by varying a range of stellar parameters such as inclination, radial velocity, Ω_{eq}, $\delta\Omega$, period and $v\sin i$ as done in previous chapters. In summary, it may be concluded that a more complex dynamo is operating on HD 76298 than on the present-day Sun.

Differential rotation was undertaken on HD 76298 using these magnetic features. The χ^2-landscape is shown in Figure 4.17 for Stokes V. The relatively large error ellipse, like that found in the Stokes I data, was due to the variation in the $v\sin i$. When measuring

the differential rotation using the magnetic features, the equatorial rotation rate $\Omega_{\rm eq}$ was $2.15^{+0.10}_{-0.11}$ rad d^{-1}, with a photospheric shear $\delta\Omega$ of $0.34^{+0.01}_{-0.16}$ rad d^{-1}. A comparison with those parameters found using the Stokes I and V information is shown in Figure 4.17. There is significant difference between the two measurements, even allowing for the large error ellipses obtained using the Stokes V information. The error ellipse with the Stokes V in particular, is very large. This difference has been observed on other stars of similar spectral type such as HD 141943 (Marsden et al., 2011b). However, this star is much larger than HD 141943 and is similar in size to HD 106506 (Chapter 3). Yet HD 106506 showed limited variation between the two measurements, and certainly within the respective errors of the measurements. This may imply that the features may be anchored at different depths of the convective zone. An alternative yet intriguing explanation for the varying differential rotation values from Stokes I and Stokes V could be offered by the work of Korhonen and Elstner (2011). Using dynamo calculations, they discovered that large starspots do not necessarily follow the actual differential rotation of the star, but have more solid-body like behaviour, whereas the true surface differential rotation is only recovered if small magnetic features are added to the simulations. These competing explanations must be treated with caution until further Stokes V data is obtained for this star.

As previously discussed, HD 76298 may be an evolved FK Comae-type star. The FK Comae star HD 19978 also exhibits similar magnetic field topology and variation (Petit et al., 2004b) and in particular rings of azimuthal fields, again indicating the presence of a dynamo operating near the surface of the star. Korhonen et al. (2009) reported magnetic field measurements on FK Comae and derived starspot locations, including high latitude spots, on the surface of this star.

HD 76298 has similar properties to HD 106506 (see Chapter 3). Both of these solar-type stars may be classified as intermediate mass stars. Table 4.5 show the similarities between the two. One major exception is that HD 106506 rotates twice as fast, and has a *laptime* almost half (using the brightness features), when compared to HD 76298. This observation needs to be treated cautiously. The DI process was not able to recover many low latitude spot features on HD 76298. This is shown in Figure 4.5 where both 2010 and 2011 maps have predominantly mid- to high-latitude features. Hence the χ^2 minimisation technique might not have been able to adequately track the evolution of these features as effectively as the magnetic maps. Hence any conclusion regarding the

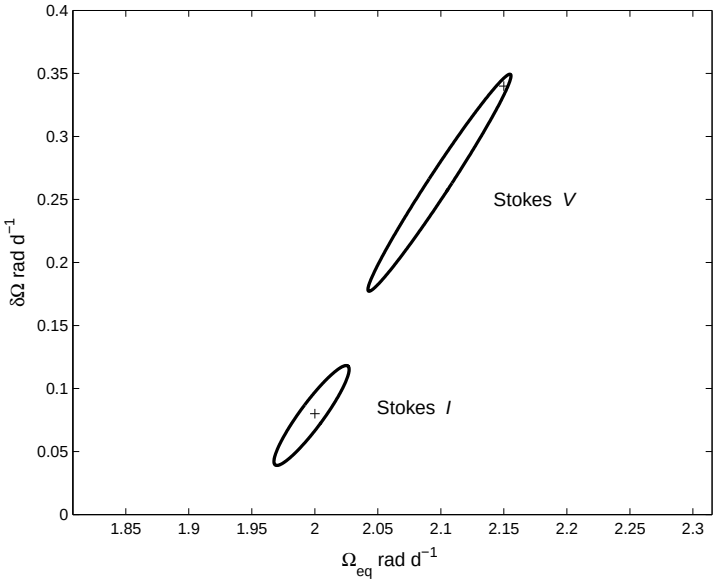

Figure 4.17: This shows a graph of the error ellipses for the differential rotation measurements for both the Stokes I (lower) and the Stokes V (upper). These error ellipses were generated by varying some of the stellar parameters, including the star's inclination ($\pm$ 10^o), $v\sin i$ ($\pm$ 0.5 km s^{-1}) and the Stokes I spot coverage or the Stokes V global magnetic field ($\pm$ 10%).

Table 4.5: A comparison between two stars HD 76298 and HD 106506.

parameter	HD 76298	HD 106506
Spectral type	G1V	G0V
Equatorial period, d	3.14±0.1	1.39±0.01
Inclination angle, ^{o}	55±5	65±5
Photospheric Temperature, T_{phot}, K	6000±30	5900±50
ΔTemp = T_{phot} - T_{spot}, K	1900	1900
Stellar Radius: $R_\odot$	$2.2^{+0.6}_{-0.4}$	2.15±0.26
Stellar Mass: $M_\odot$	1.6^{+2}_{-2}	1.5±0.1
Projected Rotational Velocity, $v\sin i$, km s^{-1}	39.5±0.5	79.5±0.5
Stokes I:$\delta\Omega$, rad d^{-1}	$0.09^{+0.03}_{-0.04}$	$0.21^{+0.02}_{-0.03}$
Stokes I: *laptime*, d	70^{+56}_{-17}	30^{+5}_{-3}
Stokes I:$\delta\Omega$, rad d^{-1}	$0.34^{+0.01}_{-0.16}$	0.24±0.03
Stokes V: *laptime*, d	$18.5^{+16.5}_{-0.5}$	26^{+4}_{-3}

relationship between *laptime* and rotational velocities (apart from the fact that this is a sample size of two) using the brightness maps needs to be treated with extreme caution. When one considers using the magnetic features, the error bars overlap between the two $\delta\Omega$ measurements.

4.5.3 Chromospheric activity and circumstellar material

There appears to be limited evidence of variability in the chromosphere; however, there is a very dense chromosphere as shown in Figure 4.14 with strong emission in the core of the Hα line. There is evidence of the presence of circumstellar material surrounding this star. This is supported by the filling in of the wings of the Hα profile indicative of circumstellar material as shown in Figure 4.15. The first gaussian profile has a FWHM of 40 km s^{-1} (which matches the $v\sin i$ of the star) while the second gaussian profile has a FWHM of 156 km s^{-1} which is interpreted as being due to the circumstellar material around this young star. The presence of circumstellar material in the form of a disk produces a large velocity shear at the base of the convective zone as a result of star-disk interaction (Bouvier, 2008). Hence this could be further evidence of the reason for the lack of a lithium line in a very young star. Even so, the presence of circumstellar material is not conclusive proof of the youthful nature of HD 76298

as disk-like structures have been observed in FK Comae-type stars (Kjurkchieva and Marchev, 2005; Korhonen et al., 2009).

4.6 Conclusions

HD 76298 is an active solar-type star with a significant level of differential rotation that is substantially higher than that observed on the Sun. Using the brightness features, the differential rotation parameters were determined to be $\Omega_{eq} = 2.01^{+0.10}_{-0.03}$ rad d^{-1}and $\delta\Omega = 0.09^{+0.03}_{-0.04}$ rad d^{-1}. When using magnetic features, the differential rotation parameters were determined to be $\Omega_{eq} = 2.15^{+0.10}_{-0.11}$ rad d^{-1}and $\delta\Omega$ $0.34^{+0.01}_{-0.16}$ rad d^{-1}. The evolutionary status of this star remains uncertain. HD 76298 is rapidly rotating, active star with the presence of circumstellar material and strong azimuthal magnetic fields. Alternatively, this star could be an evolved FK Comae-type star that also exhibits all these features. HD 76298 is an important result in that it shows a strong azimuthal magnetic field unlike that on Sun and, if it is an FK Comae-type star, one of the few evolved stars that exhibit magnetic fields consistent with those observed on young stars.

Chapter 5

Magnetic Fields on Young, Moderately Rotating Sun-like stars: HD 35296

5.1 Introduction

HD 35296 (V111 Tau) is a wide binary star (Eggleton and Tokovinin, 2008) in the constellation of Taurus. It has a Right Ascension $05^h24^m25.46380^s$ and Declination $^+17^o23^{'}00.7166^{''}$ (J2000.0 van Leeuwen, 2007). This star is considered to be moderate rotator (MR) according to the definition by Waite et al. (2011a). MR stars have $v\sin i$ values between 5 $\mathrm{km\,s^{-1}}$ and 20 $\mathrm{km\,s^{-1}}$ with this upper limit considered the critical velocity where dynamo saturation has been theorised to slow the angular momentum loss of rapidly rotating stars (e.g. Irwin et al., 2007; Krishnamurthi et al., 1997; Barnes et al., 1999). Below 20 $\mathrm{km\,s^{-1}}$, the strength of the star's magnetic dynamo is thought to be related to the star's rotation rate but above this speed, it is believed that dynamo saturation is occurring where the strength of the star's magnetic dynamo is no longer dependent upon stellar rotation. However, the division of targets based on this criteria using 20 $\mathrm{km\,s^{-1}}$as the upper limit will be affected by the unknown inclination angle. With a mean *sin i* of 0.64, $v\sin i$ can only be used as a statistical measure of rotation rate as the true rotational velocity, v, could vary greatly depending on the inclination angle. HD 35296 is a suitable star to investigate the magnetic fields in this regime as it has a $v\sin i$ of 15.9 $\mathrm{km\,s^{-1}}$ (Ammler-von Eiff and Reiners, 2012). The aim of this

investigation is to map the surface of this sun-like star with a view to measuring the rotational shear on its surface and to measure and to map the magnetic field structure on the surface of this star.

5.2 Fundamental Parameters of HD 35296

HD 35296 is a F8V star (Montes et al., 2001). It has a parallax of 69.51 ± 0.38 mas (van Leeuwen, 2007) giving a distance of 14.39 ± 0.08 pc or 54.78 ± 0.35 ly. HD 35269 is estimated to be $1.06^{+0.06}_{-0.05}$ $M_{\odot}$ (Holmberg et al., 2009) with an effective temperature of 6170K (Casagrande et al., 2011). Samus et al. (2009) identified HD 35296 as a BY Draconis-type variable star, meaning that it undergoes rotational modulations due to the presence of starspots and other chromospheric activity. The range of age estimates of this star in the literature is quite wide, with Holmberg et al. (2009) estimating an age of 3.3 Gyr while some authors list this star as young as 20 Myr or as old as 7.5 Gyr (e.g. Chen et al., 2001; Barry, 1988, respectively). However, the equivalent width of the Li I 670.78 nm was measured to be 99 mÅ after correcting for the nearby 670.744 nm Fe-I line (Soderblom et al., 1993b,a). This is consistent with the measurement of 94.3 mÅ by Takeda and Kawanomoto (2005); thus indicating that this star could be young. When placing this star on the theoretical isochrones of Siess et al. (2000), the age of this star is between 20 Myr to 50 Myr. Li and Hu (1998) argued that HD 35296 is a member of the Taurus-Auriga star forming region that may have reached the Zero-Age Main Sequence (ZAMS). Hence it is likely that this star is quite youthful. Bryden et al. (2006) investigated this star as part of a frequency study of debris disks around solar-type stars using the Spitzer telescope. They placed an upper limit of 6.2×10^{-6} $L_{dust}/L_{\star}$ from the 70 μm emission, equating to a temperature of the dust being ∼50 K, or at Kuiper Belt distances in our own Solar system (Bryden et al., 2006). Dermott et al. (2002) used observations and modelling to derive an estimate of $\sim 10^{-8}$ to 10^{-7} $L_{dust}/L_{\star}$ for the asteroid belt of our own Solar system. Perhaps this system might have a disk system similar to our own.

5.3 Observations and Analysis

HD 35296 was observed at the Télescope Bernard Lyot (TBL - Observatoire du Pic du Midi, France) in January/February in 2007 and 2008. A journal of observations is shown in Table 5.1. There was no simultaneous photometry undertaken on this star, unlike HD 106506.

5.3.1 High Resolution Spectropolarimetric Observations from the TBL

High resolution spectropolarimetric data were obtained using NARVAL at TBL. Initial reduction was completed using the dedicated pipeline reduction software LibreESpRIT software package developed for NARVAL (Donati et al., 1997, 2003b). Silvester et al. (2012) demonstrated that NARVAL was a very stable instrument, with resolution and S/N being constant over the four years of data studies from 2006-2010. This reduced data was kindly supplied by Dr Pascal Petit, from L'Institut de Recherche en Astrophysique et Planétologie (IRAP) at l'Université Paul Sabatier. When preparing the LSD profiles, an F8 line mask, created from the Kurucz atomic database and ATLAS9 atmospheric models (Kurucz, 1993), was used.

Due to the length of time between the two observing seasons on HD 35296, the phases for the 2007 run were calculated using an epoch of HJD = 2454133.871035 whereas the 2008 run used an epoch of HJD = 2454497.871035. The epoch for 2008 was selected as being close to the mid-point of the observing season, but was an integral number of rotations since the mid-point of the 2007 run based on the 3.5 day period of the star. The fundamental parameters for HD 35296 are listed in Table 5.2.

5.4 Observations and Analysis

5.4.1 Image Reconstruction: Stokes *I* Doppler imaging

Brightness images could not be reconstructed for HD 35296, as its LSD intensity profiles were not sufficiently deformed by any surface features present to recover reliable spot information. The $v \sin i$ of HD 35296 was determined to be 16 km s^{-1}, which is very low for DI. However, the imaging code was still used to establish the values of a number of basic parameters, including the star's inclination angle, projected rotational velocity, $v \sin i$, and radial velocity, v_{rad}. This was achieved by systematically varying each

Table 5.1: The Journal of spectropolarimetric observations of HD 35296 using NARVAL at TBL.

UT Date	UT middle	Exp. Time[1] (sec)	Stokes V Mean S/N[2]	FAP[3]	Detection?
2007 Jan 26	21:10:23	4×300	19762	2.297×10^{-1}	no detection
2007 Jan 27	20:18:17	4×600	39439	0.000	definite
2007 Jan 29	19:29:15	4×600	38358	0.000	definite
2007 Feb 02	21:17:29	4×300	4223	0.000	definite
2007 Feb 03	20:15:21	4×300	29940	3.259×10^{-3}	marginal
2007 Feb 04	20:06:35	4×300	25137	0.000	definite
2007 Feb 08	20:30:51	4×300	25639	0.000	definite
2008 Jan 19	20:01:46	4×300	17208	0.000	definite
2008 Jan 20	21:45:01	4×300	20581	0.000	definite
2008 Jan 21	19:42:27	4×300	24563	0.000	definite
2008 Jan 21	20:53:24	4×200	22146	6.044×10^{-13}	definite
2008 Jan 22	20:09:11	4×300	21913	1.336×10^{-2}	no detection
2008 Jan 23	20:10:31	4×300	21825	0.000	definite
2008 Jan 24	20:39:32	4×300	13296	6.423×10^{-4}	marginal
2008 Jan 25	20:15:17	4×300	19723	0.000	definite
2008 Jan 26	20:14:43	4×300	21148	0.000	definite
2008 Jan 27	20:30:50	4×300	21245	0.000	definite
2008 Jan 28	21:56:43	4×300	21245	1.333×10^{-9}	definite
2008 Jan 29	20:50:19	4×300	25946	2.114×10^{-12}	definite
2008 Feb 02	20:45:15	4×300	24375	0.000	definite
2008 Feb 04	20:20:19	4×300	27669	1.572×10^{-7}	definite
2008 Feb 05	20:21:18	4×300	22909	8.613×10^{-4}	marginal
2008 Feb 06	21:11:07	4×300	25579	4.767×10^{-11}	definite
2008 Feb 09	20:34:17	4×300	24555	9.282×10^{-11}	definite
2008 Feb 10	19:13:58	4×300	29354	0.000	definite
2008 Feb 11	20:39:11	4×300	25414	4.446×10^{-10}	definite
2008 Feb 12	20:45:32	4×300	27269	0.000	definite
2008 Feb 13	20:39:30	4×300	24182	5.212×10^{-11}	definite
2008 Feb 14	21:00:08	4×300	24386	0.000	definite
2008 Feb 15	20:37:06	4×300	28120	0.000	definite

[1] Each sequence of 4x300=1200 seconds exposures (for example). After each exposure, the "rotating half-wave retarder" of the polarimeter is rotated between $+45^o$ and -45^o so as to remove instrumental polarization signals from the telescope and the polarimeter.

[2] Signal-to-noise (S/N) of the resulting Stokes V profile.

[3] FAP: False Alarm Probability. See Section 3.3.2 for more details.

Table 5.2: The parameters used to produce the maximum-entropy image reconstructions of HD 35296, including those associated with surface differential rotation.

Parameter	HD 35296
Spectral Type [1]	F8V
Equatorial Period [2]	3.5 ± 0.2 d
Inclination Angle	65 ± 5^o
Projected Rotational Velocity, $v\sin i$	16.0 ± 0.1 km s^{-1}
Photospheric Temperature, T_{phot} [3]	6080 K
Spot Temperature, T_{spot}	–
Radial Velocity, v_{rad}	38.1 ± 0.1 km s^{-1}
Stellar radius [4]	1.13 $R_\odot$
Convection Zone Depth	0.178 ± 0.004 $R_\star$
	0.201 ± 0.009 $R_\odot$
Age [5]	30-60 Myr
Mass [4]	1.10 $M_\odot$
Stokes I: Ω_{eq}	–
Stokes I: $\delta\Omega$	–
Stokes V: Ω_{eq}	1.80 ± 0.01 rad d^{-1}
Stokes V: $\delta\Omega$	0.28 ± 0.08 rad d^{-1}
Epoch used (HJD)	2454133.871035 (2007)
	2454497.871035 (2008)

[1] Montes et al. (2001)

[2] Using Stokes V data.

[3] Holmberg et al. (2009)

[4] Based on the theoretical isochrones of Siess et al. (2000)

[5] Li and Hu (1998)

parameter in order to minimize the χ^2 value, as done in previous chapters. The "best fit" to the data was then assumed to be the set of optimum parameters and it was these parameters that gave the minimum χ^2 value are shown in Table 5.2 and were adopted when producing the final ZDI maps.

5.4.2 Zeeman Doppler imaging: magnetic features on the surface of HD 35296

The magnetic topology was determined for HD 35296 using ZDI. The Stokes V data was used to reconstruct radial, azimuthal and meridional fields. The modelling strategy of Donati and Brown (1997) was used to construct the magnetic field topology on HD 35296, as was done for HD 106506 (Chapter 3) and HD 75298 (Chapter 4). This mapping procedure involved utilising the spherical harmonic expansions of the surface magnetic field, as implemented by Donati et al. (2006b). The maximum spherical harmonic expansion of $l_{max} = 30$, resolving the star into 30 equatorial elements, was selected as this was the minimum value where any further increase did not produce any difference in the topology of the magnetic field recovered. Figure 5.1 shows the magnetic maps for HD 35296 for the 2007 and 2008 datasets. The associated fits between the modelled data and the actual profiles are shown in Figure 5.2 for HD 35296. The full set of parameters used to produce these maps, including differential rotation, are listed in Table 5.2.

5.4.3 Surface differential rotation using Stokes V

The differential rotation of HD 35296, using Stokes V, was measured for the 2008 data using the χ^2 minimisation technique using the method described in Section 2.6. Using the magnetic signatures, HD 35296 has an equatorial rotational velocity, Ω_{eq}, of 1.80 ± 0.01 rad d^{-1} with rotational shear, $\delta\Omega$, of 0.28 ± 0.08 rad d^{-1}. This translates to a *laptime* of $\approx 22^{+9}_{-5}$ d. Differential rotation was not attempted on the 2007 data due to the limited number of profiles obtained. This is consistent with similar observations of other F-type stars by Reiners (2006) and Ammler-von Eiff and Reiners (2012); however, Reiners (2006) found no evidence of differential rotation using the Fourier transform method of line profile analysis on HD 35296. Reiners (2006) conducted a direct comparison between the Fourier transform method and Doppler imaging using HD 307938 (R58) in IC 2602. Marsden et al. (2005) used DI to measure a shear of $\delta\Omega$

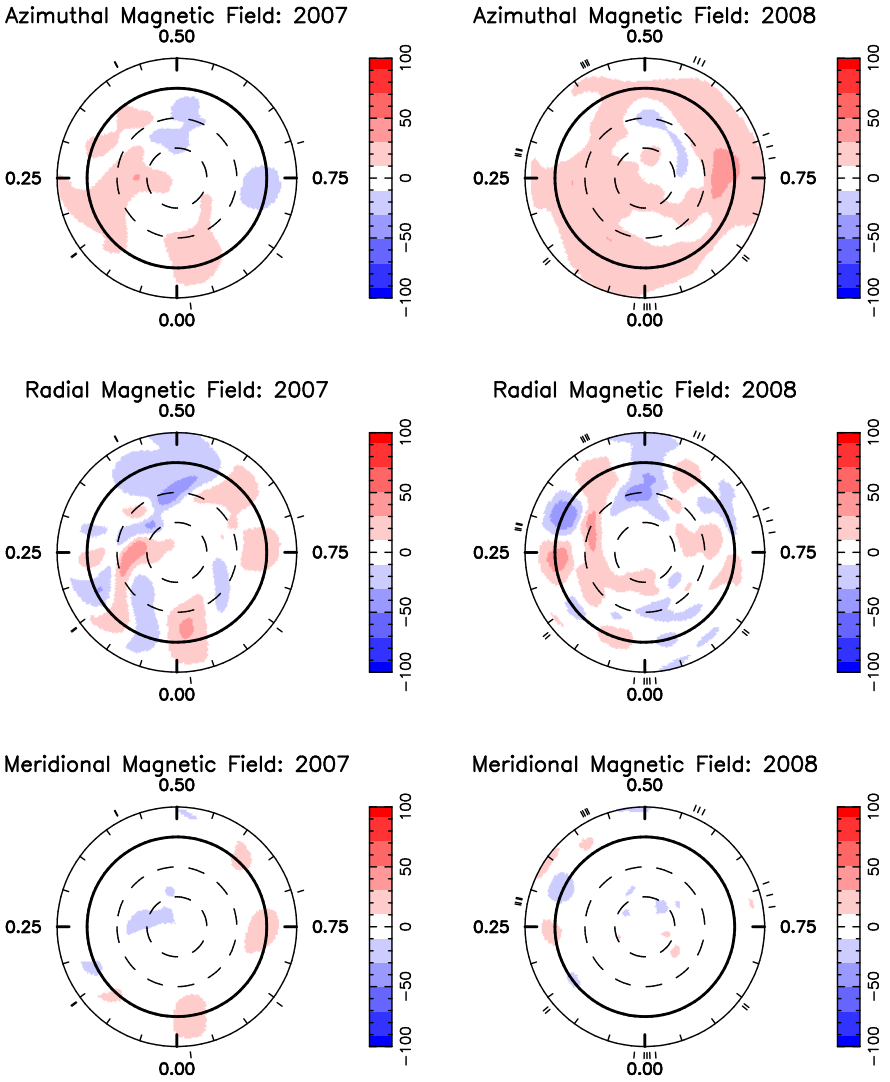

Figure 5.1: Magnetic imaging of the large-scale field for HD 35296 in both 2007 (left series) and 2008 observing seasons with differential rotation, as measured using the 2008 Stokes V data, incorporated into the modelling strategy. The 2007 data has a mean field modulus of 13.2 G whereas the 2008 data was 15.8 G. These maps are polar projections extending down to -30^o. The bold lines denote the equator and the dashed lines are +30^o and +60^o latitude parallels. The radial ticks indicate the phases at which this star was observed.

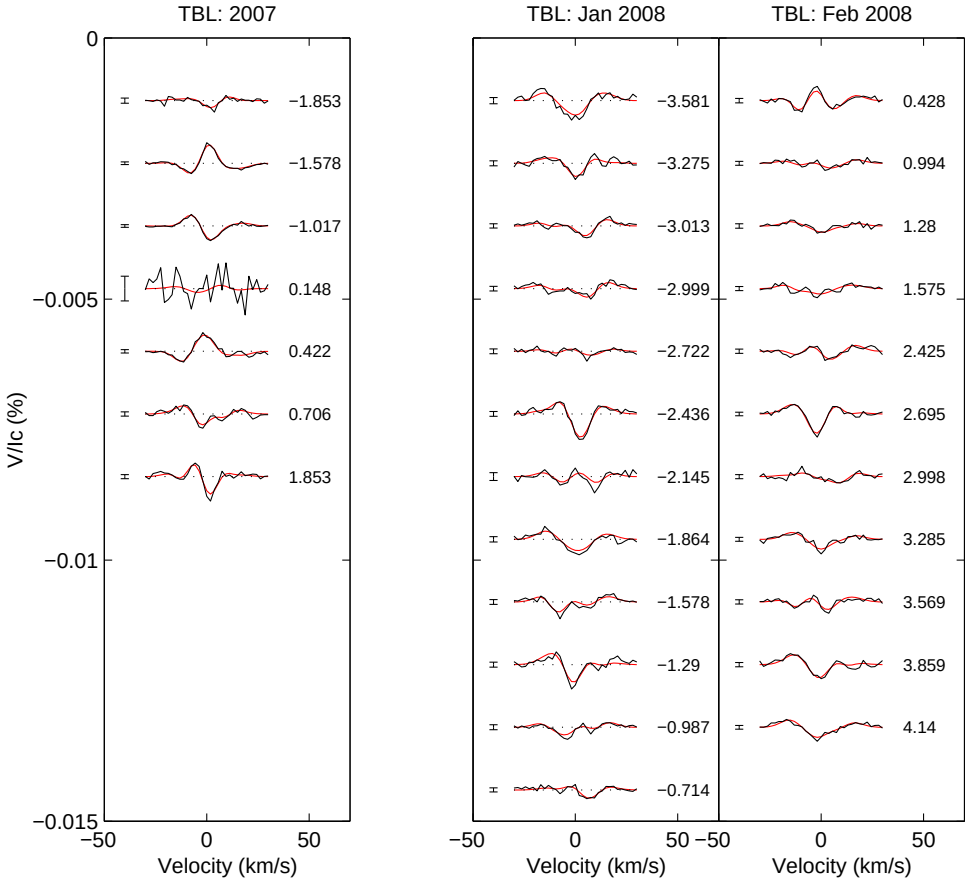

Figure 5.2: The maximum-entropy fits to the LSD profiles for HD 35296 during 2007 (left panel) and again in 2008 (right panels). Differential rotation from 2008 was incorporated into the analysis of the 2007 data. The observed Zeeman signatures are shown in black while the fit to the data is shown as red (thin) lines. The rotational cycle and $\pm$ 0.5σ error bars of each observation are shown next to each profile

$= 0.025 \pm 0.015$ rad d^{-1}. Using the Fourier transform method, the threshold for solid-body rotation, q_2/q_1, is 1.76 where q_1 and q_2 are the first two zeros of the line profile's Fourier transform. Reiners (2006) argued that a small shear would have only a small effect on the Fourier transform. In addition, R58 has a large polar spot. Reiners (2006) argue that this will have more of an effect on q_2/q_1 than any small deviation from solid-body rotation. This does not answer the question why HD 35296's differential rotation was measured using ZDI but not Fourier transform method. Reiners (2006) measured $q_2/q_1 = 1.75$, only marginally less than solid-body rotation yet this work, using ZDI, measured a rotational shear, $\delta\Omega$, of 0.28 ± 0.08 rad d^{-1}. One would expect this to give a q_2/q_1 ~1.50 to 1.60. The reason for this disparity remains unclear.

The error estimation for the differential rotation measurements was done by individually varying stellar parameters such as inclination, $v \sin i$, and global magnetic field across a physically reasonable range. Figure 5.3 demonstrates how the error estimate is made while Section C.4 in Appendix C lists the actual results. The error bars on each individual measurement represents the 1-σ errors in each paraboloid fit with the final ellipse generated to encompass all the differential rotation values. The grid of χ^2 values for each $\Omega_{\rm eq}$ and $\delta\Omega$, coupled with the appropriate variation ellipse, is shown in Figure 5.4 for the 2008 data. The differential rotation parameters were incorporated into the mapping process, resulting in the maps shown in Figure 5.1. The differential rotation parameters found for HD 35296 for the 2008 observing run were used in the mapping process for the 2007 data.

5.4.4 Magnetic field and dependence on latitude

The magnetic maps produced for HD 35296 show complex, and evolving, magnetic topologies from 2007 to 2008. Figure 5.5 shows the fractional magnetic field strength as a function of latitude for each field orientation for HD 35296. This is based on Equation 5.1.

$$F(\theta) = \frac{B(\theta) cos(\theta) d\theta}{2} \tag{5.1}$$

where F(θ) is the fractional magnetic field strength at latitude θ, B(θ) is the average magnetic field strength at latitude θ, and $d\theta$ is the width of each latitude ring. This is similar to Equation 3.5 except S(θ), the average spot occupancy in that equation, is

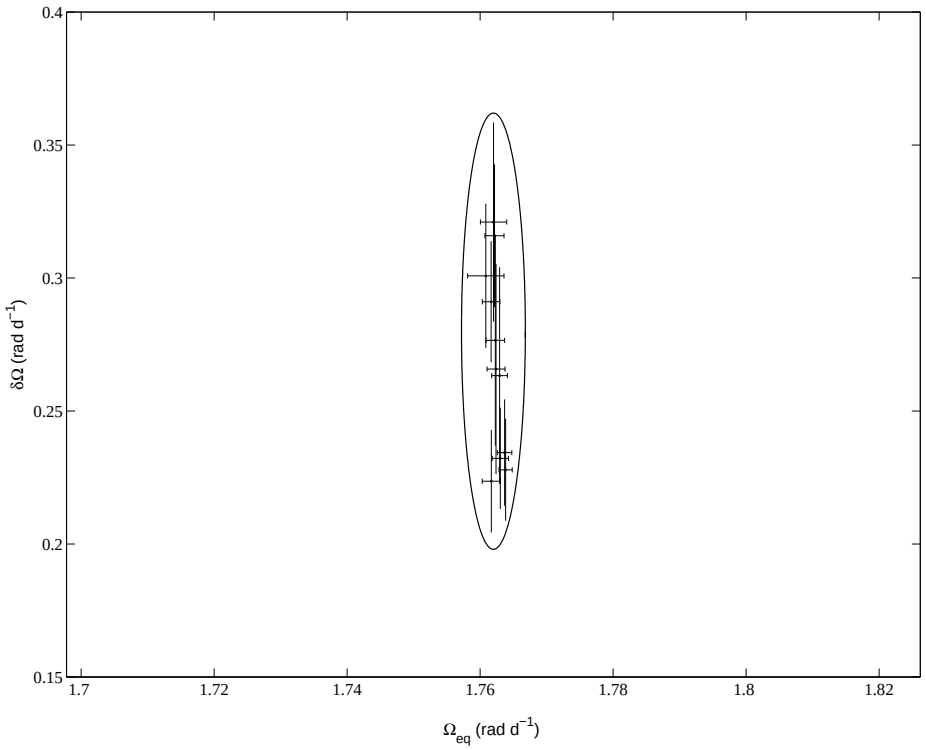

Figure 5.3: The determination of the overall error estimate for differential rotation of HD 35296 using the Stokes V data. Each datapoint is the result of paraboloid fit of the reduced-χ^2 landscape for each individual differential rotation value, given a specific change in a particular parameter such as inclination ($\pm 5^o$), $v \sin i$ (± 0.5 km s^{-1}) and global magnetic field ($\pm 10\%$). The error bar on each datapoint being 1-σ errors in the paraboloid fit.

now defined as B(θ), the average magnetic field strength. In order to determine the robustness of each measurement, a number of parameters were varied so as to place limits on the fractional magnetic field at each latitude for each of the orientations. These parameters, along with the variations, were: $v \sin i$ (± 0.5 km s^{-1}), inclination angle ($\pm 5^o$), period (± 0.2 d), v$_{rad}$ (± 0.1 km s^{-1}), $\Omega_{\rm eq}$ ($\pm^{0.006}_{0.009}$ rad d^{-1}) and $\delta\Omega$ (± 0.077 rad d^{-1}). These measured variations in the field strengths are shown by the shaded regions while the values for the optimum parameter set are shown as a solid line for the 2007 data and a dotted line for the 2008 data.

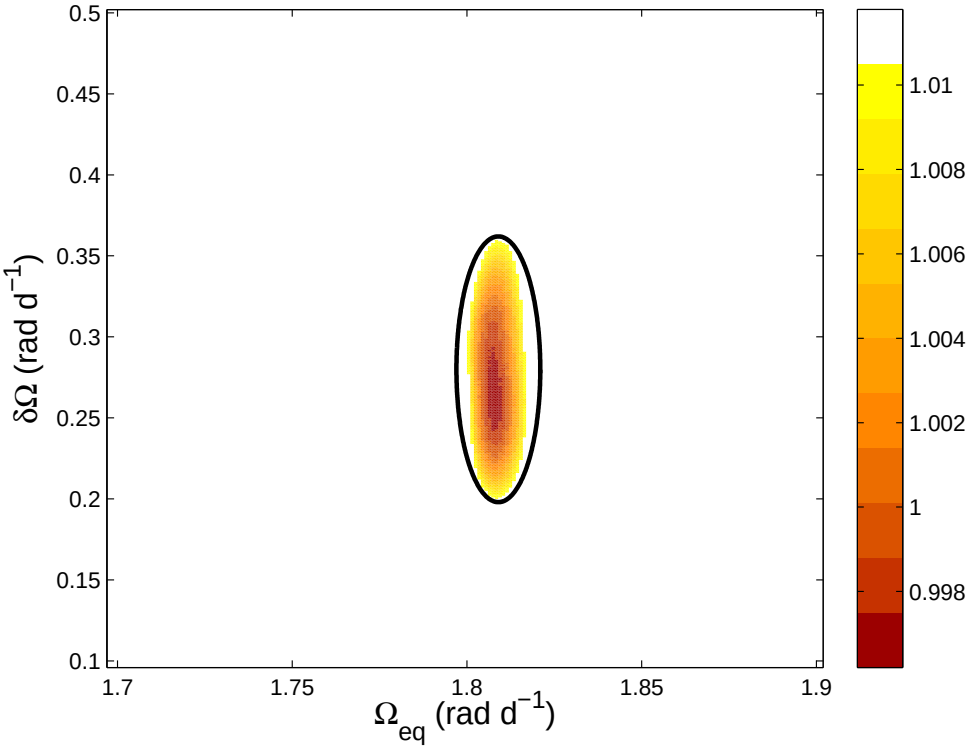

Figure 5.4: Differential rotation using Stokes V: HD 35296 in 2008. This is a 3-σ projection. The error ellipse, as shown in in Figure 5.3, encompasses a range of Ω_{eq} - $\delta\Omega$ pairs found by varying such parameters as $v\sin i$, magnetic field strength and inclination.

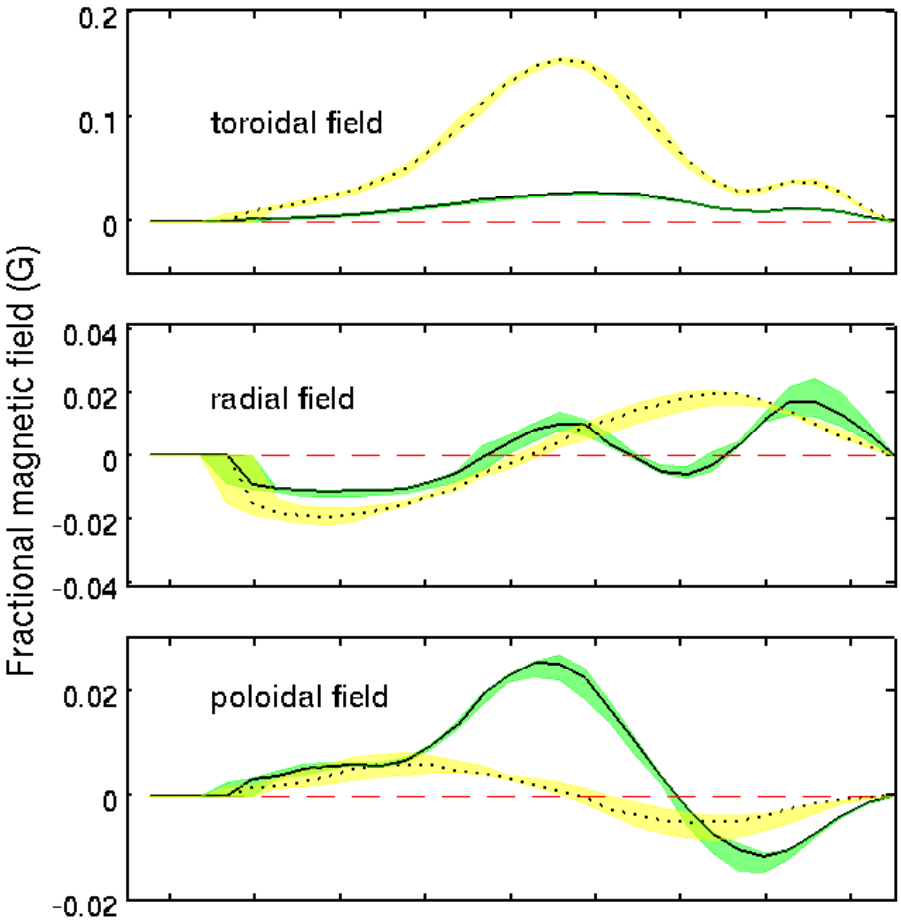

Figure 5.5: Variation of the respective magnetic field orientations for HD 35296 for 2007 and 2008 as a function of stellar latitude. The top panel is the poloidal field, the middle panel is that of the toroidal field while the lower panel shows the radial field. The shaded regions show the variation in the strength at each latitude point as determined by varying parameters: $v \sin i$ (± 0.5 km s^{-1}) and inclination angle ($\pm 5^o$). The dotted line with the yellow shading is for 2008 data while the solid line with the green shading is the 2007 data. This is based on the value of the magnetic field strength at each latitude, as defined by Equation 5.1.

5.4.5 Chromospheric activity

Unlike the spectropolarimetry data from the AAT, NARVAL extends into the blue region of the electromagnetic spectrum, enabling coverage of the Ca II H (396.85 nm) & K (396.37 nm) lines and also into the near infra-red region to include the Ca II Infrared Triplet (IRT) (849.8, 854.2 and 866.2 nm) lines (see Section 2.5.3). As a result, chromospheric activity can also be deduced using the Ca II H & K and Ca II Infrared Triplet (IRT) as well as the Hα spectral lines. The two Ca II H & K absorption lines are the most widely used optical indicators of chromospheric activity as their source functions are collisionally controlled hence are very sensitive to electron density and temperature. The Ca II IRT lines share the upper levels of the H & K transitions and are formed in the lower chromosphere Montes et al. (2004). The Hα spectral line is also collisionally filled in as a result of the higher temperatures and is formed in the middle of the chromosphere and is often associated with plages and prominences (e.g. Thatcher and Robinson, 1993; Montes et al., 2004).

The $N_{Ca\,II\,HK}$-index for HD 35296 was determined using the procedure as explained in Wright et al. (2004). With NARVAL spectra, the Ca II H & K region is not well normalised with the pipe-line reduction due to the dense distribution of photospheric lines (Morgenthaler et al., 2012). In order to improve the continuum normalisation, Morgenthaler et al. (2012) matched the continuum of the star's spectra (ξ Boötis, Sp-Type: G8V[1]) to that of a synthetic normalised spectrum from the POLLUX database (Palacios et al., 2010) with similar T_{eff} and $log(g)$. This process was initially adopted for HD 35296, except the overlapping order was removed prior to renormalising the spectra. Renormalising the spectra involved selecting a number of small spectral windows between 380 nm and 410 nm and the area bounded by the wavelength window and the spectrum itself was determined for both the template spectrum and that of HD 35296. The ratio of the template star to the target star was calculated for each window and a fourth order polynomial was fitted to determine the correction factor for the target star's spectrum. However, it was found that simply removing the overlapping order was sufficient as renormalising the spectra (with the overlapping order removed) made little to no difference to the final result. Nevertheless, the continuum was checked against that of the continuum of the synthetic normalised spectrum from the POLLUX

[1] Ruck and Smith (1995)

database (Palacios et al., 2010). In all cases,the continuum matched reasonably well and hence was not corrected for as done by Morgenthaler et al. (2012).

The resulting $N_{Ca\ II HK}$-index was converted to match the Mount Wilson S-values (Duncan et al., 1991) using the transformation shown in Equation 5.2.

$$S\text{-}index = \frac{C_1 H + C_2 K}{C_3 V_{HK} + C_4 R_{HK}} + C_5 \tag{5.2}$$

where H and K is the flux determined in the line cores from the two triangular bandpasses with a full-width at half maximum (FWHM) of 0.1 nm. Two 2 nm-wide rectangular bandpasses R_{HK} and V_{HK}, centred on 400.107 and 390.107 nm, respectively, were used for the continuum flux in the red and blue sides of the H and K lines. The transformation coefficients were determined by Marsden et al. (2013: *in preparation*) by matching ∼120 stars that were common to both the TBL database and that of the Mount Wilson project (Wright et al., 2004). These coefficients were: C_1 = -1.287 × 10^{+3}, C_2 = -2.502 × 10^{+2}, C_3 = -8.877 × 10^{+2}, C_4 = 4.271 × 10^{+2} and C_5 = 1.183 × 10^{-3}.

Two further activity indices were also used. The first is the Hα spectral line and the second are the Ca II IRT lines. The continuum was checked against that of the continuum of the synthetic normalised spectrum from the POLLUX database (Palacios et al., 2010). In both cases the continuum matched reasonably well and hence was not corrected for as in the case with of Ca II H & K spectral lines. The TBL Hα-index was determined using Equation 5.3.

$$N_{H\alpha}\text{-}index = \frac{F_{H\alpha}}{V_{H\alpha} + R_{H\alpha}} \tag{5.3}$$

where $F_{H\alpha}$ is the flux determined in the line core from the bandpass with a FWHM of 0.2 nm. Two 0.22 nm-wide rectangular bandpasses $V_{H\alpha}$ and $R_{H\alpha}$, centred on 655.885 and 656.730 nm, respectively, were used for the continuum flux in the red and blue sides of the Hα line. The TBL CaIRT-index was determined using Equation 5.4.

$$N_{CaIRT}\text{-}index = \frac{\sum F_{IRT}}{V_{IRT} + R_{IRT}} \tag{5.4}$$

where $\sum F_{IRT}$ is the total flux determined in the line cores of the three spectral lines, at 849.8023, 854.2091 and 866.2141 nm, using bandpass with a FWHM of 0.1 nm. Two 0.5 nm-wide rectangular bandpasses V_{IRT} and R_{IRT}, centred on 847.58 and 870.49 nm,

Table 5.3: HD 35296: Activity indices using the Ca II H&K, Hα and Ca II IRT spectral lines.

Index	2007	2008
S-index[1]	0.312 ± 0.007	0.310 ± 0.012
$N_{H\alpha}$	0.310±0.004	0.309±0.003
N_{CaIRT}	0.898±0.025	0.890±0.014

[1]The resulting N_{CaIIHK}-index was converted to match the Mount Wilson S-values (Duncan et al., 1991) using the transformation shown in Equation 5.2.

respectively, were used for the continuum flux in the red and blue sides of the Ca II IRT spectral lines.

Figure 5.6 shows the variation in the Ca II H & K lines, Ca II IRT and Hα spectral lines during 2007 (left panels) and 2008 (right panels) for HD 35296. The epoch for the 2007 data was set to the middle of the observation run whereas the epoch of the 2008 data was set to 104 stellar rotations from the 2007 epoch and was close to the middle of the 2008 observation run. The index was measured for each Stokes I spectra, then combined in sets of four, coinciding with a cycle of 4 sub-exposures as explained in Section 2.5.2. The average of these four indices was determined with the error bar being the minimum and maximum values for that set. The data from 2007 shows limited variation, either due to the reduced coverage or a more stable chromosphere. During the following year, HD 35296 was observed to have a greater modulation of the S-index, CaIRT-index and Hα-index. The average S-index for 2007 was 0.312 ± 0.007 and for 2008 was 0.310 ± 0.012. This is consistent with the average S-index of 0.308 ± 0.07 from the Mount Wilson survey (Duncan et al., 1991). Table 5.3 shows the average S-index, $N_{H\alpha}$ and N_{CaIRT} indices for 2007 and 2008. Each value is the average over the observing run with the error showing the variation during this time, most likely as a result of modulation due to the rotation of the star.

The S-index is independent from the colour of the star. However, there is also a photospheric contribution to the Ca II H & K lines, hence to the S-index. Middelkoop (1982) developed a transformation from the S-index into a value that is indicative of the chromospheric emission by removing the photospheric component. This relationship is

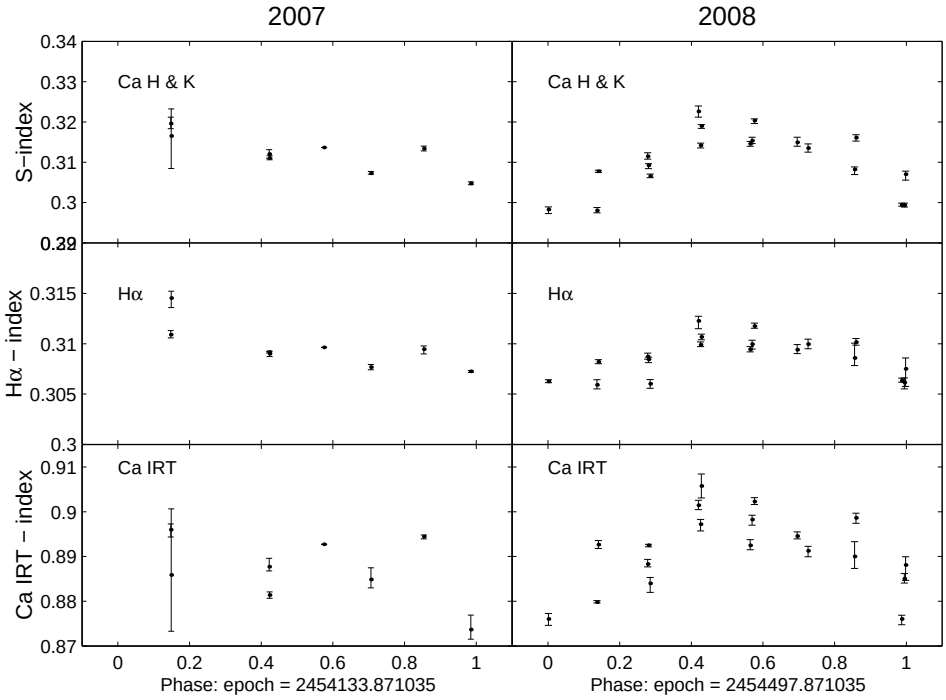

Figure 5.6: The variation in the Ca II H & K lines (upper), Hα (middle) and Ca II IRT (lower) spectral lines during 2007 (left) and 2008 (right) for HD 35296. The data coverage in 2007 was not as complete hence little variation was observed. However, the more dense coverage in 2008 reveals modulation of all three indices. The index was measured for each Stokes I spectra, then combined in sets of four, coinciding with a cycle of 4 sub-exposures as explained in Section 2.5.2. The average of these four indices was determined and the error bar being the minimum and maximum values for that set. The average for each index for 2007 and 2008 are listed in Table 5.3.

shown in Equation 5.5.

$$R_{HK} = 1.34 \times 10^{-4} C_{cf} S. \tag{5.5}$$

where S is the S-index and C_{cf} is the conversion factor, based on the (B-V) colour index of the star, and is shown in Equation 5.6. This conversion factor, listed in Equation 5.6 was the result of the improvements made by Rutten (1984) to that developed by Middelkoop (1982) by extending the range of main-sequence stars to $0.3 \leq$ B-V ≤ 1.7.

$$\log C_{cf} = 0.25(B-V)^3 - 1.33(B-V)^2 + 0.43(B-V) + 0.24 \tag{5.6}$$

Noyes et al. (1984) developed a further correction factor to remove the photospheric contribution to the flux in the Ca II line cores, as shown in Equation 5.7.

$$R_{phot} = -4.898 + 1.918(B-V)^2 - 2.893(B-V)^3 \tag{5.7}$$

in the colour range $0.44 \leq$ B-V ≤ 0.82, to make the final correction factor, $R^{'}_{HK}$, as shown in Equation 5.8.

$$R'_{HK} = R_{HK} - R_{phot} \tag{5.8}$$

Using the transformation values from Rutten (1984) and the equations listed above, $Log(R'_{HK})$ was determined as -4.39 $\pm$ 0.02. This was an average value of the $Log(R'_{HK})$ over the 2008 observing run with the error based on the minimum and maximum values.

Noyes et al. (1984) found that there was a correlation between the Rossby number, (Ro), and $Log(R'_{HK})$. The Rossby number is the ratio of the inertial to Coriolis forces in fluid flow. In stellar systems, the Rossby number describes how strongly the Coriolis force is capable of effective convective eddies (Donati and Landstreet, 2009). It is defined as the ratio of the observed rotation period, P_{obs} to the convective turnover time, τ_c, as shown in Equation 5.9.

$$R_o = \frac{P_{obs}}{\tau_c} \tag{5.9}$$

The convective turnover time is based on the ratio of mixing length to scale height. Noyes et al. (1984) suggested that the Rossby number is a "major determinant of surface

magnetic activity in lower main sequence stars". Wright et al. (2011) developed an empirical formula to determine the convective turnover time, and is valid for a range of masses $0.09 \leq M/M_{\odot} \leq 1.36$.

$$log\tau_c = 1.16 - 1.49log\frac{M}{M_{\odot}} - 0.54log^2\frac{M}{M_{\odot}} \tag{5.10}$$

The convective turnover time for HD 35296 was estimated to be 9.1 d, with a Rossby number of 0.38. These values are used when comparing the differential rotation of HD 35296 with two further sun-like stars HD 29613 (Chapter 6) and EK Draconis (Chapter 7).

5.5 Discussion

From the results presented in this chapter, HD 35296 is a young sun-like star whose moderately rapid rotation has led to very complex surface magnetic fields. Figure 5.1 shows the maps from 2007 and in 2008. The azimuthal magnetic field is predominately positive in 2008 when compared with that observed in 2007. This may be an artefact of the reduced number of profiles used in 2007. Reducing the number of profiles in the 2008 dataset, to match the same number, and phase, of the observed profiles obtained in 2007, it was observed that the global mean magnetic field strength was reduced slightly to 11.2 G but remained strongly positive azimuthal magnetic field. This is shown in Figure 5.7 where the 2007 data (left column) is compared with the data taken in 2008 using the reduced number of profiles (middle column). In order to make a full comparison of the maps, those that were generated using the full amount of data have been included in that figure (right column). Hence one may conclude that the azimuthal magnetic field has changed from 2007 to 2008 with a reduction in the magnitude of the radial field during the same time frame.

The magnetic field on HD 35296 was predominately poloidal in 2007, with $\sim$82$\pm$4% of the total magnetic energy. The $\pm$4% is the "variation bar", as described in Section 3.5.2, and was derived by systematically modifying a number of parameters, as explained in Section 5.4.4. Even with the sparse phase coverage, HD 35296 remained strongly poloidal when varying the range of parameters. By 2008, the field had reorganised itself to a $\sim$50% Poloidal-Toroidal configuration. In 2007, both the poloidal and toroidal components have the majority of their magnetic energy spread across the higher order

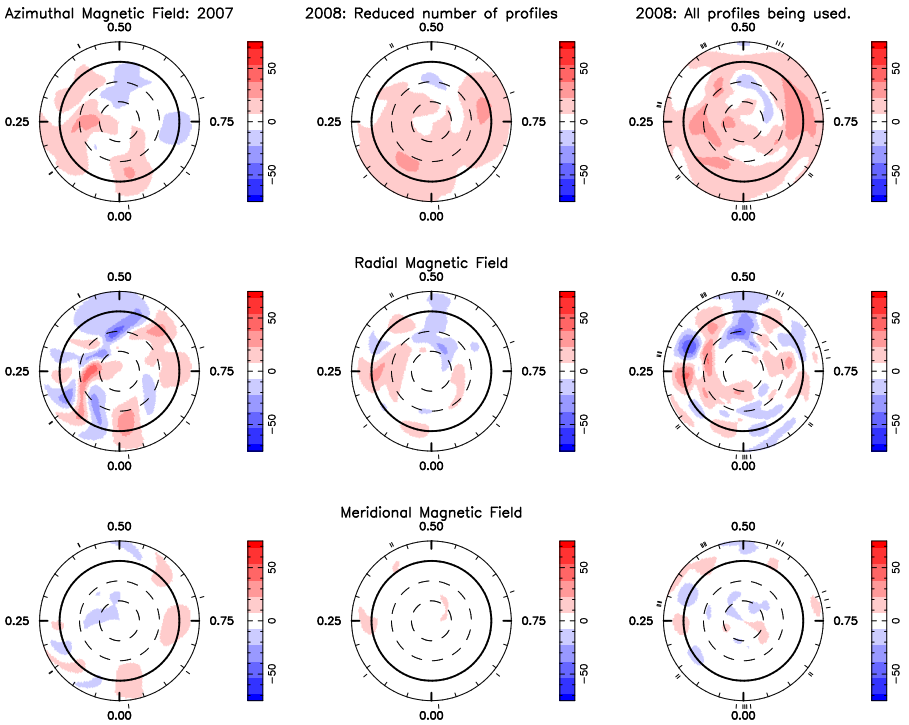

Figure 5.7: Magnetic imaging of the large-scale field for HD 35296 in both 2007 (left series), 2008 but using reduced number of profiles to match the 2007 dataset (middle series) and 2008 observing seasons, using the full set of data. Each map has differential rotation, as measured using the 2008 Stokes V data, incorporated into the modelling strategy. The 2007 data has a global magnetic field strength of 13.2 G. The 2008 data, using the reduced number of profiles, has a global magnetic field strength value of 11.2 G whereas the 2008 data was 15.8 G. These maps are polar projections extending down to -30^o. The bold lines denote the equator and the dashed lines are +30^o and +60^o latitude parallels. The radial ticks indicate the phases at which this star was observed.

terms ($\ell \geq 4$), although in 2008, the toroidal field could be described as a simple dipole field ($\ell = 1$ mode) enclosing ∼60% of the magnetic energy of that toroidal energy. This is shown in Table 5.4 and in Figure 5.1. There are two possible reasons for this "reorganisation" of the field from 2007 to 2008. One is that the reduced number of profiles used in the 2007 data may be responsible for this variation. Alternatively, the magnetic topologies had significantly changed. When reducing the number of profiles in the 2008 dataset, to match the same number of profiles obtained in 2007, it was observed that the global mean magnetic field strength was reduced slightly. Hence it may be concluded that the variation in the mean field strength, 13.2 G in 2007 to 15.8 G in 2008, is more likely an artifact of the reduced number of profiles used rather than any significant and intrinsic physical change in the mean stellar magnetic field strength. However, when using the reduced number of profiles in the 2008 data, the balance of the poloidal-toroidal field configuration remained similar, ∼ 50-50%, when compared with the balance using all of the profiles. The symmetry of the poloidal and toroidal fields also remain similar with the poloidal field being strongly non-axisymetric while the toroidal field remains strongly axisymetric. This is shown in Table 5.4 that gives a full listing of the various components for this star. Figure 5.5 shows an apparent reversal of polarity in the radial magnetic field at higher latitudes? How reliable is that conclusion? Figure 5.8 shows the same plot as seen in Figure 5.5 except this figure includes the latitudinal distribution for the 2008 data with the reduced number of profiles, as explained above. This clearly shows that the toroidal field is recovered when using a reduced number of profiles. However, the radial and poloidal fields do have some differences. The reduced number of profiles in 2007 has had an impact on the latitude distribution of the radial and meridional fields, meaning that any apparent reversal at higher latitudes from 2007 to 2008 must be treated with caution. In summary, this work demonstrates the evolving nature of the magnetic topology as it has substantially changed its orientation during the course of one year from one of being strongly poloidal to a more balanced configuration.

Petit et al. (2008) infer that a rotation period lower than ∼12 d is necessary for the toroidal magnetic energy to dominate over the poloidal component. HD 35296 is a moderately rapidly rotating star that appears to have a large azimuthal component. These results are consistent with observations of other rapidly rotating stars exhibit-

Table 5.4: Magnetic quantities derived from the set of magnetic maps for HD 35296. Both the poloidal and toroidal components are listed along with the relative weightings in each geometry.

B_{mean} (G)	geometry	Ener[1] (%)	dipole[2] (%)	quad.[2] (%)	oct.[2] (%)	higher[2] order. (%)	axi.[1] (%)	axi.[2] (%)
2007 data								
13.2	poloidal	82±4	19±5	5±1	15±3	61±4	7±4	8±9
	toroidal	18±4	36±7	12±4	5±3	48±8	13±3	73±7
2008 data								
15.8	poloidal	52±6	8±2	13±1	7±4	72±4	10±5	19±7
	toroidal	48±6	61±5	7±5	4±3	28±6	40±4	82±4
2008 data with reduced number of profiles to match the 2007 dataset								
11.2	poloidal	43±3	26±5	20±7	13±6	42±9	5±4	12±10
	toroidal	57±3	73±7	14±6	3±2	9±2	54±3	93±2

[1] % of the total magnetic energy available. [2] % of the respective poloidal or toroidal field geometry. Listed also is the fraction of the poloidal or toroidal magnetic energy in the dipolar ($\ell = 1$), quadrupolar ($\ell = 2$), octupolar ($\ell = 3$) and [3] higher order multipole ($\ell \geq 4$) components as well as the fraction of energy of each component stored in the axisymmetric component ($m < \ell/2$) and the fraction of the total energy stored in each component ($m = 0$).

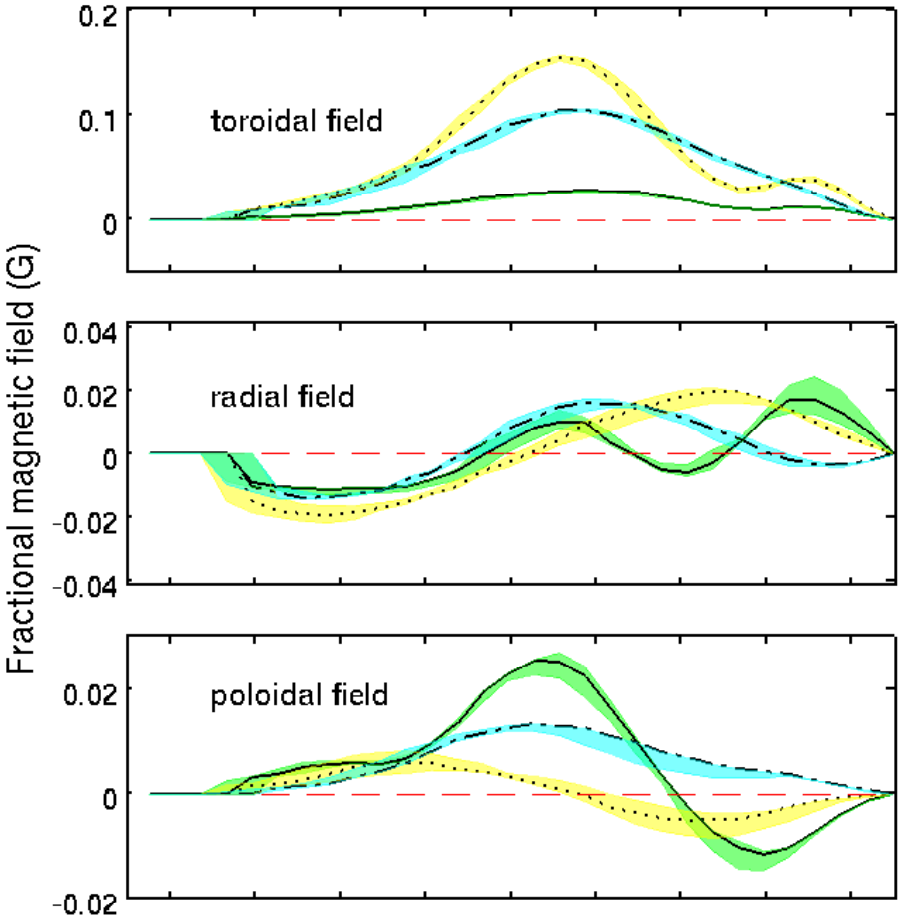

Figure 5.8: Variation of the respective magnetic field orientations for HD 35296 for 2007 and 2008 as a function of stellar latitude, including using reduced number of profiles with the 2008 data. The top panel is the toroidal field, the middle panel is that of the radial field while the lower panel shows the poloidal field. The shaded regions show the variation in the strength at each latitude point as determined by varying parameters: $v \sin i$ (± 0.5 km s^{-1}) and inclination angle ($\pm 5^o$). The dotted line with the yellow shading is for 2008 data, the dot-dash line with cyan shading is for the 2008 data using the same number of profiles (at approximately the same phase) as the 2007 data while the solid line with the green shading is the 2007 data. This is based on the value of the magnetic field strength at each latitude, as defined by Equation 5.1.

ing similarly strong azimuthal magnetic fields such as AB Doradus (SpType = K0V[1]), LQ Hydrae (SpType = K0V[2]) and HR 1099 (SpType = K2:Vnk[3]) (Donati et al., 2003b), HD 171488 (SpType = G2V[1]) (Jeffers and Donati, 2008; Marsden et al., 2006), HD 141943 (SpType = G2[4]) (Marsden et al., 2011a) and HD 106506 (SpType = G1V[3]) (Chapter 3). These strong azimuthal magnetic fields may be connected to the toroidal component of the large-scale dynamo field, and by analogy with dynamo models developed for the Sun (Petit et al., 2004a). In the Sun, the toroidal field is thought to be confined to the interface between the radiative core and the convective zone. However, observations of these strong surface azimuthal magnetic fields on these (and other) active solar-type stars have been interpreted by Donati et al. (2003b) as the underlying dynamo processes being distributed throughout the entire convective zone. In summary, the observations of significant toroidal fields in HD 35296 could indicate that the dynamo is operating very close to the surface of the star, or even throughout the whole convective zone.

HD 35296 is a moderately active star. During 2007, the chromosphere was relatively stable but in 2008 the chromosphere was more variable and showed modulation as a result of the rotation of the star. There was enhanced activity at phase ~ 0.5, as shown in Figure 5.6. When matching this to the 2008 magnetic maps in Figure 5.1 there appears to be an area where the radial field is negative in a predominately positive field. One can speculate that this negative field at phase ~ 0.5 is inducing the enhanced activity occurring in the low- to mid-levels in the chromosphere.

5.6 Conclusions

HD 35296 is a moderately rapidly rotating star that exhibits moderate levels of chromospheric activity, magnetic field structures and surface differential rotation that is similar to the more massive stars HD 106506 and HD 76298. This variation in the chromospheric activity, with rotational phase, was based on modulation of the Ca II H & K, Ca II Infrared Triplet and Hα spectral lines. Using the magnetic signatures, HD 35296 has an equatorial rotational velocity, Ω_{eq} of 1.80 ± 0.01 rad d^{-1} with rotational shear,

[1] Torres et al. (2006)
[2] Montes et al. (2001)
[3] Gray et al. (2006)
[4] Torres et al. (2006)

$\delta\Omega$ of 0.28 ± 0.08 rad d^{-1}. This translates to a *laptime* of $\approx 22^{+9}_{-5}$ d, significantly faster than that observed on the Sun. Even thought this star is a more moderately rotating star, it can be concluded that the dynamo operating on HD 35296 is similar to that of other active, rapidly rotating stars and is most likely a distributed dynamo operating throughout the convective zone. This work demonstrates the evolving nature of the magnetic topology HD 35296.

Chapter 6

Magnetic Fields on Young, Moderately Rotating Sun-like stars: HD 29615

6.1 Introduction

HD 29615 (HIP 21632) is a rapidly rotating, sun-like star in the constellation of Eridanus. It has a Right Ascension $04^h38^m43.94188^s$ and Declination $^-27^o02'01.8056''$ (J2000.0 van Leeuwen, 2007). Apart from this thesis, ZDI has been achieved on a small sample of single, early G-type stars such as HD 171488 (V889 Her, SpType = G2V[1]) (Marsden et al., 2006; Jeffers and Donati, 2008; Jeffers et al., 2011) and HD 141943 (SpType = G2[2]) (Marsden et al., 2011a,b). All of these stars, including those in this thesis, show significant levels of differential rotation using brightness (where possible) and magnetic features. Jeffers and Donati (2008) observed HD 171488 and measured $\Omega_{eq} = 4.93 \pm 0.05$ rad d^{-1} and $\delta\Omega = 0.52 \pm 0.04$ rad d^{-1} using spot features while $\Omega_{eq} = 4.85 \pm 0.05$ rad d^{-1} and $\delta\Omega = 0.47 \pm 0.04$ rad d^{-1} using magnetic features. These levels of differential rotation are similar to an earlier study by Marsden et al. (2006) of $\Omega_{eq} = 4.789 \pm 0.013$ rad d^{-1} and $\delta\Omega = 0.402 \pm 0.044$ rad d^{-1} (using spot features). Marsden et al. (2011b) observed HD 141943 and found $\Omega_{eq} = 2.86 \pm 0.02$ rad d^{-1} and $\delta\Omega = 0.24 \pm 0.03$ rad d^{-1} using spot features while $\Omega_{eq} = 4.89 \pm 0.05$ rad d^{-1} and $\delta\Omega$

[1] Montes et al. (2001)
[2] Torres et al. (2006)

$= 0.45 \pm 0.08$ rad d^{-1} on their 2010 data set (and slightly lower with $\delta\Omega = 0.36 \pm 0.09$ rad d^{-1} for their 2007 data). All these solar-type stars also exhibit complex magnetic topologies.

The aim of this investigation is to map the surface of HD 29615 (HIP 21632) with a view to measuring the rotational shear on its surface and to measure and to map the magnetic field structure on the surface of this star and to compare to the above rapidly rotating stars and also to the moderately rotating stars HD 35296 (SpType = F8V[1], Period = 3.5 d) in Chapter 5 and EK Draconis (SpType = G1.5V[1], Period = 2.5 d) in Chapter 7.

6.2 Fundamental Parameters of HD 29615

HD 29615 is a G3V star (Torres et al., 2006). The *HIPPARCOS* space mission measured a parallax of 18.27 ± 1.02 mas (van Leeuwen, 2007), giving a distance of $54.7^{+3.2}_{-2.9}$ pc or 178^{+11}_{-9} ly. Waite et al. (2011a) used the bolometric corrections of Bessell et al. (1998) and the formulations within that appendix to estimate the radius of HD 29615 to be 0.96 ± 0.04 R$_\odot$ and the luminosity to be $0.93^{+0.12}_{-0.11}$ $L_\odot$, while Allende Prieto and Lambert (1999) estimated 1.0 $R_\odot$. Zuckerman and Song (2004) proposed that HD 29615 was a member of the Tucana/Horologium Association indicating an age of ∼30 Myr. The youthful nature of HD 29615 was confirmed by Waite et al. (2011a) citing an enhanced Li I 670.78 nm with an equivalent width of 190 ± 2 mÅ. Waite et al. (2011a) also observed a magnetic field on this star, along with a varying emission equivalent width for the Hα line in the range from ∼ 370 mÅ to ∼ 500 mÅ demonstrating the presence of a very active, and variable, chromosphere.

The photospheric temperature, 5820 K, was estimated using the (V-I) colour index and Equation 2.2 while the temperature of the spots, 3920 K, was estimated from the relationship developed by Berdyugina (2005) based on a star's spectral type (see Figure 7, page 27 of that work). The radius of the star was determined using the relationship in Equation 6.1.

$$2\frac{LogR}{LogR_\odot} = \frac{M_{bol} - 4.74}{-2.5} - 4\frac{T_{eff\star}}{T_{eff\odot}} \tag{6.1}$$

[1] Montes et al. (2001)

where $R_{\odot}$ is the stellar radius, $T_{eff\star}$ is the effective temperature of the star while $T_{eff\odot}$ is the Sun's effective temperature, as listed in Table 1.1. M_{bol} is the absolute bolometric magnitude and was determined using the bolometric corrections of Bessell et al. (1998). An estimate of the radius is required to determine the inclination angle which was found using:

$$sini = \frac{P \cdot vsini}{2\pi R_{\star}} \tag{6.2}$$

where P is the rotational period, $v\sin i$ is the projected rotational velocity and $R_{\star}$ is the radius of the star. The inclination angle was calculated to be 70 ± 5^{o}.

6.3 Observations and Analysis

HD 29615 was observed at the Anglo-Australian Telescope (AAT) in November/December, 2009. A journal of observations is shown in Table 6.1. There was no simultaneous photometry undertaken on this star, unlike HD 106506.

6.3.1 High Resolution Spectropolarimetric Observations from the AAT

High resolution spectropolarimetric data were again obtained from the AAT using the UCLES/SEMPOL combination (Semel, 1989; Semel et al., 1993; Donati et al., 2003b). The setup of this combination was identical (as close as possible) to that described in Section 3.3.2. For this run, the dispersion of ∼0.004958 nm at order # 129 was measured, again giving a resolution of approximately 71000. The mean pixel resolution for this AAT spectra was determined to be 1.689 $\mathrm{km\,s^{-1}pixel^{-1}}$, and the central wavelength was 522.002 nm with full wavelength coverage from 437.71 nm to 681.56 nm. These values are identical to those obtained in 2007 for HD 106506 (see Chapter 3).

6.3.2 Spectropolarimetric Analysis

An identical approach to the reduction of the HD 106506 data, as explained in Section 3.3.3, was completed using ESpRIT (Donati et al., 1997, 2003b). Again, a G2 line mask, created from the Kurucz atomic database and ATLAS9 atmospheric models (Kurucz, 1993), was used during the LSD process. The modelling strategy tends to "favour" an inclination angle of $\sim 60^{o}$. When the inclination angle is determined using the modelling strategy, such as that used in Chapters 3 and 4, it is checked against calculations that

Table 6.1: The Journal of spectropolarimetric observations of HD 29615 using the AAT.

UT Date	UT middle	Exp. Time[1] (sec)	Stokes V Mean S/N[2]	FAP[3]	Detection?
2009 Nov 25	11: 3:28	4×700	5567	0.000	Definite
2009 Nov 25	14:37:12	4×700	6337	0.000	Definite
2009 Nov 25	16:29:33	4×700	4908	0.000	Definite
2009 Nov 27	10:23:36	4×700	6171	0.000	Definite
2009 Nov 27	13:28: 5	4×700	6978	2.182×10^{-12}	Definite
2009 Nov 27	16:28: 2	4×700	5610	1.195×10^{-10}	Definite
2009 Nov 28	10:10:47	4×700	3821	3.997×10^{-15}	Definite
2009 Nov 28	13:13: 8	4×700	5971	2.853×10^{-14}	Definite
2009 Nov 28	16:15:29	4×700	4280	3.343×10^{-11}	Definite
2009 Nov 29	10: 8:37	400 + 3×700	5785	2.340×10^{-01}	No detection
2009 Nov 29	13:23: 8	4×700	4604	4.315×10^{-11}	Definite
2009 Nov 29	16:23:23	4×700	3493	1.373×10^{-01}	No detection
2009 Nov 30	11: 5:48	4×700	3283	5.480×10^{-06}	Definite
2009 Nov 30	16:18:40	4×700	3713	1.421×10^{-14}	Definite
2009 Dec 1	11: 2:55	4×700	6353	0.000	Definite
2009 Dec 1	14:13:39	4×700	4961	9.615×10^{-13}	Definite
2009 Dec 2	10:36:24	4×700	6158	2.988×10^{-07}	Definite
2009 Dec 2	13: 4: 1	4×700	6176	0.000	Definite
2009 Dec 2	16: 3:39	4×700	4651	2.314×10^{-13}	Definite
2009 Dec 3	10:27:35	4×700	4228	4.638×10^{-08}	Definite
2009 Dec 3	13:33:32	4×700	6312	0.000	Definite

[1] Each sequence of 4 × 700 = 2800 seconds exposures (for example). After each exposure, the "rotating half-wave retarder" of the polarimeter is rotated between $+45^o$ and -45^o so as to remove instrumental polarization signals from the telescope and the polarimeter.

[2] Signal-to-noise (S/N) of the resulting Stokes V profile.

[3] FAP: False Alarm Probability. See Section 3.3.2 for more details.

are based on parameters such as colour, distance etc. Where it is very different, as in this case, it was decided to go with the calculated value rather than the modelled value. Section 6.4.1 briefly revisits this assumption.

6.4 Observations and Analysis

6.4.1 Image reconstruction: Stokes I Doppler imaging

As done in previous chapters, *ZDICAM* was used to produce brightness maps using the Stokes I data. The full set of parameters that gave the minimum χ^2 value are shown in Table 6.2 and were adopted when producing the final Doppler imaging map as shown in the top right panel of Figure 6.1, with the associated fits between the model and the actual profiles being shown in Figure 6.2. This brightness map does have differential rotation incorporated into the imaging process, which is explained in more detail in Section 2.6. Even if one uses an inclination angle of 60^o, the maps are still very similar and so were the differential rotation parameters.

6.4.2 Zeeman Doppler imaging: magnetic features on the surface of HD 29615

The magnetic topology was determined for HD 29615 using ZDI. The Stokes V data was used to reconstruct radial, azimuthal and meridional fields. Again, the modelling strategy of Donati and Brown (1997) was used to construct the magnetic field topology on HD 29615 using the spherical harmonic expansion $\ell_{max} = 30$. Figure 6.1 shows the magnetic maps generated for HD 29615. The associated fits between the modelled data and the actual profiles are shown in Figure 6.3. The full set of parameters used to produce these maps, including differential rotation, are listed in Table 6.2.

Figure 6.4 shows the fractional magnetic field strength as a function of latitude for each orientation for HD 29615 and is based on Equation 5.1. In order to determine the robustness of each measurement, a range of parameters were varied within the error estimate so as to place limits on the fractional magnetic field at each latitude for each of the orientations. These parameters include the rotational period, $v\sin i$, inclination angle, v_{rad}, Ω_{eq} and $\delta\Omega$. These measured variations are shown by the shaded regions while the values for the optimum parameter set are shown as the solid line.

Table 6.2: The parameters used to produce the maximum-entropy image reconstructions of HD 29615, including those associated with surface differential rotation.

Parameter	HD 29615
Spectral Type[1]	G3V
Equatorial Period	2.34±0.2 d[2]
Inclination Angle	70 ± 5^{o}
Projected Rotational Velocity, $v\sin i$	19.5±0.3 km s^{-1}
Photospheric Temperature, T_{phot}	5820 K
Spot Temperature, T_{spot}	3920 K
Radial Velocity, v_{rad}	19.3±0.1 km s^{-1}
Stellar radius [3]	1.0 $R_{\odot}$
Convection zone depth[4]	0.252±0.011 $R_{\star}$
	$0.254^{+0.027}_{-0.007}$ $R_{\odot}$
Age [5]	20-30 Myr
Stellar mass [3]	0.95 $M_{\odot}$
Stokes I: Ω_{eq}	$2.67^{+0.09}_{-0.01}$
Stokes I: $\delta\Omega$	$0.09^{+0.04}_{-0.02}$
Stokes V: Ω_{eq}	$2.75^{+0.07}_{-0.04}$
Stokes V: $\delta\Omega$	$0.58^{+0.14}_{-0.12}$
Epoch used (HJD)	2455165.0110599

[1] Torres et al. (2006)

[2] Using Stokes I data

[3] Allende Prieto and Lambert (1999)

[4] based on Equations 5.9 and 5.10. See Section 5.4.5 in Chapter 5 for more details

[5] Zuckerman and Song (2004)

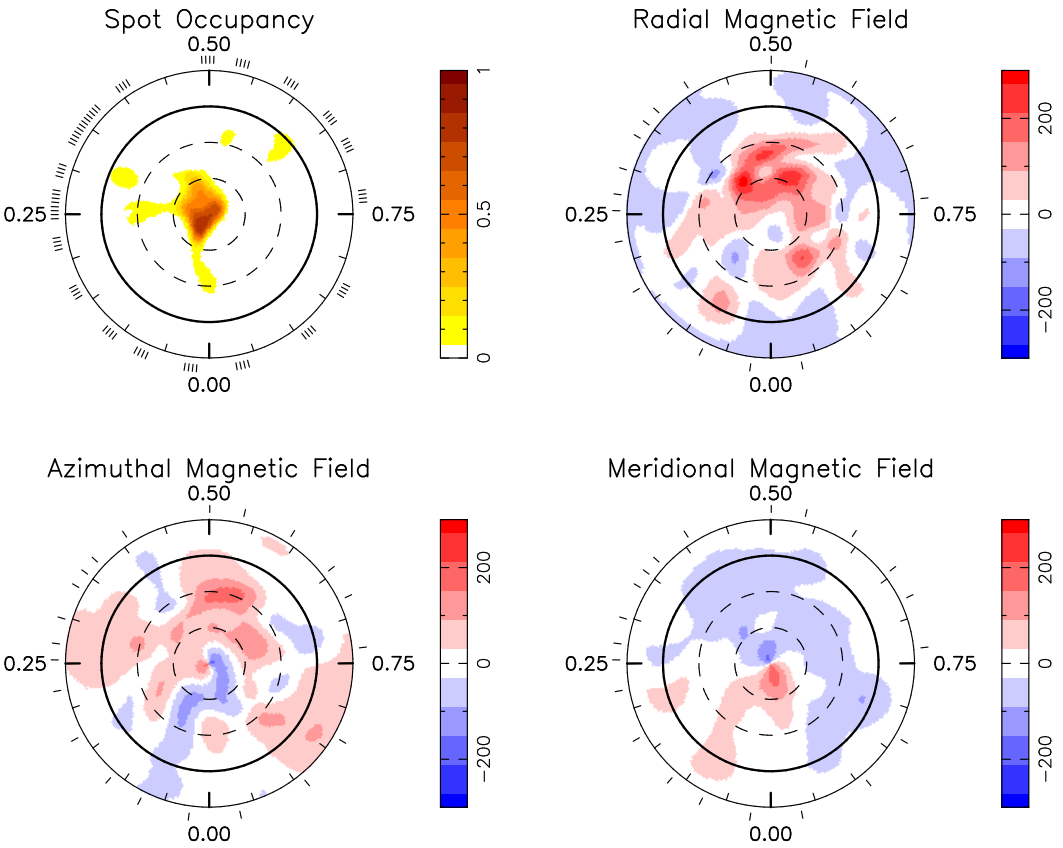

Figure 6.1: The maximum-entropy brightness and magnetic image reconstructions for HD 29615. These maps are polar projections extending down to -30^o. The bold lines denote the equator and the dashed lines are +30^o and +60^o latitude parallels. The radial ticks indicate the phases at which this star was observed. Differential rotation, as measured using the Stokes I and V profiles respectively, has been incorporated into the analysis of the maps. The brightness data has a spot coverage of 2.4% while the Stokes V has a global magnetic field strength 72 G.

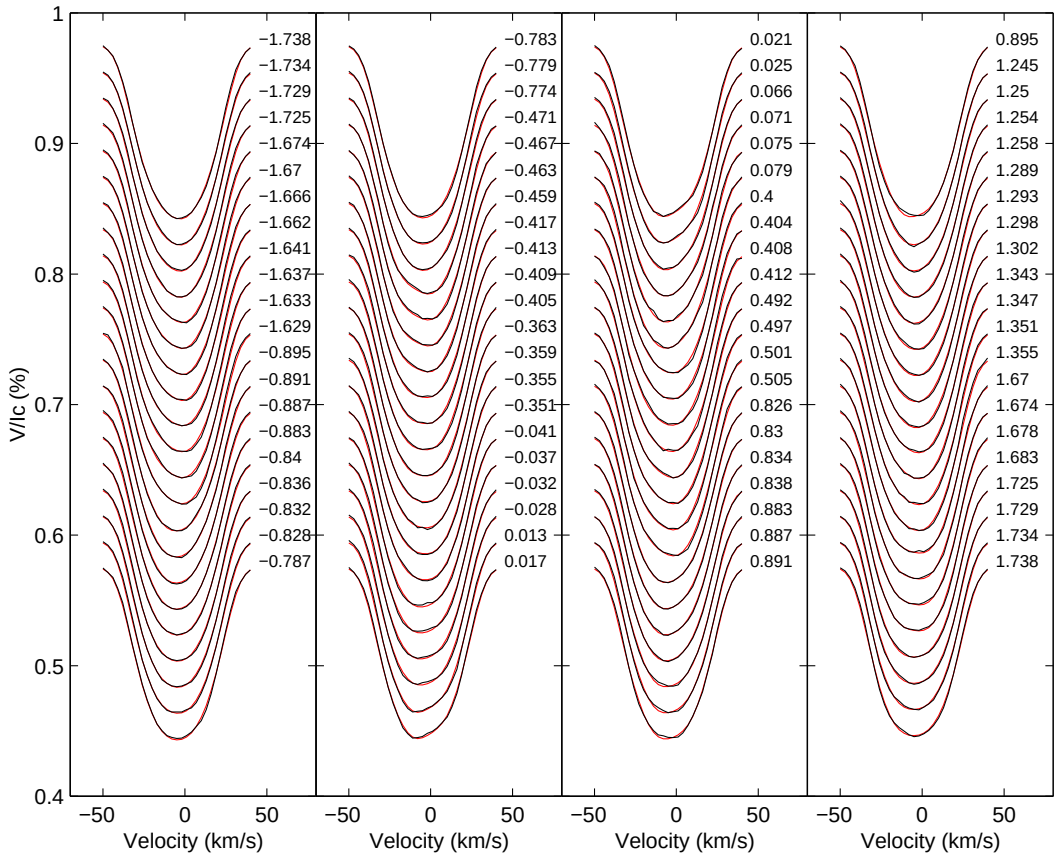

Figure 6.2: The maximum-entropy fits to the Stokes I LSD profiles for HD 29615 with surface differential rotation incorporated into the analysis. The red lines represent the modelled lines produced by the Doppler imaging process whereas the black lines represent the actual observed LSD profiles. Each successive profile has been shifted down by 0.020 for graphical purposes. The rotational phases at which the observations took place are indicated to the right of each profile.

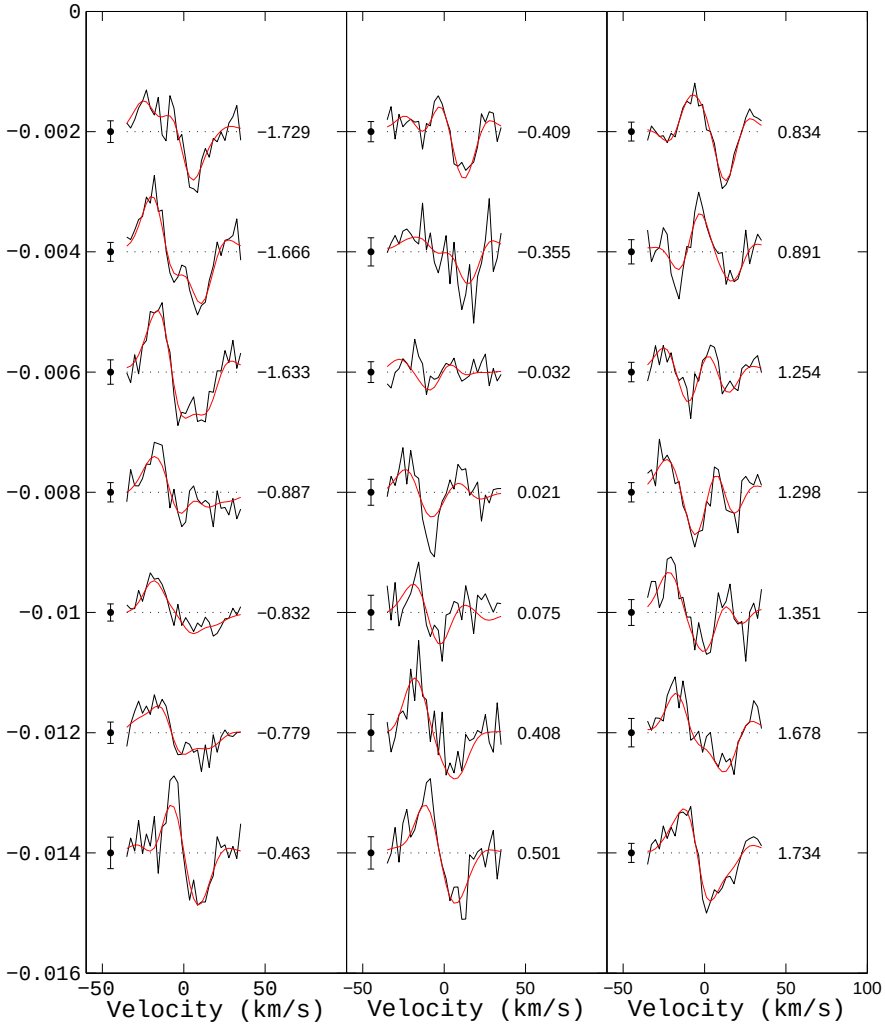

Figure 6.3: The maximum-entropy fits to the Stokes V LSD profiles for HD 29615 with surface differential rotation incorporated into the analysis. The black lines represent the observed Zeeman signatures, while the red (thin) line represent the modelled lines. Each successive profile has been shifted down by 0.002 for graphical purposes. The rotational phases at which the observations took place are indicated to the right of each profile. The error bars to the left of each profile are $\pm$ 0.5 σ.

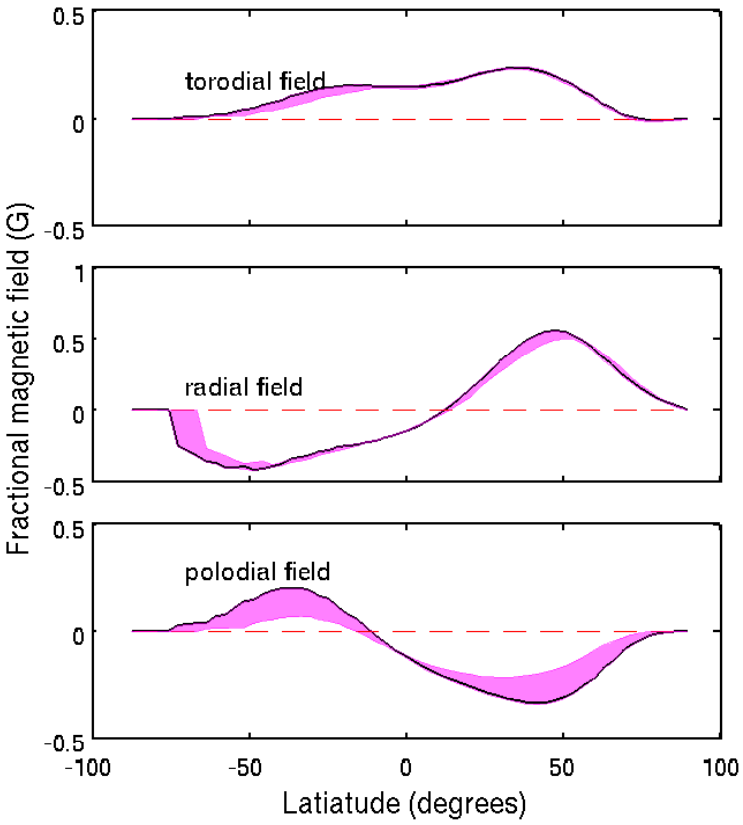

Figure 6.4: Variation of the respective magnetic orientations for HD 29615 as a function of stellar latitude. The shaded regions show the variation in the strength at each latitude point as determined by the error in the measurement of the rotational period, $v\sin i$, inclination angle, v_{rad}, Ω_{eq} and $\delta\Omega$. This is based on the value of the magnetic field strength at each latitude, as defined by Equation 5.1.

6.4.3 Differential rotation using Stokes I and V

The differential rotation of HD 29615, using both Stokes I and Stokes V, were measured using the χ^2-minimisation technique using Equation 2.15, described in Section 2.6. Using the brightness (spot) features observed, HD 29615 has an equatorial rotational velocity, Ω_{eq} of $2.67^{+0.09}_{-0.01}$ rad d^{-1} with rotational shear, $\delta\Omega$ of $0.09^{+0.04}_{-0.02}$ rad d^{-1}. However, using the magnetic features observed, HD 29615 has an equatorial rotational velocity, Ω_{eq} of $2.75^{+0.07}_{-0.04}$ rad d^{-1} with rotational shear, $\delta\Omega$ of $0.58^{+0.14}_{-0.1}$ rad d^{-1}.
The error estimation for the differential rotation measurements was done by individually varying stellar parameters such as inclination, $v \sin i$, spot occupancy (for Stokes I) and global magnetic field (for Stokes V) across a physically reasonable range. To determine the magnitude of this variation, the result of each individual differential rotation value, including the error in the paraboloid fit, was graphed onto the $\Omega_{\rm eq}$ and $\delta\Omega$ parameter space. The final ellipse was generated to encompass all the differential rotation values. Figure 6.5 demonstrates how this error estimate was made using the Stokes V data. The error bars on each individual measurement represents the 1-σ errors in each paraboloid fit. The actual data used to find the error ellipse for the Stokes I and V are listed in Section C.5 in Appendix C. Figure 6.6 shows the χ^2 landscape with the error-ellipse superimposed on that landscape.

6.4.4 Chromospheric activity: Emission Component $H\alpha$ line

Chromospheric activity was deduced using the Hα spectral line. Figure 6.7 shows how the emission component varied during the rotation of HD 29615. The EEW was measured for each spectrum, then combined in sets of four, coinciding with a cycle of 4 sub-exposures as explained in Section 2.5.2. The average of these four EEW's was determined and the error bar being the minimum and maximum values for that set. This supports the variable nature of the mid-level chromosphere, first observed by Waite et al. (2011a). The maximum chromospheric activity for HD 76298 was measured to be log $R'_{H\alpha} = {}^{-}4.36 \pm 0.01$ in 2009. This was measured using the same procedure as explained in Section 3.4.3. Further activity indices's, such as the Ca II H & K and Ca II Infrared Triplet (IRT) were not considered as the AAT data does not extend into these wavelength regions.

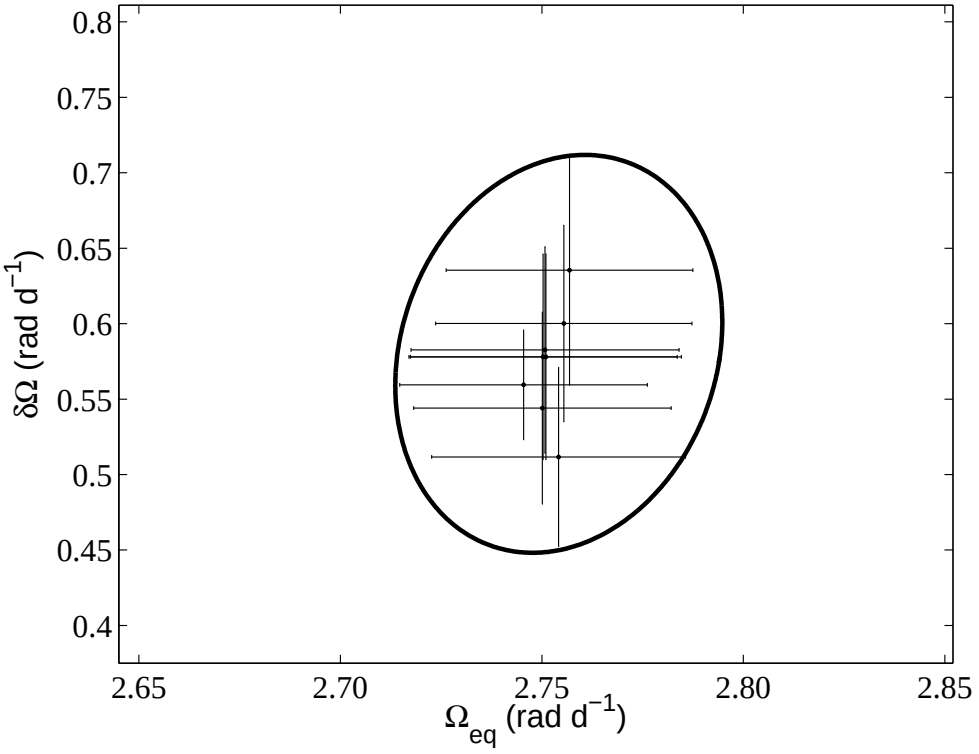

Figure 6.5: The determination of the overall error estimate for differential rotation of HD 29615 using the Stokes V data. Each data point is the result of paraboloid fit of the reduced-χ^2 landscape for each individual differential rotation value, given a specific change in a particular parameter such as inclination, $v\sin i$ and global magnetic field across a physically reasonable range. The error bar on each data point being 1-σ errors in the paraboloid fit.

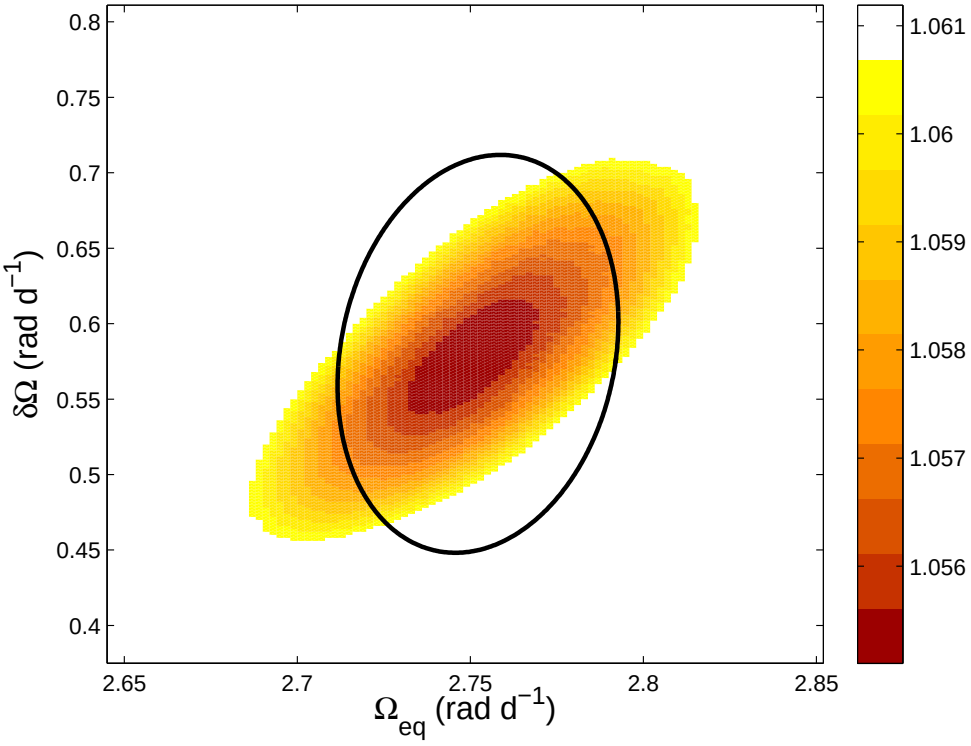

Figure 6.6: Determining the differential rotation, using χ^2 minimisation technique, based on the Stokes V data for HD 29615. This is a 2-σ projection using the optimum set of parameters, as listed in Table 6.2. Superimposed on this grid is the error ellipse (thick line) that encompasses a range of Ω_{eq} - $\delta\Omega$ pairs found by varying such parameters as $v\sin i$, magnetic field strength and inclination. How this ellipse was generated is shown in Figure 6.5.

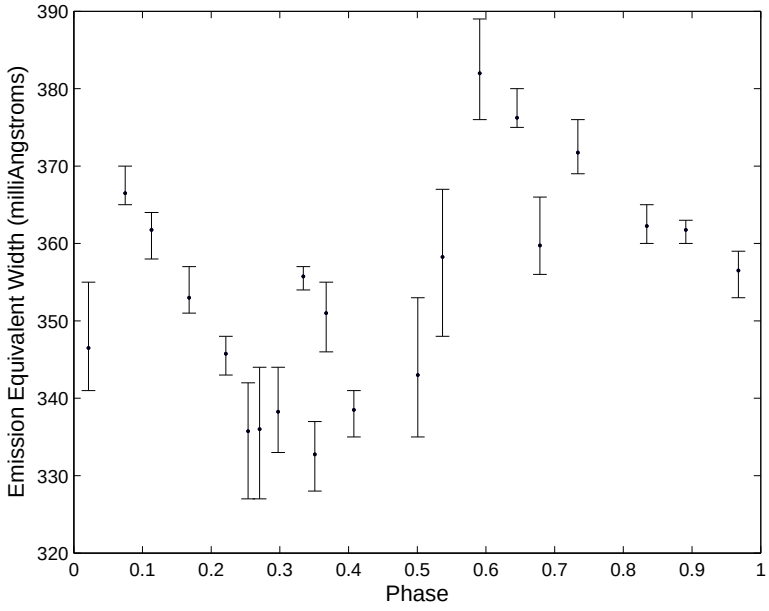

Figure 6.7: The variation in the chromospheric activity versus phase for HD 29615. The chromospheric indicator was the emission component of the Hα line. The EEW was measured for each spectra, then combined in sets of four, coinciding with a cycle of 4 sub-exposures as explained in Section 2.5.2. The average of these four EEW's was determined and the error bar represent the minimum and maximum values for that set.

6.5 Discussion

From the results presented in this chapter it is evidence that HD 29615 is a young, Sun-like star whose moderately rapid rotation has led to very complex surface topology. The brightness map, in Figure 6.1 (top left panel), shows a predominate polar spot extending down to latitude $\sim 60^o$ from phase, ϕ, 0.0 to 0.5 yet were restricted to much higher latitudes for $\phi = 0.5$ to 1.0. This could be due to the 20% more phase coverage and in particular, at $\phi = 0.25$ and $\phi = 0.35$ where there were multiple epochs (two separate nights for the same phase). This will have improved the quality of the mapping process at these points on the star. There is also evidence of spot evolution with several "misfits" between the modelled and observed data, as shown in Figure 6.2. For example, at rotational phase, ϕ, -0.041 to -0.028 and again at 0.670 to 0.680, *ZDICAM* could not recover the additional feature observed in the line profile. This could be the result of a relatively high inclination angle or simply spot evolution. Like other stars investigated in this thesis, HD 29615 demonstrates the variable nature of these young solar-type stars.

Whereas the polar spot is very prominent, there appears limited spot coverage at mid- to lower-latitudes, unlike other solar type stars like HD 106506 (Chapter 3) and HD 76298 (Chapter 4). The spot filling factor (the level of spot coverage over the entire stellar surface) is 2.4%. One explanation is that the relatively high inclination angle precluded the extraction of lower latitude features from being adequately mapped in these brightness maps. The magnetic maps, in Figure 6.1, show azimuthal, meridional and radial magnetic field structures. The azimuthal magnetic field is strongly positive although not a complete ring of field, unlike that observed on HD 106506. The radial field is also strongly positive at the higher latitudes, from approximately $+30^o$ to the pole. Again this in unlike other stars observed in this thesis that appear to have a mixed polarity across the surface. HD 29615 was observed to be strongly poloidal with $77 \pm 3\%$ of the magnetic energy being held in this configuration. Of this, almost 35% of the poloidal component is dipolar ($\ell = 1$) with remaining energy spread across the other modes ($\ell = \geq 2$). Table 6.3 gives a full listing of the various components for this star. Like HD 35296, HD 29615 appears to have a large azimuthal component which Donati et al. (2003b) interpreted as the underlying dynamo processes are capable of

Table 6.3: Magnetic quantities derived from the set of magnetic maps for HD 29615. Both the poloidal and toroidal components are listed along with the relative weightings in each geometry.

B_{mean} (G)	geometry	Ener[1] (% tot)	dipole[2] (%)	quad.[2] (%)	oct.[2] (%)	higher[2,3] order(%)	axi.[1] (%)	axi.[2] (%)
72	poloidal	73±4	35±16	11±8	12±4	41±10	35±10	49±12
	toroidal	27±4	32±10	12±8	12±7	45±14	22±4	33±10

[1] % of the total magnetic energy available.
[2] % of the respective poloidal or toroidal field geometry and the fraction of the poloidal or toroidal magnetic energy in the dipolar ($\ell = 1$), quadrupolar ($\ell = 2$), octupolar ($\ell = 3$) and [3] higher order multipole ($\ell \geq 4$) components as well as the fraction of energy of each component stored in the axisymmetric component ($m < \ell/2$) and the fraction of the total energy stored in each component ($m = 0$).

generating fields directly in the subsurface region (e.g. Dikpati et al., 2002) and could be distributed throughout the whole convective zone (e.g. Lanza et al., 1998).

Figure 6.4 shows the fractional magnetic field strength as a function of latitude for each orientation for HD 29615 using Equation 5.1 as the basis of this plot. The toroidal field is strongly positive at all latitudes whereas the poloidal field shows a significant positive field at lower latitudes but a predominately negative field at higher latitudes. This is consistent with the maps displayed in Figure 6.1. Generally, both HD 35296 (Chapter 5) and HD 29615 are similar stars in their rotation rates (similar $v \sin i$) yet have dissimilar distributions of magnetic fields in all three orientations although the toroidal and radial fields have similar latitudinal distributions.

Donati et al. (2003a) found that in some early K-dwarf stars, the level of differential rotation measured from brightness features is usually lower when compared with the levels found when using magnetic features. Their interpretation of this variation is that the brightness features and the magnetic features are anchored at different depths within the convective zone of the star. Similar variations were observed in the rotational shear ($\delta\Omega$) measurement for HD 29615. When using brightness features, the rotational shear is $0.09^{+0.04}_{-0.02}$ rad d^{-1} whereas when using magnetic features, $\delta\Omega$ was measured to be $0.58^{+0.14}_{-0.12}$ rad d^{-1}. This could be one possible interpretation concerning this significant variation, as shown in Figure 6.8, in the rotational shear as measured by

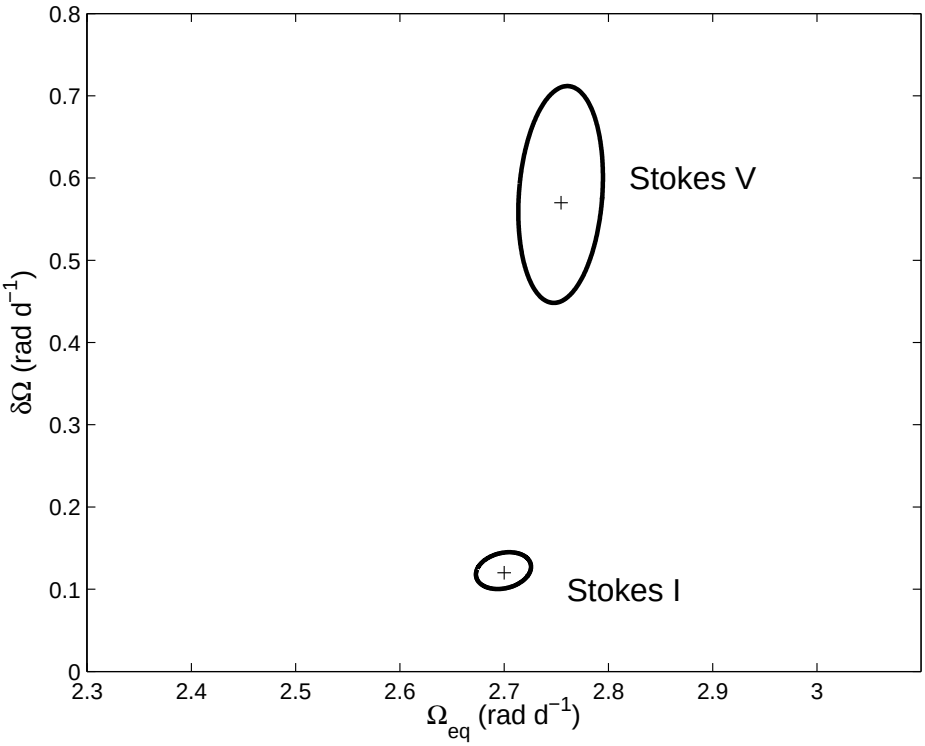

Figure 6.8: Differential rotation using Stokes I and V for HD 29615. The brightness (spot) features produce an equatorial rotational velocity, Ω_{eq} of $2.67^{+0.09}_{-0.01}$ rad d^{-1} with rotational shear, $\delta\Omega$ of $0.09^{+0.04}_{-0.02}$ rad d^{-1}. However, using the magnetic features observed, HD 29615 has an equatorial rotational velocity, Ω_{eq} of 2.75 ± 0.04 rad d^{-1}with a rotational shear, $\delta\Omega$ of $0.58^{+0.14}_{-0.12}$ rad d^{-1}.

the magnetic and spot features. As discussed in Chapter 4, an alternative explanation may be offered by the work of Korhonen and Elstner (2011). They propose that small magnetic features (Stokes V) rather than large spots (Stokes I) are more likely to recover the true magnitude of the surface differential rotation as large starspots have more solid-body like behaviour. Hence this value of the differential rotation obtained using the brightness maps needs to be treated with caution.

HD 29615, like HD 171488 ($\delta\Omega \approx 0.40 \rightarrow 0.56$ rad d^{-1}), has extreme levels of rotational shear with a $\delta\Omega = 0.58^{+0.14}_{-0.12}$ rad d^{-1}, making this the highest value yet for differential rotation found using ZDI. HD 171488 has a 1.33 d rotation period with a $v\sin i = 38$

$\mathrm{km\,s^{-1}}$ whereas HD 29615 has a rotational period of 2.34 d with a $v \sin i = 19.5\ \mathrm{km\,s^{-1}}$. Given that both HD 171488 and HD 29615 have similar photospheric temperatures and ages, it appears that rotation rate has a limited effect on rotational shear as found by Barnes et al. (2005a). The Rossby number, one of the key parameters for measuring the efficiency of magnetic field generation (Donati and Landstreet, 2009), can be calculated using Equation 5.9. The Rossby number for HD 29615 was estimated to be 0.14; very similar to that value determined for HD 171488 by Jeffers et al. (2011) of 0.116. (One should note that when using Equation 5.10 based on the work of Wright et al. (2011), and the mass listed in Jeffers et al. (2011), the Rossby number for HD171488 calculates to be 0.14). Both stars have relatively low Rossby numbers and extremely high levels of surface differential rotation.

Kitchatinov and Olemskoy (2011) and Küker et al. (2011) used numerical simulations, based on mean-field hydrodynamics theory, to investigate differential rotation on a number of parameters. Kitchatinov and Olemskoy (2011) showed that the level of differential rotation is dependent on effective temperature. Küker et al. (2011) found, when holding the effective temperature constant, the depth of the convection zone has a "big impact on stellar rotation". They demonstrated that the extreme surface shear of stars such as HD 171488 (and by implication HD 29615) can only be explained with a shallow convection zone. However, the CZD for HD 29615 was estimated to be 0.252 $\pm$ 0.011 $R_\star$, as determined from the stellar evolution models of Siess et al. (2000). The value for the B-V (or V-I) colour was that found in ESA (1997) (date accessed: 31, January, 2013) and the absolute magnitude was determined from the maximum visual magnitude determined by the *HIPPARCOS* space mission. O'Neal et al. (1996) found that on some heavily spotted stars, the observed maximum V magnitude underestimates the brightness of the unspotted star by $\sim$ 0.3-0.4 mag. HD 106506 (see Chapter 3) had a visual magnitude of $\sim$8.54, yet the unspotted magnitude was determined to be 8.38 (using the imaging code). However, as there was limited knowledge of the fractional spottedness of many of the stars that had their differential rotation already determined by other authors (discussed in Chapter 8), it was decided to use the maximum visual magnitude listed in the *HIPPARCOS* database with the caveat that this is possibly leads to an overestimate of the true CZD.

When compared with the CZD for HD 171488 of 0.206 $R_\star$ or 0.233 $R_\odot$ (Jeffers et al., 2011), HD 29615 has a CZD of 0.252 $R_\star$. However, in absolute terms, HD 29615

is approximately 1 $R_{\odot}$ so its CZD is ∼0.25 $R_{\odot}$. This would indicate that absolute CZD (physical depth) might be a better indicator than relative CZD (in terms of $R_{\star}$). Nevertheless, the differential rotation, found from ZDI needs a larger sample size of late F-/early G-type stars before further conclusions can be made in this regard. This is addressed in more detail in Chapter 8.

There was evidence of the existence of plage-like behaviour on HD 29615 when considering the Hα emission as shown in Figure 6.7. This emission reaches a maximum at approximately phase = 0.6. There appears to be an enhanced magnetic feature in the azimuthal magnetic field at this phase with an even more enhanced magnetic feature in the radial magnetic field trailing slightly, at approximately phase = 0.5, as shown in Figure 6.1. One can theorise that the enhanced positive radial magnetic field is contributing to the activity in the upper chromosphere, perhaps with the production of plages or even prominences at mid-latitude, very similar in latitude to those activities observed on the Sun.

6.6 Conclusions

HD 29615 is a relatively youthful star that exhibits high levels magnetic activity, in the form of chromospheric activity, and surface differential rotation. This variation in the chromospheric activity, with rotational phase, was based on the modulation of the Hα emission. Using the brightness (spot) features observed, HD 29615 has an equatorial rotational velocity, Ω_{eq} of $2.67^{+0.09}_{-0.01}$ rad d^{-1} with a rotational shear, $\delta\Omega$ of $0.09^{+0.04}_{-0.02}$ rad d^{-1}. However, this value needs to be treated with caution as there were limited low- and mid-latitude features recovered during the imaging process. Using the magnetic features observed, HD 29615 has an equatorial rotational velocity, Ω_{eq} of $2.75^{+0.07}_{-0.04}$ rad d^{-1} with a rotational shear, $\delta\Omega$ of $0.58^{+0.14}_{-0.12}$ rad d^{-1} making this one of the highest values yet found for differential rotation using ZDI. Such extreme levels of rotational shear can only be explained with a shallow convection zone although the theoretical models of Siess et al. (2000) indicate that HD 29615 has a relatively large convection zone. Based on the magnetic maps, it can be concluded that the dynamo operating on this moderately rotating star is similar to that of other active, rapidly rotating stars and is most likely a distributed dynamo operating throughout the convective zone.

Chapter 7

Magnetic Fields on Young, Moderately Rotating Sun-like stars: The infant Sun EK Draconis

7.1 Introduction

The focus of this chapter is the young solar analogue EK Draconis (HD 129333, HIP 71631). It has a Right Ascension $14^h39^m00.216^s$ and Declination $+64^o17'29.84''$ (J2000.0 Hög et al., 2000). It is an ideal proxy of the infant Sun at a near- zero-age main-sequence (ZAMS) age and as a result, has been the subject of many multi-wavelength campaigns using a range of telescopes such as the NASA's Hubble Space Telescope (HST) (e.g. Ayres and France, 2010; Linsky et al., 2012), the Far Ultraviolet Spectroscopic Explorer (FUSE) (e.g. Guinan et al., 2003), the Extreme Ultraviolet Explorer (EUVE) (e.g. Audard et al., 1999), the Röntgensatellit X-ray observatory (ROSAT) (e.g. Güdel et al., 1995) and ESA's X-ray Multi-Mirror Mission (XMM-*Newton*) (e.g. Scelsi et al., 2005) to name a few. In addition, a range of techniques have been utilised such as speckle interferometry, direct imaging, photometry (both broadband and Strömgren), Doppler imaging (DI), and now with this project, ZDI.

EK Draconis has been the focus of many longitudinal photometric studies, some spanning ∼45 years. For example, Dorren and Guinan (1994) found activity underwent

cyclic variations with an activity cycle of ∼12 years. Baliunas et al. (1995) reported variability, with no apparent periodicity, in the Mount Wilson Ca II H & K project. Järvinen et al. (2005) found periodicities in the total spot area on a range of time-scales longer than 45 years, with additional variations of ∼10.5 years. They tracked two major spot groups separated by approximately 180^o, calling them active longitudes. They suggested that there were periodic switches of the dominant activity between the active longitudes resulting in a "flip-flop" cycle of ∼4.5 years. Frölich et al. (2002) has observed a dimming of 0.0057 ± 0.0008 mag yr^{-1} since 1975, that has even been more pronounced in recent times. Messina and Guinan (2003) noted the rotational period ranged from 2.551 d to 2.886 d. They showed evidence of period variation with two rotational periods detected in several seasons, each decreasing monotonically along with each starspot cycle. One period is ∼2.8 d while a second is ∼2.6 d (see Figure 8 from Messina and Guinan, 2003).

Further evidence of the enhanced, solar-like, activity occurring on EK Draconis has been observed by several authors. Güdel et al. (1995) found that EK Draconis is a steady emitter of microwaves and soft X-rays. Dorren et al. (1995) observed in X-rays and measured an X-ray luminosity $L_\times$ (0.2-2.4 keV) = $(7.5\text{-}11.5)\times10^{22}$ J s^{-1}. Audard et al. (1999) observed 16 flares with energies in the range of 3×10^{26} to 6×10^{27} Joules using two week-long EUVE observations. The enhanced levels of activity with these frequent flares superimposed on a quiescent emission level is 2-3 orders of magnitude larger than that on the Sun. Scelsi et al. (2005) reported observing a ∼10 ks flare using ESA's XMM-*Newton* telescope. Further flaring activity, with two distinct flares during a 20 minute period, was observed by Ayres and France (2010) using the Cosmic Origins Spectrograph (COS) on the HST. All this showing EK Draconis to be an active young Sun.

For a time, EK Draconis was considered an infant sun (Dorren and Guinan, 1994); however, Duquennoy and Mayor (1991) determined that it has a secondary component with a mass of $\geq$0.37 $M_\odot$ with a preliminary orbit ∼ 4575 d. Metchev and Hillenbrand (2004) used adaptive optics on the 5 m Palomar Telescope to directly image EK Draconis thereby confirming the existence of this secondary component. This is shown in Figure 7.1. They did speculate of the possibility of EK Draconis being a triple system but König et al. (2005) ruled out the possibility of a third companion using speckle in-

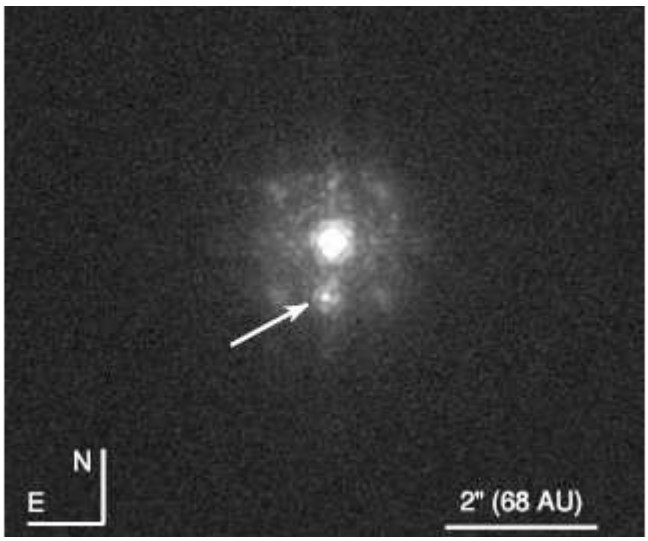

Figure 7.1: The image of EK Draconis taken with the 5 m Palomar telescope using adaptive optics. This image was taken through a narrow-band (1%) Brγ (2.166μm) filter. Image: taken from Metchev and Hillenbrand (2004)

terferometry and further concluded that EK Draconis is "one of the few nearby young stars that will evolve similarly to the Sun".

Strassmeier and Rice (1998) used Doppler imaging (DI) to map the spot topography on the surface of EK Draconis. They found photosphere-to-spot temperature differences of ∼1200K and ∼400K with a polar spot located at latitude $\sim^{+}70$ to $^{+}80^{o}$. Järvinen et al. (2007) also produced DI maps showing both low- and high-latitude spot features. In addition, they observed the wings of the 8662 Å Ca II Infrared Triplet lines and concluded that the photosphere is very similar to that of the Sun.

7.2 Fundamental Parameters of EK Draconis

EK Draconis (HD 129333) is a G1.5V star and is considered the best proxy for a young Sun (e.g. Järvinen et al., 2007; Strassmeier and Rice, 1998). The *HIPPARCOS* space mission measured a parallax of 29.30 ± 0.37 mas (van Leeuwen, 2007), giving a distance of $34.13^{+0.44}_{-0.43}$ pc or 111.3 ± 1.4 ly. Järvinen et al. (2007) used the isochrones from Granzer et al. (2000) to estimate its age to be between 30-50 Myr with a mass of 1.06 $M_{\odot}$ (Wright et al., 2011). Järvinen et al. (2007) estimated an effective photospheric

temperature of 5750K, log $g = 4.5$, microturbulence $\xi_t = 1.6 \pm 0.1$ km s^{-1} with a metallicity of $[M/H] = 0.0 \pm 0.05$. DI maps have been produced by Strassmeier and Rice (1998) and Järvinen et al. (2007). Strassmeier and Rice (1998) showed EK Draconis had a significant high-latitude spot although not a polar spot as observed on other rapidly rotating, sun-like stars. Similar results were again shown by Järvinen et al. (2007).

7.3 Observations and Analysis

EK Draconis was observed at the Canada-France-Hawaii Telescope (CFHT) during December 2006 and the Télescope Bernard Lyot (TBL) during January/February, 2007. A journal of observations is shown in Tables 7.1 and 7.2 respectively. There was no simultaneous photometry undertaken on this star.

This reduced data was kindly supplied by Dr Jean-Françios Donati, from L'Institut de Recherche en Astrophysique et Planétologie (IRAP) at l'Université Paul Sabatier. When preparing the LSD profiles, a G2 line mask, created from the Kurucz atomic database and ATLAS9 atmospheric models (Kurucz, 1993), was used.

7.3.1 High Resolution Spectropolarimetric Observations from the CFHT and TBL

High resolution spectropolarimetric data were obtained using ESPaDOnS at the CFHT and NARVAL at the TBL. Both have a mean pixel resolution of 1.8 km s^{-1} per pixel with the spectral coverage from $\sim$ 370 nm to 1048 nm with a resolution of $\sim$ 68000. The grating has 79 gr/mm with a 2k×4.5k CCD detector covering 40 orders (orders #22 to #61). Both ESPaDOnS and NARVAL consist of one fixed quarter-wave retarder sandwiched between 2 rotating half-wave retarders and coupled to a Wollaston beamsplitter. Initial reduction was completed using LibreESpRIT (Donati et al., 1997). A G2 line mask, as used with previous stars in this thesis, was used in during the LSD process. A journal of the observations are shown in Tables 7.1 (CFHT) and 7.2 (TBL).

7.3.2 Solar Contamination Corrections

There was some severe solar contamination, due to the observations being taken close to sun-rise, in the red-wing of the Stokes I LSD profile for the CHFT data on most

Table 7.1: The journal of spectropolarimetric observations of EK Draconis using the CFHT.

UT Date	UT middle	Exp. Time[1] (sec)	Stokes V Mean S/N[2]	FAP[3]	Detection?
2006 Nov 30	16:17:34	4×60	4310	4.441×10^{-15}	Definite
2006 Dec 05	16:10:53	4×60	5384	1.998×10^{-15}	Definite
2006 Dec 06	16:12:30	4×100	8291	0.000	Definite
2006 Dec 07	16: 9:35	4×180	10850	0.000	Definite
2006 Dec 07	16:21:37	4×60	6415	0.000	Definite
2006 Dec 08	16:12:36	4×150	8254	0.000	Definite
2006 Dec 09	16:15:40	4×120	8649	0.000	Definite
2006 Dec 10	16:12:58	4×150	9157	0.000	Definite
2006 Dec 11	16:12:43	4×120	8063	0.000	Definite

[1] Each sequence of $4 \times 100 = 400$ seconds exposures (for example). After each exposure, the "rotating half-wave retarder" of the polarimeter is rotated between $+45^o$ and -45^o so as to remove instrumental polarization signals from the telescope and the polarimeter.
[2] Signal-to-noise (S/N) of the resulting Stokes V profile.
[3] FAP: False Alarm Probability. See Section 3.3.2 for more details.

Table 7.2: The journal of spectropolarimetric observations of EK Draconis using the TBL.

UT Date	UT middle	Exp. Time[1] (sec)	Stokes V Mean S/N[2]	FAP[3]	Detection?
2007 Jan 26	6:39:37	4×300	6446	0.000	Definite
2007 Jan 27	5:49:08	4×300	7058	0.000	Definite
2007 Jan 28	5:18:08	4×300	7603	1.412×10^{-07}	Definite
2007 Jan 29	5:16:09	4×300	9244	0.000	Definite
2007 Jan 30	5:07:46	4×300	6215	0.000	Definite
2007 Feb 01	4:44:47	4×300	6240	0.000	Definite
2007 Feb 02	5:54:59	4×300	8026	0.000	Definite
2007 Feb 03	5:32:38	4×300	8522	0.000	Definite
2007 Feb 04	5:49:48	4×300	9129	0.000	Definite
2007 Feb 15	6:20:12	4×300	7531	0.000	Definite
2007 Feb 17	4:16:00	4×300	925	8.601×10^{-02}	No detection
2007 Feb 18	4:16:06	4×300	7079	4.831×10^{-08}	Definite
2007 Feb 19	3:10:57	4×300	8469	0.000	Definite
2007 Feb 22	2:27:53	4×300	8484	0.000	Definite
2007 Feb 28	1:59:43	4×300	1517	4.513×10^{06}	Definite
2012 Jan 12	6:11:54	4×300	9959	0.000	Definite
2012 Jan 13	5:37:09	4×300	9502	0.000	Definite
2012 Jan 14	5:20:28	4×300	8206	0.000	Definite
2012 Jan 15	5:20:07	4×300	8149	0.000	Definite
2012 Jan 16	5:01:48	4×300	7770	0.000	Definite
2012 Jan 17	4:36:18	4×300	6175	0.000	Definite
2012 Jan 18	4:28:34	4×300	8276	0.000	Definite
2012 Jan 23	5:59:36	4×300	8930	0.000	Definite
2012 Jan 24	5:06:37	4×300	8127	0.000	Definite
2012 Feb 09	1:25:37	4×300	7797	0.000	Definite

[1] Each sequence of 4 × 300 = 1200 seconds exposures (for example). After each exposure, the "rotating half-wave retarder" of the polarimeter is rotated between $+45^o$ and -45^o so as to remove instrumental polarization signals from the telescope and the polarimeter.

[2] Signal-to-noise (S/N) of the resulting Stokes V profile.

[3] FAP: False Alarm Probability. See Section 3.3.2 for more details.

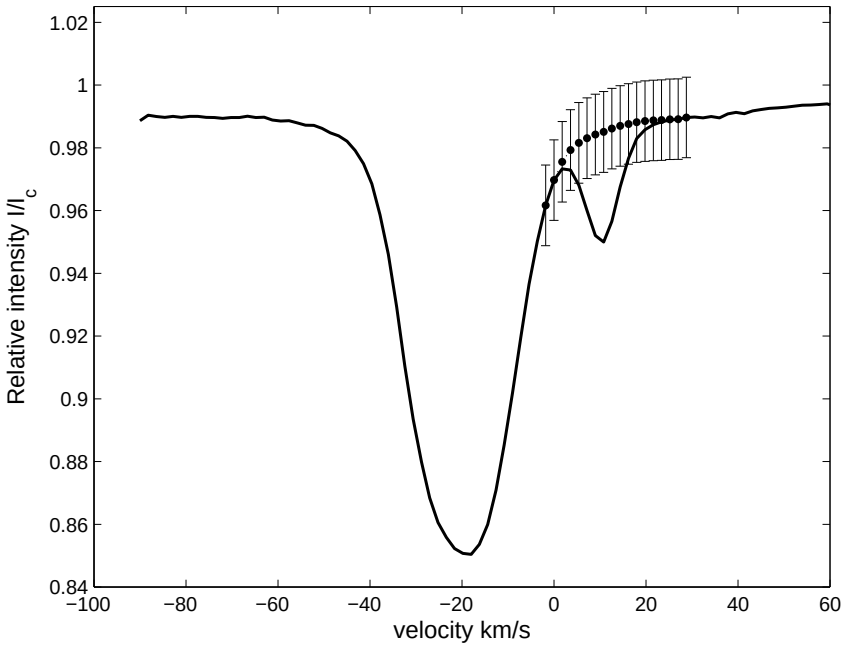

Figure 7.2: A typical solar contaminated Stokes I LSD profile of EK Draconis taken at the CHFT. This particular profile was taken on December 06, 2006 at UT 16:24:21, at an hour angle = -3.531 through an airmass = 1.813. The solid line is the original profile whereas the dotted line is the section of the profile that was replaced with a non-contaminated profile taken earlier in the evening. The error bars were increased in that region so that the imaging code would effectively "ignore" that part of the profile.

nights and some contamination in the TBL data. This is shown clearly in Figure 7.2 where there is a dip in the observed LSD profile at $v\sin i$ ∼10.5 $\mathrm{km\,s^{-1}}$. However, there appeared to be no contamination in the corresponding Stokes V LSD profile. To correct for this solar contamination, the first Stokes I LSD profile for that night, if it was free of the contamination, was used to simply replace the contaminated section of the other three LSD profiles, as shown in Figure 7.2. If it appeared that the first LSD profile had been contaminated, then an average LSD profile (from another evening) was used for that section. Subsequently, the error bars were increased by a factor of 100 in that region so that the imaging code would effectively "ignore" that part of the contaminated profile when producing the brightness maps.

7.4 Photospheric and Chromospheric Features

During the 2006/7 observing run, the first spectropolarimetric spectrum was taken at the CHFT on HJD: 2454070.17567 (November 29, 2006) and the last taken at the TBL on HJD: 2454159.58858 (February 27, 2007). The phases of the observations were based on the epochs shown in Table 7.3. During the 2012 observation run, the first spectropolarimetric spectrum was taken at the TBL on HJD: 2455938.75066 (January 12, 2012) and the last taken on HJD: 2455966.56461 (February 8, 2012).

7.4.1 Image Reconstruction: Stokes *I* Doppler imaging map and surface differential rotation

7.4.1.1 CFHT and TBL: 2006/7

There has been some debate in the literature regarding the temperature of the spots occurring on EK Draconis. Järvinen et al. (2007) used DI to determine the spots were only 500K cooler than the surrounding photosphere. Strassmeier and Rice (1998) also used DI and found spot temperatures that were 400K and 1200K cooler than the surrounding photosphere. Scheible and Guinan (1994) noted that the spot temperature was approximately 460 K less the surrounding photosphere using modelling of photometric lightcurves. However, O'Neal et al. (2004) used the TiO bands at 7055 Å and 8860 Å and found that the spot temperatures were $\sim$ 3800 K, concluding that these temperatures were closer to the typical minimum sunspot umbral temperatures (e.g. Penn et al., 2003). During the modelling of the CFHT and TBL data, a relatively warm starspot temperature (T_{spot}=5250K) was initially used. The starspot temperature was systematically reduced to determine the best fit of the modelled data to the observed data, in a minimum χ^2 sense. It was found that ΔTemp = 1700K provided the best fits to the data. Any further reduction in the spot temperature made little difference to the resulting fits. This is consistent with the spot temperatures expected of early G-type stars, and supports the relationship developed by Berdyugina (2005) (see Figure 7 on page 27 of that work). Hence the adopted spot temperature used in the DI maps was set to 4050K.

There have been a range of rotational periods for EK Draconis found in the literature. Many authors have found, and used, a period of $\sim$2.5 to 2.9 d. König et al. (2005) used radial velocity variations in their speckle observations to infer a period of 2.767

Table 7.3: The parameters used to produce the maximum-entropy image reconstructions of EK Draconis.

Parameter	EK Draconis (HD 129333)
Spectral Type [1]	G1.5V
Optical rotational period[2]	2.755 ± 0.06d (2006/7)
Inclination Angle [3]	60 ± 5^o
Projected Rotational Velocity, $v\sin i$	16.8 ± 0.2 km s^{-1}
Photospheric Temperature, T_{phot} [3]	5750 K
Spot Temperature, T_{spot}	4050 K
Radial Velocity, v_{rad}	-20.2 ± 0.1 km s^{-1}
Stellar radius [4]	0.99 $R_\odot$
Convection zone depth[5]	0.243 ± 0.003 $R_\star$
	$0.241^{+0.004}_{-0.002}$ $R_\odot$
Age [3]	30-50 Myr
Mass [4]	1.06 $M_\odot$
Stokes I: Ω_{eq}	$2.51^{+0.019}_{-0.015}$ rad d^{-1}
Stokes I: $\delta\Omega$	$0.34^{+0.02}_{-0.048}$ rad d^{-1}
Stokes V: Ω_{eq}	$2.53^{+0.049}_{-0.050}$ rad d^{-1}
Stokes V: $\delta\Omega$	$0.44^{+0.21}_{-0.12}$ rad d^{-1}
Epoch used (HJD)	2454076.112060 (Dec 2006)
	2454131.492060 (Jan 2007)
	2454153.644060 (Feb 2007)
	2455952.379670 (Jan 2012)

[1] Torres et al. (2006)

[2] Using Stokes I data, with the error estimate the FWHM of the "trough" in Figure 7.3.

[3] Järvinen et al. (2007)

[4] Wright et al. (2011)

[5] based on Equations 5.9 and 5.10. See Section 5.4.5 in Chapter 5 for more details

$\pm$ 0.005 d. As mentioned in Section 7.1, Messina and Guinan (2003) used long-term photometry to investigate surface differential rotation and found variation in the period. They found two rotational periods over several seasons, both showing monotonical decreases along with each starspot cycle with solar-like behaviour. Güdel et al. (1995) reported a period of $2.6^{+0.04}_{-0.03}$ d period in radio while a 2.75 $\pm$ 0.05 d period in the optical spectrum. They also observed periodicity in the X-ray light curve. By using auto-correlation analysis, they found a "broad secondary maximum around P = 2.53 d". In order to refine the period for the 2006/7 dataset at this epoch, the modelling strategy was used by systematically modifying the rotational period and to determine the best fit, in a χ^2 sense, to the Stokes I data. For each rotational period - χ^2 combination, the multiplication factors were adjusted. In effect, this process generated the best possible map for each rotational period for a range of periods. Figure 7.3 (upper left panel) shows the results of this process. This approach is similar to that adopted by Petit et al. (2008) when finding periods of some slowly rotating sun-like stars, except they were using Stokes V information. Figure 7.3 show the two attempts to determine the period. When using the complete dataset, a period of 2.755 $\pm$ 0.057 d was found. The error estimate is the Full Width at Half Maximum (FWHM) of the "trough". This can be interpreted as an optical rotational period for EK Draconis at this epoch, and is consistent with such values as obtained by König et al. (2005). When using the TBL dataset (January 26 to February 28, 2007), a period of 2.760 d was found. This slight variation could be due to two reasons: the data from two different telescopes and/or spot evolution. One should note that a value of 2.600 d produced a minimum χ^2 = 1.7. This is shown in Figure 7.3 (upper panel). This value is similar to that obtained by Strassmeier and Rice (1998) and Järvinen et al. (2007). However, this period was not observed when modelling the data taken at TBL hence was decided not to use this particular value for the rotational period of EK Draconis.

The modelled fits to the complete 3-month dataset was very poor. A coarse map using all data is shown in Figure 7.4. The period used to produce this map was 2.755 d but the χ^2 value was found to be 2.25. The spot coverage for this map was 3%. Restricting the modelling to that data obtained from the TBL also proved problematic with a the χ^2 value of 2.40 with a spot coverage, also of 3% with a period of 2.760 d. Figure 7.3 (upper panel) shows the results of this process using the TBL data. Changing the parameters such as $v\sin i$ had no major affect on the overall "shape" of the graph,

and hence the position of the local minimum, only affecting the absolute χ^2 value. In both situations, the modelling strategy could not recover features to the noise level. Temporal variation in spots are not unusual on solar-type stars. For example, Barnes (1999) observed such variability on G-dwarf stars in the α Persei cluster in time-scales of less than a month while Donati et al. (2003a) observed temporal variability on the RS CVn-type star HR 1099 (SpType: K2:Vnk[1]) occurring on time-scales as short as a fortnight. Dorren and Guinan (1994) noted significant changes to the spot distribution on EK Draconis in the order of a few days. Notwithstanding Järvinen et al. (2007) conclusion that differential rotation was low on EK Draconis, given the difficulty in modelling the data, it was concluded that there was significant spot evolution as a result of either spot emergence and/or differential rotation.

Differential rotation was attempted on the complete, 3-month dataset. Estimates for the level of differential rotation were made, with the results shown in Table 7.4. The result was very coarse and when some of the parameters varied, no result was produced at all. Differential rotation was also attempted on the TBL dataset only, using data from January 26 to February 28, 2007. The differential rotation parameters found were: $\Omega_{eq} = 2.50^{+0.02}_{-0.07}$ rad d^{-1} with $\delta\Omega = 0.33^{+0.05}_{-0.15}$ rad d^{-1} as listed in Table 7.4. There was still evidence of spot evolution as the minimum χ^2 value was 1.54, meaning that even accounting for differential rotation, the process could not get down the noise level of the data. In addition, no meaningful map was produced with reasonable fits. Hence the conclusion was that there has been significant emergence and evolution of the spots during the 3-month period, consistent with the observations of EK Draconis by Dorren and Guinan (1994). As a result, it was decided to "split" the dataset into three separate sets. The first was the CFHT data from November 30, to December 11, 2006. The second data set was taken at the TBL from January 25 to February 4, 2007 while the third dataset was taken from February 15 to February 28, 2007. Assuming solid-body rotation, the three maps are shown in Figure 7.6 (left series of panels). The three zero-epochs used were: HJD = 2454076.112060, 2454131.492060 and 2454153.644060 respectively. In addition, a dynamic spectrum was also produced for each dataset by subtracting the mean LSD profile from each of the individual profiles with the resulting profiles plotted as this dynamic spectrum. These dynamic spectra are shown in Figure 7.5. Differential rotation was attempted on all three individual datasets. However,

[1] Montes et al. (2001)

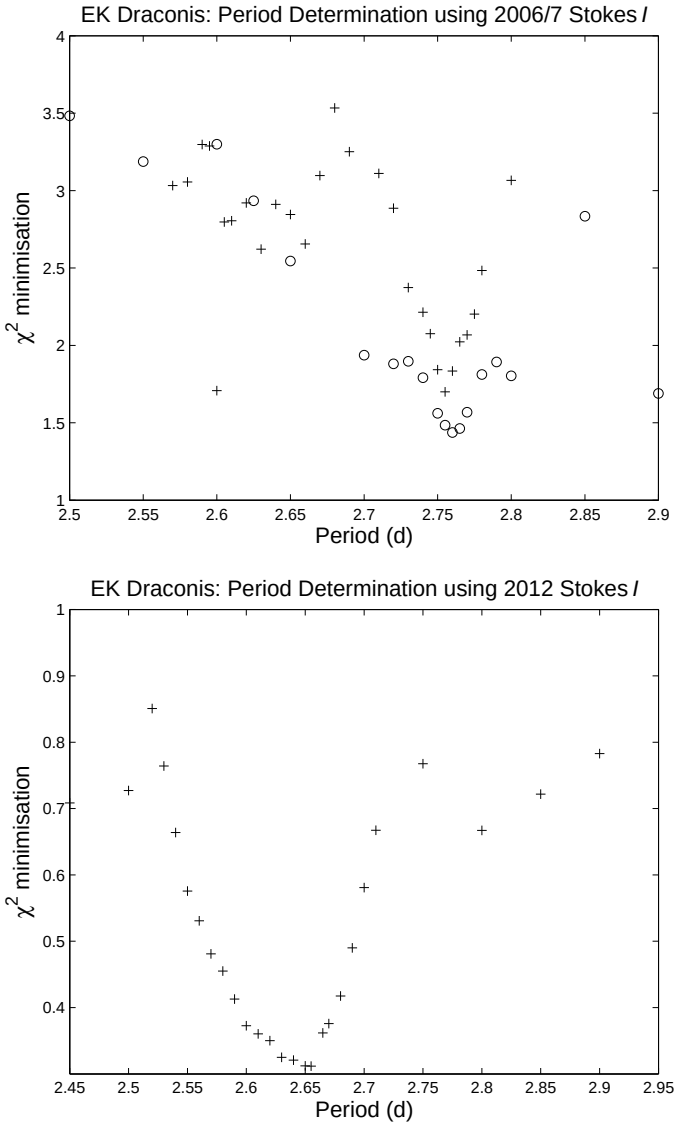

Figure 7.3: The results of systematically changing the rotational period and determining the minimum χ^2 for the difference between the modelled and actual Stokes I data for each period for 2006/7 data (upper panel) and 2012 (lower panel). In the 2006/7 data, the complete 3-month dataset was used, and are shown as '+' in the plot. The 'o' represent the results of using only the TBL data (January 26 to February 28, 2007). Even this simple "test" demonstrates the spot evolution/emergence on this star.

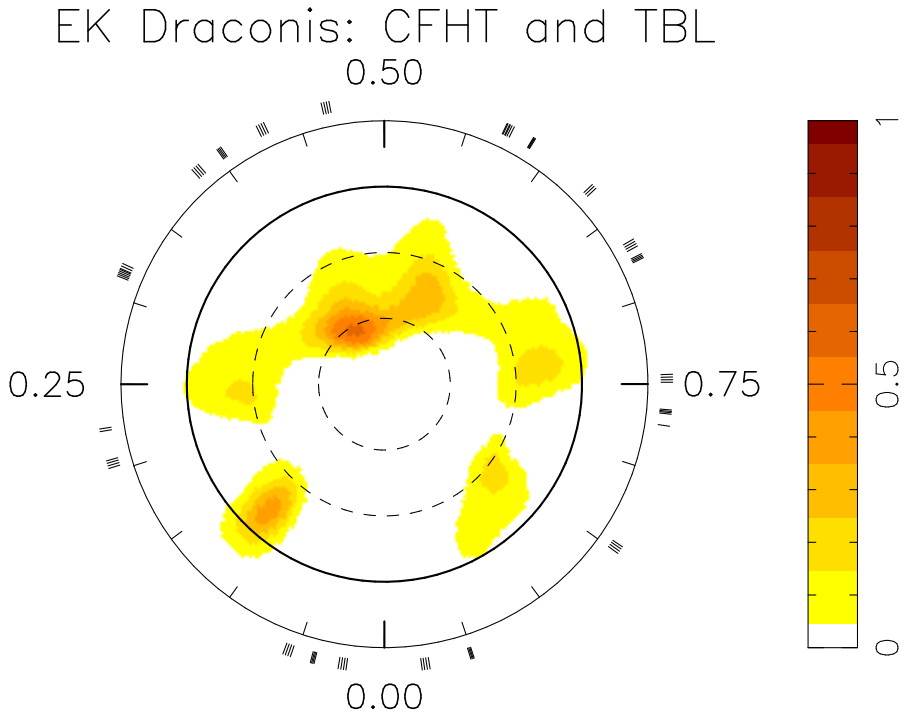

Figure 7.4: Map of EK Draconis using the using the full dataset of Stokes I information, assuming a period of 2.755 d but using $\chi^2 = 2.2$. The spot coverage was 3%. This map is a polar projection extending down to -30^o. The bold lines denote the equator and the dashed lines are +30^o and +60^o latitude parallels. The radial ticks indicate the phases at which this star was observed spectroscopically.

the first and third datasets did not achieve any measurable values. The first dataset has a similar number of profiles (36 profiles from 8 separate observations covering 12 nights) when compared with the second dataset (33 profiles from 8 separate observations covering 11 nights) but still no differential rotation was measured. Poor phase overlap could be responsible for this, along with some of the profiles effectively having a section removed from the analysis due to the solar contamination (see Section 7.3.2). The third dataset had limited number of profiles (19 profiles from 6 observations covering 13 nights). The differential rotation measurement for the January 2007 TBL data are shown in Table 7.4. These were consistent with those results found from the full dataset and the TBL dataset. However, the differential rotation measurement found from the January 2007 dataset provided robust results across a range of various parameters. Hence it was concluded that the differential rotation found in the smaller dataset is more reliable, given the constraint of a small number of profiles. The χ^2 minimisation landscape is shown in Figure 7.7. This graph shows a plot of the error ellipses for the differential rotation measurements for the Stokes I data. These error ellipse was generated by varying some of the stellar parameters, including the star's inclination ($\pm$ 10^o) and the spot coverage ($\pm$ 10%). Applying this differential rotation measurement to the three datasets, the maps that were produced are shown in Figure 7.6 (right panels). The associated modelled fits are shown in Figures 7.8, 7.9 and 7.10 respectively. Table 7.5 shows additional parameters used in the mapping process.

7.4.1.2 TBL: 2012

A similar approach was adopted, as described in Section 7.4.1.1, in determining the period for the 2012 dataset. These results shown in Figure 7.3 (lower panel). The minimum χ^2 occurred at a period of 2.655 days. Again, this was interpreted as a optical rotational period for EK Draconis at this epoch, and is within the range of values as measured by König et al. (2005). Differential rotation was unsuccessfully attempted on the 2012 data using the Stokes I information. Applying the differential rotation parameters found in 2007 for the 2012 data did not produce any meaningful map. This places some doubt on the differential rotation on EK Draconis for Stokes I being constant. Assuming solid-body rotation, the Stokes I map is shown in Figure 7.11 and the fits are shown in Figure 7.12.

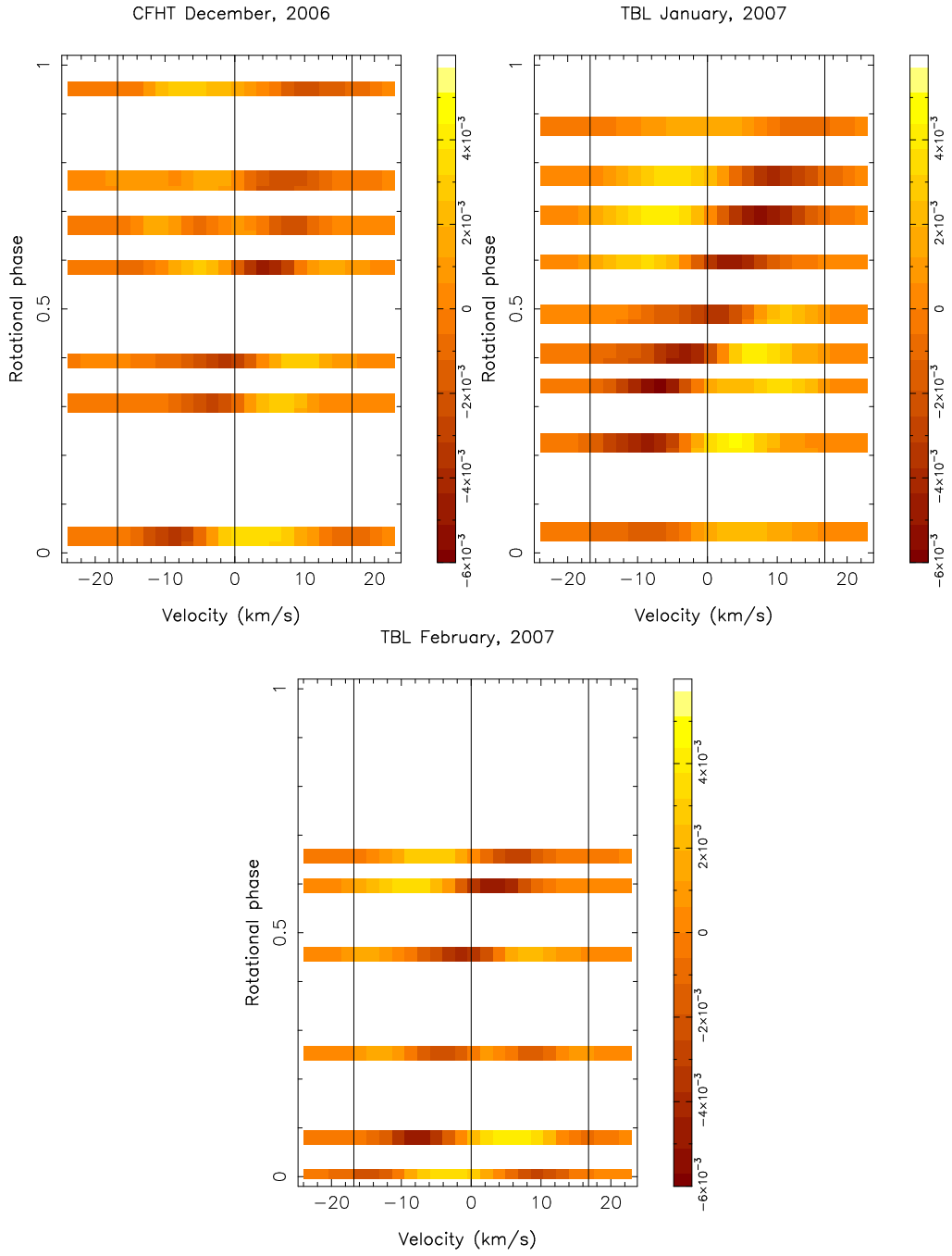

Figure 7.5: Dynamic spectra for EK Draconis using December, 2006, (top left) January 2007 (top right) and February 2007 (bottom) data. Each individual profile was produced by subtracting a mean LSD profile from that particular dataset from each observed profile. The three zero-epochs used were: HJD = 2454076.310035, 2454131.33035 and 2454153.37035 respectively.

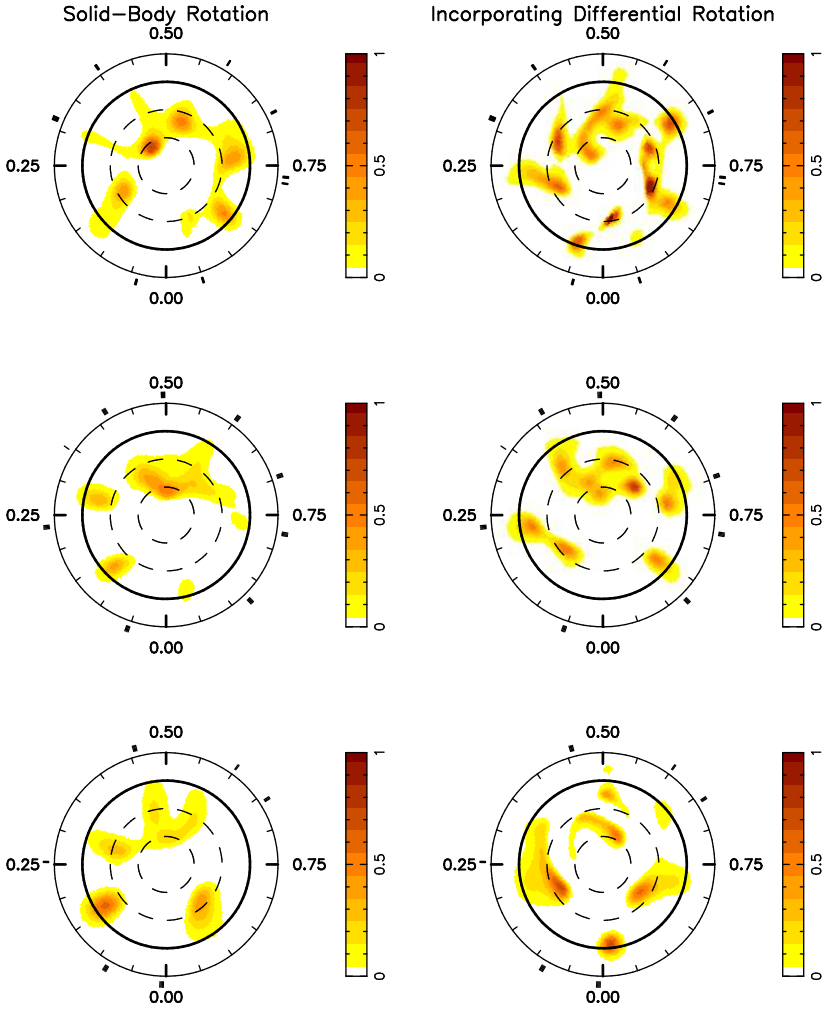

Figure 7.6: The maps produced from "splitting" of the data into three separate epochs. The left panels assume solid-body rotation while the right panels show the maps produced assuming differential rotation parameters being incorporated into the imaging process. The top maps were using data taken $\sim$ December, 2006. The middle maps were using data taken $\sim$ January 2007 while the bottom maps were using data taken $\sim$February, 2007. The epoch for each map was approximately the centre of that particular run, but the phases were matched using the period of 2.755 d. The three zero-epochs used were: HJD = 2454076.310035, 2454131.33035 and 2454153.37035 respectively. These maps are polar projections extending down to -30^o. The bold lines denote the equator and the dashed lines are +30^o and +60^o latitude parallels. The radial ticks indicate the phases at which this star was observed spectroscopically. The spot coverage and χ^2 values for each map are shown in Table 7.5.

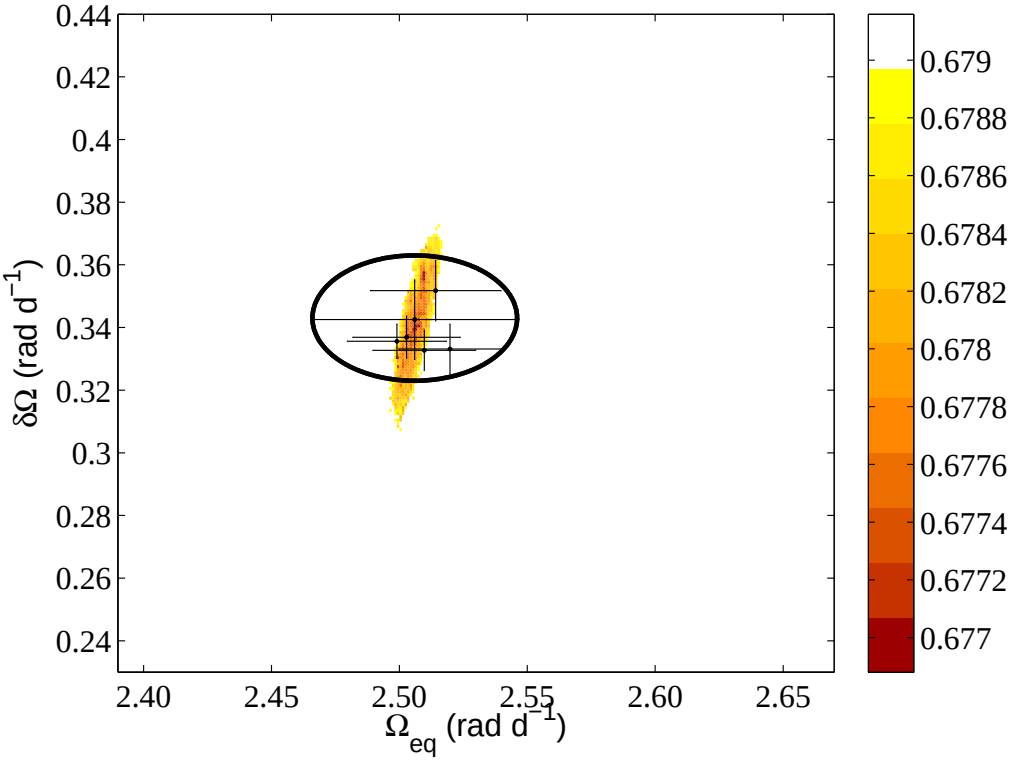

Figure 7.7: Surface differential rotation χ^2 minimisation landscape for the Stokes I for EK Draconis using the January 2007 dataset. The coloured landscape shows the χ^2 values obtained systematically changing the Ω_{eq} and $\delta\Omega$ pairs for the optimum parameter set, as listed in Table 7.4. This is a 1-σ projection, with the darker colours indicating a lower χ^2 value. Superimposed on this graph is the error ellipse for the differential rotation measurements. This ellipse was generated by varying some of the stellar parameters, including the star's inclination ($\pm$ 10^o) and the spot coverage. The error bars on each individual measurement are 1-σ errors in the paraboloid fit.

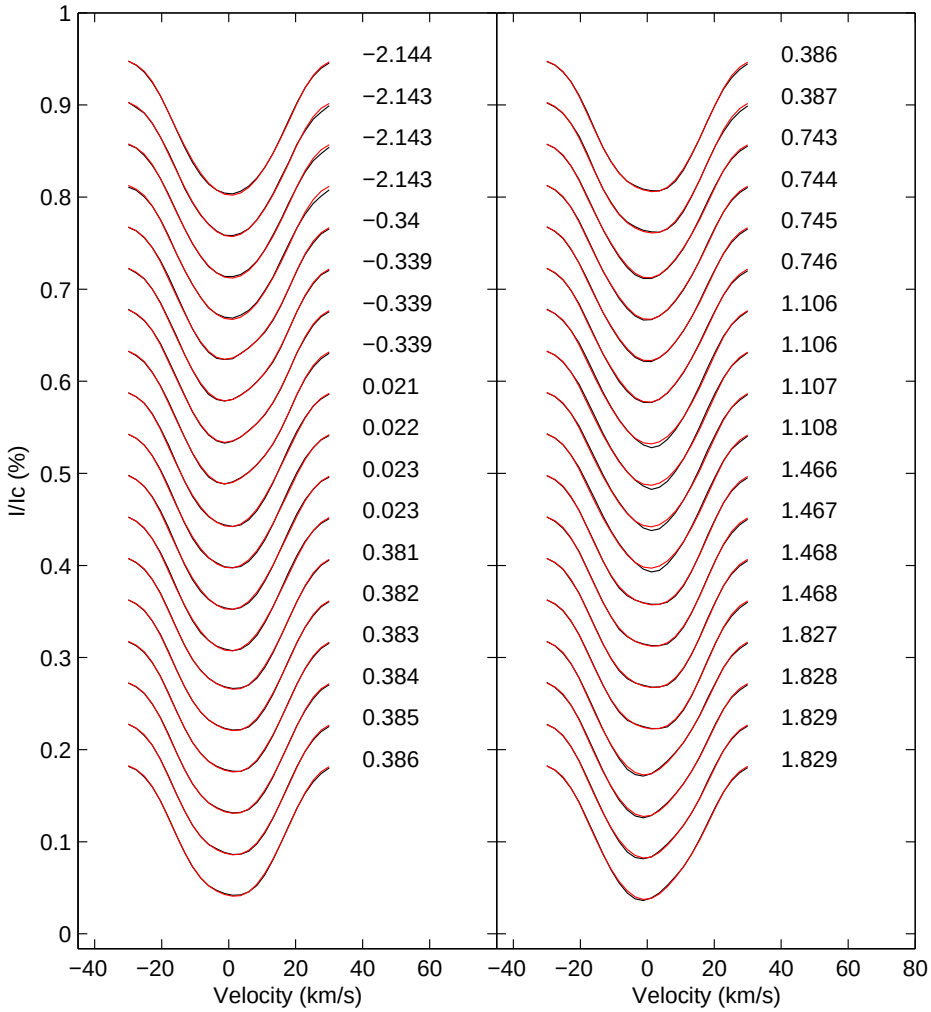

Figure 7.8: The maximum-entropy fits to the Stokes I LSD profiles for EK Draconis during the Nov 30 to Dec 10 CFHT observing run, with the January 2007 TBL surface differential rotation incorporated into the analysis. The red lines represent the modelled lines produced by the Doppler imaging process whereas the black lines represent the actual observed LSD profiles. Each successive profile has been shifted down by 0.045 for graphical purposes. The rotational phases at which the observations took place are indicated to the right of each profile.

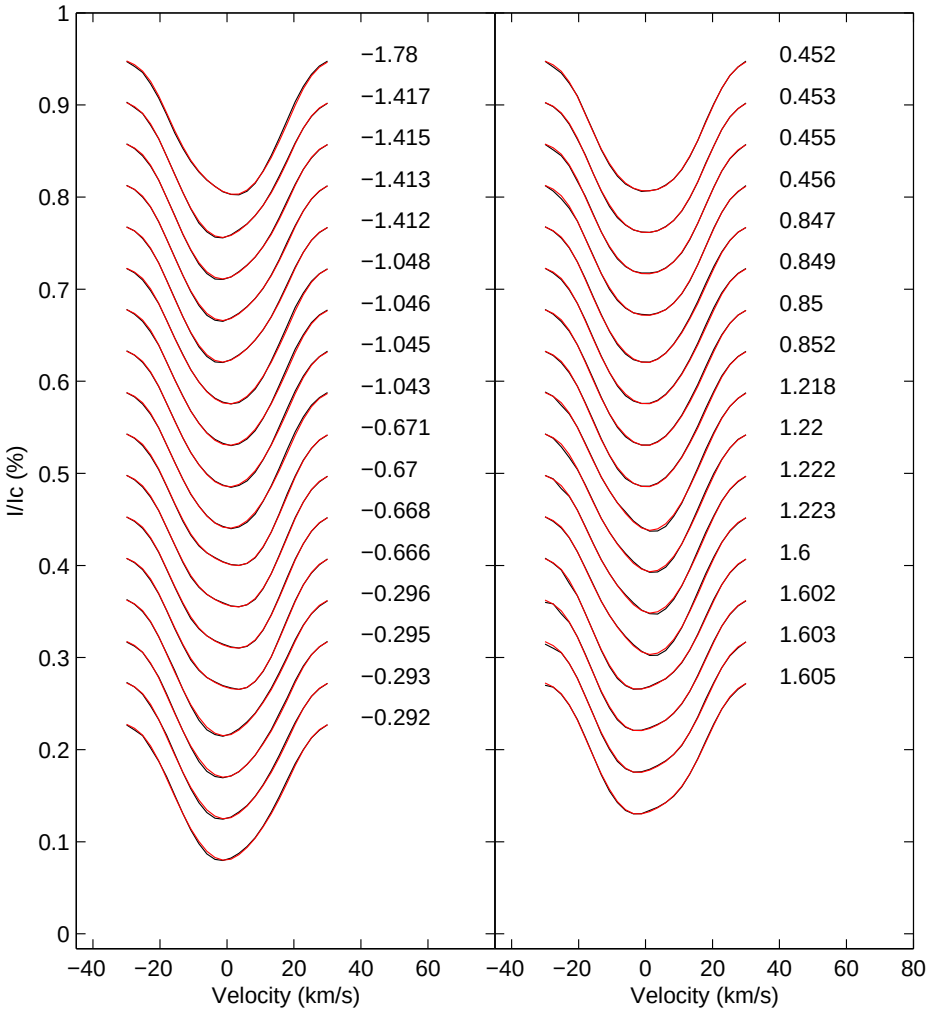

Figure 7.9: The maximum-entropy fits to the Stokes I LSD profiles for EK Draconis during the Jan 25 to Feb 03 2007 TBL observing run, with surface differential rotation incorporated into the analysis. The red lines represent the modelled lines produced by the Doppler imaging process whereas the black lines represent the actual observed LSD profiles. Each successive profile has been shifted down by 0.045 for graphical purposes. The rotational phases at which the observations took place are indicated to the right of each profile.

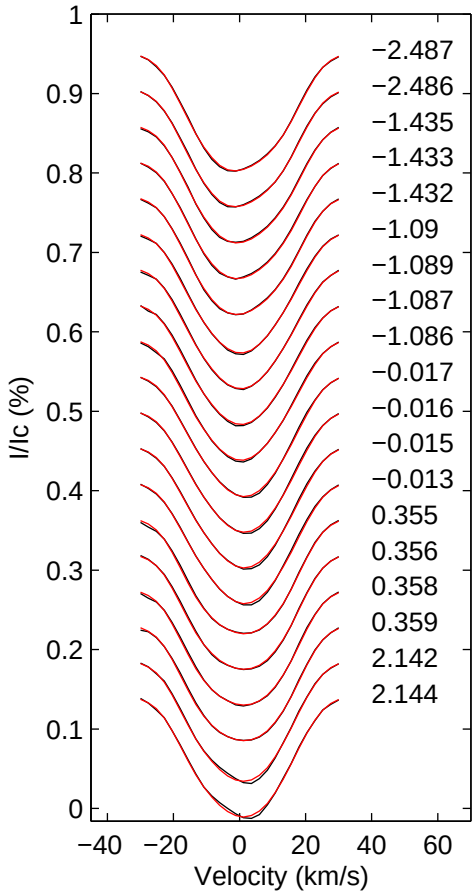

Figure 7.10: The maximum-entropy fits to the Stokes I LSD profiles for EK Draconis during the Feb 14 to Feb 27 2007 TBL observing run, with the January 2007 TBL surface differential rotation incorporated into the analysis. The red lines represent the modelled lines produced by the Doppler imaging process whereas the black lines represent the actual observed LSD profiles. Each successive profile has been shifted down by 0.045 for graphical purposes. The rotational phases at which the observations took place are indicated to the right of each profile.

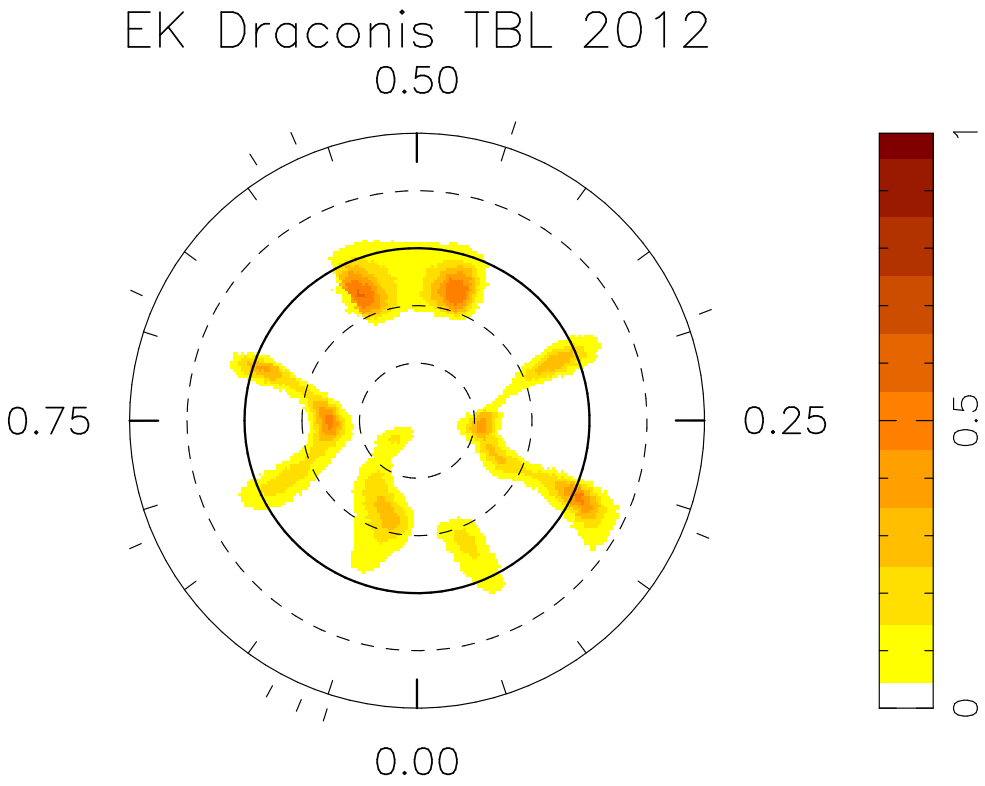

Figure 7.11: The maximum-entropy brightness reconstruction using the Stokes I LSD profiles for the TBL 2012 data. This assumes solid-body rotation. This map is a polar projection extending down to -30^o. The bold lines denote the equator and the dashed lines are +30^o and +60^o latitude parallels. The radial ticks indicate the phases at which this star was observed spectroscopically.

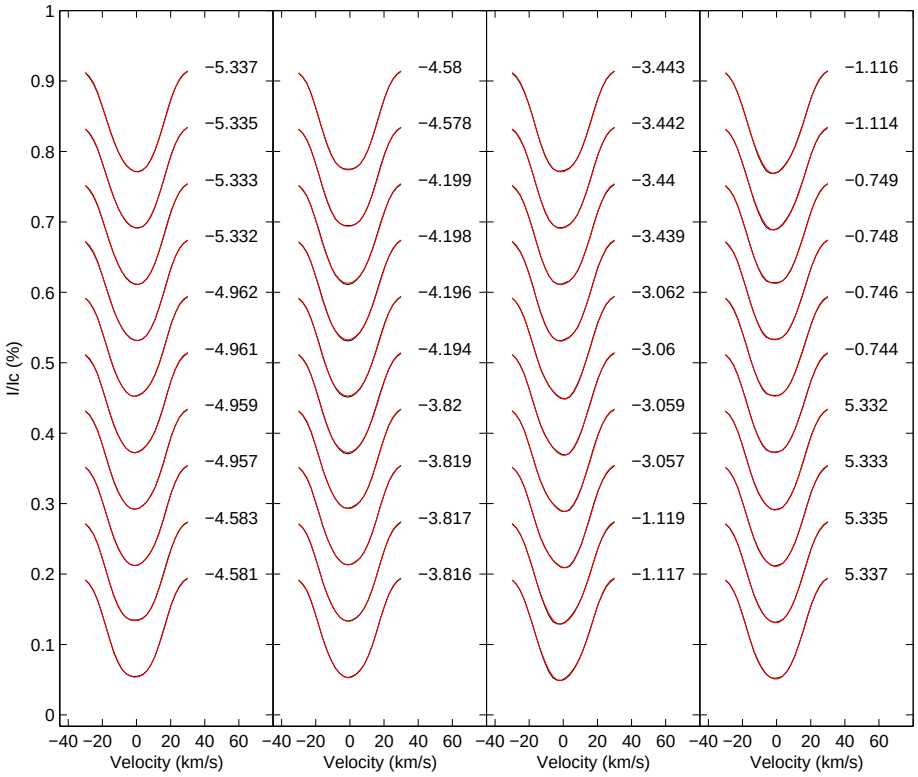

Figure 7.12: The maximum-entropy fits using the Stokes I LSD profiles for the TBL 2012 data. This assumes solid-body rotation. The red lines represent the modelled lines produced by the Doppler imaging process whereas the black lines represent the actual observed LSD profiles. Each successive profile has been shifted down by 0.08 for graphical purposes. The rotational phases at which the observations took place are indicated to the right of each profile.

Table 7.4: The differential rotation parameters found for EK Draconis. The full 3-month dataset was used as was the January/February 2007 and January 2007 subsets of the complete run.

Parameter	Full Data set[1]	TBL Jan/Feb 2007	TBL Jan 2007[2]
Zero-Epoch used[3]	2454114.87806	2454143.17937	2454131.25902
Stokes I			
Ω_{eq} rad d^{-1}	$2.48^{+0.01}_{-0.02}$	$2.50^{+0.02}_{-0.07}$	$2.51^{+0.02}_{-0.02}$
$\delta\Omega$ rad d^{-1}	$0.32^{+0.09}_{-0.03}$	$0.33^{+0.05}_{-0.15}$	$0.34^{+0.02}_{-0.05}$
Stokes V			
Ω_{eq} rad d^{-1}	–	–	$2.53^{+0.05}_{-0.05}$
$\delta\Omega$ rad d^{-1}	–	–	$0.44^{+0.21}_{-0.12}$

[1] The period used was 2.755 d, as shown in Figure 7.3.

[2] The period used was 2.523 d, the equatorial period.

[3] The zero-epoch (HJD) was the middle of that particular dataset under consideration.

7.4.2 Zeeman Doppler imaging and surface differential rotation

As the brightness maps were produced using the three different datasets, so were the magnetic maps for the 2006/7 datasets. In the first instance, it was assumed that the star had solid-body rotation with the resulting maps shown in Figure 7.13. Differential rotation was attempted on all three datasets, using the technique explained in Section 2.6. Only the January, 2007 dataset produced any meaningful results. The differential parameters were estimated as Ω_{eq} of 2.53 $\pm$ 0.05 rad d^{-1} with the rotational shear, $\delta\Omega$, of $0.44^{+0.21}_{-0.12}$ rad d^{-1}. Table 7.4 lists the differential rotation parameters used in the mapping of all three datasets, while additional parameters are listed in Table 7.5. The χ^2 minimisation landscape is shown in Figure 7.14. This graph shows a plot of the error ellipses for the differential rotation measurements for the Stokes V data. These error ellipse was generated by varying some of the stellar parameters, including the star's inclination ($\pm$ 10^o) and the Stokes V global magnetic field ($\pm$ 10%). Applying the differential rotation parameters to all three datasets produced the maps shown in Figure 7.15. The associated modelled fits are shown in Figure 7.16.

Differential rotation was unsuccessfully attempted on the 2012 data, using the Stokes V data. As a result, differential rotation parameters found in the January 2007 data,

Table 7.5: The additional mapping parameters used for EK Draconis for each of the individual brightness (Stokes I) and magnetic (Stokes V) maps.

Parameter	Dec, 2006	Jan, 2007	Feb, 2007	Jan, 2012
Date Commenced	Nov, 30	Jan, 26	Feb, 15	Jan, 12
Date Completed	Dec, 11	Feb, 04	Feb, 28	Feb, 09
Stokes I				
Assuming solid-body rotation				
χ^2	1.45	2.0	1.60	0.35
spot coverage	3.5 %	2.8 %	2.9 %	3.4 %
incorporating Differential rotation				
χ^2	0.55	0.95	1.0	–
spot coverage	5.2 %	3.7 %	3.6 %	–
Stokes V				
Assuming solid-body rotation				
χ^2	1.10	1.15	1.05	2.50
Global magnetic field	93 G	90 G	71 G	88 G
incorporating Differential rotation				
χ^2	1.10	1.00	1.00	1.25
Global magnetic field	86 G	73 G	59 G	100 G

listed in Table 7.4, were applied to the Stokes V maps for the 2012 data. These 2012 maps are shown Figure 7.20 and the fits are shown in the right-most column in Figure 7.16.

Tables 7.6 and 7.7 show a comparison between the two magnetic geometries: poloidal and toroidal magnetic fields for EK Draconis for the 2006/7 data considering both solid-body rotation and differential rotation parameters incorporated into the data. In these two tables, the first number is that from solid-body rotation while the second number is that from differential rotation. Whereas some variation exists between those listed for solid-body rotation and those for differentially rotating body, the overall balance between poloidal and toroidal appears to be maintained, as is the symmetry of the fields. It should be noted that applying the differential rotation parameters to the February 2007 data had the effect of recovering more of the poloidal field and less of the toroidal field. This particular dataset was very sparse and was likely to have contributed to the imbalance observed between the solid-body versus differentially-rotating body. In summary, the magnetic field was evolving from a dominant toroidal field to a more balanced poloidal-toroidal field. The poloidal field was predominately non-axisymmetric while the toroidal field as almost entirely axisymmetric. This is consistent with other stars in this thesis.

Figure 7.18 shows a range of plots of the fractional magnetic field strength as a function of latitude for the poloidal field (top series), toroidal field (middle series) and radial field (bottom series) for the 3 distinct datasets, with that obtained at the CFHT on the left, the January 2007 TBL data is in the middle series of frames while the February 2007 TBL is the right series of frames. In each of these two figures, the shaded (coloured) regions indicate the error in the fractional magnetic field strength at each latitude point. This was found by systematically changing key parameters such as differential rotation parameters, $v \sin i$, rotational period, radial velocity and inclination in a similar way as the errors are estimated when determining the magnitude of the errors in the differential rotation measurement.

It appears that the poloidal field has undergone a reversal from essentially a negative field in late 2006/early 2007 to an essentially positive poloidal field in February 2007. This is also clearly seen in Figure 7.19. The toroidal field appears to be weakening during this period. However, the February dataset has fewer profiles hence this "weakening" may be a result of the reduced profiles. In Chapter 5, HD 35296 appeared to

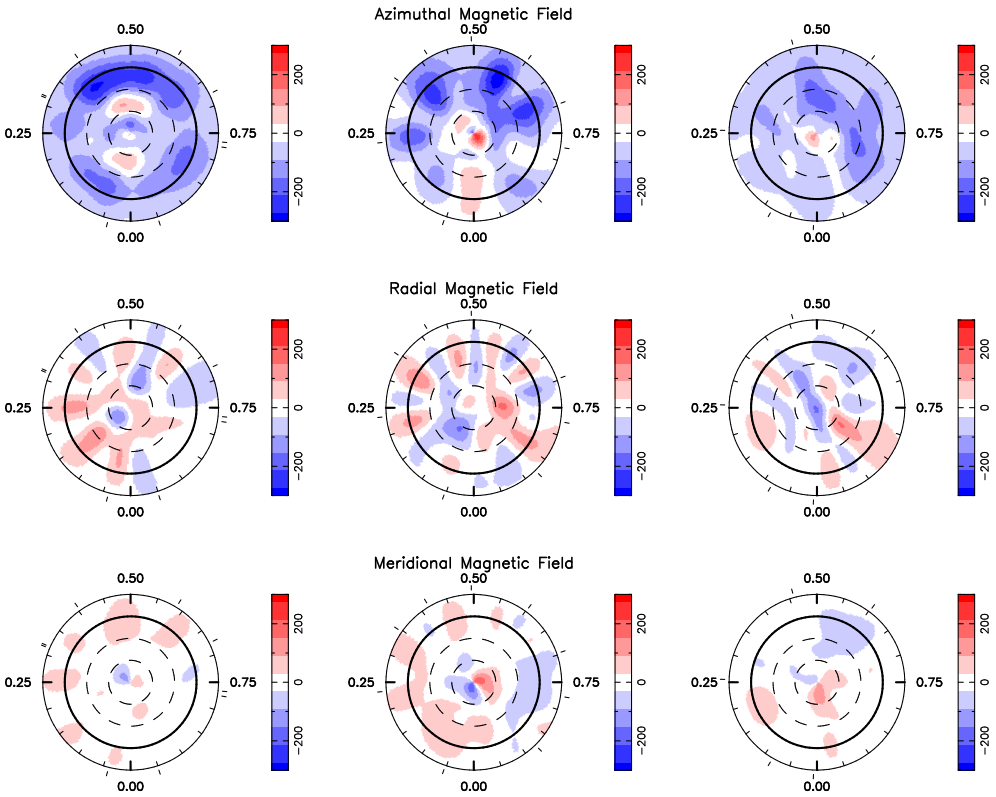

Figure 7.13: Maps for Stokes V EK Draconis assuming Solid-Body rotation with a rotational period of 2.755 d. The left column shows the magnetic maps from the 30 Nov to 11 Dec, 2006 run at the CFHT, with a global magnetic field of 93 G. The middle maps are based on data taken at the TBL from the Jan 25 - Feb 04, 2007, with a global magnetic field of 90 G. The right column shows the maps based on the data taken at the TBL from the Feb 15 - Feb 28, 2007, with a global magnetic field of 71 G. From top to bottom: azimuthal, radial and meridional fields. These maps are polar projections extending down to -30^o. The bold lines denote the equator and the dashed lines are +30^o and +60^o latitude parallels. The radial ticks indicate the phases at which this star was observed spectroscopically. The scale of the magnetic images are in Gauss.

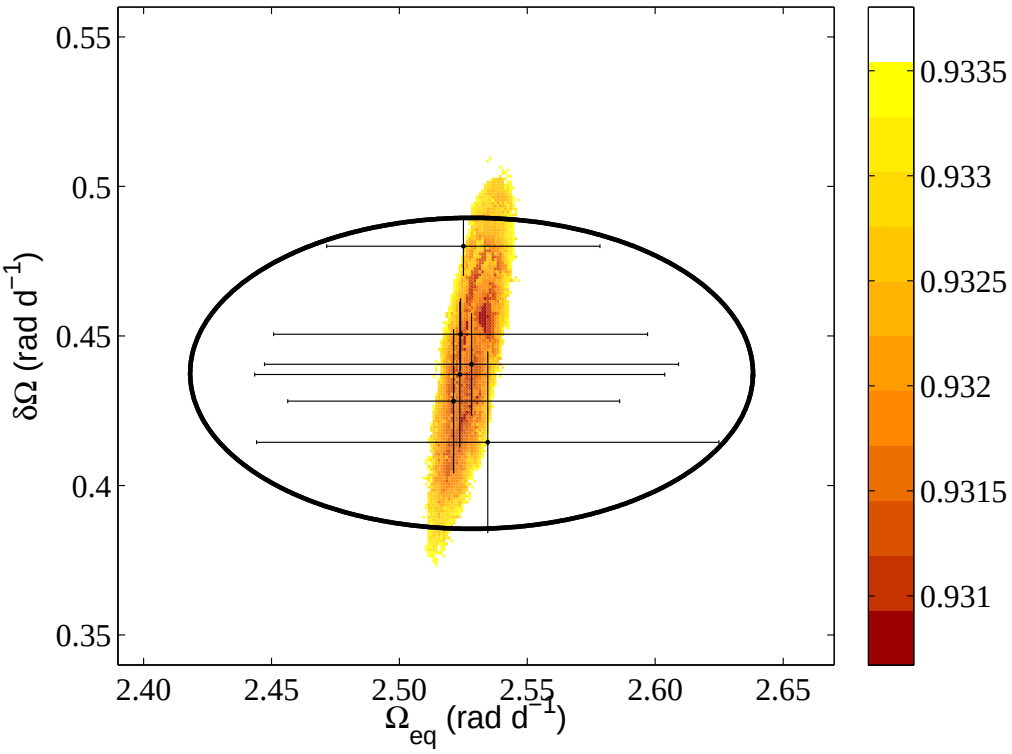

Figure 7.14: Surface differential rotation χ^2 minimisation landscape for the Stokes V for EK Draconis using the January 2007 dataset. The coloured landscape shows the χ^2 values obtained systematically changing the Ω_{eq} and $\delta\Omega$ pairs for the optimum parameter set, as listed in Table 7.4. This is a 1-σ projection, with the darker colours indicating a lower χ^2 value. Superimposed on thesis graph is the error ellipse for the differential rotation measurements. These error ellipse was generated by varying some of the stellar parameters, including the star's inclination ($\pm$ 10^o) and the Stokes V global magnetic field ($\pm$ 10%). The error bars on each individual measurement are 1-σ errors in the paraboloid fit.

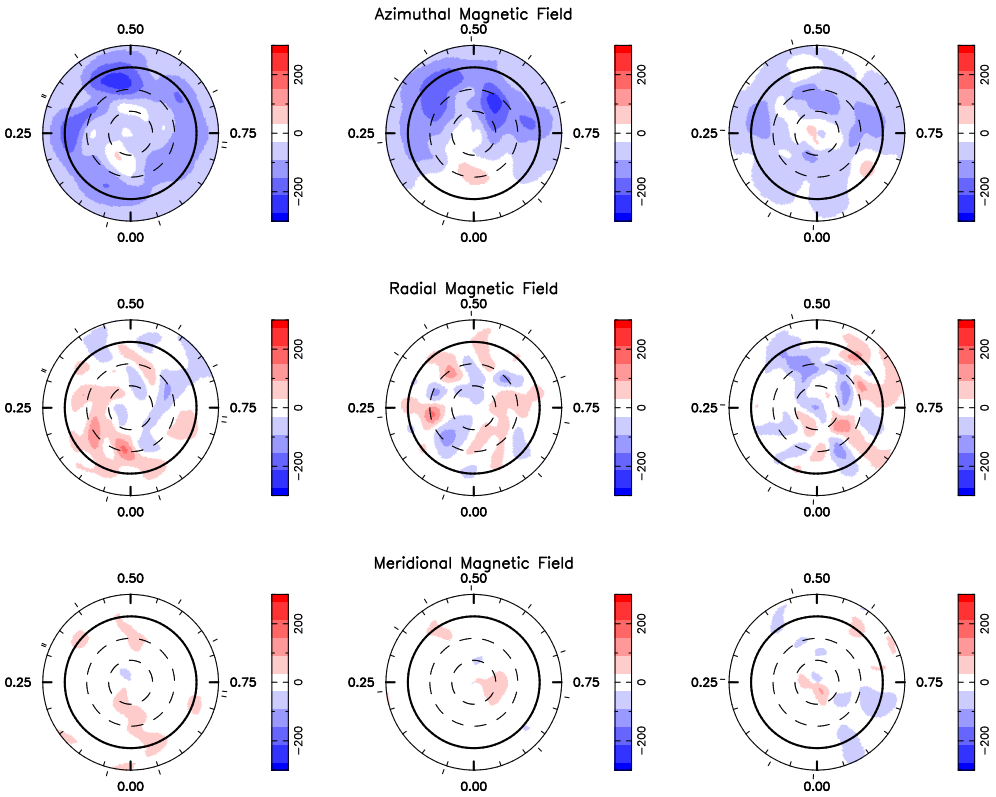

Figure 7.15: Maps for Stokes V EK Draconis assuming differential rotation, based on Jan 2007 measurement. The left column shows the magnetic maps from the 30 Nov to 11 Dec, 2006 run at the CFHT, with a global magnetic field of 86 G. The middle maps are based on data taken at the TBL from the Jan 25 - Feb 04, 2007, with a global magnetic field of 73 G. The right column shows the maps based on the data taken at the TBL from the Feb 15 - Feb 28, 2007, with a global magnetic field of 59 G. From top to bottom: azimuthal, radial and meridional fields. These maps are polar projections extending down to -30^o. The bold lines denote the equator and the dashed lines are +30^o and +60^o latitude parallels. The radial ticks indicate the phases at which this star was observed spectroscopically. The scale of the magnetic images are in Gauss.

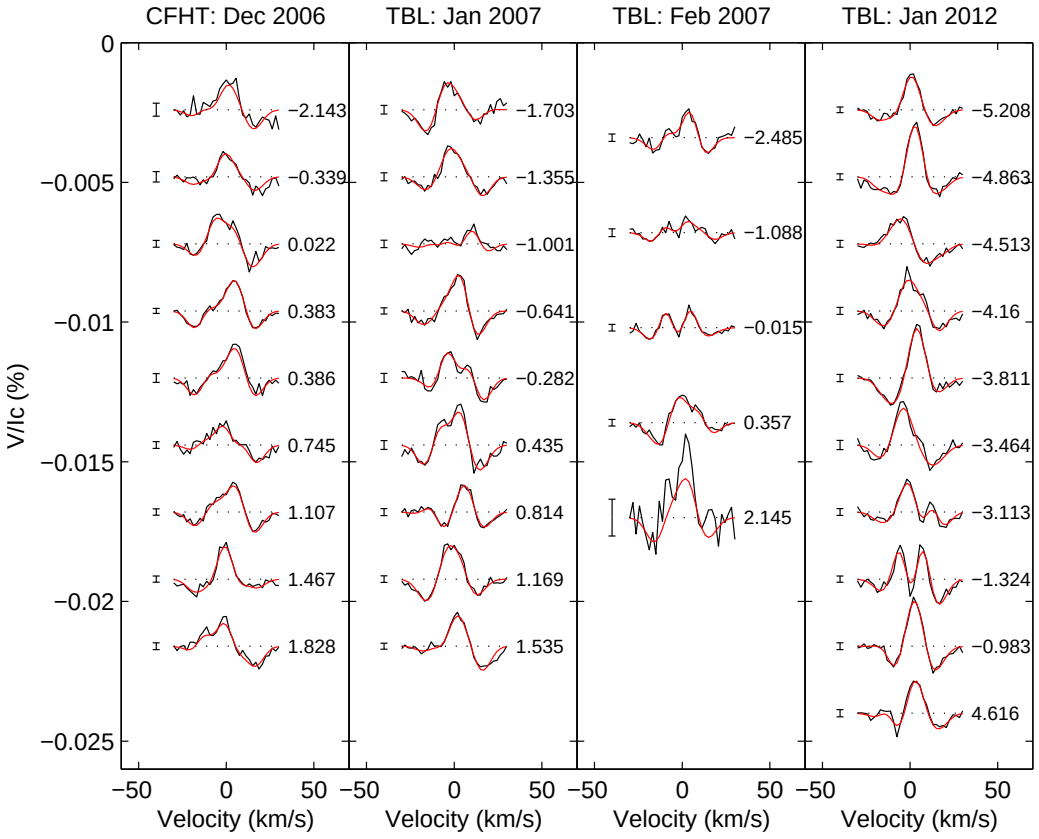

Figure 7.16: The maximum-entropy fits to the Stokes V LSD profiles for EK Draconis with surface differential rotation, as measured using the Stokes V profiles during the January observation run, incorporated into the analysis. The red (thick) lines represent the modelled lines produced by the Zeeman Doppler imaging process whereas the thin lines represent the actual observed LSD profiles. Each successive profile has been shifted down by 0.0024 for graphical purposes. The error bar on the left of each profile is plotted to $\pm$ 0.5σ. The rotational phases, in terms of the number of rotational cycles, at which the observations took place are indicated to the right of each profile. Each column represents an observation run.

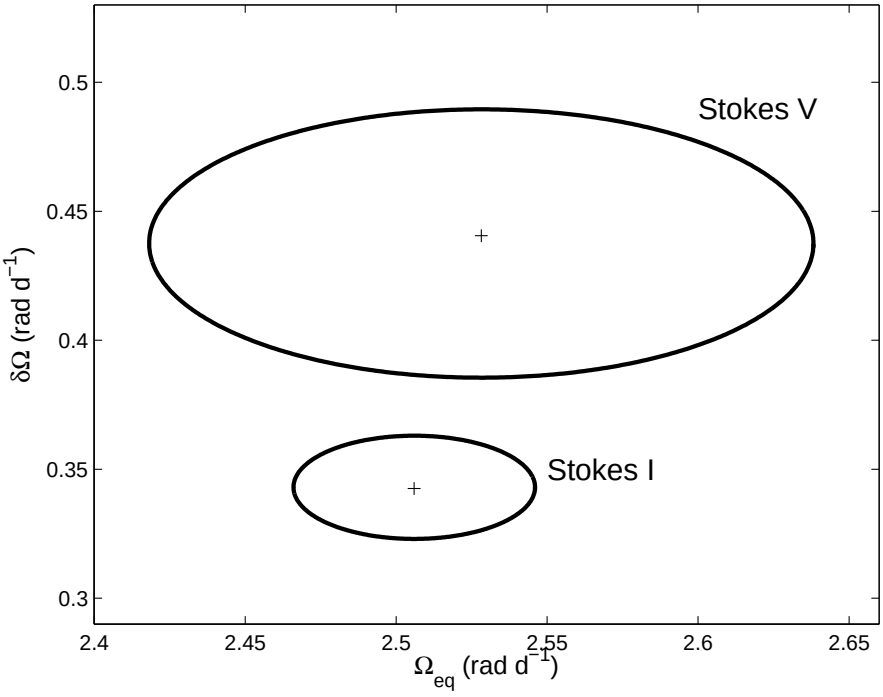

Figure 7.17: The two error ellipses for the differential rotation measurements, for both the Stokes I and the Stokes V, superimposed on the same plane. These error ellipses were generated by varying some of the stellar parameters, including the star's inclination ($\pm$ 10^o) and the Stokes I spot coverage or the Stokes V global magnetic field ($\pm$ 10%), as shown in Figures 7.7 and 7.14.

Table 7.6: A comparison between the two geometries: poloidal and toroidal magnetic fields for EK Draconis for the 2006/7 and 2012 data considering both solid-body rotation and differential rotation parameters incorporated into the data. In case case, the first number is that from Solid-Body rotation while the second number is that assuming differential rotation. The differential rotation parameters were those found using the Stokes V data during the 2007 subset.

Map	Total Energy	poloidal[1] (%)	dipole[2] (%)	quad.[2] (%)	oct.[2] (%)	higher orders[2,3]
CFHT Dec 06	9802 v 10078	22 v 20	32 v 30	10 v 12	7.6 v 11	50 v 47
TBL Jan 07	9553 v 8753	42 v 37	33 v 43	14 v 15	8 v 7	45 v 35
TBL Feb 07	6232 v 5107	34 v 42	33 v 14	10 v 10	9 v 11	49 v 66
TBL Jan 12	12837 v 14490	34 v 45	19 v 8	20 v 11	14 v 13	48 v 69
	Total Energy	toroidal[1] (%)	dipole[2] (%)	quad.[2] (%)	oct.[2] (%)	higher order[2,3]
CFHT Dec 06	9802 v 10078	78 v 80	84 v 86	4 v 4	4 v 4	9 v 6
TBL Jan 07	9553 v 8753	58 v 63	77 v 75	9 v 15	2 v 3	12 v 7
TBL Feb 07	6232 v 5107	66 v 58	81 v 70	11 v 13	1 v 2	7 v 14
TBL Jan 12	12837 v 14490	66 v 55	54 v 65	24 v 7	11 v 2	10 v 26

[1] % of the total magnetic energy available.

[2] % of that particular field geometry.

Listed also is the fraction of the poloidal or toroidal magnetic energy in the dipolar ($\ell = 1$), quadrupolar ($\ell = 2$), octupolar ($\ell = 3$) and [3]higher order multipole ($\ell \geq 4$) components.

have undergone a reversal in the radial field from 2007 to 2008. However, when using fewer profiles in the 2008 data, to match the number and phase of the individual profiles, the radial field was not recovered to the same level of detail. Hence this apparent reversal in the radial field may well be as a result of fewer profiles due to poor phase coverage. The radial field may have undergone a major reorientation during this time but further data would be required to support this. As the toroidal field remained in the same orientation, this work cannot claim a magnetic reversal unlike other sun-like stars such as τ Boötis (Donati et al., 2008b; Fares et al., 2009).

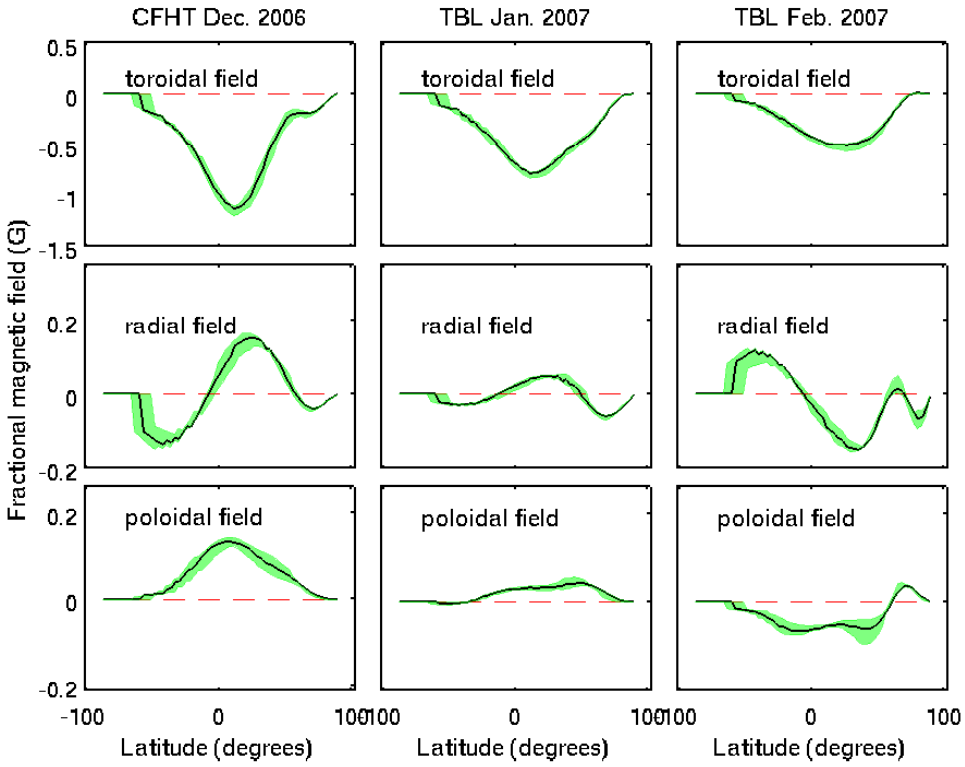

Figure 7.18: This shows a series of plots of fractional magnetic field strength (G) as a function of latitude for the poloidal field (top series), toroidal field (middle series) and radial field (bottom series) for the 3 distinct datasets, with that obtained from the December 2006 CFHT data on the left, while the January 2007 TBL data is in the middle series of frames while the February 2007 TBL is the right series of frames. The shaded (coloured) regions indicate the error in the fractional magnetic field strength at each latitude point. This was found by systematically changing key parameters such as differential rotation parameters, $v \sin i$ and inclination. Differential rotation, $\Omega_{eq} = 2.53^{+0.049}_{-0.050}$ rad d^{-1}and $\delta\Omega = 0.44^{+0.21}_{-0.12}$ rad d^{-1}, was incorporated into the analysis.

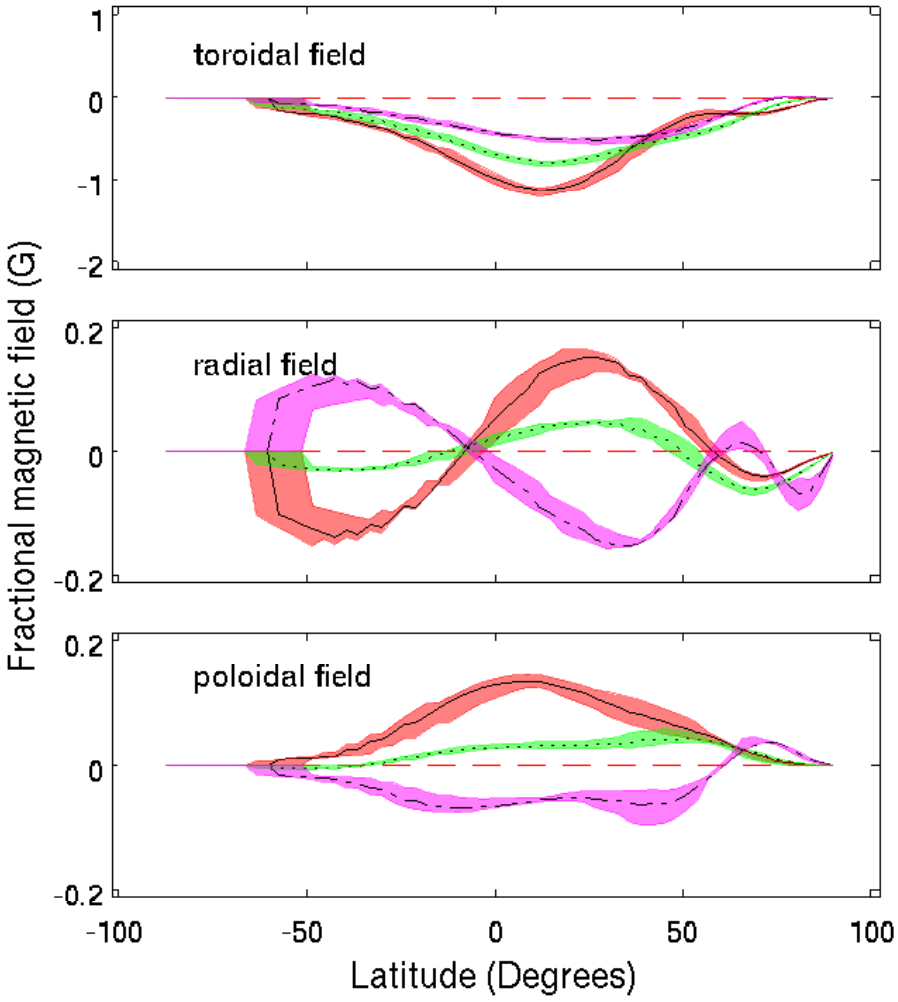

Figure 7.19: This shows a comparison of fractional magnetic field strength (G) as a function of latitude for the poloidal field (top), toroidal field (middle) and radial field (bottom) for all three datasets. The each dotted line shows the field strength while the coloured (shaded) regions indicate the error in that value at each latitude point. The red line is for the field strength from the 2006 CFHT data, the green line is that from the January 2007 TBL data while the magenta line is from the February 2007 TBL data. Differential rotation was incorporated into the analysis.

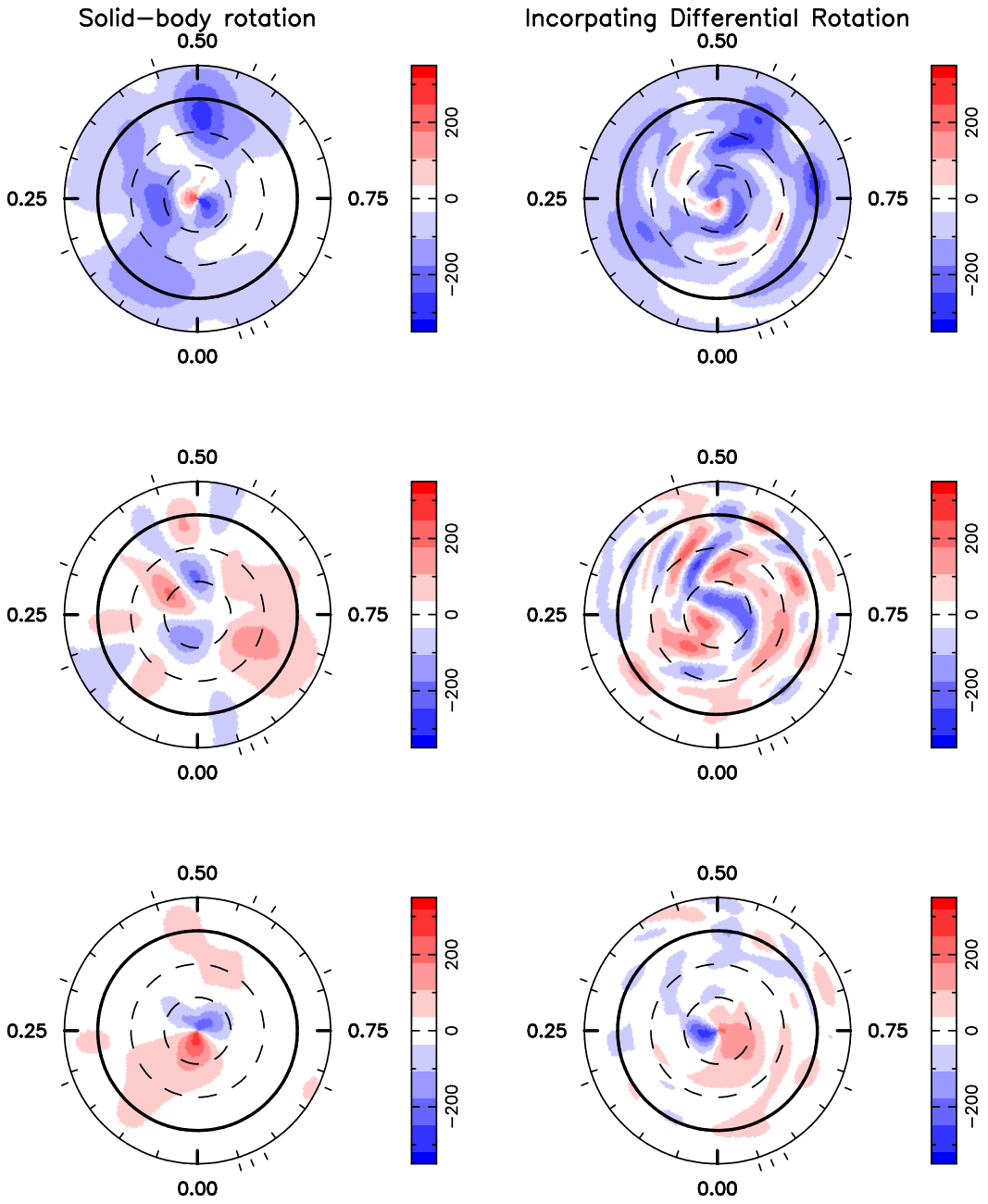

Figure 7.20: The magnetic maps for EK Draconis observed during 2012 at TBL. Solid-body rotation was assumed for the maps on the left. The maps on the right have had differential rotation, as measured from the 2007 data, incorporated into the imaging process. The azimuthal maps are along the top row, radial maps along the middle row while the meridional maps are along the bottom row. These maps are polar projections extending down to -30^o. The bold lines denote the equator and the dashed lines are +30^o and +60^o latitude parallels. The radial ticks indicate the phases at which this star was observed spectroscopically. The scale to the right of each map in in Gauss.

Table 7.7: A comparison between the symmetry of the two geometries: poloidal and toroidal magnetic fields for EK Draconis for the late-2006, early-2007 data considering both solid-body rotation and differential rotation parameters incorporated into the data. In each case, the first number is that from solid-body rotation while the second number is that from differential rotation. The differential rotation parameters were those found using the Stokes V data during the 2007 subset.

	poloidal		toroidal	
Map	axisym. (% total)[1]	non-axisym. (% total)[1]	axisym. (% total)[1]	non-axisym. (% total)[1]
CFHT Dec 06	6 v 6	13 v 12	74 v 77	3 v 2
TBL Jan 07	3 v 2	33 v 30	53 v 60	5 v 3
TBL Feb 07	7 v 10	22 v 25	63 v 53	3 v 5
TBL Jan 12	10 v 15	17 v 24	61 v 46	5 v 8

[1]The fraction of the total energy stored in the axisymmetric component (m = 0).

7.4.3 Chromospheric Activity

Chromospheric activity was measured using the Ca II H & K, Ca II Infrared Triplet (IRT) and Hα spectral lines. The $N_{Ca\,II\,HK}$-index for EK Draconis was determined using the procedure as explained in Chapter 5. Again the overlapping order was removed from the spectrum and the continuum was checked against synthetic spectra from the POLLUX database (Palacios et al., 2010). In all cases, the continuum matched reasonably well hence was not corrected for as done by Morgenthaler et al. (2012). The resulting $N_{Ca\,II\,HK}$-index was converted to match the Mount Wilson S-values (Duncan et al., 1991) using Equation 5.2. The transformation coefficients were determined by Marsden et al. (2013: *in preparation*) by matching 23 stars that were in common to both the CFHT database and the Mount Wilson project (Wright et al., 2004). The coefficients for Equation 5.2 are listed in Table 7.8.

As in Chapter 5, two further activity indices's were used. The first involves the Hα spectral line and the second involves the Ca II IRT lines. The continuum was checked against that of the continuum of the synthetic normalised spectrum from the POLLUX database (Palacios et al., 2010). In both cases, the continuum matched reasonably well hence was not corrected for as in the case with the Ca II H & K spectral lines.

Table 7.8: The coefficients, listed in Equation 5.2, as determined by Marsden et al. (2013: *in preparation*)

Coefficient	ESPaDOnS	NARVAL[1]
C_1	7.999	-1.287 $\times$ 10^{+3}
C_2	-3.904	-2.502 $\times$ 10^{+2}
C_3	1.150	-8.877 $\times$ 10^{+2}
C_4	1.289	-4.271 $\times$ 10^{+2}
C_5	-0.069	1.183 $\times$ 10^{-3}

[1] The coefficients listed in this table are the same as those used in Chapter 4.

Table 7.9: Activity indices's determined for EK Draconis.

Date	S-index[1]	$N_{H\alpha}$	N_{CaIRT}
Dec, 2006	0.612 $\pm$ 0.037	0.385 $\pm$ 0.009	1.055 $\pm$ 0.019
Jan, 2007	0.609 $\pm$ 0.048	0.392 $\pm$ 0.008	1.081 $\pm$ 0.020
Feb, 2007	0.615 $\pm$ 0.023	0.389 $\pm$ 0.006	1.052 $\pm$ 0.025
Jan, 2012	0.585 $\pm$ 0.032	0.391 $\pm$ 0.010	1.074 $\pm$ 0.019

[1]The resulting N_{CaIIHK}-index was converted to match the Mount Wilson S-values (Duncan et al., 1991) using the transformation shown in Equation 5.2.

The TBL Hα-index was determined using Equation 5.3 and the TBL CaIRT-index was determined using Equation 5.4.

Figure 7.21 shows the variation in the Ca II H & K lines, Ca II IRT and Hα spectral lines during the four separate observing runs. The epochs were set to match those used in the DI and ZDI maps. Using Equation 5.8, and based on the values from Rutten (1984) (as explained in Wright et al., 2004; Schröder et al., 2009), $LogR'_{HK}$ was determined as $-4.13^{+0.06}_{-0.08}$. Table 7.9 shows the average S-index, $N_{H\alpha}$ and N_{CaIRT} indices's for the respective datasets while Figure 7.22 shows this information graphically. Each value is the average over the observing run with the error showing the variation during this time, most likely as a result of modulation due to the rotation of the star.

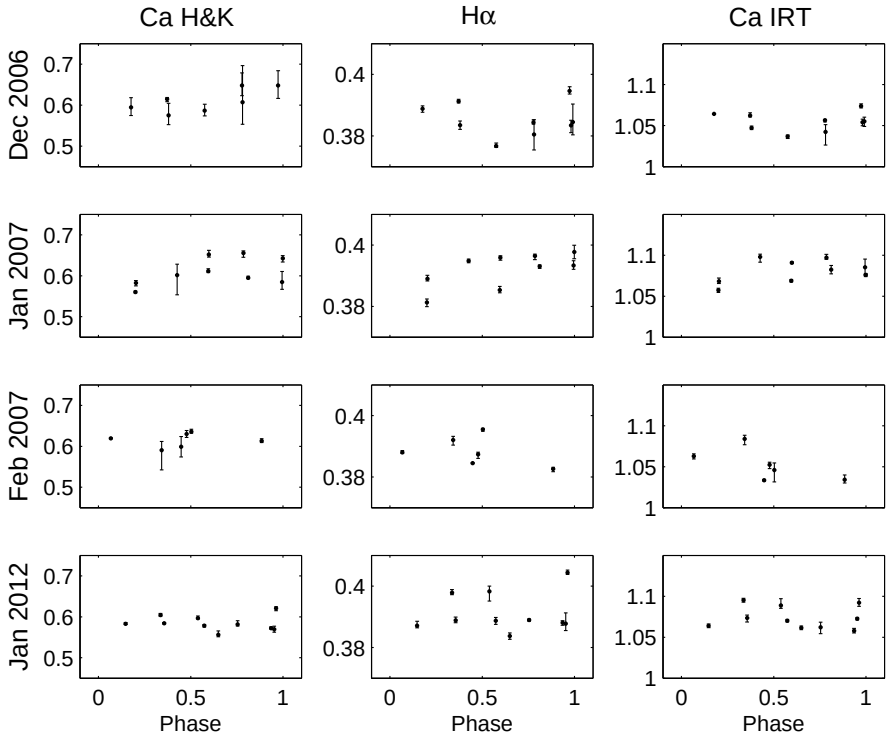

Figure 7.21: Modulation of the various chromospheric indicators due to rotational phase at different epochs. The epochs were: HJD = 2454075.22167; 2454130.72767; 2454153.43467 and 2455952.37967 and the equatorial period, based on the differential rotation measurement, was used to produce the phase of these data. The period used was 2.51 d.

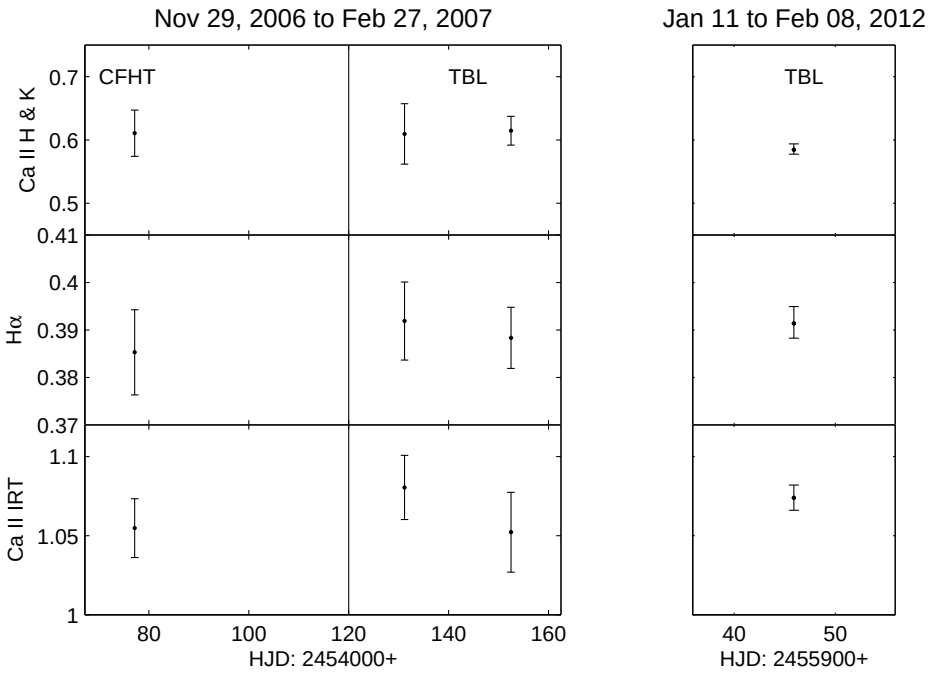

Figure 7.22: The variation in the chromospheric activity over the 2006/2007 and 2012 observing runs. The Heliocentric Julian Date (HJD) is approximately the midpoint at each epoch, matched to the exact number of rotations since the beginning of the observing run.

7.5 Discussion

The young solar analogue EK Draconis is a very active young, sun-like star that underwent significant photospheric and chromospheric changes during the 3 months of observations in 2006/7. The spot maps show large high-, mid- and low-latitude features but not a truly polar spot, unlike other young solar-type stars observed using DI. This spot arrangement was observed by others, such as Järvinen et al. (2007), who observed both high- and low-latitude spots, with one spot (epoch = 2002.16) at $\approx 60^o$ present. Strassmeier and Rice (1998) observed a dominant cool spot at a latitude $\approx 70^o$-80^o. Likewise, this project has found low- to high- latitude spots but rarely above 60^o, similar to the observation by Järvinen et al. (2007). The starspots on EK Draconis are far higher, in latitude, than where our Sun show spots. There was significant spot evolution occurring on this star, thereby supporting Dorren and Guinan (1994) observations of significant changes to the spot distribution in the order of a few days. Even when "splitting" the data, there are still some "mis-fitting" of the data as shown in Figures 7.8 (phase: 1.106 to 1.108) and 7.10 (phase: 2.142 to 2.144) that may be attributed to further spot evolution. These changes are possibly a result of the magnetic field reorganising itself from a strongly toroidal field ($\sim$80%) to a more balanced field in only 3 months, as shown in Figure 7.23. Alternatively, the mis-fitting of the data occurring near zero-velocity in this figures could be the result of *ZDICAM's* inability to adequately map high latitude spot features. As mentioned above, Strassmeier and Rice (1998) observed a dominant cool spot at a latitude $\approx 70^o$-80^o. High cadence data on EK Draconis over several nights would be required to fully constrain the brightness map and to accurately observe the spot evolution.

As mentioned in Section 7.4.1.1, Güdel et al. (1995) observed periodicity in the X-ray light curve and using auto-correlation analysis found a "broad secondary maximum around P = 2.53d". From this analysis of differential rotation, it can be concluded that Güdel et al. (1995) has observed the equatorial period of EK Draconis. Using the Stokes I information, the equatorial region of EK Draconis was rotating at $\Omega_{eq} = 2.51^{+0.019}_{-0.015}$ rad d^{-1} equating to a period of $\sim 2.50 \pm 0.02$ d. Using the Stokes V information, the equatorial region of EK Draconis was rotating at $\Omega_{eq} = 2.53 \pm 0.05$ rad d^{-1}, equating to a period of ~ 2.48 *pm* 0.05 d. Considering the size of the respective error ellipses, as

shown in Figure 7.17, the results are consistent with the observations of Güdel et al. (1995).

Petit et al. (2008) found that stars with rotation periods less than 12 days had significant surface toroidal fields while Donati and Landstreet (2009) suggests that stars with a Rossby number of ≤ 1, but more massive than 0.5 $M_{\odot}$ had substantial toroidal component with a mostly non-axisymmetric poloidal component. EK Draconis had a convective turnover time of 12.6 d with a Rossby number of 0.2. These values were calculated from Equations 5.10 and 5.9 respectively. EK Draconis has a substantial toroidal component, even though it was reorganising itself from the strongly toroidal field of $79.9^{+2.7}_{-3.3}$% in December, 2008, to $58.3^{+6.5}_{-5.6}$% by the end of February, 2007. This toroidal field remained firmly axisymmetric, with over 90% of the toroidal field being axisymmetric. The poloidal field, as shown in Figure 7.23, has increased in dominance from ∼20% in December, 2006, to ∼40% by the end of February, 2007. The poloidal field was predominantly non-axisymmetric reaching a maximum of ∼80% during the January 2007 dataset. So these observations of significant toroidal fields with non-axisymmetric poloidal fields support the findings of Petit et al. (2008) and Donati and Landstreet (2009).

Marsden et al. (2011a) found that small datasets provided difficulties in determining the magnitude and makeup of the global mean magnetic field. The analysis of the young star HD 35296 in Chapter 5 showed that reducing the number of profiles in a dataset slightly decreased the magnitude of the magnetic field recovered but had only a minor effect on the configuration of that magnetic field. The same procedure of reducing the number of profiles was conducted for EK Draconis. The CFHT and January TBL datasets were reduced in size to match the number of profiles and phase observed in the February dataset. Analysis of these reduced datasets showed that the geometry remained similar. Figure 7.23 clearly demonstrates this similarity. In this figure, the data, complete with error bars, represents the geometry derived using all the available profiles whereas the "$*$" represent the value using the reduced number of profiles. It may be deduced that the changes occurring in the balance of the poloidal-toroidal field configurations were real, and not an artifact of the reduced number of profiles. In addition, the toroidal field was predominately a dipole, axisymmetric field whereas the poloidal field was still predominately a complex, non-axisymmetric field. This is shown

in Tables 7.6 and 7.7. In summary, it may be concluded that the global magnetic field orientations during the three months had substantially changed.

EK Draconis is very similar to HD 35296 (Chapter 5) and HD 29615 (Chapter 6). All three of these sun-like stars have similar ages, masses, radii and rotational velocities. Table 7.11 highlights these similarities. All exhibit reasonably high levels of differential rotation, with *laptimes* ranging from ∼11 d for HD 29615 to ∼22 d for HD 35296.
All three of these sun-like stars exhibit azimuthal fields indicating that the dynamo generating these magnetic fields is most likely operating entirely throughout the convective zone in the form of a distributed dynamo. The toroidal fields of all three sun-like stars are strongly axisymmetric while the poloidal fields tend to be more non-axisymmetric; however, HD 29615 does not follow the other two stars with the poloidal field being predominately axisymmetric with only ∼33% of the poloidal energy held in the non-axisymmetric configuration. This has implications for the young Sun, as its dynamo must have been significantly different as it moved onto the main-sequence. The Rossby number, as explained in Section 5.4.5, is lowest in HD 29615 amongst the three stars (Ro=0.14). Donati and Landstreet (2009) suggests that with small Ro values indicating very active stars rotating fast enough to ensure that the Coriolis force strongly impacts convection. The conclusion is that the star with the lowest Rossby number also has the highest differential rotation shear, as is the case when comparing these three sun-like stars.

7.6 Conclusions

Unlike that observed by Järvinen et al. (2007), this investigation found strong differential rotation with a $\Omega_{eq} = 2.51^{+0.019}_{-0.015}$ rad d^{-1} and a $\delta\Omega = 0.34^{+0.02}_{-0.048}$ rad d^{-1} for EK Draconis when using the brightness features. When using the magnetic topologies, $\Omega_{eq} = 2.53^{+0.049}_{-0.050}$ rad d^{-1} and $\delta\Omega = 0.44^{+0.21}_{-0.12}$ rad d^{-1}. Also there was significant spot evolution occurring on this star, very similar to other G-type stars observed by Barnes (1999) (α Persei cluster) and by Donati et al. (2003a) on the RS CVn-type star HR 1099 (SpType: K2:Vnk[1]). This supports Dorren and Guinan (1994) observations of significant changes to the spot distribution in the order of a few days. These

[1] Montes et al. (2001)

Table 7.10: A comparison between the two geometries: poloidal and toroidal magnetic fields for EK Draconis. This utilises the differential rotation parameters found for the January 2007 data.

Parameter	Dec, 2006	Jan, 2007	Feb, 2007	Jan, 2012
poloidal[1]	$20.1^{+3.3}_{-2.7}$	$36.8^{+6.2}_{-2.7}$	$41.7^{+5.6}_{-6.6}$	$45.4^{+6.5}_{-6.0}$
dipole[2]	$30.4^{+10.6}_{-11.2}$	$43.1^{+5.5}_{-14.8}$	$13.5^{+7.0}_{-5.7}$	$7.6^{+9.2}_{-4.6}$
quadrupole[2]	$11.8^{+6.1}_{-4.8}$	$14.6^{+3.7}_{-2.1}$	$10.2^{+3.7}_{-5.1}$	$11.1^{+8.0}_{-8.6}$
octupole[2]	$10.7^{+1.2}_{-1.7}$	$7.4^{+5.4}_{-3.2}$	$10.5^{+4.7}_{-3.7}$	$12.5^{+5.3}_{-5.8}$
higher order [2,3]	$47.1^{+12.3}_{-9.3}$	$35.0^{+7.3}_{-4.9}$	$65.9^{+8.4}_{-5.1}$	$68.7^{+9.6}_{-6.0}$
axisymmetric[1]	$5.7^{+1.9}_{-1.3}$	$2.0^{+2.1}_{-1.2}$	$9.8^{+4.2}_{-4.1}$	$14.7^{+11.2}_{-3.8}$
non-axisymmetric[1]	$11.7^{+3.4}_{-2.9}$	$29.6^{+2.2}_{-3.1}$	$24.7^{+7.7}_{-6.8}$	$23.9^{+3.6}_{-6.8}$
axisymmetric[2]	$28.6^{+4.9}_{-8.5}$	$5.5^{+4.1}_{-3.1}$	$23.8^{+11.9}_{-11.4}$	$32.3^{+17.8}_{-8.5}$
non-axisymmetric[2]	$58.3^{+6.3}_{-7.6}$	$80.7^{+6.5}_{-15.8}$	$58.9^{+9.8}_{-10.0}$	$52.9^{+9.2}_{-16.1}$
toroidal[1]	$79.9^{+2.7}_{-3.3}$	$63.3^{+2.8}_{-6.2}$	$58.3^{+6.5}_{-5.6}$	$54.7^{+5.9}_{-6.4}$
dipole[2]	$85.6^{+2.7}_{-3.0}$	$75.3^{+5.0}_{-7.2}$	$69.8^{+5.0}_{-4.8}$	$64.8^{+6.5}_{-19.1}$
quadruple[2]	$4.0^{+2.5}_{-2.0}$	$15.2^{+6.0}_{-7.5}$	$13.4^{+4.9}_{-4.8}$	$7.0^{+3.4}_{-3.1}$
octupole[2]	$4.0^{+2.4}_{-1.3}$	$2.9^{+0.7}_{-0.8}$	$2.5^{+1.8}_{-1.2}$	$2.3^{+2.2}_{-1.6}$
higher order[2,3]	$6.4^{+2.6}_{-1.3}$	$6.6^{+3.6}_{-1.9}$	$14.4^{+3.5}_{-3.4}$	$25.7^{+20.4}_{-8.3}$
axisymmetric[1]	$77^{+2.3}_{-3.1}$	$60.4^{+2.2}_{-7.7}$	$53.2^{+5.8}_{-5.2}$	$46.0^{+6.0}_{-8.3}$
non-axisymmetric[1]	$2.5^{+1.2}_{-0.7}$	$2.8^{+1.5}_{-0.9}$	$4.5^{+0.9}_{-1.3}$	$8.10^{+6.6}_{-2.8}$
axisymmetric[2]	$96.3^{+1.0}_{-1.7}$	$95.4^{+1.5}_{-3.1}$	$91.3^{+1.6}_{-1.5}$	$84.1^{+4.9}_{-10.7}$
non-axisymmetric[2]	$3.1^{+1.5}_{-0.8}$	$4.4^{+3.0}_{-1.4}$	$7.7^{+1.3}_{-2.2}$	$14.8^{+10.8}_{-5.1}$

[1] this is a % of the total magnetic energy available.

[2] this is a % of that particular field geometry.

[3] higher order multipole magnetic fields ($\ell \geq 4$)

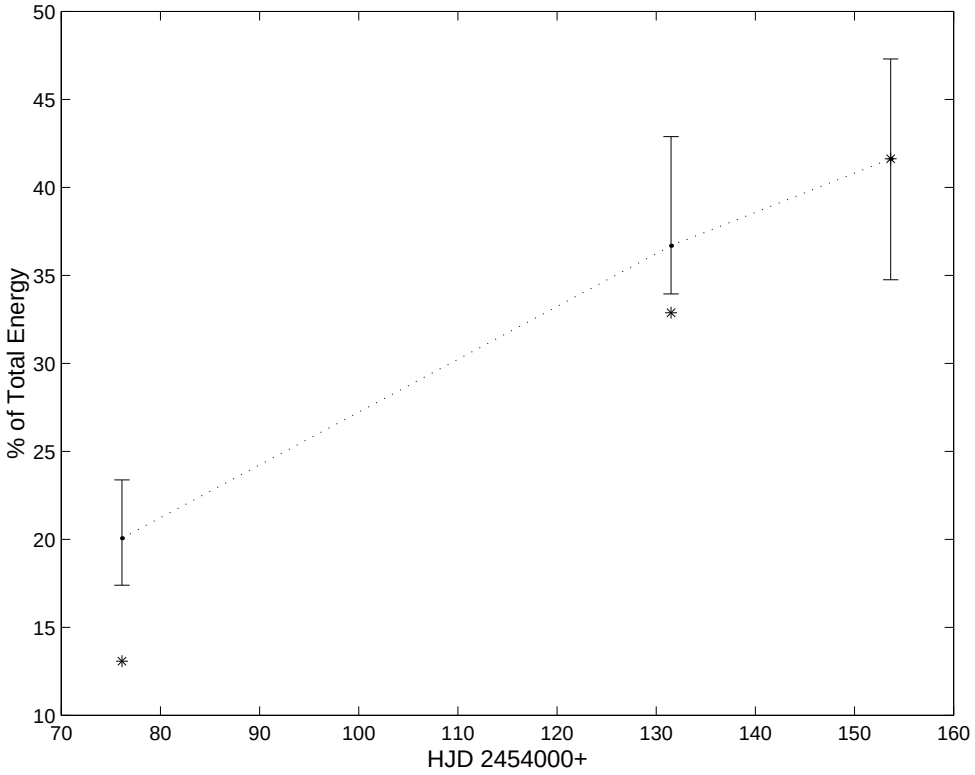

Figure 7.23: The variation in the poloidal component of the magnetic field as a function of time. The data points, represented by '**.**', are the fraction of the average poloidal component compared with the total magnetic energy. The error bars represent the range of the this fraction found by varying a number of parameters. The '$*$' represent that fraction of the total energy this is the poloidal component when using a reduced number of profiles, to match the coverage of that in February, 2007. The right panel shows the value of the average poloidal component in 2012.

Table 7.11: A comparison between the fundamental parameters of HD 35296, HD 29615 and EK Draconis

Parameter	HD 35296	HD 29615	EK Draconis
Spectral Type	F8V	G3V	G1.5V
Equatorial period, d	3.5±0.2	2.34±0.2	2.49±0.05
Inclination angle, ^{o}	65±5	70±5	60±5
Photospheric Temperature, T_{phot}, K	6080	5820±50	5750
ΔTemp = T_{phot} - T_{spot}, K	–	1900	1700
Stellar Radius: $R_\odot$	∼1.13	∼1.0	0.99
Stellar Mass: $M_\odot$	∼1.10	∼0.95	1.06
Projected Rotational Velocity, $v\sin i$, $\mathrm{km\,s^{-1}}$	16.0±0.1	19.5±0.5	16.8±0.2
Convective turnover time, d	9.1	16.2	12.6
Rossby Number	0.38	0.14	0.20
Stokes I: $\delta\Omega$, in $\mathrm{rad\,d^{-1}}$	–	$0.09^{+0.04}_{-0.02}$	$0.34^{+0.02}_{-0.048}$
Stokes I: *laptimes*, d	–	$30^{+5}_{-2.6}$	18.5^{+1}_{-3}
Stokes V: $\delta\Omega$, in $\mathrm{rad\,d^{-1}}$	0.28±0.08	$0.58^{10.12}_{+0.13}$	$0.44^{+0.21}_{-0.12}$
Stokes V: *laptimes*, d	22±5	11^{+3}_{-2}	$14^{+5}_{-0.5}$

changes are a result of the magnetic field reorganising itself from a strongly toroidal field (∼80%) to a more balanced field in only 3 months, as shown in Figure 7.23. In summary, the magnetic field was evolving from a dominant toroidal field to a more balanced poloidal-toroidal field. The poloidal field was predominately non-axisymmetric while the toroidal field as almost entirely axisymmetric. This is consistent with other stars. This shift saw enhanced chromospheric activity during this transition, as shown in Figure 7.22, before returning to similar levels when this "magnetic transition" had begun to stabilise.

Chapter 8

Discussion & Conclusions

8.1 Introduction

The role of magnetic fields in stellar studies is very broad, occurring across a substantial portion of the H-R diagram. The study of these magnetic fields provide clues on a range of stellar properties including the influence on star-formation, stellar activity and the underlying dynamo, structure, angular momentum loss and magnetic braking and most recently, influence on attendant extra-solar planets (e.g. Vidotto et al., 2013). This thesis focussed on young, late F-/early G-type stars with temperatures commensurate with that of our Sun. This work compliments the work on more massive stars (MiMeS[1]: Magnetism in Massive Stars) as well as the magnetic fields of low-mass stars (Bcool[2]). To the best of my knowledge, this is the only comprehensive research on the magnetic configurations of young solar-type stars hence is timely and relevant as it widens our understanding of magnetic activity across a broad range of stars and gives crucial clues on the possible magnetic behaviour of the young Sun.

Mapping the magnetic field topology of a number of young solar-type stars permits the investigation of the underlying stellar dynamo. Resolving the origin of the stellar dynamo helps address the more general question of how stellar magnetic cycles develop in young stars, and affect any attendant emerging planetary systems. The key aims of this thesis were:

[1] http://www.physics.queensu.ca/ wade/mimes/MiMeS_Magnetism_in_Massive_Stars.html
[2] http://bcool.ast.obs-mip.fr/Bcool/Bcool__cool_magnetic_stars.html

1. verify field structures indicative of dynamos distributed across the convective zone,

2. determine the temporal variation of surface magnetic topologies,

3. confirm strong but varying differential rotation, consistent with emerging activity cycles, is dependent on convective zone depth and rotation rate,

Five stars were identified for investigation: HD 106506, HD 76298 (HIP 43720), HD 35256 (V1119 Tau), HD 29615 (HIP 21632) and HD 129333 (EK Draconis). Each star had its magnetic topology mapped and differential rotation measured using brightness (Stokes I) and magnetic (Stokes V) features. Each star showed significant differences in the magnitude of the differential rotation and in the distribution of spots from that observed on the Sun.

8.2 Image reconstruction: Stokes I Doppler imaging and surface differential rotation

The Sun today generally has spots that are restricted to latitudes $\pm$ 30^o, although they can extend to $\pm$ 45^o during periods of solar maximum (as shown in Figure 1.7). However, young stars that rotate more rapidly than the Sun have starspots at all latitudes. HD 106506, HD 76298 and HD 29615 all have strong polar (or nearly polar) spots, coupled with mid- and lower-latitude features. The exception was EK Draconis that exhibited high-latitude but not truly polar spot features. It appeared that EK Draconis' spots were restricted to 60^o latitude. Spot mapping was not undertaken on HD 35296 as the $v\sin i$ was too low to produce any meaningful map. The exact reasons why rapidly rotating stars have polar spots are still not fully understood. One theory (Schüssler et al., 1996; Buzasi, 1997; DeLuca et al., 1997) postulates that high-latitude, but not truly polar, spots are a result of the increased Coriolis effect, due to the rapid rotation, which may have the effect of deflecting the spot features to higher latitudes as they erupt through the star's convection zone. An alternative hypothesis (Schrijver and Title, 2001; Kitchatinov and Rüdiger, 1999) involves the transport of flux through the process of meridional flow. Weber et al. (2005) have reported tentative evidence for large poleward meridional flows on early-K giants, but as yet, this has not

been detected for young solar-type stars. The case of EK Draconis is more curious. EK Draconis underwent rapid spot emergence and evolution during the three months of observations. This is not unusual as even our Sun's spots have lifetimes that range from a few days to several weeks. Barnes (1999) observed such variability on G-dwarf stars in the α Persei cluster in time-scales of less than a month while Donati et al. (2003a) observed temporal variability on the RS CVn-type star HR 1099 (SpType: K2:Vnk[1]) occurring on time-scales as short as a fortnight. Dorren and Guinan (1994) noted significant changes to the spot distribution on EK Draconis in the order of a few days. Nevertheless, many of the brightness maps suffered from poor phase coverage. High cadence data on EK Draconis over several nights would be required to fully constrain the brightness map and to accurately observe the spot evolution.

8.2.1 Differential Rotation

One of the main drivers of the stellar dynamo is differential rotation. Differential rotation was measured using the χ^2 minimisation technique developed by Donati et al. (2000), as discussed in Section 2.6. All the results from this project are listed in Tables 8.1 and 8.2. Using the Stokes I information, EK Draconis had the highest rotational shear with $\delta\Omega = 0.34^{+0.02}_{-0.05}$ rad d^{-1}. This result must be treated with an element of caution due to the poor phase coverage, coupled with rapid spot evolution observed on this star. HD 106506 had a substantial rotation shear with $\delta\Omega = 0.21^{+0.02}_{-0.03}$ rad d^{-1}. This result was based on excellent phase coverage, as observed by the radial ticks around the map in Figure 3.4. Both HD 76298 and HD 29615 had polar spots with limited low- to mid-latitude features on the photospheric surface. This may have had an unintended effect on the measurement of the surface differential rotation.

The dependence of differential rotation on effective temperature, hence convective zone depth, was first investigated by Barnes et al. (2005a) and concluded that differential rotation is dependent on the spectral type (effective temperature) with M-dwarfs rotating almost as a solid body through to early-G dwarfs exhibiting a strong rotational shear. They developed a power law, $\delta\Omega \propto T^{8.92\pm0.31}$. This project focussed on stars with effective temperatures commensurate with that of the Sun (T_{phot} from 5750 K to 6080 K). Figure 8.1 (upper panel) shows that there is a large range of differential rotation for stars with effective temperatures close to 6000 K. One of that key hypotheses

[1] Montes et al. (2001)

Table 8.1: Summary of differential rotation parameters as measured by this work using the χ^2 minimisation technique (continued in Table 8.2.

Parameter	HD 106506	HD 76298
Spectral Type	G0V[1]	G1V[1]
Photometric Period, d	1.416 ± 0.133	3.189[3]
Equatorial Period, d	1.39 ± 0.01	3.14 ± 0.1
Inclination Angle, ^{o}	65 ± 5	55 ± 5
$v\sin i$, km s^{-1}	79.5 ± 0.5	39.5 ± 0.5
v_{mag} [6]	8.5617 ± 0.0025	9.2461 ± 0.0038
T_{phot}, K	5900 ± 50	6000 ± 30
T_{spot}, K	4000 ± 50	4100 ± 30
V_{rad}, km s^{-1}	13.1 ± 0.1	2.4 ± 0.1 (2010)
		2.2 ± 0.1 (2011)
Stellar Radius, $M_\odot$ [8]	2.15 ± 0.26 [2]	$2.2^{+0.6}_{-0.4}$
CZD, $R_\star$ ($R_\odot$) [10]	0.137 (0.284)	0.206 (0.445)
Age, Myr [11]	≈10	Uncertain[12]
Mass, $M_\odot$ [11]	1.5 ± 0.1 [2]	∼1.6
Stokes I: Ω_{eq}, rad d^{-1}	4.54 ± 0.01	$2.01^{+0.10}_{-0.03}$
Stokes I: $\delta\Omega$, rad d^{-1}	$0.21^{+0.02}_{-0.03}$	$0.09^{+0.03}_{-0.04}$
Stokes V: Ω_{eq}, rad d^{-1}	4.51 ± 0.01	$2.15^{+0.10}_{-0.11}$
Stokes V: $\delta\Omega$, rad d^{-1}	0.24 ± 0.03	$0.34^{+0.01}_{-0.16}$

[1] Torres et al. (2006); [2]Montes et al. (2001); [3]Kiraga (2012); [4]Wright et al. (2011); [5]Järvinen et al. (2007); [6]Median visual magnitude taken from the *HIPPARCOS* database; [7]Holmberg et al. (2009); [8]Based on the formulation found in Bessell et al. (1998); [9]Allende Prieto and Lambert (1999); [10]CZD (Convection zone depth), based on the formulation contained in Noyes et al. (1984); [11]Based on the theoretical isochrones from Siess et al. (2000); [12]See Section 4.5.2; [13]Li and Hu (1998); [14]Zuckerman and Song (2004);

Table 8.2: Summary of differential rotation parameters as measured by this work using the χ^2 minimisation technique (continued from Table 8.1.

Parameter	HD 35296	HD 29615	EK Draconis
Spectral Type	F8V[2]	G3V[1]	G1.5V[1]
Photometric Period, d	3.56[4]	2.34 ± 0.2	2.755 ± 0.06d
Equatorial Period, d	3.49 ± 0.2	∼2.32	∼2.5
Inclination Angle, ^{o}	65 ± 5	70 ± 5	60 ± 5[5]
$v \sin i$, km s^{-1}	16.0 ± 0.1	19.5 ± 0.3	16.8 ± 0.2
v_{mag} [6]	5.1149 ± 0.0014	8.6006 ± 0.0031	7.7283 ± 0.0039
T_{phot}, K	6080 [7]	5820	5750 [5]
T_{spot}, K	–	3920	4050
V_{rad}, km s^{-1}	38.1 ± 0.1	19.3 ± 0.1	-20.2 ± 0.1
Stellar Radius, $M_\odot$ [8]	1.1	1.0 [9]	0.99 [4]
CZD, $R_\star$ ($R_\odot$) [10]	0.178 (0.201)	0.252 (0.254)	0.243 (0.241)
Age, Myr [11]	30-60 [13]	20-30 [14]	30-50 [5]
Mass, $M_\odot$ [11]	1.10	0.95 [9]	1.06 [4]
Stokes I: Ω_{eq}, rad d^{-1}	–	$2.67^{+0.09}_{-0.01}$	$2.51^{+0.019}_{-0.015}$
Stokes I: $\delta\Omega$, rad d^{-1}	–	$0.09^{+0.04}_{-0.02}$	$0.34^{+0.02}_{-0.048}$
Stokes V: Ω_{eq}, rad d^{-1}	1.80 ± 0.01	$2.75^{+0.07}_{-0.04}$	$2.53^{+0.049}_{-0.050}$
Stokes V: $\delta\Omega$, rad d^{-1}	0.28 ± 0.08	$0.58^{+0.14}_{-0.12}$	$0.44^{+0.21}_{-0.12}$

[1] Torres et al. (2006); [2]Montes et al. (2001); [3]Kiraga (2012); [4]Wright et al. (2011); [5]Järvinen et al. (2007); [6]Median visual magnitude taken from the *HIPPARCOS* database; [7]Holmberg et al. (2009); [8]Based on the formulation found in Bessell et al. (1998); [9]Allende Prieto and Lambert (1999); [10]CZD (Convection zone depth), based on the formulation contained in Noyes et al. (1984); [11]Based on the theoretical isochrones from Siess et al. (2000); [12]See Section 4.5.2; [13]Li and Hu (1998); [14]Zuckerman and Song (2004);

is that the differential rotation is dependent on convective zone depth, with the thinner the convective zone, the greater the level of differential rotation. The convective zone depth (CZD) for the young stars was estimated using the theoretical isochrones of Siess et al. (2000) and listed in Table 8.3. The value for the B-V (or V-I) colour was that found in ESA (1997) (date accessed: 31, January, 2013) and the absolute magnitude was determined from the maximum visual magnitude determined by the *HIPPARCOS* space mission. Most of these stars are heavily spotted, with HD 106506 (this work) showing a visual magnitude of ∼8.54, yet the unspotted magnitude was determined to be 8.38 (using *ZDICAM*). O'Neal et al. (1996) found that on some heavily spotted stars, the observed maximum V magnitude underestimates the brightness of the unspotted star by ∼ 0.3-0.4 mag. However, as there was limited knowledge of the fractional spottedness of many of the stars that had their differential rotation determined, it was decided to use the maximum visual magnitude listed in the *HIPPARCOS* database with the caveat that this is possibly an overestimate of the true CZD. As an internal check of the validity of this estimation, a comparison was made for stars that had published CZD's from other sources. Takeda et al. (2007) had 3 stars in common with this work. They used the Yale Rotational Evolution Code (YREC: P. Demarque et al., 2008) in its non-rotating mode to calculate stellar models. Two stars showed similar CZD but LQ Hydrae had substantial differences. Perhaps this might have been a result of a different estimate of the radius of the star. Wright et al. (2011) also used the theoretical isochrones of Siess et al. (2000) in the *ROTXRAYCAT* database[1], with two of the three stars in common with Takeda et al. (2007) and a two further stars in common with this work. In each case, the value of the CZD determined by this work was consistent with the estimates of Wright et al. (2011), to within appropriate error bars. These are listed in Table 8.3, with the error bars determined by the respective errors in the B-V and maximum visual magnitudes.

Figure 8.1 (lower panel) is a modified Marsden figure (from Marsden et al., 2011b) with more recent additions from this thesis and the work of others. This shows that as the CZD decreases, there appears to be an increase in the differential rotation. Noyes et al. (1984) found that there was a correlation between the Rossby number, (Ro), and chromospheric activity, $Log(R'_{HK})$. Figure 8.2 (upper panel) shows the relationship between the Rossby number and differential rotational shear $\delta\Omega$. The Rossby number

[1] http://heasarc.gsfc.nasa.gov/W3Browse/all/rotxraycat.html

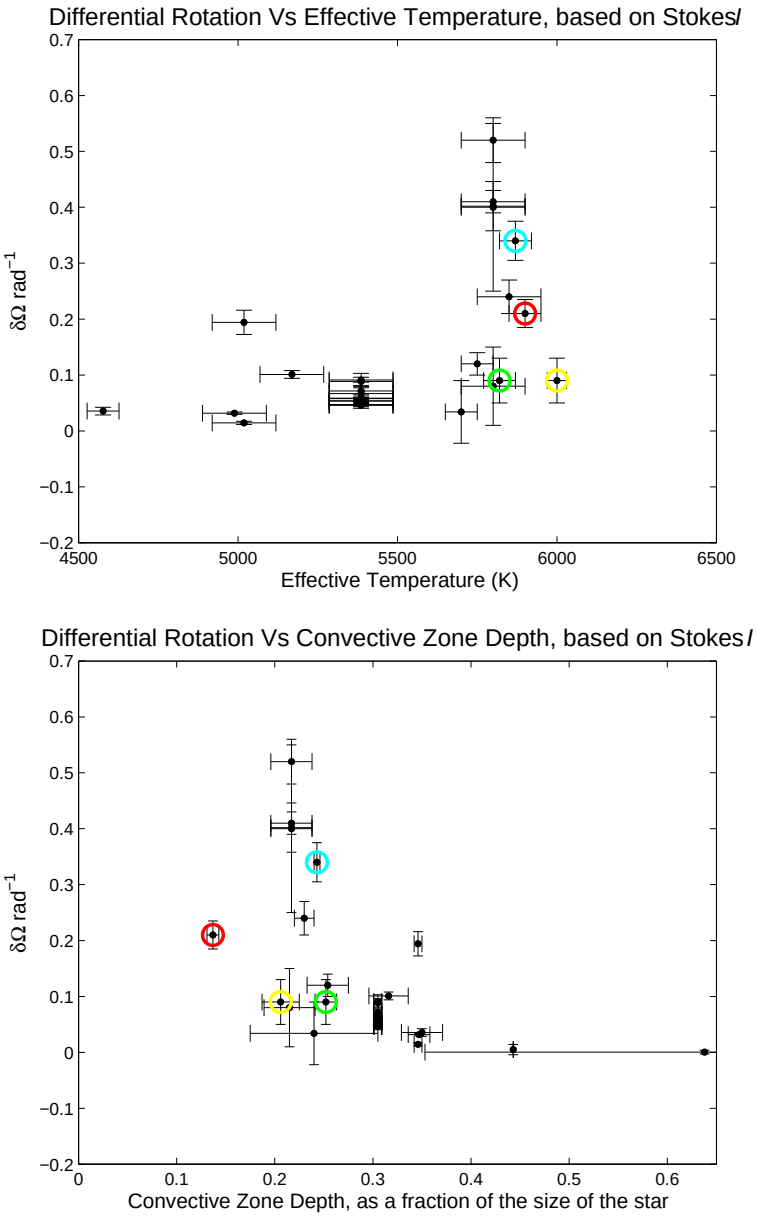

Figure 8.1: Using Stokes I data, the upper panel shows a graph of $\delta\Omega$ versus effective surface temperature, as originally produced by Barnes et al. (2005a). The lower panel shows a graph of $\delta\Omega$ versus convective zone depth. The stars added from this work are shown as circles: HD 106506 (red), HD 29615 (green), EK Draconis (cyan) and HD 76298 (yellow). Recall that a Stokes I map was not produced for HD 35296.

Table 8.3: Estimating the convective zone depth, based on the theoretical isochrones of Siess et al. (2000), compared with the estimates obtained from Takeda et al. (2007) and Wright et al. (2011)

Star	This work[1]		Takeda et al. 2007[2]		Rotxraycat[3]	
	$R_\star$	$R_\odot$	$R_\star$	$R_\odot$	$R_\star$	$R_\odot$
HD 106506	0.137±0.006	0.284±0.043	–	–	–	–
HD 35296	0.178±0.004	0.201±0.009	–	–	–	–
HD 29615	0.252±0.011	$0.254^{+0.027}_{-0.007}$	–	–	–	–
EK Draconis	0.243±0.003	$0.241^{+0.004}_{-0.002}$	0.242	0.249	0.240	0.238
HD 76298	0.206±0.019	$0.445^{+0.049}_{-0.042}$	–	–	–	–
AB Dor	0.305±0.004	$0.230^{+0.008}_{-0.005}$	–	–	–	–
LQ Lup	0.254±0.021	$0.327^{+0.074}_{-0.050}$	–	–	–	–
PZ Tel	0.316±0.020	$0.351^{+0.035}_{-0.050}$	–	–	–	–
LO Peg	0.350±0.021	$0.247^{+0.026}_{-0.030}$	–	–	–	–
R58	0.215±0.026	$0.225^{+0.023}_{-0.038}$	–	–	0.190	0.205
HD 171488	0.217±0.021	$0.230^{+0.032}_{-0.025}$	–	–	–	–
HD 141943	0.230±0.010	$0.390^{+0.028}_{-0.036}$	–	–	–	–
LQ Hya	0.346±0.004	$0.284^{+0.010}_{-0.008}$	0.287	0.204	–	–
HD 197890	0.347±0.011	0.294±0.032	–	–	–	–
EY Dra	0.638±0.285	$0.366^{+0.287}_{-0.146}$	–	–	–	–
HK Aqr	0.443[4]	0.235	–	–	–	–
HR 1817	0.180±0.009	$0.207^{+0.009}_{-0.016}$	0.169	0.190	0.180	0.216
RX J0850.1-7554	0.240±0.065	$0.340^{+0.129}_{-0.146}$	–	–	–	–

[1] As calculated during this work, and is based on the theoretical isochrones of Siess et al. (2000).

[2] Taken from the work of Takeda et al. (2007).

[3] Taken from *ROTXRAYCAT* - Stars with Rotation Periods & X-Ray Luminosities Catalog (Wright et al., 2011) that uses the theoretical isochrones of Siess et al. (2000).

[4] The error bars could not be determined for this M-dwarf star.

was calculated using the convective turnover relationship in Equation 5.10, except for HD 106506 and HD 76298 as the relationship did not extend beyond 1.3 $M_{\odot}$. For these two stars, the original relationship developed by Noyes et al. (1984) was used. For young, rapidly rotating zero-age-main-sequence stars the greater the Rossby number, the more influence the Coriolis force has on the convective eddies and hence the force's impact on convection. This could suggest that the greater the impact, the greater the rotational shear, the stronger the distributed dynamo that is operating throughout the convective zone. Figure 8.2 only includes young stars that possess a fundamentally different dynamo (a distributed or $\alpha^2 - \Omega$ dynamo). Mature stars were excluded from this graphic as they most likely possess an interface-dynamo, hence would complicate the picture.

8.3 Image reconstruction: Stokes V Zeeman Doppler imaging

Hale (1908) were the first to detect the magnetic field inside a sunspot on the Sun while Babcock (1947) was the first to use the Zeeman effect to detect a magnetic field on a star (78 Vir, SpType: A1p[1]) other than the Sun. ZDI observations at the AAT began in 1989, with the first magnetic field detected for the RS CVn evolved binary HR 1099 (Donati et al., 1992a). Studies of active, rapidly rotating stars generally show strong toroidal fields on the stellar surface (e.g. Donati et al., 1992b; Donati and Collier Cameron, 1997; Donati et al., 2003b). Petit et al. (2008) found that significant surface toroidal fields are detected on main-sequence stars whenever the rotation period is lower than ≈12 d. This is unlike the Sun where the toroidal field is likely to be present at the base of the convection zone.

8.3.1 Magnetic Field Configurations

All stars in this thesis had their magnetic topologies determined using ZDI. Each star was found to have significant near-surface azimuthal magnetic fields (toroidal component), clearly visible at the photospheric level and not buried deep within the star, unlike the Sun. Donati et al. (2003b) proposes that this could indicate that the dynamo operating in all of these stars (and other active solar-type stars) is capable of

[1] Cowley et al. (1969)

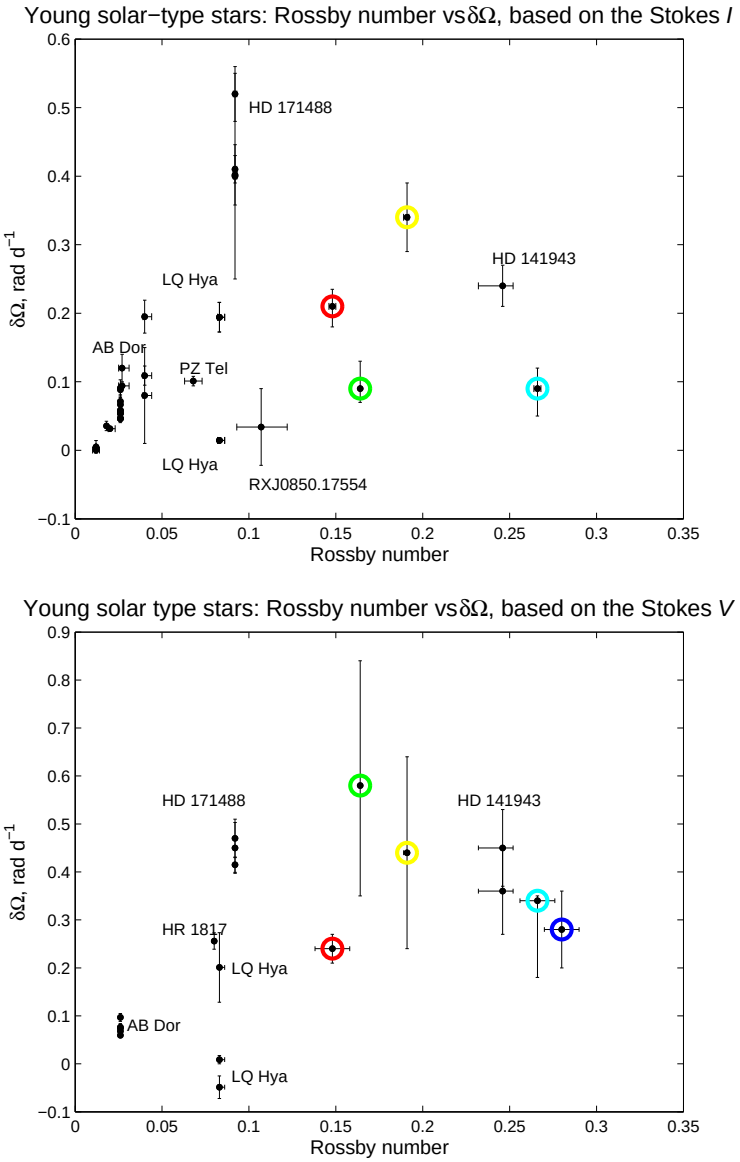

Figure 8.2: Rossby number versus $\delta\Omega$ for solar-like stars using the Stokes I (above) V (below) information. The Rossby number was calculated using the convective turnover relationship in Equation 5.10, except for HD 106506 and HD 76298 as this relationship did not extend beyond 1.3 $M_{\odot}$. For these two stars, the original relationship developed by Noyes et al. (1984) was used. The stars added from this work are shown as circles: HD 106506 (red), HD 35296 (blue), HD 29615 (green), EK Draconis (cyan) and HD 76298 (yellow). Recall that a Stokes I map was not produced for HD 35296.

generating fields directly in the subsurface region (e.g Dikpati et al., 2002) and could be distributed throughout the whole convective zone (e.g. Lanza et al., 1998). This is known as a $\alpha^2\Omega$ or distributed dynamo. This is unlike that occurring on the Sun, where it is thought to be restricted to the tachocline. The observations of azimuthal rings of magnetic fields is consistent with another model of magnetic field generation; the wreathes of azimuthal magnetic fields theorised by Brown et al. (2010), except they occur at a much higher latitude. Their 3-dimensional magnetohydrodynamics (MHD) models found that stars with increased rotation rate (up to three times that of the Sun) could produce self-generating wreathes of azimuthal field without the need for an interface layer. The increased rotation rate of the stars observed in this thesis could be deflecting the wreathes of magnetic fields to much higher latitudes, although further modelling would be required to support this conjecture. All stars studied in this thesis exhibited strong and complex magnetic fields.

Donati and Landstreet (2009) suggest that for stars with Rossby number less than one, ($Ro < 1$) but more massive than 0.5 solar mass ($M_{\odot}$) produce substantial toroidal component with a "mostly non-axisymmetric poloidal component". All stars investigated in this thesis have Rossby numbers and mass within this range. However, Figure 8.3 (bottom right panel) has two datapoints that exhibit low values in the non-axisymmetric mode in the poloidal component. One is HD 106506 with only ∼15% of the poloidal component being held the non-axisymmetric configuration and only ∼8% in the axisymmetric configuration. HD 106506 was strongly toroidal, with most of the magnetic energy held in the toroidal component and this may have affected the determination of the poloidal symmetry. The second star was HD 76298. This held ∼86% of the poloidal energy in the axisymmetric configuration. This might be due to the limited number of profiles obtained for this star. In summary, both moderate and rapid rotators have similar magnetic configurations. The symmetry of the toroidal field was also predominantly axisymmetric, as shown in Figure 8.4. There is a hint of a trend when one considers the toroidal field. It appears that the toroidal field becomes more axisymmetric ($m < \ell/2$) with increasing absolute convective zone depth, in terms of $R_{\odot}$, (Figure 8.4, bottom left panel), with a subsequent decrease in the amount of the toroidal field being held in the non-axisymmetric configuration ($m > \ell/2$) (Figure 8.4, bottom right panel). However, this is a very small sample with relatively large error

bars on each data point. This is worth investigating with a larger sample of late F-/early G-dwarf stars through the Bcool collaboration. Tables 8.4 and 8.5 shows all the results from this project, while Appendix E.1 shows the full set of results of additional stars found in the literature.

8.3.2 Temporal variation of surface magnetic fields

EK Draconis has demonstrated spot evolution beyond that expected when applying a simple, solar-like differential rotation law. This variation was observed by Dorren and Guinan (1994) and has been confirmed with this work. During the three months of observations, the poloidal field has strengthen, beginning with a predominately toroidal field in early December, 2006 to one that is almost 50-50 poloidal-toroidal. This shift saw enhanced chromospheric activity during this transition, as shown in Figure 7.22, before returning to similar levels when this "magnetic transition" had begun to stabilise. In summary, the evidence presented on the young star EK Draconis demonstrates that young stars can undergo rapid temporal variations of surface magnetic topologies; however, high cadence sampling of this star over several months would be required to support this initial statement.

How reliable are these magnetic maps, and in particular the azimuthal magnetic field maps? One possible limitation on the magnetic maps produced for the stars in this thesis arise from the independence of the brightness and magnetic maps. Typically, Stokes I and V data are taken simultaneously but the respective maps are generated separately. This thesis employed this technique, used by many other authors such as Skelly et al. (2010) (plus others already listed throughout this thesis). Rosén and Kochukhov (2012) used numerical studies to show that when effective temperature is held constant and Stokes I is not used for magnetic mapping, the magnetic field strength is underestimated from 30 to 60%. Further to this, the strength of magnetic field inside cool spots is underestimated by as much as 80 to 95%. Kochukhov et al. (2013) suggest this leads "to severe artefacts if cool spots coincide with major concentrations of the magnetic flux". Further limitations arise from using incomplete Stokes parameter sets. The full Stokes parameter set, as listed in Equation 2.7 (see Section 2.5) consists of the linear polarisation state (Stokes U and Q parameters) that are significantly weaker than the circular (Stokes V) state and are generally only observable in the brightest of stars. Donati (2003) argue that regions of mostly azimuthal field can be safely

Table 8.4: Magnetic quantities derived from the set of magnetic maps. Both the poloidal and toroidal components are listed along with the relative weightings in each geometry.

geometry	Energy[1] (%)	dipole[2] (%)	quad.[2] (%)	oct.[2] (%)	higher[2,3] order(%)	axi.[1] (%)	axi.[2] (%)
HD 106506 Global field strength = 69 G (2007)							
poloidal	30^{+2}_{-3}	10^{+2}_{-2}	11^{+1}_{-2}	10^{+1}_{-1}	68^{+3}_{-3}	28^{+3}_{-1}	8^{+1}_{-1}
toroidal	70^{+3}_{-1}	18^{+6}_{-4}	16^{+5}_{-9}	37^{+12}_{-6}	29^{+6}_{-9}	94^{+2}_{-2}	65^{+6}_{-3}
HD 76298 Global field strength = 41 G (2010)							
poloidal	70^{+5}_{-8}	14^{+10}_{-7}	8^{+8}_{-5}	10^{+4}_{-2}	69^{+13}_{-13}	25^{+11}_{-11}	36^{+13}_{-16}
toroidal	29^{+9}_{-8}	3^{+5}_{-2}	5^{+12}_{-4}	8^{+10}_{-7}	84^{+11}_{-19}	16^{+9}_{-4}	53^{+12}_{-12}
HD 76298 Global field strength = 33 G (2011)							
poloidal	93^{+1}_{-3}	74^{+4}_{-6}	2^{+1}_{-1}	4^{+1}_{-1}	21^{+5}_{-4}	80^{+3}_{-5}	86^{+3}_{-3}
toroidal	8^{+3}_{-2}	7^{+3}_{-3}	3^{+3}_{-2}	2^{+2}_{-1}	89^{+4}_{-5}	4^{+1}_{-1}	57^{+7}_{-6}
HD 35296 Global field strength = 13.2 G (2007)							
poloidal	82^{+3}_{-4}	19^{+5}_{-4}	5^{+1}_{-1}	15^{+3}_{-3}	61^{+4}_{-4}	7^{+5}_{-3}	8^{+6}_{-4}
toroidal	18^{+4}_{-3}	36^{+7}_{-7}	12^{+3}_{-4}	5^{+3}_{-2}	48^{+8}_{-5}	13^{+3}_{-2}	73^{+4}_{-7}
HD 35296 Global field strength = 15.8 G (2008)							
poloidal	52^{+6}_{-5}	8^{+2}_{-3}	13^{+1}_{-1}	7^{+4}_{-4}	72^{+4}_{-3}	10^{+5}_{-4}	19^{+7}_{-6}
toroidal	48^{+5}_{-6}	61^{+5}_{-5}	7^{+5}_{-4}	4^{+4}_{-3}	28^{+5}_{-6}	40^{+3}_{-3}	82^{+4}_{-4}
HD 29615 Global field strength = 72 G (2009)							
poloidal	73^{+4}_{-4}	35^{+16}_{-12}	11^{+8}_{-7}	12^{+3}_{-4}	41^{+10}_{-10}	35^{+10}_{-9}	49^{+12}_{-12}
toroidal	27^{+4}_{-4}	32^{+10}_{-10}	12^{+9}_{-7}	12^{+7}_{-4}	45^{+13}_{-15}	22^{+4}_{-3}	79^{+7}_{-5}

continued next page....

[1] % of the total magnetic energy available. [2] % of the respective poloidal or toroidal field geometry. [3] higher order multipole magnetic field. Listed also is the fraction of the poloidal or toroidal magnetic energy in the dipolar ($\ell = 1$), quadrupolar ($\ell = 2$), octupolar ($\ell = 3$) and higher order multipole[3] ($\ell \geq 4$) components as well as the fraction of energy of each component stored in the axisymmetric component ($m < \ell/2$) and the fraction of the total energy stored in each component ($m = 0$).

Table 8.5: Magnetic quantities derived from the set of magnetic maps. Both the poloidal and toroidal components are listed along with the relative weightings in each geometry cont.

geometry	Energy[1] (% tot)	dipole[2] (%)	quad.[2] (%)	oct.[2] (%)	higher [2,3] order (%)	axi.[1] (%)	axi.[2] (%)
EK Draconis Global field strength = 86.2 G (Dec 2006)							
poloidal	$20.1^{+3.3}_{-2.7}$	$30.4^{+10.6}_{-11.2}$	$11.8^{+6.1}_{-4.8}$	$10.7^{+1.2}_{-1.7}$	$47.1^{+12.3}_{-9.3}$	$5.7^{+1.9}_{-1.3}$	$28.6^{+4.9}_{-8.5}$
toroidal	$79.9^{+2.7}_{-3.3}$	$85.6^{+2.7}_{-3.0}$	$4.0^{+2.5}_{-2.0}$	$4.0^{+2.4}_{-1.3}$	$6.4^{+2.6}_{-1.3}$	$77^{+2.3}_{-3.1}$	$96.3^{+1.0}_{-1.7}$
EK Draconis Global field strength = 72.9 G (Jan 2007)							
poloidal	$36.8^{+6.2}_{-2.7}$	$43.1^{+5.5}_{-14.8}$	$14.6^{+3.7}_{-2.1}$	$7.4^{+5.4}_{-3.2}$	$35.0^{+7.3}_{-4.9}$	$2.0^{+2.1}_{-1.2}$	$5.5^{+4.1}_{-3.1}$
toroidal	$63.3^{+2.8}_{-6.2}$	$75.3^{+5.0}_{-7.2}$	$15.2^{+6.0}_{-7.5}$	$2.9^{+0.7}_{-0.8}$	$6.6^{+3.6}_{-1.9}$	$60.4^{+2.2}_{-7.7}$	$95.4^{+1.5}_{-3.1}$
EK Draconis Global field strength = 58.7 G (Feb 2007)							
poloidal	$41.7^{+5.6}_{-6.6}$	$13.5^{+7.0}_{-5.7}$	$10.2^{+3.7}_{-5.1}$	$10.5^{+4.7}_{-3.7}$	$65.9^{+8.4}_{-5.1}$	$9.8^{+4.2}_{-4.1}$	$23.8^{+11.9}_{-11.4}$
toroidal	$58.3^{+6.5}_{-5.6}$	$69.8^{+5.0}_{-4.8}$	$13.4^{+4.9}_{-4.8}$	$2.5^{+1.8}_{-1.2}$	$14.4^{+3.5}_{-3.4}$	$53.2^{+5.8}_{-5.2}$	$91.3^{+1.6}_{-1.5}$
EK Draconis Global field strength = 100.7 G (Jan 2012)							
poloidal	$45.4^{+6.5}_{-6.0}$	$7.6^{+9.2}_{-4.6}$	$11.1^{+8.0}_{-8.6}$	$12.5^{+5.3}_{-5.8}$	$68.7^{+9.6}_{-6.0}$	$14.7^{+11.2}_{-3.8}$	$32.3^{+17.8}_{-8.5}$
toroidal	$54.7^{+5.9}_{-6.4}$	$64.8^{+6.5}_{-19.1}$	$7.0^{+3.4}_{-3.1}$	$2.3^{+2.2}_{-1.6}$	$25.7^{+20.4}_{-8.3}$	$46.0^{+6.0}_{-8.3}$	$84.1^{+4.9}_{-10.7}$

[1] % of the total magnetic energy available. [2] % of the respective poloidal or toroidal field geometry. [3] higher order multipole magnetic field. Listed also is the fraction of the poloidal or toroidal magnetic energy in the dipolar ($\ell = 1$), quadrupolar ($\ell = 2$), octupolar ($\ell = 3$) and higher order multipole[3] ($\ell \geq 4$) components as well as the fraction of energy of each component stored in the axisymmetric component ($m < \ell/2$) and the fraction of the total energy stored in each component ($m = 0$).

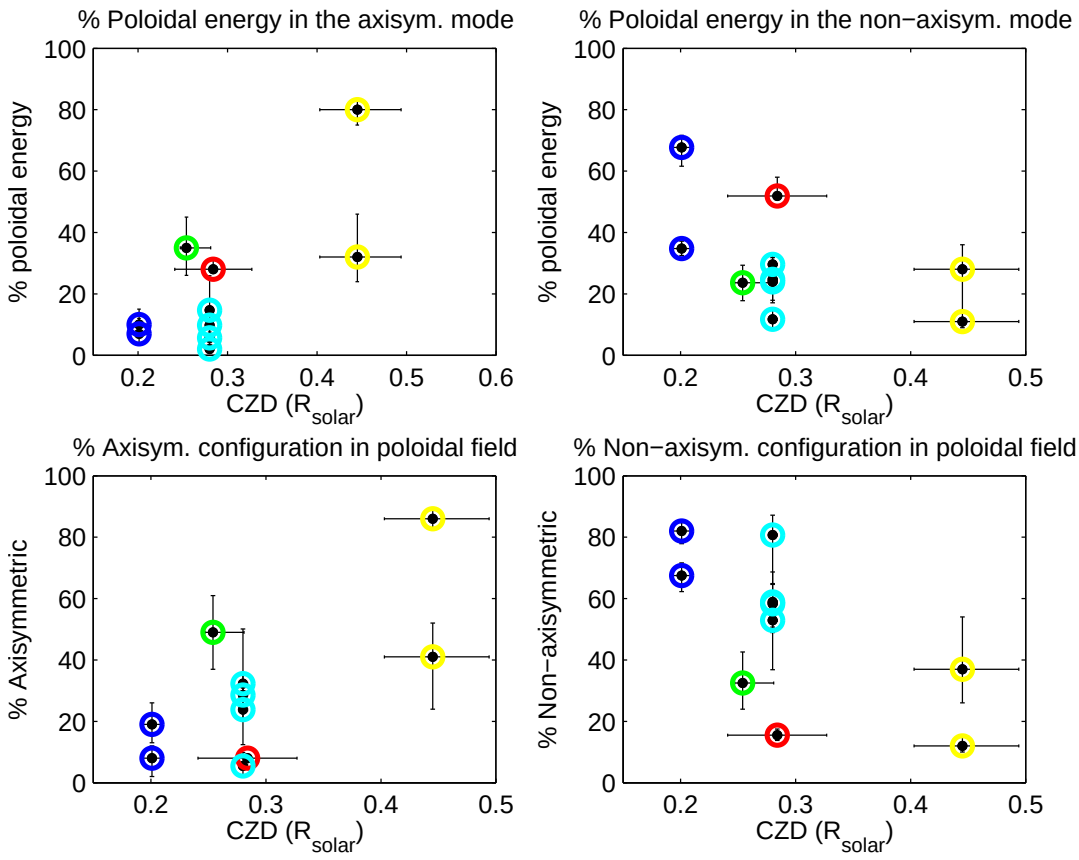

Figure 8.3: The symmetry of the poloidal field as a function of convective zone depth for the stars studied in this thesis. The top left panel shows the % poloidal energy held in the axisymmetric mode (m = 0) while the top right panel shows the % of the poloidal energy held in the non-axisymmetric mode. The bottom left panel shows the % of the poloidal energy held in the axisymmetric mode (m $< \ell/2$) with respect to the rotation axis. The bottom right panel shows the % of the poloidal energy held in the non-axisymmetric mode (m $> \ell/2$). Key: HD 106506 (red), HD 35296 (blue), HD 29615 (green), EK Draconis (cyan) and HD 76298 (yellow).

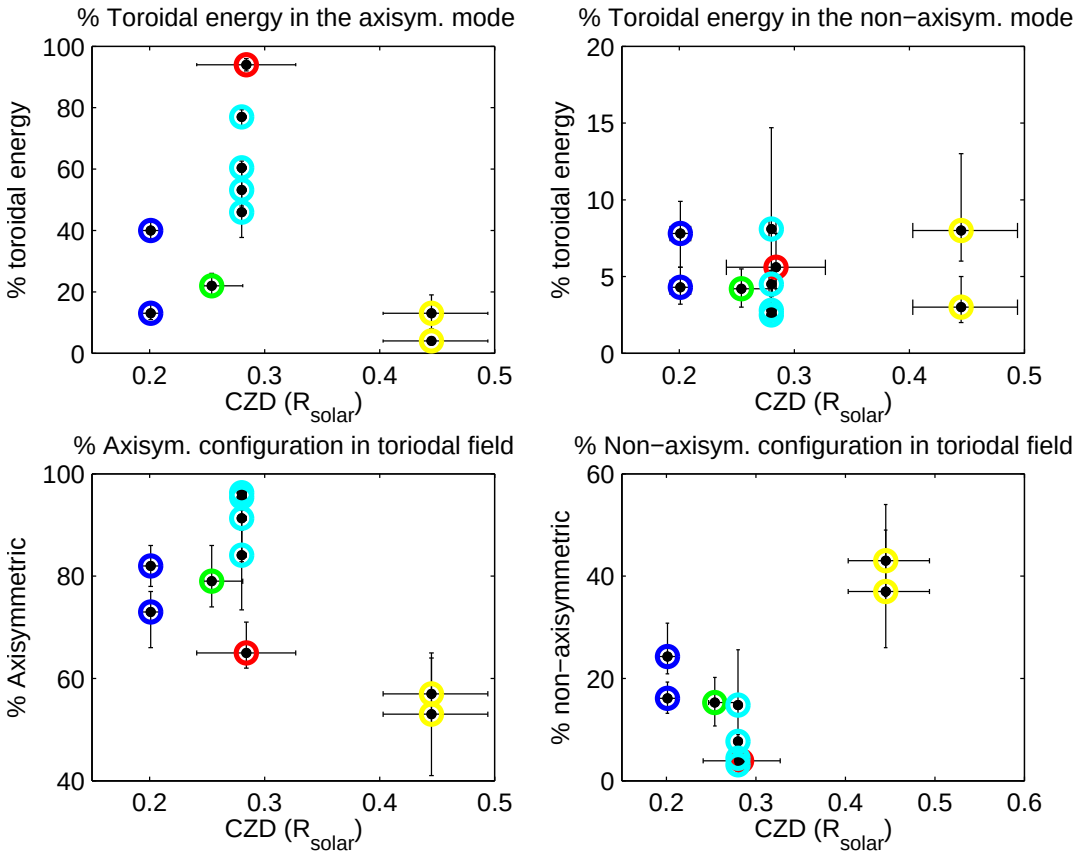

Figure 8.4: The symmetry of the toroidal field as a function of convective zone depth for the stars studied in this thesis. The top left panel shows the % toroidal energy held in the axisymmetric mode (m = 0) while the top right panel shows the % of the toroidal energy held in the non-axisymmetric mode. The bottom left panel shows the % of the toroidal energy held in the axisymmetric mode (m $<\ell/2$) with respect to the rotation axis. The bottom right panel shows the % of the toroidal energy held in the non-axisymmetric mode (m $> \ell/2$). Key: HD 106506 (red), HD 35296 (blue), HD 29615 (green), EK Draconis (cyan) and HD 76298 (yellow).

distinguished from regions of radial and meridional fields using the Zeeman signatures in circular polarisation only. Nevertheless, Kochukhov and Piskunov (2002) argue that using incomplete Stokes parameter sets do not allow for a unique reconstruction of the stellar magnetic field geometries while Kochukhov and Wade (2010) argue that magnetic models based on circular polarization only, does not recover the smaller-scale magnetic structures. Recently, Kochukhov et al. (2013) used HARPS-Pol to map the magnetic field topology of the RS CVn star II Pegasi; the first map produced using the full set of Stokes parameters (I, U, Q and V). They could not confirm the presence of persistent azimuthal field rings found in other RS CVn stars using Stokes V alone. This technique of using all four Stokes parameters is still in its infancy but the prospect of confirming, or otherwise, the results of this thesis remains uncertain. The current instrumentation will confine the use of this approach to the brightest of stars.

8.3.3 Differential Rotation

As mentioned previously, differential rotation is dependent on effective temperature and hence convection zone depth. Figure 8.5 (upper panel) shows that there continues to be a jump in the level of differential rotation from ∼5800 K. This could be due to the relatively small sample size of stars below 5800 K yet warmer stars, with effective temperatures greater than ∼6050 K appear not to follow that trend. For example, HD 35296 (T_{eff}=6170), HR 1817 (T_{eff}= 6131 K Mengel, 2005) and HD 197890 (T_{eff}=6168 K Fares et al., 2012) appear not to follow this trend. Both HD 35296 and HR 1817 are relatively young stars and HD 179949 has a hot Jupiter-sized planet in orbit (Butler et al., 2006). More data is required on these three stars to confirm these findings, and on a larger sample of late F-type stars with $T_{eff} \geq 6050$ K using the χ^2 minimisation techniques before any further conclusions can be made regarding the dependence of effective temperature on differential rotation. Figure 8.5 (lower panel) is a modified Marsden figure (from Marsden et al., 2011b) with more recent additions. Whereas Figure 8.1 (lower panel) continues to support the notion put forward by Marsden et al. (2011b), the picture is more clouded when considering the magnitude of differential rotation when using the magnetic (Stokes V) information. ξ Boo (Morgenthaler et al., 2012) show high levels of differential rotation and have relatively large convective zone, 0.330 ± 0.02, as determined from the theoretical models of Siess et al. (2000). One possible explanation for the relatively high levels of differential rotation on

ξ Bo"otis for the size of the convective zone could be in the way this measurement was determined. ξ Boo is a relatively slow rotator, with a $v\sin i = 2.9$ km s^{-1}(Gray, 1984). Morgenthaler et al. (2012) used a spherical harmonic expansion $l_{max} \leq 10$, although $l_{max} = 5$ would have been appropriate as well as there were no discernible improvements in the difference between the modelled and observed LSD profiles increasing the l_{max} beyond this lower limit. The reduced number of resolution elements in the mapping process may have had an unintended "increase" in the level of differential rotation observed using the χ^2 minimisation technique. Reviewing Equation 5.9, as the Rossby number increases, the convective turnover time, τ_{conv}, decreases leading to the CZD decreasing. Using the Stokes V information, it appears to be a trend in increasing differential rotation as Rossby number increases, albeit a tenuous trend as shown in Figure 8.2. This work adds further evidence to this hypothesis of increasing differential rotation with decreasing CZD, albeit a very scattered relationship.

HD 29615 was found to have one of the highest values found for differential rotation using ZDI. This sun-like star has a rotational shear, $\delta\Omega$ of $0.58^{+0.14}_{-0.12}$ rad d^{-1}. Barnes et al. (2005a) and Kitchatinov and Olemskoy (2011) showed that the level of differential rotation is dependent on effective temperature. Küker et al. (2011) found, when holding the effective temperature constant, the depth of the convection zone has a "big impact on stellar rotation". They demonstrated that the extreme surface shear of stars such as HD 171488 (V889 Her, SpType = G2V[1]) (Marsden et al., 2006; Jeffers and Donati, 2008; Jeffers et al., 2011), and by implication HD 29615, can only be explained with a shallow convection zone. However, the CZD for HD 29615 was estimated to be 0.252 $\pm$ 0.011 $R_\star$ (0.254 $R_\odot$), as determined from the stellar evolution models of Siess et al. (2000). The reason why HD 29615 having such a large rotational shear remains unclear.

Three of the five targets showed significantly different rotational shear when using Stokes I and V data. These are reproduced in Table 8.6. Donati et al. (2003a) found that in some early K-dwarf stars, the level of differential rotation measured from brightness features is usually lower when compared with the levels found when using magnetic features. Their interpretation of this variation is that the brightness features and the magnetic features are anchored at different depths within the convective zone of the star. An alternative yet intriguing explanation for the varying differential rotation

[1] Montes et al. (2001)

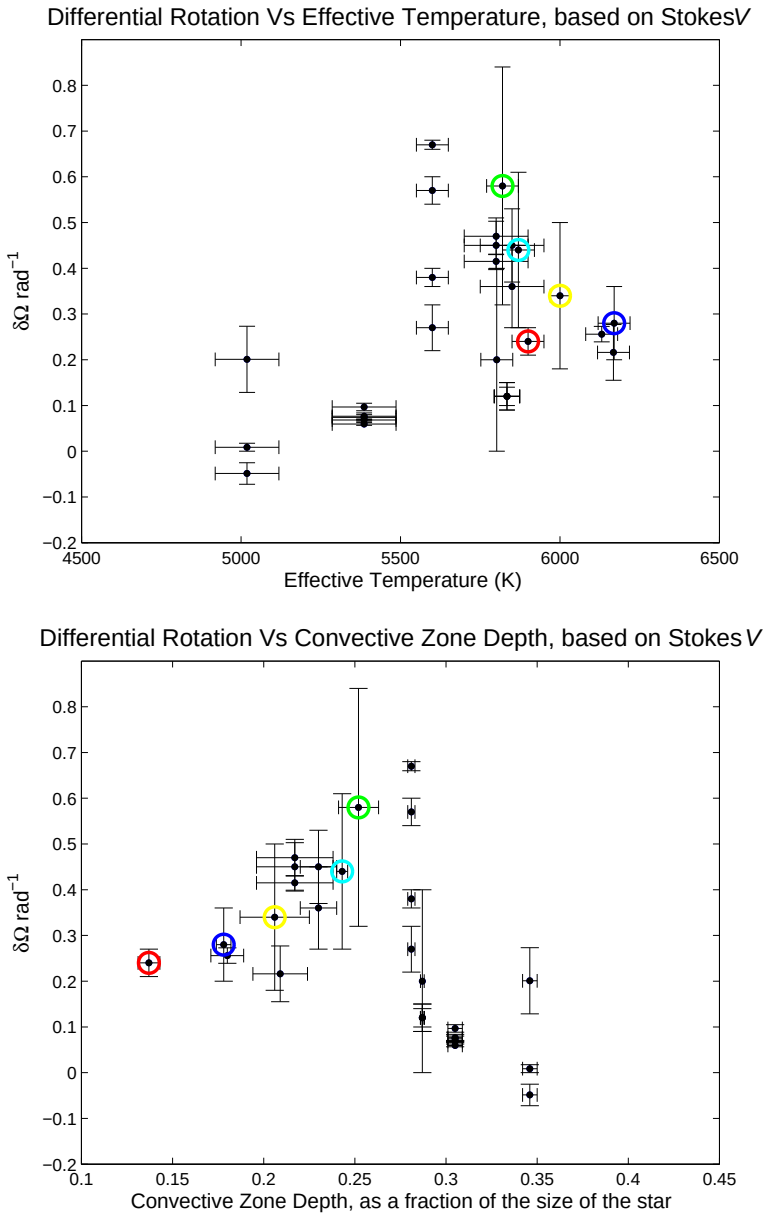

Figure 8.5: Using Stokes V data, the upper panel shows a graph of $\delta\Omega$ versus effective surface temperature, as originally produced by Barnes et al. (2005a). The lower panel shows a graph of $\delta\Omega$ versus convective zone depth. The stars added from this work are shown as circles: HD 106506 (red), HD 35296 (blue), HD 29615 (green), EK Draconis (cyan), HD 35296 (blue) and HD 76298 (yellow).

Table 8.6: Comparison of the rotation shear for both Stokes I and V for all five targets.

star	$\delta\Omega$, rad d^{-1}	
	Stokes I	Stokes V
HD 106506	$0.21^{+0.02}_{-0.03}$	0.24 ± 0.03
HD 76298	$0.09^{+0.03}_{-0.04}$	$0.34^{+0.01}_{-0.16}$
HD 35296	–	0.28 ± 0.08
HD 29615	$0.09^{+0.04}_{-0.02}$	$0.58^{+0.14}_{-0.12}$
EK Draconis	$0.34^{+0.02}_{-0.048}$	$0.44^{+0.21}_{-0.12}$

values from Stokes I and Stokes V could be offered by the recent work of Korhonen and Elstner (2011). Using dynamo calculations, they discovered that large starspots do not necessarily follow the actual differential rotation of the star, but have more solid-body like behaviour, whereas the true surface differential rotation is only recovered if small magnetic features are added to the simulations. These competing explanations must be treated with caution until further Stokes V data is obtained for a number of these stars.

The hypothesis regarding the strong but varying differential rotation consistent with emerging activity cycles could not be proved nor disproved as there were insufficient epochs to track this concept. However, recent theoretical work by Brown et al. (2010) has shown that young stars can undergo "attempted" reversals where the magnetic field begins to break-up, a signature of an impending reversal, only to reinforce again in the original direction.

In summary, evidence has been presented that supports the hypothesis that young solar-type stars under investigation have significant azimuthal magnetic fields, which can be interpreted as toroidal fields, being produced by a $\alpha^2\Omega$ dynamo that is distributed across the convective zone (Brandenburg et al., 1989; Moss et al., 1995), where both the α-effect **and** differential rotation shear contribute to the production of the toroidal field.

8.4 Stellar activity and the age of stars

As stated in Chapter 1, the relationship between stellar magnetic activity, age and rotation has been firmly established for main-sequence stars (MS), including the Sun.

Table 8.7: Comparison of Chromospheric Activity Indicators for all five targets.

star	AAT $H\alpha$	NARVAL/ESPaDOnS		
	log $R'_{H\alpha}$ [1]	S-index [2]	$N_{H\alpha}$-index	N_{CaIRT}-index
HD 106506	$^{-}4.21 \pm 0.02$	–	–	–
HD 76298	$^{-}4.18 \pm 0.01$	–	–	–
HD 35296 (2007)	–	0.312 ± 0.007	0.310 ± 0.004	0.898 ± 0.025
HD 35296 (2008)	–	0.310 ± 0.012	0.309 ± 0.00	0.890 ± 0.014
HD 29615	$^{-}4.36 \pm 0.01$	–	–	–
EK Dra (2006/7)	–	0.612 ± 0.048	0.389 ± 0.012	1.063 ± 0.037
EK Dra (2012)	–	0.585 ± 0.032	0.391 ± 0.010	1.074 ± 0.019

[1]This is the maximum value.

[2]The N_{CaIIHK}-index was converted to match the Mount Wilson S-values (Duncan et al., 1991) using the transformation shown in Equation 5.2.

This activity is driven by the magnetic field that is generated within the star's convective zone with the primary driver of this generation being differential rotation. All target stars exhibited chromospheric activity, as measured by a number of indices such as the Ca II H (396.85 nm) & K (396.37 nm) lines, the Hα (656.28 nm) line and also the near infra-red Ca II Infrared Triplet (IRT) (849.8, 854.2 and 866.2 nm) lines. Three southern hemisphere targets (HD 106506, HD 76298 and HD 29615) only had the emission equivalent width of Hα line measured as a proxy for chromospheric activity as SEMPOL did not extend into the spectral regions to record the Ca II H & K and IRT lines. The two northern hemisphere targets (HD 35296 and EK Draconis) were able to be investigated using all these chromospheric indicators. Table 8.7 is a summary of the results.

HD 76298 provides a conundrum with regard to its age. It is chromospherically active, rapidly rotating star with a dominant polar spot. It has measurable magnetic fields, particularly with the surface azimuthal field. In addition, there is evidence of circumstellar material present. However, this star had no measurable lithium line usually observed in young stars. HD 76298 could be young pre-main sequence star, or an evolved FK Comae-type star. Further data on this star would be required to confirm its evolutionary status.

The evidence presented in this work supports the current belief that the dynamo operating on young, rapidly rotating stars is fundamentally different from that operating on the Sun today. Figure 8.6 shows the relationship between $\delta\Omega$ and age. The upper panel shows the data based on the Stokes I information and the lower panel shows the data based on the Stokes V information. Given the large errors in the age estimates of some of these stars, it is difficult to draw any conclusions. However, there does appear to be a trend with decreasing differential rotation with age for young solar-type stars, particularly when one considers the figure using the Stokes V data.

8.5 Directions for future work

8.5.1 Temporal evolution of magnetic fields

Sunspots are a temporary phenomena that result from the Sun's magnetic fields inhibiting the convective flow of energy to the photosphere. These spots have lifetimes ranging from a few days to several weeks and tend to be restricted to the equatorial regions on the Sun. These time-scales are not an uncommon occurrence on stars. Donati et al. (2003a) observed variability on time-scales as short as a fortnight on the RS CVn-type star HR 1099 (SpType: K2:Vnk[1]) while Barnes (1999) observed such variability on G-dwarf stars in the α Persei cluster in time-scales less than a month. So it is not unreasonable to suggest that some variability would be observed on stars investigated in this thesis could be a result of both faculae and starspot emergence and evolution. The intermediate mass stars HD 106506 and HD 76298 as well as the sun-like star HD 29615 exhibited minor "mis-fitting" of the data that could be attributed to spot evolution (and/or faculae) on timescales of approximately two weeks. However, the variability due to spot evolution was very rapid on EK Draconis and it is this star that would provide the best target for ongoing studies of the variability of the stellar magnetic field. This star showed variation in its spot occupancy maps during a three month campaign indicating both spot evolution and spot emergence. The temporal variation of the surface magnetic topologies, from a strongly toroidal field ($\sim$80%) to a more balanced poloidal-toroidal field within a three month observing run, indicates that EK Draconis should be the focus of a long term study with the prospect of the onset of activity cycles, albeit chaotic, similar to that observed on the Sun. In addition

[1] Montes et al. (2001)

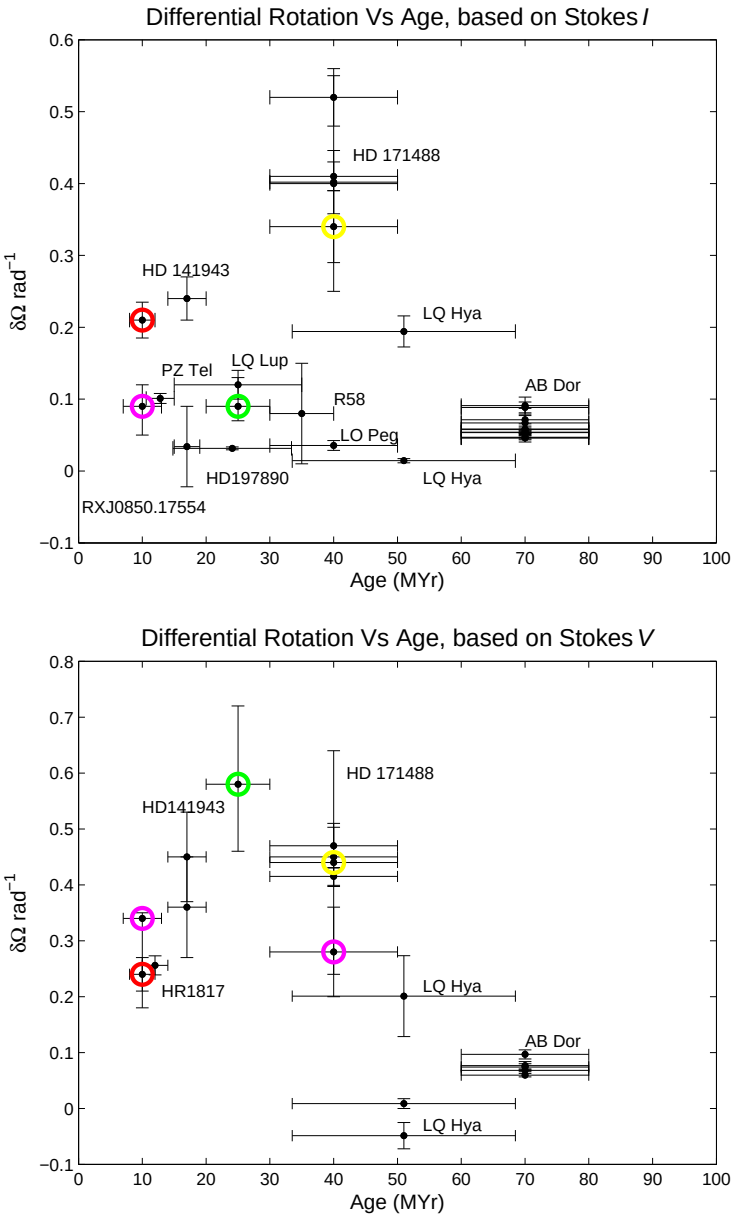

Figure 8.6: This shows a graph of $\delta\Omega$ versus age with the upper panel using Stokes I while the bottom panel is using Stokes V data. The stars added from this work are shown as circles: HD 106506 (red), HD 35296 (blue), HD 29615 (green), EK Draconis (cyan) and HD 76298 (yellow). Recall that a Stokes I map was not produced for HD 35296.

to a long-term observing programme to monitor the field configurations, high-cadence observations would be required so as to constrain the magnetic maps in greater detail. One can argue that several studies has demonstrated the presence of activity cycles, such as the Mount Wilson H & K project, (Baliunas et al., 1995) or photometry surveys (Messina and Guinan, 2002, 2003) that have several decades of data. These are indirect measures of determining activity cycles. ZDI is the best method to determine cycles as one can actually observe the polarity reversal of the magnetic fields, and is most likely the only method in the foreseeable future to directly measure this change.

EK Draconis is the only target that did not possess a truly polar spot, although HD 35296 was not mapped using the Stokes I data as the $v \sin i$ was too low for DI. Spots were restricted to $\sim 60^o$ latitude on EK Draconis. This is similar to the present-day Sun, although this restriction is more limited to $\pm$ 30^o except during solar maximum where the latitudes can extend higher on the surface to $\pm$ 45^o (as shown in Figure 1.7). König et al. (2005) concluded that EK Draconis is "one of the few nearby young stars that will evolve similarly to the Sun" adding further support for the need of long-term, high-cadence, magnetic observations on this star to track the variation in the toroidal-poloidal configurations during such cycles.

This study observed stars that appear to have relatively large convection zones yet high levels of differential rotation. More work needs to be undertaken by probing a wider range of stellar parameters, from fully convective M-dwarfs to mid-F stars using χ^2 minimisation techniques. In addition, an investigation into how the magnetic energy splits between the poloidal and toroidal field components, between the axisymmetric and non-axisymmetric components and the level of surface differential rotation associated to these magnetic characteristics would prove beneficial in understanding the primary driver of the magnetic field on young stars, including the young Sun and its effects on emerging planetary systems. The relationship between the level of differential rotation and the role in the symmetry of the poloidal and toroidal fields will constrain the modern dynamo theories operating in young solar-type stars.

8.5.2 Magnetic fields and effects on emerging planetary systems

Radial velocity (RV) surveys have been utilised to search for extra-solar (exo-) planets. These surveys have been successful in finding planets around mature stars as well as low mass stars such as M-dwarfs. However, stellar activity precludes the search for planets

around young sun-like stars due to the inherit stellar activity masking the RV signature of orbiting exo-planets. Recently, Moulds et al. (2013) have investigated a technique to remove the spot signatures from the stellar line profiles of activity stars, with $v \sin i$ from 10 to 50 $\mathrm{km\,s^{-1}}$. They showed that the stellar RV "jitter" could be reduced by more than 80% thereby permitting the observations of the presence of hot-Jupiter sized planets. Spectropolarimetry could also be utilised in detecting emerging planets around young sun-like stars as a way of accounting for the "jitter" often confusing these radial velocity surveys. Reiners et al. (2013) has already explored the effect magnetic fields have on the RV signature of stars. They found that the Zeeman effect alone can be "comparable to that caused by temperature contrast". Their simulations showed that a "spot magnetic field of ∼1000 G can produce a similar RV amplitude as a spot temperature contrast of ∼1000 K". Further simulations could be used to determine the benefits of using ZDI to account for this "jitter".

Magnetic activity of a planet-hosting star is thought to affect the orbiting exo-planets, especially the close-by planets. This will shed light on the environment where planets form and evolve in general, and possibly also on the conditions under which our own Earth was formed. Vidotto et al. (2013) have considered the effects on the magnetic field around M-dwarf stars and the influence on potentially habitable planets. They stressed the importance of understanding the host-star's magnetic topology when investigating the planetary magnetospheres of Earth-like planets that would affect their habitability. However, this would be beyond the current instrumentation available to the scientific community. This would only be possible with the next generation instrumentation such as **S**ectro**P**olarimétre **I**nfra-**Rou**ge (SPIRou[1]) at the CFHT. SPIRou has two scientific goals: the first is the search for habitable Earth-like planets orbiting low-mass stars while the second is to explore the impact of magnetic fields on star and planet formation. SPIRou will be capable of simultaneously measuring both the large- and small-scale fields of dMe stars. The advantage of SPIRou operating in the near infrared (IR) wavelengths is that "jitter" noise is four to five times smaller in the IR compared to the visible[2], although there are more telluric lines to deal with in the IR region. With *KEPLER* space observatory in operation[3] and NASA announcing the Transiting

[1] http://www.cfht.hawaii.edu/en/projects/SPIRou/

[2] http://www.cfht.hawaii.edu/en/news/UM2013/presentations/Session4-RDoyon.pdf

[3] At the time of submitting this thesis, *KEPLER* has encountered a malfunction and is not operating. The future of the *KEPLER* mission is uncertain.

Exoplanet Survey Satellite[1] (TESS) being scheduled for a 2017 launch, SPIRou will be an ideal instrument to characterize the new these super-Earths found using these space-based observatories.

8.6 Conclusions

This investigation found that all stars observed had strong azimuthal magnetic fields, consistent with a dynamo that is operating throughout the convective zone and is fundamentally different from the dynamo currently operating on the Sun today. Also observed was temporal variation of the magnetic fields on some of these stars although the emergence activity cycles were not observed. Unfortunately, none of the stars produced a "magnetic reversal" like that observed on stars such as τ Boo (Donati et al., 2008b; Fares et al., 2009). When considering the Sun's evolutionary path, the dynamo must have changed from a distributed dynamo, one this operating throughout the convective zone, to one of an interface dynamo, operating at the base of the convective zone with a shell like structure within that zone. One of the key drivers is differential rotation. Evidence has been presented that supports the hypothesis that the differential rotation is dependent on convective zone depth, albeit a relationship that is rather scattered with more data points required to tighten, (or otherwise) this relationship. One final thought: given the scatter in the data when considering the role of the depth of the convection zone with differential rotation, perhaps all young solar-type stars are as individual as human beings.

[1] http://www.nasa.gov/home/hqnews/2013/apr/HQ_13-088_Astro_Explorer_Mission_.html *dateaccessed* : *July21*, *2013*

References

C. Abia, Y. Pavlenko, and P. de Laverny. The formation of lithium lines in the atmospheres of super Li-rich AGB stars. *Astronomy & Astrophysics*, 351:273–282, 1999. 88

C. Allende Prieto and D.L. Lambert. Fundamental parameters of nearby stars from the comparison with evolutionary calculations: masses, radii and effective temperatures. *Astronomy & Astrophysics*, 352:555–562, 1999. 22, 144, 148, 212, 213

M. Ammler-von Eiff and A. Reiners. New measurements of rotation and differential rotation in A-F stars: are there two populations of differentially rotating stars? *Astronomy & Astrophysics*, 542:A116–, 2012. 48, 119, 124

S.M. Ammons, S.E. Robinson, J. Strader, G. Laughlin, D. Fischer, and A. Wolf. The N2K consortium. iv. New temperatures and metallicities for more than 100,000 FGK dwarfs. *The Astrophysical Journal*, 638(2):1004–1017, 2006. 292, 294, 296, 298

M. Audard, M. Güdel, and E.F. Guinan. Implications from extreme-ultraviolet observations for coronal heating of active stars. *The Astrophysical Journal*, 513:L53–L56, 1999. 163, 164

T. Ayres and K. France. Warm coronal rain on young solar analog EK Draconis? *ApJL*, 723:L38–L43, 2010. 163, 164

H.W. Babcock. Zeeman effect in stellar spectra. *The Astrophysical Journal*, 105:105–119, 1947. 217

H.W Babcock. The topology of the Sun's magnetic field and the 22-year cycle. *The Astrophysical Journal*, 133:572–589, 1961. 9, 10

A. Baglin, M. Auvergne, C. Catala, E. Michel, and COROT Team. Asteroseismology with the space mission COROT: photometric performances targets and mission profile. In *SOHO 10/GONG 2000 Workshop: Helio- and asteroseismology at the dawn of the millennium, 2-6 October 2000, Santa Cruz de Tenerife, Tenerife, Spain.*, pages 395–398. ESA Publications Divsion, 2001. 27

C.A.L. Bailer-Jones. Bayesian inference of stellar parameters and interstellar extinction using parallaxes and multiband photometry. *Monthly Notices of the Royal Astronomical Society*, 411(1):435–452, 2011. 304

S.L. Baliunas, J.H. Horne, A. Porter, D.K. Duncan, J. Frazer, H. Lanning, A. Misch, J. Meuller, R.W. Noyes, D. Soyumer, A.H. Vaughan, and L. Woodard. Time-series measurements of chromospheric Ca II H and K emission in cool stars and the search for differential rotation. *The Astronomical Journal*, 294:310–325, 1985. 48

S.L. Baliunas, R.A. Donahue, W.H. Soon, J.H. Horne, J. Frazer, L. Woodard-Eklund, M. Bradford, L.M. Rao, O.C. Wilson, Q. Zhang, W. Bennett, J. Briggs, S.M. Carroll, D.K. Duncan, D. Figueroa, H.H. Lanning, T. Misch, J. Mueller, R.W. Noyes, D. Poppe, A.C. Porter, C.R. Robinson, J. Russell, J.C. Shelton, T. Soyumer, A.H. Vaughan, and J.H. Whitney. Chromospheric variations in main-sequence stars. *The Astronomical Journal*, 438(1):269–287, 1995. 15, 17, 164, 232

J.R. Barnes. The highly spotted photosphere of the young rapid rotator Speedy Mic. *Monthly Notices of the Royal Astronomical Society*, 364:137–145, 2005. 322

J.R. Barnes. *Doppler imaging of late type stars*. PhD thesis, THE UNIVERSITY OF ST. ANDREWS, 1999. 36, 69, 173, 203, 211, 230

J.R. Barnes, A. Collier Cameron, D.J. James, and J.-F. Donati. Doppler images from dual-site observations of southern rapidly rotating stars - I. Differential rotation on PZ Tel. *Monthly Notices of the Royal Astronomical Society*, 314:162–174, 2000. 16, 320, 321

J.R. Barnes, D.J. James, and A. Collier Cameron. Differential rotation and star-spot evolution on HK Aqr in 2001 and 2002. *Monthly Notices of the Royal Astronomical Society*, 352:589–599, 2004. 322

J.R. Barnes, A. Collier Cameron, J.-F. Donati, D.J. James, S.C. Marsden, and P. Petit. The dependence of differential rotation on temperature and rotation. *Monthly Notices of the Royal Astronomical Society*, 357(1):L1–L5, 2005a. 17, 48, 49, 81, 85, 160, 211, 215, 226, 227, 322

J.R. Barnes, A. Collier Cameron, T.A. Lister, G.R. Pointer, and M.D. Still. LO Peg in 1998: star-spot patterns and differential rotation. *Monthly Notices of the Royal Astronomical Society*, 356:1501–1508, 2005b. 322

S. A. Barnes, S. Sofia, C. F. Prosser, and J. R. Stauffer. Rotation periods of late-type stars in the young open cluster IC 2602. *The Astrophysical Journal*, 516(1):263–275, 1999. 119, 281

S.A. Barnes. On the rotational evolution of solar- and late-type stars, its magnetic origins, and the possibility of stellar gyrochronology. *The Astrophysical Journal*, 586:464–479, 2003. 15

D. C. Barry. The chromospheric age dependence of the birthrate, composition, motions, and rotation of late F and G dwarfs within 25 parsecs of the Sun. *The Astrophysical Journal*, 334:436–448, 1988. 120

G. Basri, L.M. Walkowicz, N Batalha, R.L. Gilliland, J. Jenkins, W.J. Borucki, D. Koch, D. Caldwell, A.K. Dupree, D.W. Latham, S. Meibom, S. Howell, and T. Brown. Photometric variability in Kepler target stars: The sun among stars a first look. *The Astrophysical Journal*, 713:L155–L159, 2010. 27

Sarbani Basu and H.M. Antia. Seismic measurement of the depth of the solar convection zone. *Monthly Notices of the Royal Astronomical Society*, 287:189–198, 1997. 3

E.P. Belserene. Rythms of a variable star. *Sky and Telescope*, 76(3):288, 1988. 58

S.V. Berdyugina. Starspots: A key to the stellar dynamo. *Living Reviews in Solar Physics*, pages 1–62, 2005. 34, 64, 94, 144, 170

S.V. Berdyugina. Stellar magnetic elds across the H-R diagram: Observational evidence. In *Cosmic Magnetic Fields: from Planets, to Stars and Galaxies*, volume 259, pages 323–332. Proceedings IAU Symposium, 2009. 14

S.V. Berdyugina. Surface imaging by the Occamian approach. Basic principles, simulations, and tests. *Astronomy & Astrophysics*, 338:97–105, 1998. 34

M.S. Bessell, F. Castelli, and B. Plez. Model astmospheres broad-band colors, bolometric corrections and temperature calibrations for O-M stars. *Astronomy & Astrophysics*, 333:231, 1998. 29, 30, 52, 63, 64, 87, 96, 144, 145, 212, 213, 287, 288, 292, 294, 296, 298, 304

V.V. Bobylev, G.A. Goncharov, and A.T. Bajkova. Vizier on-line data catalog: J/azh/83/821, 2006. Date accessed December 27, 2010. 300

B.W. Bopp and R.E. Stencel. The FK Comae stars. *The Astrophysical Journal*, 247: L131–L134, 1981. 14, 89

J. Bouvier. Lithium depletion and the rotational history of exoplanet host stars. *Astronomy & Astrophysics*, 489(3):L53–L56, 2008. 88, 116, 284, 292

A. Brandenburg. The case for a distributed solar dynamo shaped by near-surface shear. *The Astrophysical Journal*, 625(1):539–547, 2005. 9

A. Brandenburg, F. Krause, R. Meinel, D. Moss, and I. Tuominen. The stability of nonlinear dynamos and the limited role of kinematic growth rates. *Astronomy & Astrophysics*, 213:411, 1989. 18, 112, 228

B.P. Brown, M.K. Browning, A.S. Brun, M.S. Miesch, and J. Toomre. Persistent magnetic wreaths in a rapidly rotating sun. *The Astrophysical Journal*, 711(1):424–438, 2010. 21, 82, 219, 228

C.J. Brown. *Doppler imaging of active young stars*. PhD thesis, University of Southern Queensland, 2011. 49, 320, 321, 322

S.F. Brown, J.-F. Donati, D.E. Rees, and M. Semel. Zeeman-Doppler imaging of solar-type and Ap stars IV. Maximum entropy reconstruction of 2D magnetic topologies. *Astronomy & Astrophysics*, 250(2):463–474, 1991. 34, 35, 64

G. Bryden, C.A. Beichman, D.E. Trilling, G.H. Rieke, E.K. Holmes, S.M. Lawler, K.R. Stapelfeldt, M.W. Werner, T.N. Gautier, M. Blaylock, K.D. Gordon, J.A. Stansberry, and K.Y.L. Su. Frequency of debris disks around solar-type stars: First results from a *SPITZER* MIPS survey. *The Astrophysical Journal*, 636:1098–1113, 2006. 120

E. Budding, C. Bembrick, B.D. Carter, N. Erkan, M. Jardine, S.C. Marsden, R. Osten, P. Petit, M. Semel, O.B. Slee, and I. Waite. Multisite, multiwavelength studies of the active cool binary CC Eri. *ApSS*, 304(1-4):13–16, 2006. 45

R.P. Butler, J.T. Wright, G.W. Marcy, D.A. Fischer, S.S. Vogt, C.G. Tinney, H.R.A. Jones, B.D. Carter, J.A. Johnson, C. McCarthy, and A.J. Penny. Catalog of nearby exoplanets. *The Astrophysical Journal*, 646(1):505–522, 2006. 225

D.L. Buzasi. Polar magnetic activity and spin-down on the lower main sequence. *The Astrophysical Journal*, 484:855–861, 1997. 81, 210

P. Calibari, F Moreno-Insertis, and M. Schussler. Emerging flux tubes in the solar convection zone. 1: Asymmetry, tilt, and emergence latitude. *The Astrophysical Journal*, 441(2):886–902, 1995. 18

M. Cantiello and J. Braithwaite. Magnetic spots on hot massive stars. *Astronomy & Astrophysics*, 534(id.A140):1–8, 2011. 21

B.D. Carter, S. Brown, J.-F. Donati, D. Rees, and M Semel. Zeeman Doppler imaging of stars with the AAT. *Publications of the Astronomical Society of Australia*, 13(2): 150–155, 1996. 39, 45, 287

B.D. Carter, R.P. Butler, C.G. Tinney, H.R.A. Jones, G.W. Marcy, C. McCarthy, D.A. Fischer, and A.J. Penny. A planet in a circular orbit with a 6 year period. *The Astrophysical Journal*, 593:L43–L46, 2003. 13

L. Casagrande, R. Schoenrich, M. Asplund, S. Cassisi, I. Ramirez, J. Melendez, T. Bensby, and S. Feltzing. New constraints on the chemical evolution of the solar neighbourhood and galactic disc(s). improved astrophysical parameters for the Geneva-Copenhagen survey. *Astronomy & Astrophysics*, 530:A138–, 2011. 22, 120

C. Catala, J.-F. Donati, E. Shkolnik, D. Bohlender, and E. Alecian. The magnetic field of the planet-hosting star ξ Bootis. *Monthly Notices of the Royal Astronomical Society*, 374(1):L42–L46, 2007. 318, 319

G. Cayrel de Strobel. Stars resembling the Sun. *Astronomy & Astrophysics Review*, 7 (3):243–288, 1996. 13

C. Chabrier and I. Baraffe. Structure and evolution of low-mass stars. *Astronomy & Astrophysics*, 327:1039–1053, 1997. 12

W.J. Chaplin, T. Appourchaux, Y. Elsworth, R.A. García, G. Houdek, C. Karoff, T.S. Metcalfe, J. Molenda-Żakowicz, M.J.P.F.G. Monteiro, M.J. Thompson, T.M. Brown, J. Christensen-Dalsgaard, R.L. Gilliland, H. Kjeldsen, W.J. Borucki, D. Koch, J.M. Jenkins, J. Ballot, S. Basu, M. Bazot, T.R. Bedding, O. Benomar, A. Bonanno, I.M. Brandão, H. Bruntt, T.L. Campante, O.L. Creevey, M.P. Di Mauro, G. Doğan, S. Dreizler, P. Eggenberger, L. Esch, S.T. Fletcher, S. Frandsén, N. Gai, P. Gaulme, R. Handberg, S. Hekker, R. Howe, D. Huber, S.G. Korzennik, J.C. Lebrun, S. Leccia, M. Martic, S. Mathur, B. Mosser, R. New, P.-O. Quirion, C. Régulo, I.W. Roxburgh, D. Salabert, J. Schou, S.G. Sousa, D. Stello, G.A. Verner, T. Arentoft, C. Barban, K. Belkacem, S. Benatti, K. Biazzo, P. Boumier, P.A. Bradley, A.-M. Broomhall, D.L. Buzasi, R.U. Claudi, M.S. Cunha, F. D'Antona, S. Deheuvels, A. Derekas, A. García Hernndez, M.S. Giampapa, M.J. Goupil, M. Gruberbauer, J.A. Guzik, S.J. Hale, M.J. Ireland, L.L. Kiss, I.N. Kitiashvili, K. Kolenberg, H. Korhonen, A.G. Kosovichev, F. Kupka, Y. Lebreton, B. Leroy, H.-G. Ludwig, S. Mathis, E. Michel, A. Miglio, J. Montalbán, A. Moya, A. Noels, R.W. Noyes, P.L. Pallé, L. Piau, H.L. Preston, T. Roca Cortés, M. Roth, K.H. Sato, J. Schmitt, A.M. Serenelli, V. Silva Aguirre, I.R. Stevens, J.C. Suárez, M.D. Suran, R. Trampedach, S. Turck-Chiéze, K. Uytterhoeven, R. Ventura, and P.A. Wilson. The asteroseismic potential of Kepler: First results for solar-type stars. *The Astrophysical Journal*, 713:L169–175, 2010. 27

P. Charbonneau. Dynamo models of the solar cycle. *Living Reviews in Solar Physics*, 7(3):1–91, 2005. 11

P. Charbonneau. Solar and stellar dynamo models, 2009. URL www.vsp.ucar.edu/Heliophysics/pdf/Charbonneau_Heliophysics2009.pdf. Date Accessed: 04/12/2012. 18

P. Charbonneau and K.B. MacGregor. Magnetic fields in massive stars. I. Dynamo models. *The Astrophysical Journal*, 559(2):1094–1107, 2001. 20

P. Charbonneau and K.B. MacGregor. Solar interface dynamos. II. Linear, kinematic models in spherical geometry. *The Astrophysical Journal*, 486:484–495, 1997. 9

C. Charbonnel and S.C. Balachandran. The nature of the lithium rich giants. Mixing episodes on the rgb and early-agb. *Astronomy & Astrophysics*, 359:563–572, 2000. 88

Y.Q. Chen, P. E. Nissen, T. Benoni, and G. Zhao. Lithium abundances for 185 main-sequence stars: Galactic evolution and stellar depletion of lithium. *Astronomy & Astrophysics*, 371:943–951, 2001. 120

A. Collier Cameron. Modelling stellar photospheric spots using spectroscopy. In *Surface Inhomogeneities on Late-Type Stars, Proceedings of a colloquium held at Armagh Observatory, Northern Ireland, 24-27 July, 1990*, volume 397, pages 33–45. Springer-Verlag, Heidelberg, 1992. 34, 35, 64

A. Collier Cameron and J.-F. Donati. Doin the twist: secular changes in the surface differential rotation on AB Doradus. *Monthly Notices of the Royal Astronomical Society*, 329:L23–L27, 2002. 16, 320, 321

A. Collier Cameron, J.-F. Donati, and M. Semel. Stellar differential rotation from direct starspot tracking. *Monthly Notices of the Royal Astronomical Society*, 330(3): 699–706, 2002. 16, 44

K.R. Covey, M.A. Agüeros, J.L. Lemonias, N.M. Law, A.L. Kraus, and the Palomar Transient Factory Collaboration. The age-rotation-activity relation: From Myrs to Gyrs. *arXiv:1012.0061v1 [astro-ph.SR]*, 2010. 15

A. Cowley, C. Cowley, M. Jaschek, and C. Jaschek. A study of the bright A stars. I. A catalogue of spectral classifications. *The Astronomical Journal*, 74(3):375–406, 1969. 217

G. Cutispoto, L. Pastori, L. Pasquini, J.R. de Medeiros, G. Tagliaferri, and J. Andersen. Fast-rotating nearby solar-type stars. I. Spectral classifcation, $v \sin i$, Li abundances and x-ray luminosities. *Astronomy & Astrophysics*, 384:491–503, 2002. 51, 318, 319

L. da Silva, C. A. O. Torres, R. de la Reza, G. R. Quast, C. H. F. Melo, and M. F. Sterzik. Search for associations containing young stars (SACY) III. Ages and Li abundances. *Astronomy & Astrophysics*, 508:833–839, 2009. 22, 88

D. de Souza, J. Zorec, S. Jankov, F. Vakili, L. Abe, and E. Janot-Pacheco. Stellar differential rotation and inclination angle from spectro-interferometry. *Astronomy & Astrophysics*, 418:781–794, 2004. 28

P.T. de Zeeuw, R. Hoogerwerf, J.H.J. de Bruijne, A.G.A. Brown, and A. Blaauw. A *HIPPARCOS* census of the nearby OB Associations. *The Astronomical Journal*, 117 (1):354–399, 1999. 51, 304

E.E. DeLuca, Y. Fan, and S.H. Saar. The emergence of magnetic flux loops in sun-like stars. *The Astrophysical Journal*, 481:369, 1997. 19, 81, 210

S.F. Dermott, D.D. Durda, K. Grogan, and T.J.J. Kehoe. Asteroidal dust. In W.F. Bottke Jr, A. Cellino, P. Paolicchi, and R.P. Binzel, editors, *Asteroids III*, pages 423–442. University of Arizona Press, Tucson, 2002. 120

A.J. Deutsch. Harmonic analysis of the periodic spectrum variables. In B. Lehnert, editor, *Electromagnetic Phenomena in Cosmical Physics*, volume 6 of *IAU Symposia*, pages 209–221, Cambridge; New York, 1958. Cambridge University Press. 31

W. Dieckvoss and O. Heckmann. AGK3 catalogue, 1975. 278

M Dikpati and P. Charbonneau. A Bacbock-Leighton flux transport dynamo with solar-like differential rotation. *The Astrophysical Journal*, 518:508–520, 1999. 9

M. Dikpati, T. Corbard, M.J. Thompson, and P.A. Gilman. Flux transport solar dynamos with near-surface radial shear. *The Astrophysical Journal*, 575(1):L41–L45, 2002. 82, 158, 219

M. Dikpati, G. de Toma, P.A. Gilman, C.N. Arge, and O.R. White. Diagnostics of polar field reversal in solar cycle 23 using a flux transport dynamo model. *The Astrophysical Journal*, 601(2):1136–1151, 2004. 1, 10

J.D. do Nascimento Jr, J.S. da Costa, and J.R. De Medeiros. Rotation and lithium abundance of solar-analog stars. Theoretical analysis of observations. *Astronomy & Astrophysics*, 519:id:A101, 2010. 284

A. Domiciano de Souza, M. Hadjara, F. Vakili, P. Bendjoya, F. Millour, L. Abe, A. C. Carciofi, D. M. Faes, P. Kervella, S. Lagarde, A. Marconi, J.-L. Monin, G. Niccolini,

R. G. Petrov, and G. Weigelt. Beyond the diffraction limit of optical/IR interferometers. I. Angular diameter and rotation parameters of Achernar from differential phases. *Astronomy & Astrophysics*, 545:A130, 2012. 28

J.-F. Donati. Magnetic feedback on stellar convective zones. In J. Trujillo-Bueno and J. Sánchez Almeida, editors, *Solar Polarization 3*, volume 307, pages 529–538. ASP Conference Series, 2003. 220

J.-F. Donati and S.F. Brown. Zeeman-Doppler imaging of active stars. V. Sensitivity of maximum entropy magnetic maps to field orientation. *Astronomy & Astrophysics*, 326:1135–1142, 1997. 34, 35, 42, 64, 73, 124, 147

J.-F. Donati and A. Collier Cameron. Differential rotation and magnetic polarity patterns on AB Doradus. *Monthly Notices of the Royal Astronomical Society*, 291(1): 1–19, 1997. 16, 217, 318, 319, 320, 321

J.-F. Donati and A. Collier-Cameron. Differential rotation and magnetic polarity patterns on AB Doradus. *Monthly Notices of the Royal Astronomical Society*, 291(1): 1–19, 1997. 44, 45, 48

J.-F. Donati and J.D. Landstreet. Magnetic fields of nondegenerate stars. *Annual Review of Astronomy & Astrophysics*, 47(1):333–370, 2009. 84, 112, 135, 160, 202, 203, 219

J.-F. Donati, M. Semel, and F. Praderie. Zeeman-Doppler imaging of active stars. II - Numerical simulation and first observational results. *Astronomy & Astrophysics*, 225(2):467–478, 1989. 36

J.-F. Donati, S.F. Brown, M. Semel, D.E. Rees, R.C. Dempsey, J.M. Matthews, G.W. Henry, and D.S. Hall. Photospheric imaging of the RS CVn system HR 1099. *Astronomy & Astrophysics*, 265(2):682–700, 1992a. 14, 44, 217

J.-F. Donati, M. Semel, and D.E. Rees. Circularly polarized spectroscopic observations of RS CVn systems. *Astronomy & Astrophysics*, 265(2):669–681, 1992b. 14, 22, 44, 45, 62, 217

J.-F. Donati, M. Semel, B.D. Carter, D.E. Rees, and A. Collier Cameron. Spectropolarimetric observations of active stars. *Monthly Notices of the Royal Astronomical Society*, 291:658–682, 1997. 22, 27, 34, 36, 38, 44, 45, 46, 50, 62, 121, 145, 166, 279, 286, 287

J.-F. Donati, A. Collier Cameron, G. A. J. Hussain, and M. Semel. Magnetic topology and prominence patterns on AB Doradus. *Monthly Notices of the Royal Astronomical Society*, 302(3):437–456, 1999. 108

J.-F. Donati, M. Mengel, B.D. Carter, S. Marsden, A. Collier Cameron, and R. Wichmann. Surface differential rotation and prominences of the Lupus post T Tauri star RX J1508.6-4423. *Monthly Notices of the Royal Astronomical Society*, 316(3): 699–715, 2000. 16, 44, 48, 49, 77, 108, 211, 320, 321

J.-F Donati, A. Collier Cameron, and P. Petit. Temporal fluctuations in the differential rotation of cool active stars. *Monthly Notices of the Royal Astronomical Society*, 345 (4):1187–1899, 2003a. 16, 17, 69, 158, 173, 203, 211, 226, 230, 320, 321, 322

J.-F. Donati, A. Collier Cameron, M. Semel, G.A.J. Hussain, P. Petit, B.D. Carter, S.C. Marsden, M. Mengel, A. López Ariste, S.V. Jeffers, and D.E. Rees. Dynamo processes and activity cycles of the active stars AB Doradus, LQ Hydrae and HR 1099. *Monthly Notices of the Royal Astronomical Society*, 345(4):1145–1186, 2003b. 18, 34, 36, 45, 46, 58, 62, 66, 82, 84, 94, 112, 121, 141, 145, 157, 217, 276, 279, 283

J.-F. Donati, C. Catala, J.D. Landstreet, and P. Petit. ESPaDOnS: The new generation stellar spectro-polarimeter. performances and first results. In *Solar Polarization 4*, volume 358, pages 362–368. Astronomical Society of the Pacific Conference Series, 2006a. 28

J.-F. Donati, I.D. Howarth, M.M. Jardine, P. Petit, C. Catala, J.D. Landstreet, J.-C. Bouret, E. Alecian, J.R. Barnes, T. Forveille, F. Paletou, and N. Manset. The surprising magnetic topology of τ Sco: fossil remnant or dynamo output? *Monthly Notices of the Royal Astronomical Society*, 370(2):629–644, 2006b. 40, 73, 124

J.-F. Donati, J. Morin, P. Petit, X. Delfosse, T. Forveille, M. Auriére, R. Cabanac, B. Dintrans, R. Farés, T. Gastine, M. M. Jardine, F. Ligniéres, F. Paletou, J. C. Ramirez Veléz, and S. Théado. Large-scale magnetic topologies of early m

dwarfs. *Monthly Notices of the Royal Astronomical Society*, 390(2):545–560, 2008a. 42

J.-F. Donati, C. Moutou, R. Farés, D. Bohlender, C. Catala, M. Deleuil, E. Shkolnik, A. Collier Cameron, M. M. Jardine, and G. A. H. Walker. Magnetic cycles of the planet-hosting star τ Bootis. *Monthly Notices of the Royal Astronomical Society*, 385 (3):1179–1185, 2008b. 17, 41, 193, 234

J.D. Dorren and E.F. Guinan. HD 129333: The Sun in its infancy. *The Astrophysical Journal*, 428:805–818, 1994. 163, 164, 173, 201, 203, 211, 220

J.D. Dorren, M. Güdel, and E.F. Guinan. X-ray emission from the Sun in its youth and old age. *The Astrophysical Journal*, 448:431–436, 1995. 164

D.K. Duncan, A.H. Vaughan, O.C. Wilson, G.W. Preston, J. Frazer, H. Lanning, A. Misch, J. Mueller, D. Soyoumer, L. Woodard, S.L. Baliunas, R.W. Noyes, L.W. Hartmann, A. Porter, C. Zwaan, F. Middelkoop, and R.G.M. Rutten. Ca II H and K measurements made at Mount Wilson observatory, 1966-1983. *Astrophysical Journal Supplement Series*, 76:383–430, 1991. 132, 133, 197, 198, 229

A. Duquennoy and M. Mayor. Multiplicity among solar-type stars in the solar neighbourhood II. Distribution of the orbital elements in an unbiased sample. *Astronomy & Astrophysics*, 248:485–524, 1991. 164

P.P. Eggleton and A.A. Tokovinin. A catalogue of multiplicity among bright stellar systems. *Monthly Notices of the Royal Astronomical Society*, 389(2):869–879, 2008. 119

ESA. The *HIPPARCOS* and *TYCHO* catalogues, ESA SP-1200, 1997. Date Accessed:. 52, 160, 214, 318, 319

R. Fares, J.-F. Donati, C. Moutou, D. Bohlender, C. Catala, M. Deleuil, E. Shkolnik, A. Collier Cameron, M. M. Jardine, and G. A. H. Walker. Magnetic cycles of the planet-hosting star τ Bootis - II. A second magnetic polarity reversal. *Monthly Notices of the Royal Astronomical Society*, 398(3):1383–1391, 2009. 41, 193, 234

R. Fares, J.-F. Donati, C. Moutou, M. Jardine, A.C. Cameron, A.F. Lanza, D. Bohlender, S. Dieters, A.F. Martínez Fiorenzano, A. Maggio, I. Pagano, and E.L. Shkolnik. Magnetic field, differential rotation and activity of the hot-jupiter-hosting star HD 179949. *Monthly Notices of the Royal Astronomical Society*, 423(2):1006–1017, 2012. 225, 322

U. Feldman, E. Landi, and N.A. Schwadron. On the sources of fast and slow solar wind. *JGR*, 110:A07109, 2005. 5

H.-E. Fröhlich, A. Frasca, G. Catanzaro, A. Bonanno, E. Corsaro, J. Molenda-Żakowicz, A. Klutsch, and D. Montes. Magnetic activity and differential rotation in the young sun-like stars KIC 7985370 and KIC 7765135. *Astronomy & Astrophysics*, 543:A146, 2012. 27, 48

H.-F. Frölich, R. Tschäpe, G. Rüdiger, and K.G. Strassmeier. EK Draconis: Long-term photometry on Sonneberg sky-patrol plates. *Astronomy & Astrophysics*, 391: 659–663, 2002. 164

E. Gerth and Y.V. Glagolevskij. On generating and derived magnitudes of stellar magnetic fields. In V. Glagolevskij, Yu, D.O. Kudryavtsev, and I.I. Romanyuk, editors, *Magnetic Stars*, volume 1 of *SAO International Meeting and Workshop*, pages 1–18, SAO, Nizhnij Arkhyz, Russia, 2004. 41

S. Godier and J.-P. Rozelot. The solar oblateness and its relationship with the structure of the tachocline and of the Suns subsurface. *Astronomy & Astrophysics*, 355:365–374, 2000. 1

A.V. Goncharskii, V.V. Stepanov, V.L. Kokhlova, and A.G. Yagola. Reconstruction of local line profiles from those observed in an Ap spectrum. *Soviet Astronomy Letters*, 3:147–149, 1977. 31, 34

G.A. Gontcharov. Pulkovo compilation of radial velocities for 35495 *HIPPARCOS* stars in a common system. *Astronomy Letters*, 32(11):759–771, 2006. 295

J.A. Graham. UBVRI standard stars in the E-Regions. *Astronomical Society of the Pacific*, 94:244–265, 1982. 31, 54, 56, 57

Th. Granzer, M. Schüssler, P. Caligari, and K.G. Strassmeier. Distribution of starspots on cool stars. II. Pre-main-sequence and ZAMS stars between 0.4 $M_{\odot}$ and 1.7 $M_{\odot}$. *Astronomy & Astrophysics*, 355:1087–1097, 2000. 19, 165

D.F. Gray. Measurements of rotation and turbulence in F, G, and K dwarfs. *The Astrophysical Journal*, 281:719–722, 1984. 226

D.F. Gray. *The Observation and Analysis of Stellar Photospheres*. Cambridge: Cambridge University Press, second edition, 1992. 281

R.O. Gray and C.J. Corally. *Stellar spectral classification*. Princeton University Press, 2009. 13

R.O. Gray, C.J. Corbally, R.F. Garrison, M.T. McFadden, E.J. Bubar, C.E. McGahee, A.A. O'Donoghue, and E.R. Knox. Contributions to the nearby stars (NStars) project: spectroscopy of stars earlier than M0 within 40 pc – the southern sample. *The Astronomical Journal*, 132:161–170, 2006. 31, 38, 141, 318, 319

M. Güdel, J.H.M.M. Schmitt, A.O. Benz, and N.M. Elias. The corona of the young solar analog EK Draconis. *Astronomy & Astrophysics*, 301:201–212, 1995. 163, 164, 172, 201, 202

M. Güdel, E.F. Guinan, and S.L. Skinner. The x-ray Sun in time: A study of the long-term evolution of coronae of solar-type stars. *The Astrophysical Journal*, 483: 947–960, 1997. 15

P. Guillout, A. Klutsch, A. Frasca, R. Freire Ferrero, E. Marilli, G. Mignemi, K. Biazzo, J. Bouvier, R. Monier, G. Motch, and M. Sterzik. A spectroscopic survey of the youngest field stars in the solar neighbourhood. I. The optically bright sample. *Astronomy & Astrophysics*, 504(3):829–843, 2009. 88, 284, 292

E.F. Guinan, I. Ribas, and G.M. Harpe. Far-ultraviolet emissions of the sun in time: Probing solar magnetic activity and effects on evolution of paleoplanetary atmospheres. *The Astrophysical Journal*, 594:561–572, 2003. 163

G.E. Hale. On the probably existence of a magnetic field in sun-spots. *The Astrophysical Journal*, 28:315–343, 1908. 8, 217

G.E. Hale, F. Ellerman, S.B. Nicholson, and A.H. Joy. The magnetic polarity of sunspots. *The Astrophysical Journal*, 49:153–P11, 1919. 10

C. Han, S.-H. Park, H.-I. Kim, and K. Chang. Detection of stellar spots from the observations of caustic-crossing binary-lens gravitational microlensing events. *Monthly Notices of the Royal Astronomical Society*, 316:665–670, 2000. 29

D.M. Harrington. *Stellar spectropolarimetry with HiVIS: Herbig AE/BE stars, circumstellar environments and optical pumping*. PhD thesis, University of Hawaii, 2008. 37

D.H. Hathaway. Solar physics: The corona, 2012a. URL http://solarscience.msfc.nasa.gov/corona.shtml. Date Accessed: 12/05/2012. 4

D.H. Hathaway. Solar physics: The transition region, 2012b. URL http://solarscience.msfc.nasa.gov/t_region.shtml. Date Accessed: 12/05/2012. 4

S.L. Hawley, J.E. Gizis, and I.N. Reid. The palomar/MSU nearby star spectroscopic survey.II.The southern M dwarfs and investigation of magnetic activity. *The Astronomical Journal*, 112(6):2799–2827, 1996. 12

C. Hayashi. Stellar evolution in early phases of gravitational contraction. *Publications of the Astronomical Society of Japan*, 13:450–452, 1961. 88

M.A. Hendry, H.M. Bryce, and D. Valls-Gabaud. The microlensing signatures of photospheric starspots. *Monthly Notices of the Royal Astronomical Society*, 335:539–549, 2002. 29

T.J. Henry, D.R. Soderblom, R.A. Donahue, and S.L. Baliunas. A survey of Ca II H and K chromospheric emission in southern solar-type stars. *The Astronomical Journal*, 111:439–465, 1996. 51

L.G. Henyey, R. LeLevier, and R.D. Levée. The early phases of stellar evolution. *Astronomical Society of the Pacific*, 67:154–160, 1955. 88

D. Heyrovský and D. Sasselov. Detecting stellar spots by gravitational microlensing. *The Astrophysical Journal*, 529:69–76, 2000. 29

T. Hinse, R. Michelson, U. Joergensen, K. Gozdiewski, and A. Mikkola. Dynamics and stability of telluric planets within the habitable zone of extrasolar planetary systems - numerical simulations of test particles within the HD 4208 and HD 70642 systems. *Astronomy & Astrophysics*, 488:1133–1147, 2008. 13

E. Hög, C. Fabricius, V.V. Makarov, S. Urban, T. Corbin, G. Wycoff, U. Bastian, P. Schwekendiek, and A. Wicenec. The Tycho-2 catalogue of the 2.5 million brightest stars. *Astronomy & Astrophysics*, 355:L27–L30, 2000. 163

J. Holmberg, B. Nordström, and J. Andersen. The Geneva-Copenhagen survey of the solar neighbourhood. III. Improved distances, ages, and kinematics. *Astronomy & Astrophysics*, 501(3):941–947, 2009. 120, 123, 212, 213, 296

N. Houk. *Michigan catalogue for the HD stars*, volume 2. Ann Arbor, Univ. of Michigan, 1978. 278

N. Houk. *Michigan catalogue for the HD stars*, volume 3. Ann Arbor, Univ. of Michigan, 1982. 278

N. Houk and A.P. Cowley. *Michigan catalogue for the HD stars*, volume 1. Ann Arbor, Univ. of Michigan, 1975. 278, 318, 319

N. Houk and M. Smith-Moore. *Michigan catalogue for the HD stars*, volume 4. Ann Arbor, Univ. of Michigan, 1988. 278

N. Houk and C. Swift. *Michigan catalogue for the HD stars*, volume 5. Ann Arbor, Univ. of Michigan, 1999. 278

S. Hubrig, M. Schöller, R.S. Schnerr, J.F. González, R. Ignace, and H.F. Henrichs. Magnetic field measurements of O stars with FORS1 at the VLT. *Astronomy & Astrophysics*, 490:793–800, 2008. 14

K.-H. Hwang and C. Han. Characterization of stellar spots in next-generation microlensing surveys. *The Astrophysical Journal*, 709:327–331, 2010. 29

J.L. Innis, D.W. Coates, K. Thompson, and T. Lloyd Evans. Observations of active-chomosphere stars III - Photometry of PZ Tel 1979-1985. *Monthly Notices of the Royal Astronomical Society*, 242:306–310, 1990. 318, 319

J. Irwin, S. Hodgkin, S. Aigrain, L. Hebb, J. Bouvier, C. Clarke, E. Moraux, and D. M. Bramich. The monitor project: rotation of low-mass stars in the open cluster NGC 2516. *Monthly Notices of the Royal Astronomical Society*, 377(2):741–758, 2007. 119, 281

J. Jackson and R.H. Stoy. *Cape Photographic Catalogue for 1950.0 zone -30 to -64*. Ann. Cape Obs., 1954. 278

S. Jankov, A. Domiciano de Souza Jr, C. Stehlé, F. Vakili, K. Perraut-Rousselet, and O. Chesneau. Interferometric-Doppler imaging of stellar surface abundances. In W.A. Traub, editor, *Interferometry for Optical Astronomy II*, volume 4838 of *SPIE Proceedings*, pages 587–593, Bellingham, U.S.A., 2003. International Society for Optical Engineering. 28

S.P. Järvinen, S.V. Berdyugina, and K.G. Strassmeier. Spots on EK Draconis: Active longitudes and cycles from long-term photometry. *Astronomy & Astrophysics*, 440: 735–741, 2005. 164

S.P. Järvinen, S.V. Berdyugina, H. Korhonen, I. Ilyin, and I. Tuominen. EK Draconis magnetic activity in the photosphere and chromosphere. *Astronomy & Astrophysics*, 472:887–895, 2007. 22, 165, 166, 170, 171, 172, 173, 201, 203, 212, 213

R. Jayawardhana, J. Coffey, A. Scholz, A. Brandeker, and M.A. Van Kerkwijk. Accretion disks around young stars: Lifetimes, disk locking, and variability. *The Astrophysical Journal*, 648:1206–1218, 2006. 15

J. Jefferies, B.W. Lites, and A. Skumanich. Transfer of line radiation in a magnetic field. *The Astrophysical Journal*, 343:920–935, 1989. 42

S.V. Jeffers and J.-F. Donati. High levels of surface differential rotation on the young G0 dwarf HD 171488. *Monthly Notices of the Royal Astronomical Society*, 390(2): 635–644, 2008. 16, 36, 41, 49, 81, 82, 84, 92, 141, 143, 226, 320, 321

S.V. Jeffers, J.R. Barnes, and A. Collier Cameron. The latitude distribution of star-spots on He 699. *Monthly Notices of the Royal Astronomical Society*, 331(3):666–672, 2002. 79

S.V. Jeffers, J.-F. Donati, E. Alecian, and S.C. Marsden. Observations of non-solar-type dynamo processes in stars with shallow convective zones. *Monthly Notices of the Royal Astronomical Society*, 411(2):1301–1312, 2011. 17, 41, 49, 143, 160, 226, 320, 321

R.D. Jeffries, D.J. James, and G.E. Bromage. RE 1816+541: a northern hemisphere analogue to the low-mass rapid rotator HK Aqr. *Monthly Notices of the Royal Astronomical Society*, 271(2):476–480, 1994. 318, 319

C.M. Johns-Krull and J.A. Valenti. Detection of strong magnetic fields on M Dwarfs. *The Astrophysical Journal*, 459:L95–L98, 1996. 12

N.V. Kharchenko and S. Roeser. Vizier on-line data catalog: I/280B/ascc, 2009. Date accessed December 27, 2010. 295

N.V. Kharchenko, R.-D. Scholz, A.E. Piskunov, S. Röser, and E. Schilbach. Astrophysical supplements to the ASCC-2.5: Ia. radial velocities of 55000 stars and mean radial velocities of 516 galactic open clusters and associations. *Astronomische Nachrichten*, 328(9):889–896, 2007. 296

M. Kiraga. ASAS photometry of ROSAT sources. I. Periodic variable stars coincident with bright sources from the ROSAT all sky survey. *Acta Astronomica*, 62:67–95, 2012. 94, 96, 212, 213

L.L. Kitchatinov. Theory of differential rotation and meridional circulation. In *Solar and Astrophysical Dynamos and Magnetic Activity, Proceedings IAU Symposium 294, 2012*, volume 294, page arXiv: 1210.7041v1. Cambridge University Press, 2013. 7, 17

L.L. Kitchatinov and S.V. Olemskoy. Differential rotation of main-sequence dwarfs and its dynamo-efficiency. *Monthly Notices of the Royal Astronomical Society*, 411: 1059–1066, 2011. 7, 19, 160, 226

L.L. Kitchatinov and G. Rüdiger. Differential rotation models for late-type dwarfs and giants. *Astronomy & Astrophysics*, 344:911–917, 1999. 19, 81, 210

D.P. Kjurkchieva and D. V. Marchev. Hα observations of the star FK Com. *Astronomy & Astrophysics*, 2005:221–233, 2005. 117

O. Kochukhov and N. Piskunov. Doppler Imaging of stellar magnetic fields. II. Numerical experiments. *Astronomy & Astrophysics*, 388:868–888, 2002. 225

O. Kochukhov and G.A. Wade. Magnetic Doppler imaging of α^2 canum venaticorum in all four stokes parameters. Unveiling the hidden complexity of stellar magnetic fields. *Astronomy & Astrophysics*, 513(id.A13):1–15, 2010. 225

O. Kochukhov, S. Bagnulo, G.A. Wade, L. Sangalli, N. Piskunov, J.D. Landstreet, P. Petit, and T.A.A. Sigut. Magnetic Doppler imaging of 53 Camelopardalis in all four Stokes parameters. *Monthly Notices of the Royal Astronomical Society*, 414: 613–632, 2004. 38

O. Kochukhov, V. Makaganiuk, and N. Piskunov. Least-squares deconvolution of the stellar intensity and polarization spectra. *Astronomy & Astrophysics*, 524:id.A5, 2010. 34, 44

O. Kochukhov, V. Makaganiuk, N. Piskunov, F. Snik, S.V. Jeffers, C.M. Johns-Krull, C.U. Keller, M. Rodenhuis, and J.A. Valenti. First detection of linear polarization in the line profiles of active cool stars. *The Astrophysical Journal Letters*, 732(2): L19–L22, 2011. 38

O. Kochukhov, M.J. Mantere, T. Hackman, and I. Ilyin. Magnetic field topology of the RS CVn star II Pegasi. *Astronomy & Astrophysics*, 550(id A84):1–19, 2013. 40, 220, 225

C. Koen and L. Eyer. New periodic variables from the *HIPPARCOS* epoch photometry. *Monthly Notices of the Royal Astronomical Society*, 331(1):45–59, 2002. 87, 275, 276

C. Koen, D. Kilkenny, F. Van Wyk, and F. Marang. UBV(RI)$_c$JHK observations of *HIPPARCOS*-selected nearby stars. *Monthly Notices of the Royal Astronomical Society*, 403:1949–1968, 2010. 318, 319

K. Kolenberg, R. Szabó, D. W. Kurtz, R. L. Gilliland, J. Christensen-Dalsgaard, H. Kjeldsen, T.M. Brown, J.M. Benkö, M. Chadid, A. Derekas, M. Di Criscienzo, E. Guggenberger, K. Kinemuchi, A. Kunder, Z. Kolláth, G. Kopacki, P. Moskalik, J.M. Nemec, J. Nuspl, R. Silvotti, M.D. Suran, W.J. Borucki, D. Koch, and J.M. Jenkins. First Kepler results on RR Lyrae stars. *The Astrophysical Journal*, 713: L198L203,, 2010. 27

B. König, E.W. Guenther, J. Woitas, and A.P. Hatzes. The young active binary star EK Draconis. *Astronomy & Astrophysics*, 435:215–223, 2005. 164, 170, 172, 176, 232

M Kopf. *Zeeman-Doppler Imaging of active late-type stars*. PhD thesis, University of Potsdam, 2008. 34

H. Korhonen and D. Elstner. Investigating variation of latitudinal stellar spot rotation and its relation to the real stellar surface rotation. *Astronomy & Astrophysics*, 532 (id.A106):1–8, 2011. 114, 159, 228

H. Korhonen, S. Hubrig, S.V. Berdyugina, Th. Granzer, T. Hackman, M. Schöller, K.G. Strassmeier, and M. Weber. First measurement of the magnetic field on FK Com and its relation to the contemporaneous star-spot locations. *Monthly Notices of the Royal Astronomical Society*, 295(1):282–289, 2009. 114, 117

Zs. Kövári, J. Bartus, K.G. Strassmeier, K. Vida, M. Švanda, and K. Oláh. Anti-solar differential rotation on the active K-giant σ Geminorum. *Astronomy & Astrophysics*, 474(1):165–168, 2007. 49

A. Krishnamurthi, M. H. Pinsonneault, S. Barnes, and S. Sofia. Theoretical models of the angular momentum evolution of solar-type stars. *The Astrophysical Journal*, 480:303–323, 1997. 119, 281

J.R. Kuhn, R. Bush, M. Emilio, and J.R. Scholl. The precise solar shape and its variability. *Science*, 337(6102):1638–1640, 2012. 1

J. Küker, G. Rüdiger, and M. Schultz. Circulation-dominated solar shell dynamo models with positive alpha-effect. *Astronomy & Astrophysics*, 374:301–308, 2001. 10

M. Küker, G. Rüdiger, and L.L. Kitchatinov. The differential rotation of G dwarfs. *Astronomy & Astrophysics*, 530:A48–, 2011. 160, 226

R.L. Kurucz. CDROM #13 (ATLAS9 atmospheric models) and #18 (ATLAS9 and SYNTHE routines) spectral line databases, 1993. 43, 62, 89, 93, 121, 145, 166, 281

E. Landi Degl'Innocenti and M. Landi Degl'Innocenti. Quantum theory of line formation in a magnetic field. *Solar Physics*, 27:319–329, 1972. 42

K.R. Lang. *Astrophysical Formulae*. Springer, 2000. 4, 6

A.F. Lanza, M. Rodonò, and R. Rosner. Orbital period modulation and magnetic cycles in close binaries. *Monthly Notices of the Royal Astronomical Society*, 296(4): 893–902, 1998. 82, 158, 219

J.Z. Li and J.Y. Hu. Newly discovered candidate weak-line T Tauri stars in the surrounding area of the Taurus-Auriga region. *Astronomy and Astrophysics Supplement*, 132:173–179, 1998. 22, 120, 123, 212, 213, 278, 288

F. Ligniéres, P. Petit, T. Böhm, and M. Auriére. First evidence of a magnetic field on Vega. Towards a new class of magnetic A-type stars. *Astronomy & Astrophysics*, 500(3):L41–L44, 2009. 20

J.L. Linsky, R. Bushinsky, T. Ayres, J. Fontenla, and K. France. Far-ultraviolet continuum emission: Applying this diagnostic to the chromospheres of solar-mass stars. *The Astrophysical Journal*, 745(1):ID25, 2012. 163

J. MacDonald and D.J. Mullen. Magnetic fields in massive stars: dynamics and origin. *Monthly Notices of the Royal Astronomical Society*, 348(2):702–716, 2004. 20

K.B. MacGregor and P. Charbonneau. Solar interface dynamos. I. Linear kinematic models in cartesian geometry. *The Astrophysical Journal*, 486:484–495, 1997. 9

S. Madsen, D. Dravins, and L. Lindegren. Astrometric radial velocities. III. *HIPPARCOS* measurements of nearby star clusters and associations. *Astronomy & Astrophysics*, 381:446–463, 2002. 296

E.E. Mamajek. How accurately can we age-date solar-type dwarfs using activity/rotation diagnostics? In *IAU Symp. No 258, The Ages of Stars:*, volume 258, pages 375–382. Springer-Verlag, Heidelberg, 2009. 15

E.E. Mamajek and L.A. Hillenbrand. Improved age estimation for solar-type dwarfs using activity-rotation diagnostics. *The Astronomical Journal*, 687:1264–1293, 2008. 15

E.E. Mamajek, M.R. Meyer, and J. Liebert. Post-T Tauri stars in the nearest OB association. *The Astronomical Journal*, 124(3):1670–1694, 2002. 296

A. Marino, G. Micela, G. Peres, and S. Sciortino. X-ray rotational modulation of a supersaturated star in IC 2391. *Astronomy & Astrophysics*, 407:L63–L66, 2003. 282

S.C. Marsden, I.A. Waite, B.D. Carter, and J.-F. Donati. Doppler imaging and surface differential rotation of young open cluster stars - I. HD 307938 (R58) in IC 2602. *Monthly Notices of the Royal Astronomical Society*, 359(2):711–724, 2005. 35, 36, 49, 64, 65, 79, 92, 94, 124, 273, 318, 319, 320, 321

S.C. Marsden, J.-F. Donati, M. Semel, P. Petit, and B.D. Carter. Surface differential rotation and photospheric magnetic field of the young solar-type star HD 171488 (V889 Her). *Monthly Notices of the Royal Astronomical Society*, 370(1):468–476, 2006. 16, 35, 41, 49, 62, 81, 84, 103, 141, 143, 226, 318, 319, 320, 321

S.C. Marsden, B.D. Carter, and J.-F. Donati. The chromospheric emission of solar-type stars in the young open clusters IC 2391 and IC 2602. *Monthly Notices of the Royal Astronomical Society*, 399(2):888–905, 2009. 20, 282

S.C. Marsden, M.M. Jardine, J.C. Ramírez Vélez, C.J. Brown, B.D. Carter, J.-F. Donati, N. Dunstone, R. Hart, M. Semel, and I.A. Waite. Magnetic fields and differential rotation on the pre-main sequence - I. The early-G star HD 141943 - brightness and magnetic topologies. *Monthly Notices of the Royal Astronomical Society*, 413(3): 1922–1938, 2011a. 18, 41, 44, 64, 82, 84, 94, 141, 143, 202, 275, 318, 319

S.C. Marsden, M.M. Jardine, J.C. Ramírez Vélez, C.J. Brown, B.D. Carter, J.-F. Donati, N. Dunstone, R. Hart, M. Semel, and I.A. Waite. Magnetic fields and differential rotation on the pre-main sequence - II. The early-G star HD 141943 - coronal magnetic field, hα emission and differential rotation. *Monthly Notices of the Royal Astronomical Society*, 413(3):1939–1948, 2011b. 17, 18, 41, 44, 45, 64, 84, 114, 143, 214, 225, 275, 320, 321

E.L. Martín and A. Claret. Stellar models with rotation: an exploratory application to pre-main sequence lithium depletion. *Astronomy & Astrophysics*, 306:408–416, 1996. 284

M.J. Martínez González, A. Asensio Ramos, T.A. Carroll, M. Kopf, J.C. Ramírez Vélez, and M. Semel. PCA detection and denoising of Zeeman signatures in polarised stellar spectra. *Astronomy & Astrophysics*, 486(2):637–646, 2006. 34

B.D. Mason, T.J. Henry, W.I. Hartkopf, T. Ten Brummelaar, and D.R. Soderblom. A multiplicity survey of chromospherically active and inactive stars. *The Astronomical Journal*, 116(6):2975–2983, 1998. 51

B.D. Mason, G.L. Wycoff, W.I. Hartkopf, G.G. Douglass, and C.E. Worley. The 2001 US Naval Observatory double-star CD-ROM. I. The Washington double star catalog. *The Astronomical Journal*, 122:3466–3471, 2001. 320, 321

G. Mathys. Global stellar magnetic elds: the crossover from fossils to dynamos. In *IAU XXVI General Assembly, 14-25 August, 2006*, volume 14, pages 285–286. International Astronomical Union, 2007. 14

E.W. Maunder. Note on the distribution of Sun-spots in heliographic latitude, 1874 to 1902. *Monthly Notices of the Royal Astronomical Society*, 64:747–761, 1904. 10

J. Meléndez and I. Ramírez. HIP 56948: A solar twin with a low lithium abundance. *The Astrophysical Journal*, 669:L89–L92, 2007. 13

J. Meléndez, M. Bergemann, J.G. Cohen, M. Endl, A.I. Karakas, I. Ramírez, W.D. Cochran, D. Yong, P.J. MacQueen, C. Kobayashi, and M. Asplund. The remarkable solar twin HIP 56948: A prime target in the quest or other Earths. *Astronomy & Astrophysics*, 543:A29, 2012. 13

M.W. Mengel. The active young solar-type star HR 1817 (= HD 35850). Master's thesis, University of Southern Queensland, 2005. 49, 225

S. Messina and E. F. Guinan. Magnetic activity of six young solar analogues I. Starspot cycles from long-term photometry. *Astronomy & Astrophysics*, 393:225–237, 2002. 17, 232

S. Messina and E. F. Guinan. Magnetic activity of six young solar analogues II. Starspot cycles from long-term photometry. *Astronomy & Astrophysics*, 409:1017–1030, 2003. 17, 48, 49, 164, 172, 232

S. Messina, N. Pizzolato, E.F. Guinan, and M. Rodon. Dependence of coronal x-ray emission on spot-induced brightness variations in cool main sequence stars. *Astronomy & Astrophysics*, 410:671–684, 2003. 318, 319

L. Mestel. The solar-stellar connection - magnetic braking and stellar activity. *Astronomical Society of Australia, Proceedings*, 10(1):3–7, 1992. 15

S.A. Metchev and L.A. Hillenbrand. Initial results from the palomar adaptive optics survey of young solar-type stars: A brown dwarf and three stellar companions. *The Astrophysical Journal*, 617:1330–1346, 2004. 164, 165

G. Micela, S. Sciortino, S. Serio, G.S. Vaiana, J. Bookbinder, L. Golub, F.R. Harnden Jr, and R. Rosner. Einstein x-ray survey of the Pleiades: The dependence of x-ray emission on stellar age. *The Astrophysical Journal*, 292:172–180, 1985. 19

F. Middelkoop. Magnetic structure of cool stars IV. Rotation and Ca II H and K emission of main-sequence stars. *Astronomy & Astrophysics*, 107:31–35, 1982. 133, 135

MKO. Mt kent observatory, 2010. URL `http:\orion.mko.usq.edu.au`. Date Accessed: 01/01/2010. 30

S. Mohanty and G. Basri. Rotation and activity in mid-M to L field dwarfs. *The Astronomical Journal*, 583:451–472, 2003. 20

D. Montes, J. López-Santiago, M.C. Gálvez, M.J. Fernández-Figueroa, E. De Castro, and M. Cornide. Late-type members of young stellar kinematic groups I. Single stars. *Monthly Notices of the Royal Astronomical Society*, 328:45–63, 2001. 17, 22, 48, 69, 88, 120, 123, 141, 143, 144, 173, 203, 211, 212, 213, 226, 230, 318, 319

D. Montes, I. Crespo-Chacón, M.C. Gálvez, M.J. Fernández-Figueroa, J. López-Santiago, E. de Castro, M Cornide, , and J. Hernán-Obispo. Cool stars: Chromospheric activity, rotation, kinematic and age. In A. Ulla and M. Manteiga, editors,

Lecture Notes and Essays in Astrophysics I: Proceedings of the Astrophysics Symposium held during the First Centennial of the Royal Spanish Physical Society, volume 119. Real Sociedad Española de Física, 2004. 73, 77, 103, 131, 283, 284

A. Morgenthaler, P. Petit, S. Saar, S.K. Solanki, J. Morin, S.C. Marsden, M. Auriére, B. Dinstrans, R. Fares, T. Gastine, J. Lanoux, F. Ligniéres, F. Paletou, J.C. Ramírez Vélez, S. Théado, and V. Van Grootel. Long-term magnetic field monitoring of the sun-like star ξ Bootis A. *Astronomy & Astrophysics*, 540:A138, 2012. 131, 132, 197, 225, 226, 322

D. Moss, D.M. Barker, A. Brandenburg, and I. Tuominen. Nonaxisymmetric dynamo solutions and extended starspots on late-type stars. *Astronomy & Astrophysics*, 294: 155–164, 1995. 18, 112, 228

V. E. Moulds, C. A. Watson, X. Bonfils, S. P. Littlefair, and E. K. Simpson. Finding exoplanets orbiting young active stars - I. technique. *Monthly Notices of the Royal Astronomical Society*, 430(3):1709–1721, 2013. 233

Y. Nazé. Hot stars observed by XMM-Newton. *Astronomy & Astrophysics*, 506(2): 1055–1064, 2009. 28

A.J. Norton, P.J. Wheatley, R.G. West, C.A. Haswell, R.A. Street, A. Collier Cameron, D.J. Christian, W.I. Clarkson, B. Enoch, M. Gallaway, C. Hellier, K. Horne, J. Irwin, S.R. Kane, T.A. Lister, J.P. Nicholas, N. Parley, D. Pollacco, R. Ryans, I. Skillen, and D.M. Wilson. New periodic variable stars coincident with ROSAT sources discovered using SuperWASP. *Astronomy & Astrophysics*, 467(2):785–905, 2007. 288

R.W. Noyes, L.W. Hartmann, S.L. Baliunas, D.K. Duncan, and A.H. Vaughan. Rotation, convection, and magnetic activity in lower main-sequence stars. *The Astrophysical Journal*, 279:763–777, 1984. 15, 63, 96, 135, 212, 213, 214, 217, 218

D. O'Neal, S.H. Saar, and J.E. Neff. Measurements of starspot area and temperature on five active, evolved stars. *The Astrophysical Journal*, 463:766–775, 1996. 160, 214

D. O'Neal, J.E. Neff, S.H. Saar, and M. Cuntz. Further results of TiO-band observations of starspots. *The Astronomical Journal*, 128:1802–1811, 2004. 170

D.B. P. Demarque, L.H. Guenther, A. Li, and C.W. Straka Mazumdar. YREC: The Yale rotating stellar evolution code. Non-rotating version, seismology applications. *Astrophysics and Space Science*, pages 31–41, 2008. 214

A. Palacios, M. Gebran, E. Josselin, F. Martins, B. Plez, M. Belmas, M. Sanguillon, and A. Lébre. Pollux: a database of synthetic stellar spectra. *Astronomy & Astrophysics*, 516:A13, 2010. 131, 132, 197

R. Pallavicini, L. Golub, R. Rosner, G.S. Vaiana, T. Ayres, and J.L. Linksy. Relations among stellar x-ray emission observed from *EINSTEIN*, stellar rotation and bolometric luminosity. *The Astrophysical Journal*, 248:279–290, 1981. 19

E.N. Parker. Hydromagnetic dynamo models. *The Astrophysical Journal*, 122:293–314, 1955. 1, 10

J.R. Parks, R.J. White, G.H. Schaefer, J.D. Monnier, and G.W. Henry. The 16th Cambridge Workshop on Cool Stars, Stellar Systems and the Sun. In M. Johns-Krull, M.K. Browning, and A.A. West, editors, *Starspot Imaging with the CHARA Array*, volume 448 of *ASP Conference Series*, pages 1217–1224, The 16th Cambridge Workshop on Cool Stars, Stellar Systems and the Sun, 2011. Astronomical Society of the Pacific. 28

M. J. Penn, W. D. Cao, S. R. Walton, G. A. Chapman, and W. Livingston. Imaging spectropolarimetry of Ti I 2231 nm in a sunspot. *Solar Physics*, 215(1):87–97, 2003. 170

M.A.C. Perryman, L. Lindegren, J. Kovalevsky, E. Høg, U. Bastian, P.L. Bernacca, M. Crézé, F. Donati, M. Grenon, M. Grewing, F. van Leeuwen, H. van der Marel, F. Mignard, C.A. Murray, R.S. Le Poole, H. Schrijver, C. Turon, F. Arenou, M. Froeschlé, and C.S. Petersen. The *HIPPARCOS* catalogue. *Astronomy & Astrophysics*, 323:L49–L52, 1997. 52, 275

P. Petit and J.-F. Donati. Magnetic mapping of solar-type stars. In F. Favata, G.A.J. Hussain, and B. Battrick, editors, *Proceedings of the 13th Cambridge Workshop on Cool Stars, Stellar Systems and the Sun*, volume 560, pages 875–878. ESA, 2005. 300

P. Petit, J.-F. Donati, and A. Collier Cameron. Differential rotation of cool active stars: the case of intermediate rotators. *Monthly Notices of the Royal Astronomical Society*, 334(2):374–382, 2002. 35, 48, 49

P. Petit, J.-F. Donati, and A. Collier Cameron. Differential rotation of cool active stars. *Astronomische Nachrichten*, 325(2):221–224, 2004a. 48, 141

P. Petit, J.-F. Donati, J.M. Oliveira, M. Auriére, S. Bagnulo, J.D. Landstreet, F. Ligniéres, T. Lüftinger, S. Marsden, D. Mouillet, F. Paletou, S. Strasser, Toqué N., and G.A. Wade. Photospheric magnetic field and surface differential rotation of the FK Com star HD 199178. *Monthly Notices of the Royal Astronomical Society*, 351(3):826–844, 2004b. 35, 49, 114

P. Petit, D. Dintrans, S.K. Solanki, J.-F. Donati, M. Auriére, F. Ligniéres, J. Morin, F. Paletou, J.C. Ramírez Vélez, C. Catala, and R. Farés. Toroidal versus poloidal magnetic fields in sun-like stars: a rotation threshold. *Monthly Notices of the Royal Astronomical Society*, 388(1):80–88, 2008. 41, 82, 138, 172, 202, 217, 300, 303, 322

P. Petit, B. Dintrans, A. Morgenthaler, V. Van Grootel, J. Morin, J. Lanoux, M. Auriére, and R. Konstantinova-Antova. A polarity reversal in the large-scale magnetic field of the rapidly rotating sun HD 190711. *Astronomy & Astrophysics*, 508:L9–L12, 2009. 41, 322

P. Petit, F. Ligniéres, G.A. Wade, M. Auriére, T. Böhm, S. Bagnulo, B. Dinstrans, A. Fumel, J. Grunhut, J. Lanouz, A. Morgenthaler, and V. Van Grootel. The rapid rotation and ocmplex magnetic field geometry of vega. *Astronomy & Astrophysics*, 523(id.A41):1–9, 2010. 20

B. Pettersson, E. Stempels, and N. Piskunov. A fiber-linked four stokes-parameter polarimeter for the SOFIN spectrometer on the nordic optical telescope. In S Arribas, E. E. Mediavilla, and F. Watson, editors, *Fiber Optics in Astronomy III*, volume 152 of *ASP Conference Series*, pages 343–346, 390 Ashton Avenue, San Francisco, CA 94112, 1998. Astronomical Society of the Pacific. 28

J.L. Phillips, S.J. Barne, W.C. Feldman, B.E. Goldstein, J.T. Gosling, C.M. Hammond, D.J. McComas, M. Neugebauer, E.E. Scime, and S.T. Suess. Ulysses solar wind plasma observations at high southerly latitudes. *Science*, 268:1030–1033, 1995. 5

R. Pinto, S. Brun, L. Jouve, and R. Grappin. Solar wind, mass and momentum losses during the solar cycle. In *Astrophysical Dynamics: From Stars to Galaxies*, volume 271, pages 359–360. Proceedings IAU Symposium, 2010. 5

R. Pinto, A.S. Brun, L. Jouve, and R. Grappin. Coupling the solar dynamo and the corona: Wind properties, mass and momentum losses during an activity cycle. *The Astrophysical Journal*, 737(2):ID72, 2011. 5

N.E. Piskunov, I. Tuominen, and O. Vilhu. Surface imaging of late-type stars. *Astronomy & Astrophysics*, 230:363–370, 1990. 34

V. Pizzo, R. Schwenn, E. Marsch, H. Rosenbauer, K.-H. Mühlhäuser, and F.M. Neubauer. Determination of the solar wind angular momentum flux from the *HELIOS* data - an observational test of the Weber and Davis theory. *The Astrophysical Journal*, 271:335–354, 1983. 5

N. Pizzolato, A. Maggio, G. Micela, S. Sciortino, and P Ventura. The stellar activity-rotation relationship revisited: Dependence of saturated and non-saturated x-ray emission regimes on stellar mass for late-type dwarfs. *Astronomy & Astrophysics*, 397:147–157, 2003. 20

G. Pojmański, G. Maciejewski, B. Pilecki, and D. Szczygiel. The all sky automated survey. catalog of variable stars. I. 0^h - 6^h Quarter of the southern hemisphere. *Acta Astronomica*, 52:397–427, 2002a. 300

G. Pojmański, G. Maciejewski, B. Pilecki, and D. Szczygiel. The all sky automated survey. catalog of variable stars. II. 6^h - 12^h Quarter of the southern hemisphere. *Acta Astronomica*, 52:397, 2002b. 318, 319

G.F. Porto de Mello and L. da Silva. HR 6060: The closest ever solar twin. *The Astrophysical Journal*, 482(2):L89–L92, 1997. 13

C.F. Prosser, S. Randich, J.R. Stauffer, J.H.M.M. Schmitt, and T. Simon. ROSAT pointed observations of the Alpha Persei cluster. *The Astronomical Journal*, 112(4): 1570–1587, 1996. 19, 282

Wichmann R., J. Bouvier, S. Allain, and Krautter J. Rotational evolution of pre-main sequence stars in Lupus. *Astronomy & Astrophysics*, 330:521–532, 1998. 318, 319

J.C. Ramírez Vélez, M. Semel, M. Stift, M.J. Martínez González, P. Petit, and N. Dunstone. Spectropolarimetric multi line analysis of stellar magnetic fields. *Astronomy & Astrophysics*, 512:A6, 2010. 34

S. Randich. On the dispersion in lithium and potassium among late-type stars in young clusters: IC 2602. *Astronomy & Astrophysics*, 377:512–521, 2001. 318, 319

S. Randich. Supersaturation in x-ray emission of cluster stars. In R. A. Donahue and J.A. Bookbinder, editors, *Cool Stars, Stellar Systems, and the Sun*, pages 501–509. ASP Conference Series 154, 1998. 19, 282

A. Reiners. Rotation- and temperature-dependence of stellar latitudinal differential rotation. *Astronomy & Astrophysics*, 446(1):267–277, 2006. 16, 48, 124, 127

A. Reiners and J.H.M.M. Schmitt. Differential rotation in rapidly rotating F-stars. *Astronomy & Astrophysics*, 412:813–819, 2003. 22, 48

A. Reiners, N. Joshi, and B. Goldman. A catalog of rotation and activity in early-M stars. *The Astronomical Journal*, 143(93):1–15, 2012. 12, 20

A. Reiners, D. Shulyak, G. Anglada-Escudé, S.V. Jeffers, J. Morin, M. Zechmeister, O. Kochukhov, and N. Piskunov. Radial velocity signatures of zeeman broadening. *Astronomy & Astrophysics*, 552(id.A103):1–11, 2013. 233

J.B. Rice. Doppler imaging of stellar surfaces - techniques and issues. *Astronomische Nachrichten*, 323(3/4):220–235, 2002. 34

J.B. Rice and K.G. Strassmeier. Doppler imaging from artificial data. testing the temperature inversion from spectral-line profiles. *Astrophysical Journal Supplement Series*, 147:151–168, 2000. 34

J.B. Rice, W.H. Wehlau, and V.L. Khokhlova. Mapping stellar surfaces by Doppler imaging - technique and application. *Astronomy & Astrophysics*, 208:179–188, 1989. 32, 34

L Rosén and O. Kochukhov. How reliable is Zeeman Doppler imaging without simultaneous temperature reconstruction? *Astronomy & Astrophysics*, 548(id.A8):1–12, 2012. 220

J.M. Rousseau, J.P. Perie, and M.T. Gachard. Stars of the southern hemisphere proposed for the *HIPPARCOS* mission. *Astronomy and Astrophysics Supplement*, 116: 301–308, 1996. 278

K. Rousselet-Perraut, C. Stehlé, T. Lanz, J.B. Le Bouquin, T. Boudoyen, M. Kilbinger, O. Kochukhov, and S. Jankov. Stellar activity and magnetism studied by optical interferometry. *Astronomy & Astrophysics*, 422:193–203, 2004. 28

M.J. Ruck and G. Smith. A fine analysis of calcium and iron lines in the spectrum of the chromospherically active G8 dwarf ξ Bootis A. *Astronomy & Astrophysics*, 304: 449–460, 1995. 131, 318, 319

G. Rüdiger, D. Elstner, and M. Ossendrijver. Do spherical α^2-dynamos oscillate? *Astronomy & Astrophysics*, 406:15–21, 2003. 20

C.T. Russell. Magnetic stress in solar system plasmas. *Australian Journal of Physics*, 52:733–751, 1999. 10

R.G.M. Rutten. Magnetic structure in cool stars. VII - absolute surface flux in Ca II H and K line cores. *Astronomy & Astrophysics*, 130:353–360, 1984. 135, 198

N.N. Samus, Durlevich O.V., and et al. Gcvs database, version 2012Apr, 2009. URL `http://www.sai.msu.su/gcvs/gcvs/`. Date Accessed: 01/01/2012. 120

SAO. SAO star catalog J2000, 1966. Date accessed December, 27, 2010. 278, 294

M.J. Sartori, J.R.D. Lépine, and W.S. Dias. Formation scenarios for the young stellar associations between galactic longitudes l = 280^o - 360^o. *Astronomy & Astrophysics*, 404:913–926, 2003. 278, 296, 303, 304

M. Saxner and Hammarbäck. An empirical temperature calibration for F dwarfs. *Astronomy & Astrophysics*, 151:372–390, 1985. 13

L. Scelsi, A. Maggio, G. Peres, and R. Pallavicini. Coronal properties of G-type stars in different evolutionary phases. *Astronomy & Astrophysics*, 432:671–685, 2005. 163, 164

M.P. Scheible and E.F. Guinan. The spotted young sun - HD 129333 (= EK Dra). *IBVS*, 4110:1–3, 1994. 170

A. Scholz. Stellar spindown: From the ONC to the Sun. In *Proceedings of the 13th Cambridge Workshop on Cool Stars, Stellar Systems and the Sun*, volume 1094, pages 61–70. AIP Conference Proceedings, 2009. 15

J. Schou, H.M. Antia, S. Basu, R.S. Bogart, R.I. Bush, S.M. Chitre, J. Christensen-Dalsgaard, M.P. di Mauro, W.A. Dziembowski, A. Eff-Darwich, D.O. Gough, D.A. Haber, J.T. Hoeksema, R. Howe, S.G. Korzennik, A.G. Kosovichev, R.M. Larsen, F.P. Pijpers, P.H. Scherrer, T. Sekii, T.D. Tarbell, A.M. Title, M.J. Thompson, and J. Toomre. Helioseismic studies of differential rotation in the solar envelope by the solar oscillations investigation using the Michelson Doppler imager. *The Astrophysical Journal*, 505:390–417, 1998. 7

C.J. Schrijver and A.M. Title. On the formation of polar spots in sun-like stars. *The Astrophysical Journal*, 551(2):1099–1106, 2001. 4, 19, 81, 210

C.J. Schrijver and C. Zwaan. *Solar and stellar magnetic activity*. Cambridge: Cambridge University Press, 2000. 5, 9, 14

C. Schröder, A. Reiners, and J.H.M.M. Schmitt. Ca II HK emission in rapidly rotating stars: Evidence for an onset of the solar-type dynamo. *Astronomy & Astrophysics*, 493:1099–1107, 2009. 198

M. Schüssler and S.K. Solanki. Why rapid rotators have polar spots. *Astronomy & Astrophysics*, 264:L13–L16, 1992. 19

M. Schüssler, P. Caligari, A. Ferriz-Mas, S.K. Solanki, and M. Stix. Distribution of starspots on cool stars. I. Young and main sequence stars of 1 $M_{\odot}$. *Astronomy & Astrophysics*, 314:503–512, 1996. 19, 81, 210

J. Semel, D.E. Rees, J.C. Ramírez Vélez, M.J. Stift, and F. Leone. Multi-line spectropolarimetry of stellar magnetic fields using principal component analysis. In *Solar Polarization 4*, volume 358, pages 355–361. Astronomical Society of the Pacific Conference Series, 2006. 34

M. Semel. Zeeman-Doppler imaging of active stars. I - Basic principles. *Astronomy & Astrophysics*, 225(2):456–466, 1989. 22, 27, 36, 45, 58, 145, 276

M. Semel, J.-F. Donati, and D.E. Rees. Zeeman-Doppler imaging of active stars. 3: Instrumental and technical considerations. *Astronomy & Astrophysics*, 278(1):231–237, 1993. 45, 46, 58, 145, 276, 279

L. Siess, Dufour E., and M. Forestini. An internet server for pre-main sequence tracks of low- and intermediate-mass stars. *Astronomy & Astrophysics*, 358:593–599, 2000. xxii, xxv, 52, 53, 63, 88, 92, 120, 123, 160, 161, 212, 213, 214, 216, 225, 226, 288, 291, 292, 296, 300, 304

J. Silvester, G. A. Wade, O. Kochukhov, S. Bagnulo, C. P. Folsom, and D. Hanes. Stokes *IQUV* magnetic Doppler imaging of Ap stars I. ESPaDOnS and NARVAL observations. *Monthly Notices of the Royal Astronomical Society*, 2012. 121

M. B. Skelly, J.-F. Donati, J. Bouvier, K. N. Grankin, Y. C. Unruh, S. A. Artemenko, and P. Petrov. Dynamo processes in the T Tauri star V410 Tau. *Monthly Notices of the Royal Astronomical Society*, 403:159–169, 2010. 220

M.B. Skelly, Y.C. Unruh, A. Collier Cameron, J.R. Barnes, J.-F. Donati, W.R. Lawson, and B.D. Carter. Doppler images and chromospheric variability of TWA 6. *Monthly Notices of the Royal Astronomical Society*, 385(2):708–718, 2008. 108

M.B. Skelly, Y.C. Unruh, J.R. Barnes, J.-F. Donati, W.R. Lawson, and A. Collier Cameron. Doppler images and chromospheric variability of TWA 17. *Monthly Notices of the Royal Astronomical Society*, 399(4):1829–1838, 2009. 108

J. Skilling and R.K. Bryan. Maximum entropy image reconstruction - general algorithm. *Monthly Notices of the Royal Astronomical Society*, 211(1):111–124, 1984. 34, 35

M.F. Skrutskie, R.M. Cutri, R. Stiening, M.D. Weinberg, S. Schneider, J.M. Carpenter, C. Beichman, R. Capps, T. Chester, J. Elias, J. Huchra, J. Liebert, C. Lonsdale, D.G. Monet, S. Price, P. Seitzer, T. Jarrett, J.D. Kirkpatrick, J. Gizis, E. Howard, T. Evans, J. Fowler, L. Fullmer, R. Hurt, R. Light, E.L. Kopan, K.A. Marsh, H.L. McCallon, R. Tam, S. Van Dyk, and S. Wheelock. The two micron all sky survey (2MASS). *The Astronomical Journal*, 131(2):1163–1183, 2006. 87

A. Skumanich. Time scales for Ca II emission decay, rotational braking, and lithium depletion. *The Astrophysical Journal*, 171:565–567, 1972. 15

O.B. Slee, E. Budding, B.D. Carter, M.W. Mengel, I. Waite, and J.-F. Donati. A multiwavelength study of CC Eridani. *Publications of the Astronomical Society of Australia*, 21(1):72–81, 2004. 45

F. Snik, O. Kochukhov, N. Piskunov, M. Rodenhuis, S Jeers, C. Keller, A. Dolgopolov, E. Stempels, V. Makaganiuk, J. Valenti, and C. Johns-Krull. The HARPS polarimeter. In *Solar Polarization Workshop 6*, volume 437, pages 237–244. ASP Conference Series: Astronomical Society of the Pacific, 2011. 28

D.R. Soderblom. A survey of chromospheric emission and rotation among solar-type stars in the solar neighborhood. *The Astronomical Journal*, 90(10):2013–2115, 1985. 13

D.R. Soderblom and J.R. King. Solar-type stars: Basic information of their classification and characterization, 2013. URL http:\orion.mko.usq.edu.au. Date Accessed: 11/01/2013. 13

D.R. Soderblom, C.A. Pilachowski, S.B. Fedele, and B.F. Jones. The evolution of the lithium abundances of solar-type stars. II - The Ursa Major group. *The Astronomical Journal*, 105(6):2299–2307, 1993a. 120, 284

D.R. Soderblom, J.R. Stauffer, J.R. Hudon, and B.F. Jones. Rotation and chromospheric emission among F, G, and K dwarfs of the pleiades. *Astrophysical Journal Supplement Series*, 85:315–346, 1993b. 29, 77, 120, 284

D.R. Soderblom, J.R. King, and T.J Henry. High-resolution spectroscopy of some very active southern stars. *The Astronomical Journal*, 116(1):396–413, 1998. 51

S.K. Solanki. The magnetic structure of sunspots and starspots. *Astronomische Nachrichten*, 323:165–177, 2002. 82

J. R. Stauffer, L. W. Hartmann, C. F. Prosser, S. Randich, S. Balachandran, B. M. Patten, T. Simon, and M. Giampapa. Rotational velocities and chromospheric/coronal activity of low-mass stars in the young open clusters IC 2391 and IC 2602. *The Astrophysical Journal*, 479:776–791, 1997. 19, 282

D Stello, S. Basu, H. Bruntt, B. Mosser, I.R. Stevens, T.M. Brown, J. Christensen-Dalsgaard, R.L.. Gilliland, H. Kjeldsen, T. Arentoft, J. Ballot, C. Barban, T.R. Bedding, W.J. Chaplin, Y.P. Elsworth, R.A. García, M. Goupil, S. Hekker, D. Huber, S. Mathur, S. Meibom, V. Sangaralingam, C.S. Baldner, K. Belkacem, K. Biazzo, K. Brogaard, J.C. Suárez, F. D'Antona, P. Demarque, L. Esch, N. Gai, F. Grundahl, Y. Lebreton, B. Jiang, N. Jevtic, C. Karoff, A. Miglio, J. Molenda-Żakowicz, J. Montalbán, A. Noels, T. Roca Cortés, I.W. Roxburgh, A.M. Serenelli, V. Silva Aguirre, C. Sterken, P. Stine, R. Szabó, A. Weiss, W.J. Borucki, D. Koch, and J.M. Jenkins. Detection of solar-like oscillations from Kepler photometry of the open cluster NGC 6819. *The Astrophysical Journal*, 713:L182L186,, 2010. 27

B. Stelzer, A. Marino, G. Micela, J. Lopez-Santiago, and C. Liefke. The UV and X-ray activity of the M dwarfs within 10 pc of the sun. *Monthly Notices of the Royal Astronomical Society*, 431(3):2063–2079, 2013. 20

P.B. Stetson. On the growth-curve method for calibrating stellar photometry with CCDs. *Astronomical Society of the Pacific*, 102:932–948, 1990. 31, 54, 57

K.G. Strassmeier. Starspots. *Astronomy & Astrophysics Review*, 17:251–308, 2009. 318, 319

K.G. Strassmeier and J.B. Rice. Doppler imaging of stellar surface structure VI. HD 129333 = EK Draconis: A stellar analog of the active young Sun. *Astronomy & Astrophysics*, 330:658–695, 1998. 31, 165, 166, 170, 172, 201, 318, 319

G. Takeda, E.B. Ford, A. Sills, F.A. Rasio, D.A. Fischer, and J.A. Valenti. Structure and evolution of nearby stars with planets. II. Physical properties of ∼1000 cool stars from the *SPOCS* catalog. *Astrophysical Journal Supplement Series*, 168:297–318, 2007. 214, 216

Y. Takeda and S. Kawanomoto. Lithium abundances of F-, G-, and K-type stars: Profile-fitting analysis of the Li I 6708 doublet. *Publications of the Astronomical Society of Japan*, 57:45–63, 2005. 120

N. Tetzlaff, R. Neuhäuser, and M.M. Hohle. A catalogue of young runaway *HIPPARCOS* stars within 3 kpc from the Sun. *Monthly Notices of the Royal Astronomical Society*, 410(1):190–200, 2011. 288, 300

J.D. Thatcher and R.D. Robinson. The chromospheres of late-type stars. II - An atlas of chromospheric lines for selected early-K stars. *Monthly Notices of the Royal Astronomical Society*, 262(1):1–19, 1993. 73, 77, 131

M.J. Thompson, J. Christensen-Dalsgaard, M. S. Miesch, and J. Toomre. The internal rotation of the Sun. *Annual Review of Astronomy & Astrophysics*, 41:599–643, 2003. 7

C.A.O. Torres, G.R. Quast, L. da Silva, R. de la Reza, C.H.F. Melo, and M. Sterzik. Search for associations containing young stars (SACY). I. Sample and searching method. *Astronomy & Astrophysics*, 460(3):695–708, 2006. 22, 45, 52, 63, 77, 82, 87, 92, 96, 141, 143, 144, 148, 171, 212, 213, 275, 278, 284, 287, 288, 291, 292, 295, 300, 302, 306, 318, 319

C. Turon, D. Egret, A. Gomez, M. Grenon, H. Jahreiss, Y. Requieme, A.N. Argue, A. Bec-Borsenberger, J. Dommanget, M.O. Mennessier, F. Arenou, M. Chareton, F. Crifo, J.C. Mermilliod, D. Morin, B. Nicolet, O. Nys, L. Prevot, M. Rousseau, and M.A.C Perryman. Version 2 of the *HIPPARCOS* input catalogue. *Bull. Inf. Cent. Donnees Astron. Strasbourg*, 43:5–6, 1993. 278, 298

Y.C. Unruh and A. Collier Cameron. The sensitivity of Doppler imaging to line profile models. *Monthly Notices of the Royal Astronomical Society*, 273(1):1–16, 1995. 35

Y.C. Unruh and A. Collier Cameron. Does chromospheric emission mimic polar starspots in Doppler images? *Monthly Notices of the Royal Astronomical Society*, 290(3):L37–L42, 1997. 79

J.A. Valenti and D.A. Fischer. Spectroscopic properties of cools stars (SPOCS). I. 1040 F, G, and K dwarfs from Keck, Lick, and AAT planet search programs. *Astrophysical Journal Supplement Series*, 159:141–166, 2005. 22

F. van Leeuwen. Validation of the new *HIPPARCOS* reduction. *Astronomy & Astrophysics*, 474(2):653–664, 2007. 28, 51, 52, 87, 119, 120, 143, 144, 165, 287, 288, 291, 292, 294, 295, 296, 298, 302, 304, 318, 319

A.A. Vidotto, M. Jardine, J. Morin, J.-F. Donati, P. Lang, and A.J.B. Russell. Effects of M dwarf magnetic fields on potentially habitable planets. *Astronomy & Astrophysics*, arXiv:1306.4789v2, 2013. 209, 233

O. Vilhu. The nature of magnetic activity in lower main sequence stars. *Astronomy & Astrophysics*, 133(1):117–126, 1984. 15, 19, 282

W. Voges, B. Aschenbach, Th. Boller, H. Bräuninger, U. Briel, W. Burkert, K. Dennerl, J. Englhauser, R. Gruber, F. Haberl, G. Hartner, G. Hasinger, M. Kürster, E. Pfeffermann, W. W. Pietsch, P. Predehl, C. Rosso, J.H.M.M. Schmitt, J. Trümper, and H.U. Zimmermann. The ROSAT all-sky survey bright source catalogue. *Astronomy & Astrophysics*, 349:389–405, 1986. 87

S.S. Vogt and G.D. Penrod. Doppler imaging of spotted stars application to the RS Canum Venaticorum stars HR 1099. *Astronomical Society of the Pacific*, 95: 565–576, 1983. 31, 32, 33, 34

S.S. Vogt, A.P. Hatzes, and A.A. Misch. Doppler imagery of the spotted RS Canum Venaticorum star HR 1099 (V711 Tauri from 1981 to 1992. *Astrophysical Journal Supplement Series*, 121:547–589, 1999. 49

G.A. Wade, J.-F. Donati, J.D. Landstreet, and S.L.S. Shorlin. Spectropolarimetric measurements of magnetic Ap and Bp stars in all four Stokes parameters. *Monthly Notices of the Royal Astronomical Society*, 313(4):823–850, 2000. 38

I.A. Waite, S.C. Marsden, B.D. Carter, and M. Mengel. High-resolution spectroscopy of some active southern stars. *Publications of the Astronomical Society of Australia*, 22(1):29–35, 2005. 22, 51, 77, 275, 281, 284, 304

I.A. Waite, S.C. Marsden, B.D. Carter, E. Alécian, C. Brown, D. Burton, and R. Hart. High-resolution spectroscopy and spectropolarimetry of some late F- / early G-type sun-like stars as targets for Zeeman Doppler imaging. *Publications of the Astronomical Society of Australia*, 28(4):323–337, 2011a. 22, 87, 88, 93, 119, 144, 153

I.A. Waite, S.C. Marsden, B.D. Carter, R. Hart, J.-F. Donati, J.C. Ramírez Vélez, M. Semel, and N. Dunstone. Magnetic fields and differential rotation on the pre-main sequence - III. The early-G star HD 106506. *Monthly Notices of the Royal Astronomical Society*, 413(3):1949–1960, 2011b. 44, 45, 92, 275, 309

E.J. Weber and L. Davis Jr. The angular momentum of the solar wind. *The Astrophysical Journal*, 148:217–227, 1967. 15

M. Weber, K.G. Strassmeier, and A. Washuettl. Indications for anti-solar differential rotation of giant stars. *Astronomische Nachrichten*, 326(3):287–291, 2005. 81, 210

G. Weigelt, V. P. Grinin, J. H. Groh, K.-H. Hofmann, S. Kraus, A. S. Miroshnichenko, D. Schertl, L. V. Tambovtseva, M. Benisty, T. Driebe, S. Lagarde, F. Malbet, A. Meilland, R. Petrov, and E. Tatulli. VLTI/AMBER spectro-interferometry of the Herbig Be star MWC 297 with spectral resolution 12 000. *Astronomy & Astrophysics*, 527: A103, 2011. 28

A.A. West, S.L. Hawley, L.M. Walkowicz, K.R. Covey, N.M. Silvestri, S.N. Raymond, H.C. Harris, J.A. Munn, P.M. McGehee, Ž. Ivezić, and J. Brinkmann. Spectroscopic properties of cool stars in the Sloan digital sky survey: An analysis of magnetic activity and a search for subdwarfs. *The Astronomical Journal*, 128(1):426–436, 2004. 12, 15

R. Wichmann, J. Krautter, E. Covino, J. M. Alcala, R. Neuhaeuser, and J.H.M.M. Schmitt. The T Tauri star population in the Lupus star forming region. *Astronomy & Astrophysics*, 320:185–195, 1997. 318, 319

P.R. Wilson, D. Burtonclay, and Y Li. The rotational structure of the region below the solar convection zone. *The Astrophysical Journal*, 489:395–402, 1997. 5

M. Wittkowski, M. Schöller, S. Hubrig, B. Posselt, and O. von der Lühe. Measuring starspots on magnetically active stars with the VLTI. *Astronomische Nachrichten*, 323:241–250, 2002. 28

B.E. Wood, H.-R. Müller, G.P. Zank, and J.L. Linsky. Measured mass-loss rates of solar-like stars as a function of age and acitivity. *The Astrophysical Journal*, 574: 412–425, 2002. 16

C.O. Wright, M.P. Egan, K.E. Kraemer, and S.D. Price. The Tycho-2 spectral type catalog. *The Astronomical Journal*, 125(1):359–363, 2003. 298

J.T. Wright, G.W. Marcy, R.P. Butler, and S.S. Vogt. Chromospheric Ca II emmission in nearby F, G, K and M stars. *Astrophysical Journal Supplement Series*, 152:261–295, 2004. 131, 132, 197, 198

N.J. Wright, J.J. Drake, E.E. Mamajek, and G.W. Henry. The stellar-activity-rotation relationship and the evolution of stellar dynamos. *The Astrophysical Journal*, 743 (1):ID48, 2011. 19, 22, 136, 160, 165, 171, 212, 213, 214, 216

N.J. Wright, J.J. Drake, E.E. Mamajek, and G.W. Henry. The stellar-activity-rotation relationship. *Astronomische Nachrichten*, 334(1):1–4, 2013. 19

A. Young, A. Skumanich, J.R. Stauffer, B.W. Bopp, and E. Harlan. A study of excess H-alpha emission in chromospherically active M dwarf. *The Astrophysical Journal*, 344:427–436, 1989. 77, 284

D.M. Zarro and A.W. Rodgers. Stellar chromospheres - Hα and Ca II K profiles. *Astrophysical Journal Supplement Series*, 53:815–868, 1983. 77, 284

B. Zuckerman and I. Song. Young stars near the Sun. *Annual Review of Astronomy & Astrophysics*, 42(1):685–721, 2004. 22, 144, 148, 212, 213, 287, 300

C. Zwaan. Elements and patterns in the solar magnetic field. *Annual Review of Astronomy & Astrophysics*, 25:83–111, 1987. 9

Appendix A

HD 106506 DI weightings

A.1 Spectroscopy and Photometry Weighting for HD 106506

The incorporation of the photometry is simply an extension of the DI process with the photometry data being fitted simultaneously with the spectroscopy data. The emphasis placed on the photometric data is determined by the weighting assigned to it. For the HD 106506 images in Figure 3.4(right panel), a weighting of 1 was assigned to the photometric data. A weighting of 1.0 on both data sets means that the relative weighting for each spectroscopic and photometric data point is equal to $1/\sigma_i^2$, where σ_i is the error bar associated with point i (Marsden et al., 2005). A weighting of 0.0 means that the photometric data is ignored in the analysis (Figure 3.4: left panel). Changing the weighting of the photometric data had a very minor impact on the resulting maps with lower latitude features still being enhanced. This is shown in Figure A.1 and Table A.1 shows the spot coverage for each of the maps.

Table A.1: Spot coverage for various spectroscopy and photometry weightings for HD 106506.

Weighting	1.00	0.75	0.50	0.20	0.10	0.00
Spot Coverage (%)	12.7	12.8	12.6	12.3	11.7	6.4

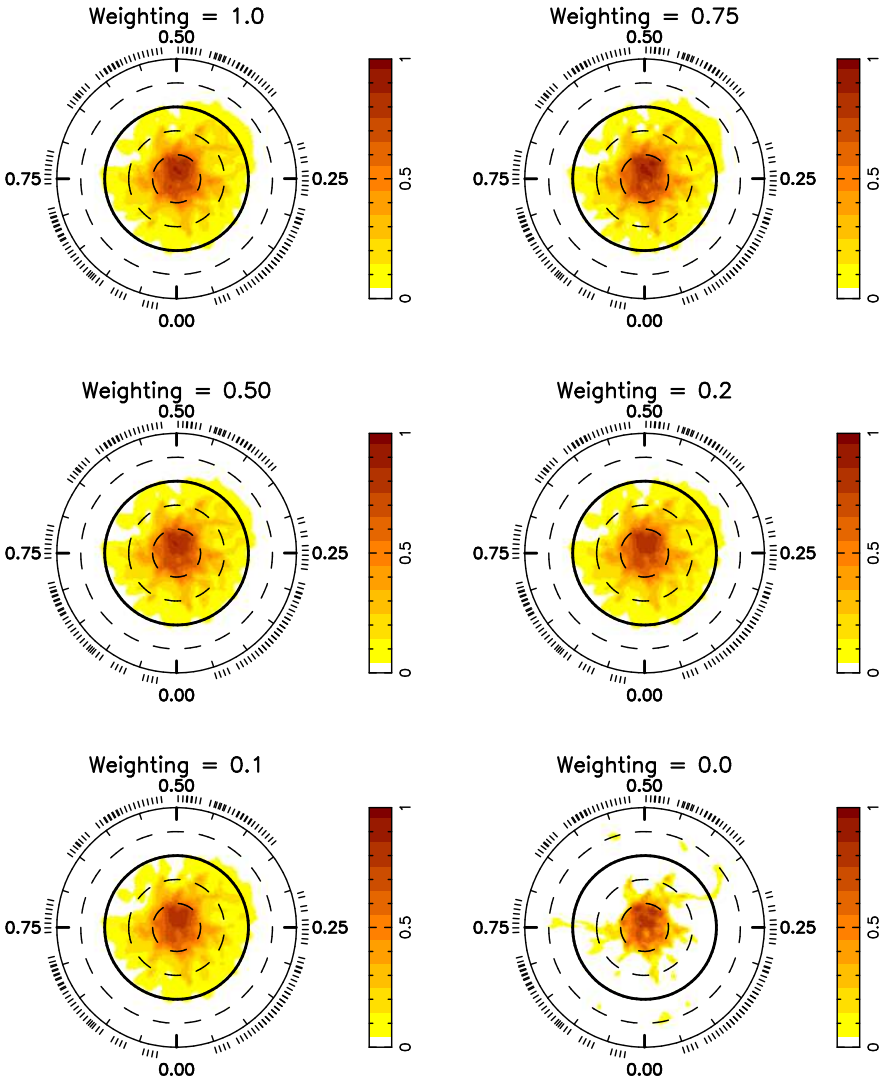

Figure A.1: HD 106506: Analysis of various spectroscopy and photometry weighting schema used in Doppler imaging

Appendix B

The search for more targets[1]

B.1 Introduction

The initial search for potential ZDI targets by Waite et al. (2005) found two pre-main-sequence stars: HD 106506 (SpType: G1V[2]) and HD 141943 (SpType: G2[2]). ZDI has been used to map the magnetic topologies of HD 106506 (Waite et al., 2011b) while Marsden et al. (2011a,b) have investigated the evolution of the magnetic topologies and variations in the surface differential rotation of HD 141943. This appendix is a follow-on from this initial search for late F-/ early G-type stars. Our search specifically aims to measure the projected rotational velocity, $v \sin i$, radial velocity, the level of magnetic and chromospheric activity, and confirm the expected youthful evolutionary status of these stars for studying the origins of the magnetic dynamo in young sun-like stars.

B.2 Observations at the Anglo-Australian Telescope

B.2.1 Selection criteria

The *HIPPARCOS* space mission (Perryman et al., 1997) has provided a wealth of stellar astrometry, and revealed many previously unknown variable stars. A large number of these unresolved variables (Koen and Eyer, 2002) are likely to be eclipsing binaries, but some are expected to be active stars with starspot modulation. From the

[1] This appendix is based on the published work: Waite, I. A., Marsden, S. C., Carter, B. D., Alécian, E., Brown, C., Burton, D., & Hart, R., 2011, *High-resolution Spectroscopy and Spectropolarimetry of Some Late F- / Early G-type Sun-like Stars as Targets for Zeeman Doppler Imaging*, PASA, 28, 323.

[2] Torres et al. (2006)

HIPPARCOS database, late F-/early G-type unresolved variable stars were extracted from the original list of Koen and Eyer (2002). To reduce the sample to a manageable number of stars, only those sun-like stars with a variability between ~ 0.04 and ~ 0.1 magnitude were selected. If the variability was less than 0.04, the spot activity (if the variability was due to starspots) on the star would unlikely be sufficient to deform the stellar profiles sufficiently for any spatial information to be recovered using the technique of Doppler imaging (DI). Any variation above ~ 0.1 would most likely be a result of a companion star eclipsing the target star. A final list of 38 stars was compiled for follow-up high-resolution spectroscopy and spectropolarimetry at the Anglo-Australian Telescope (AAT).

B.2.2 Spectroscopy

High-resolution spectra of 38 late F-/early G- type stars were observed over two nights of service observations on 14 April and 7 September, 2008 using the using the University College of London Échelle Spectrograph (UCLES) at the AAT. The EEV2 chip was used with the central wavelength set to 526.8 nm. The 31 lines per mm grating was used with a slit width of 0.73 mm and slit length of 3.18 mm for observations on the 14 April while the slit width was set to 0.74mm and slit length of 3.17mm was set for observations on 7 September, 2008. This gave an approximate resolution of 50500, extending from order #84 to order #129. The exposure time was varied to match the apparent visual magnitude of the star in order to achieve a S/N $\sim$50 in the middle orders of the Échelle spectrum. A journal of the observations is shown in Tables B.1, B.2 and B.3.

B.2.3 Spectropolarimetry

Follow-up spectropolarimetric observations of stars that exhibited rapid rotation were undertaken on a number of Director's nights (3 December, 2009; 25 March, 2010 and 14 to 17 January, 2011) to coincide with current spectropolarimetric observation runs at the AAT using the Semel Polarimeter (SEMPOL) (Semel, 1989; Semel et al., 1993; Donati et al., 2003b). Again the EEV2 chip was used, with a central wavelength of 526.8 nm and coverage from 437.6497 nm to 681.8754 nm. The dispersion of $\sim$ 0.002481 nm at order # 129, with an average resolution across the chip of approximately $\sim$ 70 000. Observations in circular polarisation (Stokes V) consists of a sequence

Table B.1: Journal of spectroscopic observations using UCLES at the AAT for the high resolution survey for more DI and ZDI targets.

HIP	Spectral Type	v_{mag}[a]	UTSTART	Exp Time (sec)	S/N[b]	v_{rad}[c] km s^{-1}	$v \sin i$[c] km s^{-1}	EEW[d] Hα (mÅ)	EqW[e] Li (mÅ)
UTDATE 2008, APR 14									
23316	G5V[1]	9.6603	10:13:49	600	77	22.8	~ 6	330 ± 6	198 ± 7
27518	G3[2]	9.3025	10:26:08	400	72	5.2	<5	-46 ± 19	<5
31021[f]	G3V[3]	9.0685	10:48:24	400	73	–	–	–	–
33111[g]	G5V[1]	8.9906	10:57:02	400	79	–	–	–	–
33699	F8V[4]	9.2374	11:05:36	400	59	29.8	<5	56 ± 10	41 ± 3
41688	G6IV/V[6]	7.1886	11:15:18	60	46	-20.4	<5	62 ± 10	66 ± 10
43720	G1V[1]	9.2461	11:18:17	400	62	2.2	38	400 ± 28	<5
46949	G2/3V[5]	9.8130	11:26:48	600	64	26.8	<5	23 ± 11	68 ± 3
48146	G6IV/V[6]	9.6767	11:39:30	600	49	0.5	<5	43 ± 9	68 ± 1
48770	G7V[1]	10.6195	11:52:21	1200	67	19.6	35	990 ± 90	234 ± 5
60894	G0/1V[7]	9.6282	12:14:57	600	29	29.4	<5	-36 ± 30	<5
62517	G0[8]	8.9576	12:27:56	400	68	-25.5	52	265 ± 25	47 ± 24
63734	F7/8V[9]	7.8606	12:36:18	200	97	1.3	~ 6	121 ± 11	141 ± 6
63936	F8[8]	9.4552	12:42:02	600	70	-10.0	<5	80 ± 8	<5
64732[f]	F5V[6]	7.7987	12:54:22	150	84	–	–	–	–
66387	G0[8]	9.8353	12:59:05	600	55	-24.1	<5	48 ± 6	<5
67651[h]	F8[10]	9.3947	13:10:25	400	57	–	–	–	–
68328	G0[11]	9.9047	13:20:13	600	76	8.8	∼6	850 ± 45	263 ± 4
69338	G1V[6]	8.9180	13:32:39	300	81	-8.6	<5	9 ± 2	61 ± 3
70053	G0[8]	9.7811	13:39:00	450	68	7.8	<5	17 ± 7	45 ± 4
71933	F8V[1]	8.6086	13:57:17	150	84	6.0	75	274 ± 25	139 ± 7
			15:20:59	150	82	-1.9	75	″	″
71966	F7V[3]	9.8070	14:01:16	450	75	9.3	<5	90 ± 10	30 ± 3
73780[f]	G0IV/V[7]	9.4234	14:10:35	300	77	–	–	–	–
75636[h]	G9V[1]	10.4691	14:17:19	900	88	43.7	50	820 ± 90	<5
77144	G1V[11]	9.5859	14:33:28	450	93	-1.6	65	466 ± 24	207 ± 7
79090	F8[8]	10.1297	14:43:39	600	60	6.1	<5	56 ± 12	46 ± 4
79688	G1V[5]	8.9993	14:56:07	200	86	12.6	11	172 ± 12	13 ± 5
89829	G5V[1]	8.8579	15:01:17	200	74	-10.6	114	280 ± 52	211 ± 13
			15:25:42	200	75	1.2	114	″	″
90899	G1V[12]	9.5388	15:06:00	450	82	-2.7	19	408 ± 14	176 ± 6
93378	G5V[1]	8.6379	15:16:07	150	76	–	225	0	322 ± 56
			15:30:48	150	68	–	229	″	″
			16:11:01	200	62	–	226	″	″
105388	G7V[1]	8.7826	16:04:01	300	58	-1.8	17	520 ± 50	216 ± 5

continued next page....

Table B.2: Journal of spectroscopic observations using UCLES at the AAT for the high resolution survey for more DI and ZDI targets continued from the previous page.

HIP	Spectral Type	v_{mag}[a]	UTSTART	Exp Time (sec)	S/N[b]	v_{rad}[c] km s^{-1}	$v \sin i$[c] km s^{-1}	EEW[d] Hα (mÅ)	EqW[e] Li (mÅ)
UTDATE 2008, SEPT 7									
5617	G2/3[7]	8.9818	13:49:05	400	70	56.5	<5	–	<5
10699	G7IV[1]	9.4109	13:58:52	600	82	39.1	7	220 ± 20	32 ± 3
11241	F8V[9]	8.9017	14:13:43	400	83	-3.5	<5	164 ± 8	98 ± 3
19072[g]	F8[8]	8.3647	18:19:56	240	79	–	–	–	–
			18:56:21	240	71	–	–	–	–
20994	G0[8]	9.8424	18:25:13	900	74	57.8	<5	85 ± 31	44 ± 2
21632[i]	G3V[1]	8.6006	14:23:12	400	81	19.5	18	385 ± 21	190 ±2
			19:04:37	400	97	19.3	18	517 ± 32	″
25848	G0[13]	9.3029	18:42:35	600	68	27.3	69	668 ± 60	250 ± 13
			19:13:43	600	65	28.7	69	″	″

Notes for Tables B.1 and B.2:

[a]v_{mag} is the median visual magnitude taken from the *HIPPARCOS* database at www.rssd.esa.int [b]S/N: Mean Signal-to-noise at Order 107, which was the centre of the spectrum. [c]The radial velocity (v_{rad}) and projected rotational velocity ($v \sin i$). The errors are estimated to be ±1 km s^{-1}, although for rapidly rotating stars with substantial deformation of the line profiles due to spot features, the errors could increase to ±3 km s^{-1} or higher. [d]EEW Hα: Emission equivalent width of the Hα line, see Section 3.3. [e]EqW Li: Equivalent width for the Li-670.78 nm spectral line. [f]Binary system. [g]Possible triple system. [h]Possible binary system. [i] This star has shown variation in the Hα profile hence both measurements for the emission equivalent width have been given.

[1]Torres et al. (2006), [2]Jackson and Stoy (1954), [3]Houk and Cowley (1975), [4]Rousseau et al. (1996), [5]Houk (1982), [6]Houk and Swift (1999), [7]Houk (1978), [8]SAO (1966), [9]Houk and Smith-Moore (1988), [10]Dieckvoss and Heckmann (1975), [11]Sartori et al. (2003), [12]Turon et al. (1993), [13]Li and Hu (1998)

Table B.3: Journal of spectroscopic observations using UCLES at the AAT for the high resolution survey for more DI and ZDI targets cont.

HIP	Spectral Type	v_{mag}[a]	UTSTART	Exp Time (sec)	S/N[b]	v_{rad}[c] km s^{-1}	$v\sin i$[c] km s^{-1}	EEW[d] Hα (mÅ)	EqW[e] Li (mÅ)
UTDATE 2008, SEPT 7									
5617	G2/3[7]	8.9818	13:49:05	400	70	56.5	<5	–	<5
10699	G7IV[1]	9.4109	13:58:52	600	82	39.1	7	220 ± 20	32 ± 3
11241	F8V[9]	8.9017	14:13:43	400	83	-3.5	<5	164 ± 8	98 ± 3
19072[g]	F8[8]	8.3647	18:19:56	240	79	–	–	–	–
			18:56:21	240	71	–	–	–	–
20994	G0[8]	9.8424	18:25:13	900	74	57.8	<5	85 ± 31	44 ± 2
21632[i]	G3V[1]	8.6006	14:23:12	400	81	19.5	18	385 ± 21	190 ±2
			19:04:37	400	97	19.3	18	517 ± 32	″
25848	G0[13]	9.3029	18:42:35	600	68	27.3	69	668 ± 60	250 ± 13
			19:13:43	600	65	28.7	69	″	″

of four exposures. After each of the exposures, the half-wave Fresnel Rhomb of the SEMPOL polarimeter was rotated between $+45^o$ and -45^o so as to remove instrumental polarisation signals from the telescope and the polarimeter. Section B.3.5 gives more details regarding spectropolarimetric observations while more details on the operation of SEMPOL is given in Semel et al. (1993), Donati et al. (1997) and Donati et al. (2003b). A journal of the observations is shown in Table B.4.

B.2.4 Data Analysis

The aim of this project is to determine the projected rotation velocity ($v\sin i$), radial velocity, level of magnetic and chromospheric activity and estimate the age of each of the targets. The chromospheric activity indicators included the Hα, magnesium triplet and sodium doublet spectral lines. The Li I 670.78 nm spectral line was used as an age indicator. The initial data reduction was completed using the ESpRIT software package (Donati et al., 1997). The technique of Least Squares Deconvolution (LSD) (Donati et al., 1997) was applied to each spectra. LSD assumes that each spectral line in the spectrum from a star can be approximated by the same line shape. LSD combines several thousand weak absorption lines to create a high signal-to-noise (S/N) single-line profile. Whereas the average S/N of a typical profile was $\sim$ 50-100, the resulting LSD profile has a combined S/N of the order of 1000 or higher. This substantial

Table B.4: Journal of Spectropolarimetric observations using SEMPOL at the AAT

HIP number	UTDATE	UT Time[a]	Exposure Time (seconds) [b]	Mean S/N[c] (Stokes V)	Magnetic Detection?	FAP[d]
21632	2008 Dec10	12:39:15	4 x 900	5898	No Detection	2.245×10^{-01}
21632	2008 Dec13	14:27:53	2 x 900 [e]	2710	Definite	4.761×10^{-06}
43720	2008 Dec09	16: 4:50	4 x 900	5304	Definite	0.000
43720	2008 Dec14	14:12:40	4 x 900	2626	No Detection	1.667×10^{-02}
43720	2009 Apr09	11: 8:13	4 x 800	3800	Definite	5.194×10^{-10}
43720	2009 Apr09	12:58:33	4 x 800	3759	Definite	6.871×10^{-12}
48770	2009 Dec03	16:42:47	4 x 750	1734	No Detection	1.528×10^{-02}
48770	2010 Apr01	10:30:40	4 x 800	2530	Definite	7.011×10^{-10}
62517	2009 Apr09	15: 7:23	4 x 800	1559	No Detection	8.504×10^{-01}
62517	2010 Apr02	12: 0:30	4 x 800	6685	Marginal Detection	1.786×10^{-03}
71933	2008 Dec18	17:44:15	4 x 900	1748	No Detection	7.146×10^{-01}
71933	2010 Apr01	15:37:08	4 x 800	8843	Definite	6.457×10^{-11}
77144	2010 Mar31	18:02:03	4 x 800	4315	Definite	0.000
77144	2010 Apr03	17:54:31	4 x 800	3783	No Detection	1.362×10^{-01}
89829	2009 Apr13	17:10:25	4 x 600	2544	No Detection	1.432×10^{-01}
89829	2010 Apr01	16:41:14	4 x 800	7274	Definite	4.663×10^{-15}
90899	2010 Mar28	17:50:20	2 x 800[e]	669	No Detection	6.837×10^{-01}
90899	2010 Apr02	17:42:47	4 x 800	3663	Marginal Detection	3.647×10^{-3}
93378	2010 Apr01	17:43:42	4 x 800	9727	No Detection	7.102×10^{-2}
105388	2008 Dec09	10:17:50	4 x 900	3822	Definite	1.732×10^{-14}
105388	2008 Dec10	10:23:32	4 x 900	3388	No Detection	5.084×10^{-01}

[a] Mid-observing time. [b] Generally a cycle consists of four sub-exposures. [c] Mean Signal-to-noise in the Stokes V LSD profile, see Section B.2.4. [d] FAP: False Alarm Probability. See Section 3.3.2 for more details. [e] Due to cloud, this cycle was reduced to two sub-exposures.

multiplex gain has the advantage of removing the noise inherent in each line profile while preserving Stokes I and V signatures. The line masks that were used to produce the LSD profile were created from the Kurucz atomic database and ATLAS9 atmospheric models (Kurucz, 1993) and were closely matched to the spectral type of each individual star.

B.3 Results and Analysis

B.3.1 Projected Rotational Velocity

The projected rotational velocity, $v \sin i$, was measured by rotationally broadening a solar LSD profile to match the LSD profile of the star. The solar spectrum was the reflected light from the Moon and was taken on the same night with the same instrumental setup. This method of determining the $v \sin i$ was shown to be reliable, particularly with rapidly rotating stars, by Waite et al. (2005) when they compared this technique with the Fast Fourier Transform technique of Gray (1992). Tables B.1, B.2 and B.3 shows the projected rotational velocities for the target stars. The error bars on each measurement are usually ± 1 km s^{-1} although for rapidly rotating stars with substantial deformation of the line profiles due to spot features, the errors could increase to ± 3 km s^{-1} or higher. The $v \sin i$ of almost two-thirds of these targets have not been previously determined.

The term Ultrafast Rotator (UFR) has been used extensively in the literature but without an explicit definition being applied. Hence the need to refine this terminology, particularly for solar-type stars. Stars that have projected rotational velocities less than 5 km s^{-1} will be considered as Slow Rotators (SR) as this is the lower limit at which accurate measurements of the $v \sin i$ of the star can be made in this dataset. Those stars with $v \sin i$ between 5 km s^{-1} and 20 km s^{-1} will be considered as Moderate Rotators (MR). This upper limit is considered a critical velocity where dynamo saturation has been theorised to slow the angular momentum loss of rapidly rotating stars (e.g. Irwin et al., 2007; Krishnamurthi et al., 1997; Barnes et al., 1999). Below 20 km s^{-1}, the strength of the star's magnetic dynamo is related to the star's rotation rate but above this speed, it is believed that dynamo saturation is occurring where the strength of the star's magnetic dynamo is no longer dependent upon stellar rotation. One empirical measure of this saturation in young solar-type stars is coronal X-ray

Table B.5: Classification of Solar-type stars based on projected rotational velocities.

Classification	$v\sin i$ range ($\mathrm{km\,s^{-1}}$)
Slow Rotator (SR)	0 - < 5
Moderate Rotator (MR)	5 - < 20
Rapid Rotator (RR)	20 - < 100
Ultra-Rapid Rotator (URR)	100 - < 200
Hyper-Rapid Rotator (HRR)	200+

emission. This emission, defined as the ratio of the star's X-ray luminosity to that of the star's bolometric luminosity (Vilhu, 1984), increases as rotation increases when it plateau's at the $v\sin i$ of $\approx$20 $\mathrm{km\,s^{-1}}$. Stauffer et al. (1997) theorised that this is consistent with dynamo saturation. Those stars with $v\sin i$ greater than 20 km $\mathrm{s^{-1}}$ to 100 km $\mathrm{s^{-1}}$ will be referred to as Rapid Rotators (RR). The upper limit of $\sim$100km $\mathrm{s^{-1}}$ was selected as at this rotational speed, the X-ray luminosity decreases below the saturated level (Randich, 1998), an effect that Prosser et al. (1996) called supersaturation. These definitions are consistent with those used by Marsden et al. (2009), Marino et al. (2003) and Prosser et al. (1996). Those stars between 100 km $\mathrm{s^{-1}}$ to 200 km $\mathrm{s^{-1}}$ will be referred to as Ultra-Rapid Rotators (URR). Stars that exceed 200 km $\mathrm{s^{-1}}$ will be referred to as Hyper-Rapid Rotators (HRR) and are likely to be very oblate. Many of the stars in this sample have not had their inclination determined, thus the $v\sin i$ is likely to be an underestimate of the true equatorial rotation of the star, and thus depending on the inclination, the star may be more rapidly rotating than indicated by the $v\sin i$. In addition, these definitions are limited to solar-type stars. Table B.5 gives a summary of the definitions used in this appendix.

B.3.2 Heliocentric Radial Velocity

Each spectrum, when extracted, was shifted to account for two effects. Initially, small instrumental shifts in the spectrograph were corrected for by using the positions of the telluric lines embedded in each spectrum. A telluric line mask was used to produce an LSD profile and the centroid of this profile was used to determine these small corrections

(Donati et al., 2003b). Secondly, the heliocentric velocity of the Earth towards the star was determined and corrected for.

The LSD profile of the star was used to measure the radial velocity of the star by first re-normalising the profile, then fitting a gaussian curve to the profile and measuring the location of the minimum. The radial velocities are listed in Tables B.1, B.2 and B.3. The error in the radial velocity was estimated to be less than ± 1 km s^{-1} although the presence of spots on the surface did have some effect on the location of the minimum, especially on stars with rotational speeds in excess of 100 km s^{-1} such as HIP 89829 where the fitting of the gaussian profile was problematic given the rapid rotation. However, Marsden et al. (*in preparation* show that when comparing this method to stable radial velocity measurements from planet search programmes, radial velocity values match to approximately $\pm$ 0.3 km s^{-1}. One should note that this error estimate is based on stars with low $v \sin i$, hence this project has assumed an error of $\pm$ 1 km s^{-1}as many of these targets have higher $v \sin i$ values than that of Marsden's.

The large variation seen in the radial velocity measurements for HIP 89829 could be a result of this star being a binary star. However, after searching for evidence of a companion star deforming the LSD profile of the spectropolarimetry data it was concluded that this star is probably single. This still does not preclude the existence of a secondary component as a very low mass companion such as an M-dwarf is likely to modify the radial velocity of the primary without generating a detectable line in the LSD profile, because the line-mask employed here is optimised for the primary, not for the companion. It was impossible to accurately measure the radial velocity of the HRR HIP 93378 due to its extreme deformation of the LSD profiles.

B.3.3 Chromospheric Indicators: Hydrogen $H\alpha$, Magnesium-I triplet and Sodium-I doublet.

The Hα, magnesium-I triplet (516.733, 517.270 and 518.362 nm) and sodium D_1 and D_2 doublet (588.995 and 589.592 nm) lines are often used as a proxies for stellar activity and in particular chromospheric activity. The Hα line is formed in the middle of the chromosphere (Montes et al., 2004) and is often associated with plages and prominences. The magnesium I triplet and sodium D_1 and D_2 doublet lines are collisionally dominated and are formed in the lower chromosphere and upper photosphere. This makes them good indicators of changes in that part of the atmosphere of stars (Montes et al., 2004).

Many authors (e.g. Zarro and Rodgers, 1983; Young et al., 1989; Soderblom et al., 1993b; Montes et al., 2004; Waite et al., 2005) determine the emission component of the Hα line by subtracting the stellar spectrum from a radial velocity-corrected, inactive star that has been rotationally broadened to match the $v \sin i$ of the target. This technique is temperature dependent, but since all of our targets have similar spectral types, a solar spectrum was used as the inactive standard star in this survey. The resulting emission equivalent width (EEW) is a measure of the active chromospheric component of these spectral lines, including the Hα line. Figure B.1 shows the core emission of the magnesium triplet and Hα line for the more active stars in this sample. Many of the likely targets for ZDI exhibit core emissions; however, the HRR star HIP 93378 exhibits no activity in either the magnesium triplet or the Hα line. This may be due to the extreme broadening of the spectral lines "washing out" the emission component.

B.3.4 Lithium-I 670.78 nm: An Age Indicator

In the absence of a companion star, an enhanced Li I 670.78 nm line can be used as an indicator of youth (Martín and Claret, 1996) for stars that are cooler than mid-G type (0.6 $\leq$ B-V $\leq$ 1.3) although this is not as useful for F-type stars where there appears to be a plateau in the depletion of the lithium due to age (Guillout et al., 2009). However, do Nascimento Jr et al. (2010) point out that there is a large range in lithium depletion for solar-type stars which may reflect different rotational histories or as a result of different mixing mechanisms such as shear mixing caused by differential rotation (Bouvier, 2008). In analysing the spectra, the equivalent width EqW$_{Li}$ was measured using the SPLOT task in IRAF. This was done so as to allow comparison with those measured by Torres et al. (2006). The error in the measured values of EqW$_{Li}$ is primarily due to uncertainties in the continuum location. When the rotational velocity, $v \sin i$, exceeded 8 km s^{-1}, the Li I spectral line is blended with the nearby 670.744 nm Fe I line. This was corrected using the same correction factor developed by Soderblom et al. (1993b,a). The correction used is shown in equation B.1.

$$EW_{Li}corr = EW_{Li} - 20(B - V) - 3 \tag{B.1}$$

Some of the results appear slightly discrepant when compared with Torres et al. (2006). It is unclear whether Torres et al. (2006) corrected for the Fe I line in their measurements

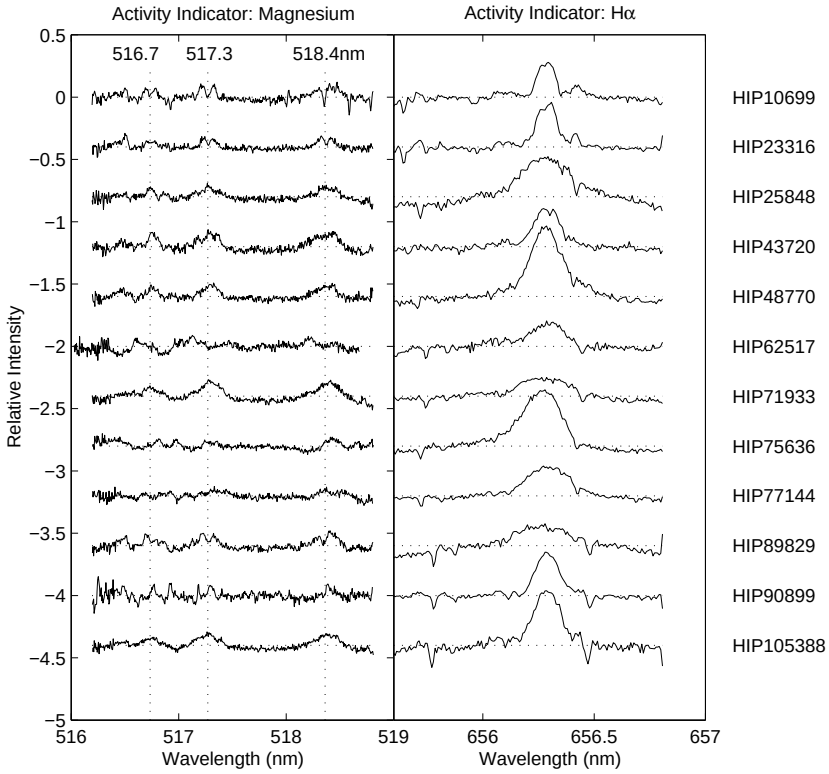

Figure B.1: The core emission in the magnesium triplet lines, left panel, and the Hα spectral line, right panel, are shown for rapid rotators in this sample. This core emission was obtained by subtracting a radial velocity corrected, rotationally-broadened solar spectrum.

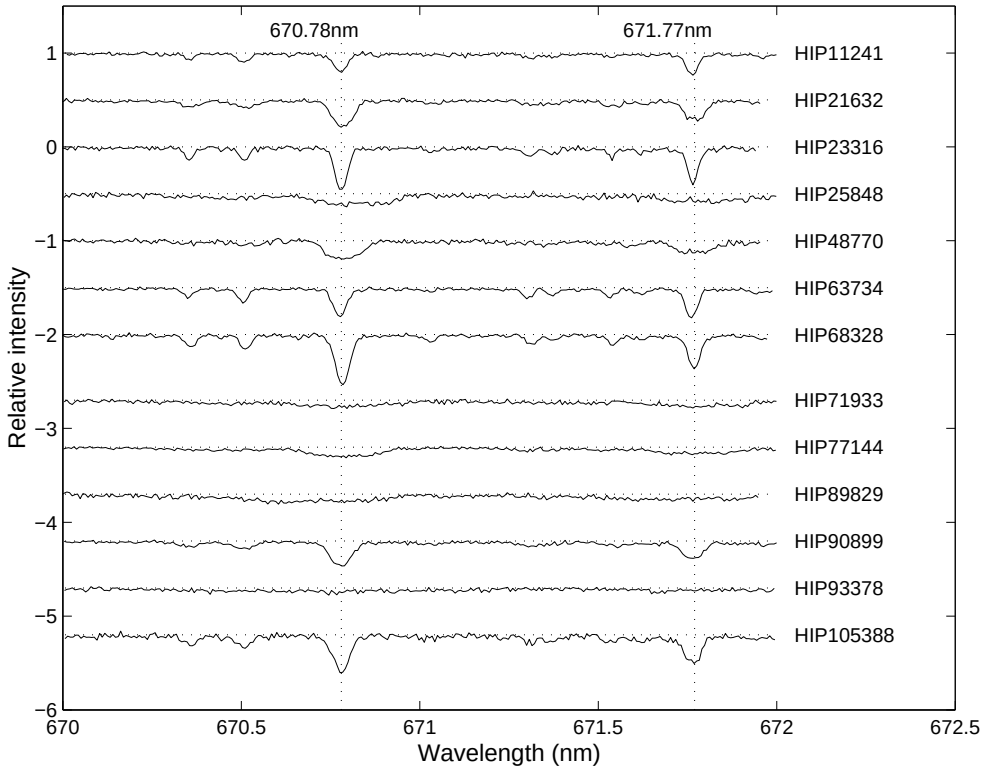

Figure B.2: The lithium-I 670.78 nm line, compared with the calcium-I 671.77 nm line, for a number of stars in this survey.

but such a difference in processing may possibly explain the discrepancies. Figure B.2 shows the strength of the Li I 670.78 nm line, compared with the nearby Ca I 671.80 nm line, for a number of stars that are likely to be future targets for the ZDI programme.

B.3.5 Spectropolarimetry

The magnetic signatures embedded in starlight are extremely difficult to detect. The typical Zeeman signature is very small, with a circular polarisation signature (Stokes V) of $\sim$0.1% of the continuum level for active stars (Donati et al., 1997). As discussed in Section B.2.3, observations in Stokes V consists of a sequence of four sub-exposures with the half-wave Fresnel Rhomb being rotated between $+45^o$ and -45^o. To detect these signatures, LSD is applied to increase the signal-to-noise of the signature when creating the Stokes V profile. The Stokes V profile is the result of constructively adding

the individual spectra from the four exposures by "pair-processing" sub-exposures corresponding to the opposite orientations of the half-wave Fresnel Rhomb. To determine the reliability of the process, a "null" profile is produced as a measure of the noise within the LSD process. This null profile is found by "pair-processing" sub-exposures corresponding to the identical positions of the half-wave Fresnel Rhomb of the SEMPOL polarimeter during each sequence of 4 sub-exposures.

When producing figures, such as Figure B.3 for example, the Stokes V (upper) and null (middle) profiles have been multiplied by 25 so as to show the variation within each profile. Both profiles have been shifted vertically for clarity. The dots on the Stokes V and null profiles are the actual data while the smooth curve is a 3-point moving average. The deformation in the Stokes V profile is a direct result of the magnetic field observed on the star while deformation in the Stokes I (intensity) profile (lower) is a result of starspots on the surface of the star. For more information on ZDI see Carter et al. (1996) and Donati et al. (1997).

For each observation a false-alarm probability (FAP) of magnetic field detection was determined. See Section 3.3.2 for more details of the FAP listed in this appendix.

B.4 Some comments on individual stars

Many of the stars in this survey exhibited some indication of activity either due to the presence of a companion star, or in the case of single stars, activity due to youth and/or rapid rotation. Each likely ZDI target will be considered in more detail in this section.

B.4.1 Moderate and rapid rotators suitable for ZDI studies

B.4.1.1 HIP 21632

HIP 21632 is a G3V star (Torres et al., 2006). The *HIPPARCOS* space mission measured a parallax of 18.27 ± 1.02 milliarcseconds (mas) (van Leeuwen, 2007), giving a distance of 178^{+11}_{-9} light-years (ly). Using the bolometric corrections of Bessell et al. (1998) and the formulations within that appendix, the effective temperature of this star was determined to be 5825 ± 45 K and the radius was estimated to be 0.96 ± 0.04 $R_\odot$. The luminosity was subsequently estimated to be $0.93^{+0.12}_{-0.11}$ $L_\odot$. Zuckerman and Song (2004) proposed that HIP 21632 was a member of the Tucana/Horologium Association indicating an age of ∼30 Myr. This star has an emission equivalent width for the Hα

line in the range from ∼385 mÅ to ∼517 mÅ demonstrating the presence of a very active, and variable, chromosphere. This variation could be due to prominences occurring on this star. Two exposures, separated by 4 hours 41.41 minutes, were taken on April 14, 2008 demonstrated noticeable variation in the core emission of the Hα line, as shown in Figure B.4. Yet there was no variation in the magnesium triplet and indeed, there was very little core emission in the three lines, with some filling-in in the wings of the lines. However, there were some minor changes in the sodium D_1 line but the variation is less than observed in the mid-level chromospheric level. There is no evidence of the presence of a companion star in the LSD profile. Torres et al. (2006) measured a radial velocity of 18.8 km s^{-1} (using cross correlation methods) and an equivalent width for the Li I line of 200 mÅ. These values are consistent with the values obtained from this survey of an average radial velocity of 19.4 ± 1 km s^{-1} and a equivalent width for the Li I line of 190 ± 2 nm (see Section B.3.4 on a possible reason for slightly discrepant values).

This star was observed spectropolarimetrically on two occasions using SEMPOL. On the first occasion, no magnetic signal was detected with a mean S/N of 5898 with 4 sub-exposures, yet achieved a definite magnetic detection with only 2 sub-exposures with a mean S/N of 2710 on the second occasion. The resulting LSD profile for this cycle is shown in Figure B.3. Whereas this star is only a moderate rotator, it is a worthwhile target for more detailed spectropolarimetric studies and was included in this thesis.

B.4.1.2 HIP 25848

HIP 25848 is a G0 weak-lined T Tau-type star (Li and Hu, 1998). It has a trigonometric parallax of 7.95 ± 1.29 mas (van Leeuwen, 2007) giving a distance of 410^{+79}_{-57} ly. Using the bolometric corrections by Bessell, Castelli, and Plez (1998), the effective temperature was estimated to be 5700 ± 130 K. Using the formulation contained in Bessell, Castelli, and Plez (1998) the star is estimated to be $\sim 1.67^{+0.23}_{-0.17}$ $R_\odot$. Placing this star on the theoretical isochrones of Siess et al. (2000), it is estimated to be 1.3 ± 0.1 $M_\odot$ with an age between 10 Myr to 20 Myr. This is shown in Figure B.5. This is consistent with the age found by Tetzlaff et al. (2011) although slightly less massive than that quoted in that appendix. Norton et al. (2007) used SuperWASP to measure a period of 0.9426 d. This survey measured a $v \sin i$ of 69 km s^{-1}. This star has an emission

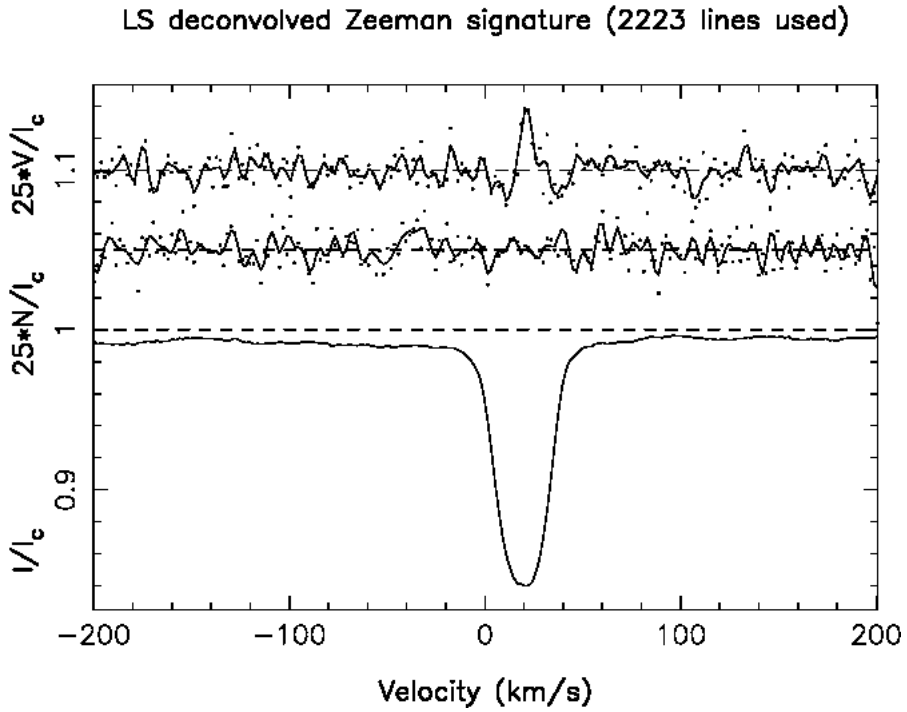

Figure B.3: The magnetic detection of young G3V star HIP 21632. The lower profile is the Stokes I LSD profile, the middle profile is the null profile and the upper profile is the Stokes V profile. The dots are the actual data while the smooth line is a moving 3-point average of the data. The Stokes V and Null profiles have been vertically shifted for clarity. In addition to this, the Stokes V and Null profiles each were multiplied by 25 in order to highlight the actual signatures. The Stokes V profile clearly shows a strong magnetic detection. This was achieved using only 2 sub-exposures with a mean S/N of 2560 in the Stokes V LSD profile.

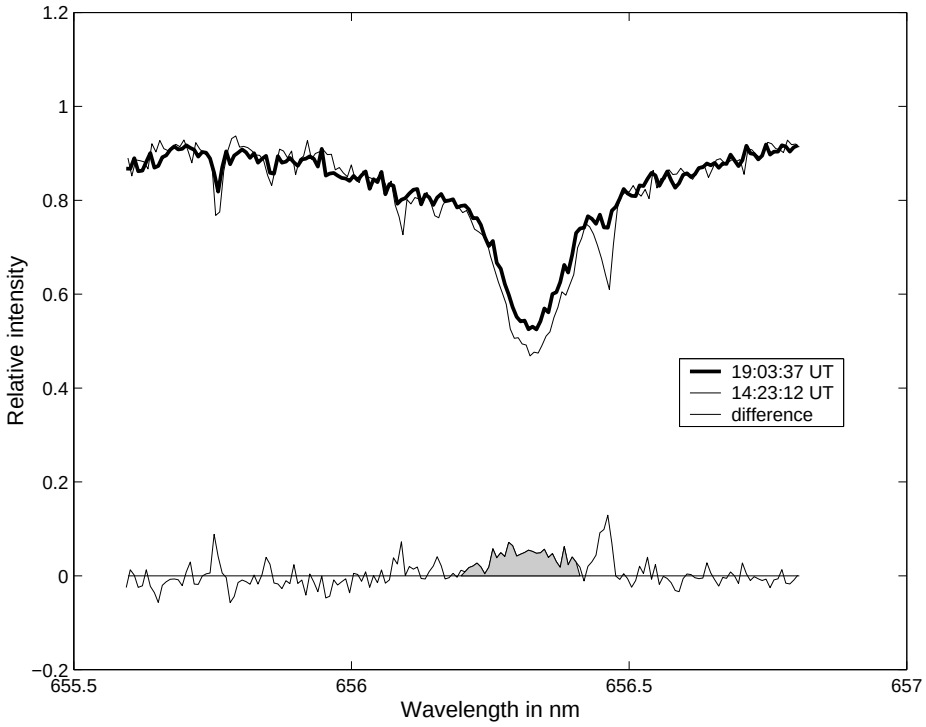

Figure B.4: The variation of the Hα profile of HIP 21632. Two exposures were taken, separated by 4 hours, 41.41 minutes. The variation in the Hα profile is shown as a shaded region in the difference spectrum. The sharp absorption line at $\sim$656.4 nm in the 12:23:12UT spectra is most likely due to telluric lines at 656.4049 and 656.4200 nm.

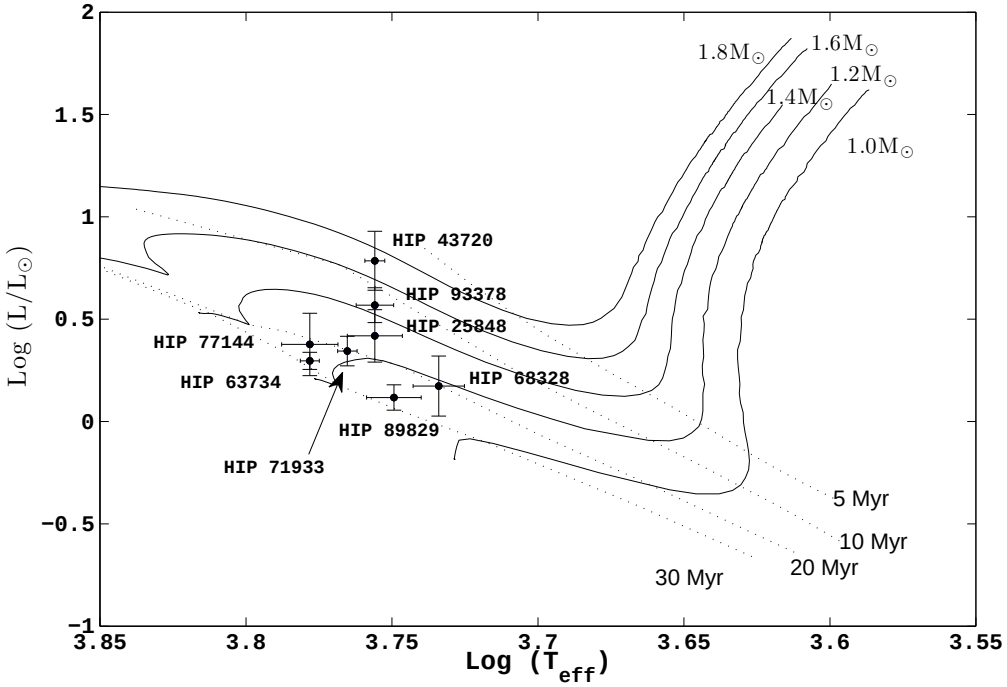

Figure B.5: The evolutionary status of some of the survey stars, based on the theoretical isochrones of Siess et al. (2000). Only those likely ZDI targets with accurate photometry were incorporated onto this diagram.

equivalent width for the Hα line of 668 $\pm$ 60 mÅ, meaning that it is very active and one of the most active stars from this survey. The sodium doublet lines were filled in, almost to the continuum. It has a very deep Li I line suggesting, in the absence of a companion star, a youthful star. No spectropolarimetric observations were obtained. With a declination of $+23^o$, it would be a difficult target for ZDI at the AAT. However, this star would be an ideal target for ESPaDOnS at the CFHT (Canada-France-Hawaii Telescope, Hawaii) or NARVAL at the TBL (Télescope Bernard Lyot, Pic du Midi, France).

B.4.1.3 HIP 43720

HIP 43720 is a particularly active, G1V star (Torres et al., 2006). It has a trigonometric parallax of 5.38 $\pm$ 0.94 mas (van Leeuwen, 2007) giving a distance of 606^{+128}_{-90} ly.

Using the star's V-I value and the formulation in Bessell, Castelli, and Plez (1998), the star's temperature was estimated to be 5700^{+40}_{-45} K while its radius was estimated to be $2.6^{+0.7}_{-0.4}$ $R_{\odot}$. Placing HIP 43720 onto the theoretical isochrones of Siess et al. (2000), as shown in Figure B.5, suggests that this star's age is $\leq$10 Myr years and has a mass of between 1.6 and 1.8 $M_{\odot}$. However, this age estimate is not supported by the depth of the Li I line, with an equivalent width of <5 mÅ. One can speculate that the lithium has already been depleted. Guillout et al. (2009) suggest that stars with deep convective envelopes, such as M-dwarfs, are very efficient at depleting the lithium concentration. Being a pre-main-sequence star, HIP 43720 may also possess a very deep convective zone. Alternatively, Bouvier (2008) suggest that this depletion may be due to large velocity shear at the base of the convective zone as a result of star-disk interaction.
There is evidence of an active chromosphere with an emission equivalent width for the Hα line of $\sim$400 $\pm$ 28 mÅ and strong emission in the magnesium triplet lines, as shown in Figure B.1. Definite magnetic fields were observed on three occasions (9 December, 2008 and 9 April, 2009) although no magnetic field was detected on a fourth observation (14 December, 2008). On that occasion, the mean S/N was $\sim$2626. Figure B.6 shows the Stokes V, null and Stokes I profile. This is an interesting target for follow-up spectropolarimetric studies at the AAT and as a result, is the subject of Chapter 4.

B.4.1.4 HIP 48770

HIP 48770 is a G7V pre-main-sequence star (Torres et al., 2006). It has a trigonometric parallax of 5.83 $\pm$ 1.55 mas (van Leeuwen, 2007) giving a distance of 554^{+199}_{-115} ly. The $v\sin i$ was measured to be 35 km s^{-1}, which is consistent with that found by Torres et al. (2006). The radial velocity was determined to be 19.6 km s^{-1}, which is different from the 22.6 km s^{-1} observed by Torres et al. (2006). There appears to be no evidence of a secondary component in the spectra; but the presence of a companion in a large orbit cannot be ruled out. HIP 48770 is very young with a prominent lithium feature, as shown in Figure B.2. Ammons et al. (2006) calculated an effective temperature of 5539 K. However, using the bolometric corrections of Bessell, Castelli, and Plez (1998), our estimate is higher at 6000 $\pm$ 300 K. It is also very active with the Hα spectral line being almost entirely filled in; and the magnesium triplet is also very strong. A visual magnitude of 10.5 would normally make it a challenging target for SEMPOL at the AAT. However, a magnetic detection was observed at the AAT demonstrating

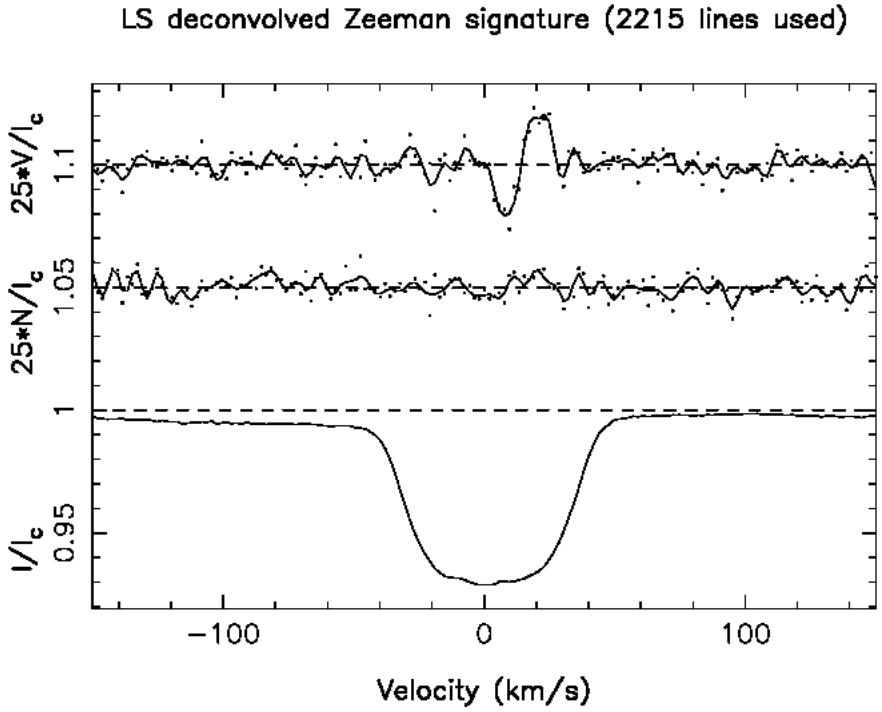

Figure B.6: The various LSD profiles, as explained in Figure B.3, for HIP 43720. The Stokes V profile (upper profile) shows evidence of a strong magnetic feature on the young star HIP 43720. The LSD profile (lower profile) has a flat bottom, possibly indicating the presence of a polar spot feature.

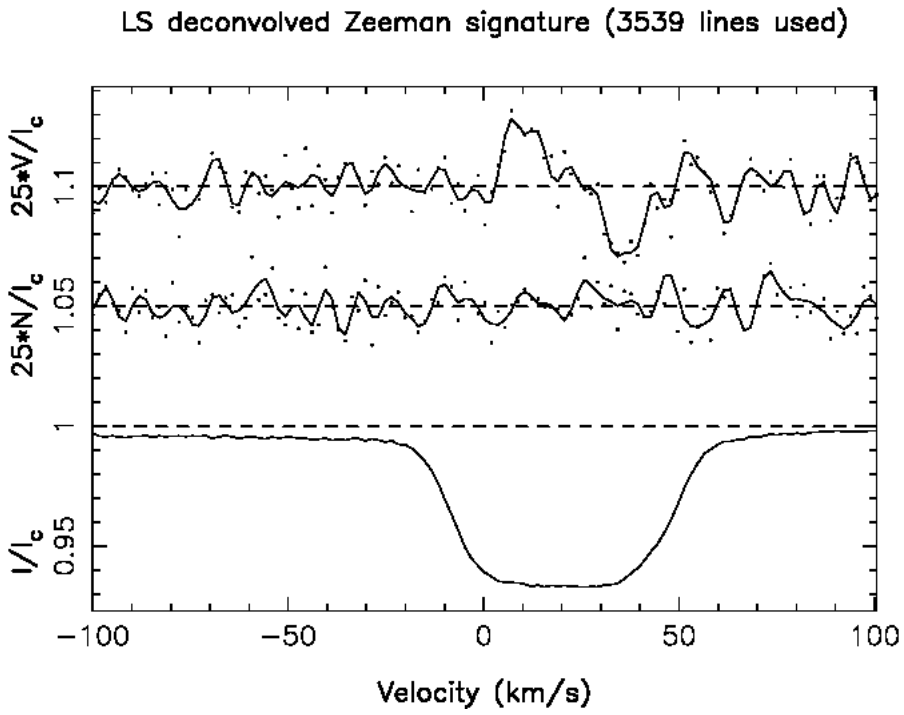

Figure B.7: The various LSD profiles, as explained in Figure B.3, for HIP 48770.

its highly active nature. The Stokes I LSD profile, along with the Stokes V profile is shown in Figure B.7.

B.4.1.5 HIP 62517

HIP 62517 is an active G0 star (SAO, 1966). It has a parallax of 2.38 ± 1.6 mas (van Leeuwen, 2007) giving a distance of 420^{+862}_{-169} ly. This star has a $v \sin i$ of 52 km s^{-1}. This particular star has a strong Hα emission of 265 mÅ coupled with some filling in of the core of the magnesium triplet. However, its lithium line is rather weak, indicating that it may not be as young as some of the other stars in the sample. Ammons et al. (2006) calculated an effective temperature of 5336 K, which is slightly higher than our estimate of 5250 ± 65 K found using the bolometric corrections of Bessell, Castelli, and Plez (1998). A marginal detection of a magnetic field was recorded on 2010, April 2, as shown in Figure B.8. The S/N was 6685. Although only two snapshots were taken several months apart, with the indications that this star is single, the global magnetic field may be relatively weak and would be difficult to recover any magnetic features

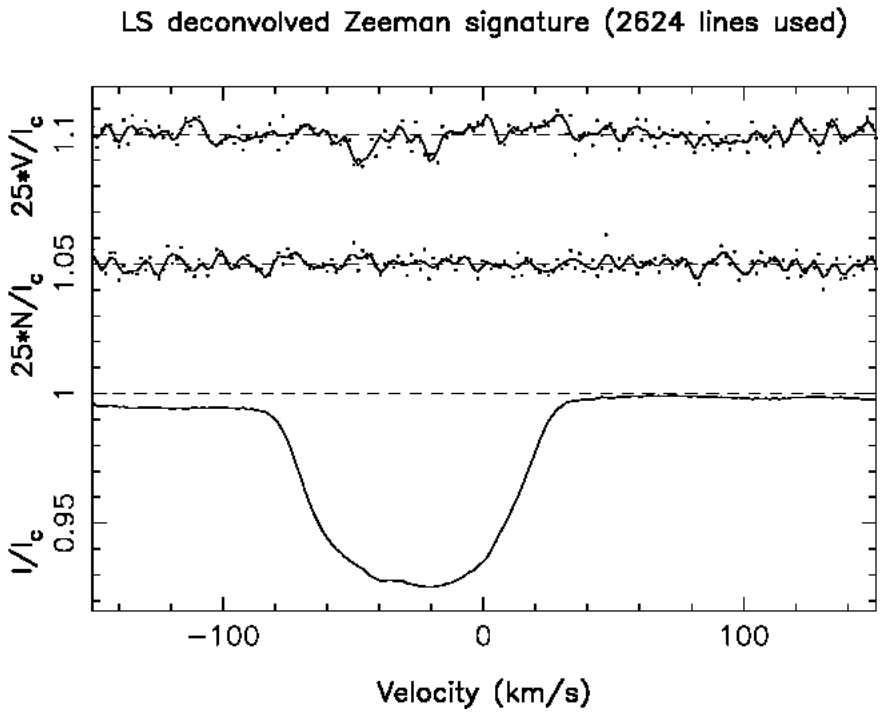

Figure B.8: The marginal magnetic detection in the Stokes V profile (upper profile) for HIP 62517. The profiles are as explained in Figure B.3.

if observed over several epochs. This makes this star a difficult target for ZDI at the AAT.

B.4.1.6 HIP 71933

HIP 71933 is a pre-main-sequence F8V star (Torres et al., 2006). It has a parallax of 11.91 ± 0.99 mas (van Leeuwen, 2007) giving a distance of 274^{+25}_{-21} ly. It has a projected rotational velocity of 75 km s^{-1}. The radial velocity was measured to be ∼4 km s^{-1}. As mentioned previously, the large spots on the surface of this star makes accurate radial velocity measurements difficult. However, Torres et al. (2006) measured 8.7 km s^{-1} while Gontcharov (2006) measured 12.3 ± 0.4 km s^{-1} and Kharchenko and Roeser (2009) measured 12.1 ± 0.4 km s^{-1}. Perhaps this star is part of a wide binary system. Torres et al. (2006) flagged that this star might be a spectroscopic binary star. If the star was a binary, and the companion's profile is overlapping the primary's profile, it could be mistaken for spots. Alternatively, the companion may be a faint M-dwarf

star thereby not deforming the profile at all. Careful consideration of the LSD profiles produced from the high-resolution spectra obtained using the normal UCLES setup (R∼50000) and spectropolarimetry (R∼70 000), suggest that the deformations are due to spots rather than a companion. However, the presence of a secondary component cannot be ruled out by this survey.

Holmberg et al. (2009) estimated the effective temperature to be 5900K while Ammons et al. (2006) estimated the temperature to be 5938K. The equivalent width of the Li I was measured to be 139 ± 7 mÅ, after accounting for the FeI blended line using equation B.1. When using the theoretical isochrones of Siess et al. (2000), as shown in Figure B.5, this star's age is estimated to be ∼20 Myr years and has a mass of ∼1.2 $M_{\odot}$.

This is a particularly active star, as shown in Figure B.1, with emission in the magnesium triplet lines and the Hα line. However, there was some core emission in the NaI D_2, but not in the D_1 line. Spectropolarimetry was conducted on two occasions, once when the seeing was very poor (∼ 2.5 to 3.5 arcsec) and only a S/N of 1748 but on the other occasion, reasonable seeing (∼1.5 arcsec) resulted in a definite detection of a magnetic field. This detection is shown in Figure B.9.

B.4.1.7 HIP 77144

HIP 77144 is a post T-Tauri G1V star Sartori et al. (2003) in the Scorpius-Centaurus group (Mamajek et al., 2002). It has a parallax of 7.12 ± 1.28 mas (van Leeuwen, 2007) giving a distance of 458^{+100}_{-70} ly. It has a $v\sin i$ of 65 km s^{-1} with a particularly strong Hα (EEW = 466 ± 2 mÅ) and Li I lines (EqW = 207 ± 7 mÅ). The temperature is estimated to be ∼6000 ± 130 K. It is approximately $1.45^{+0.25}_{-0.18}$ $R_{\odot}$ when using the bolometric corrections of Bessell, Castelli, and Plez (1998), giving a luminosity of $2.4^{+1.2}_{-0.7}$ $L_{\odot}$. This young star, when placed on the theoretical isochrones of Siess et al. (2000) gives an age of this star of ∼ 20 Myr and is approximately 1.3 ± 0.1 $M_{\odot}$. This is shown in Figure B.5. The radial velocity was measured to be -1.6 km s^{-1}, which is consistent with that found by Madsen et al. (2002) and Kharchenko et al. (2007) to within the respective errors of each measurement. A definite magnetic field was detected on 2010, March 31, with a mean S/N in the Stokes V profile of 4315. This magnetic detection is shown in Figure B.10.

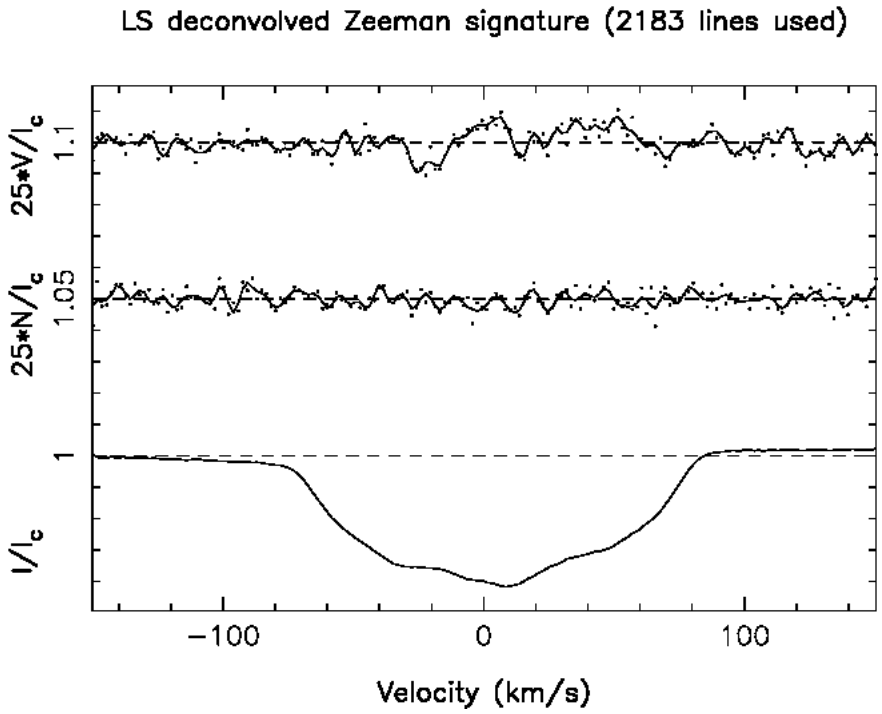

Figure B.9: The various LSD profiles, as explained in Figure B.3, for HIP 71933. The S/N for this was 8843.

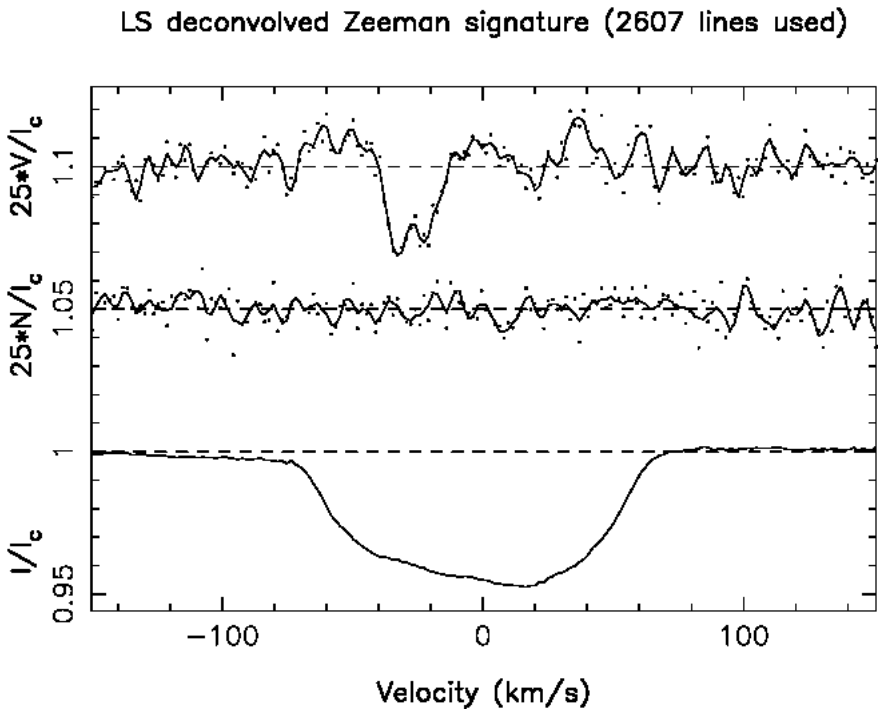

Figure B.10: The various LSD profiles, as explained in Figure B.3, for HIP 77144.

B.4.1.8 HIP 90899

HIP 90899 is a G1V star (Turon et al., 1993). According to *HIPPARCOS* database, this star has a parallax of 10.87 ± 1.34 mas (van Leeuwen, 2007), giving a distance of 300^{+42}_{-33} ly. Using the V-I determined by the *HIPPARCOS* Star Mapper Photometry, a value of 0.62 ± 0.03 gives a temperature of 6090^{+130}_{-140} K using the formulation given in Bessell, Castelli, and Plez (1998). This is consistent with other authors such as Wright et al. (2003) (6030 K) and Ammons et al. (2006) (5988 K). Using the bolometric corrections of Bessell, Castelli, and Plez (1998) gives a radius of $0.97^{+0.10}_{-0.08}$R$_\odot$ and a luminosity of $1.13^{+0.37}_{-0.25}$ L$_\odot$. This star has an emission equivalent width for the Hα line of 408 ± 14 mÅ, with some filling of the core of the magnesium triplet lines, meaning that it is a very active star. It has a very deep Li I line with an equivalent width of 176 ± 6 mÅ, suggesting that, in the absence of a companion star, is youthful in nature. The magnetic detection, as shown in Figure B.11 was only marginal but still, at a $v \sin i$ of 19 km s^{-1}, the magnetic topologies should be recoverable at the AAT.

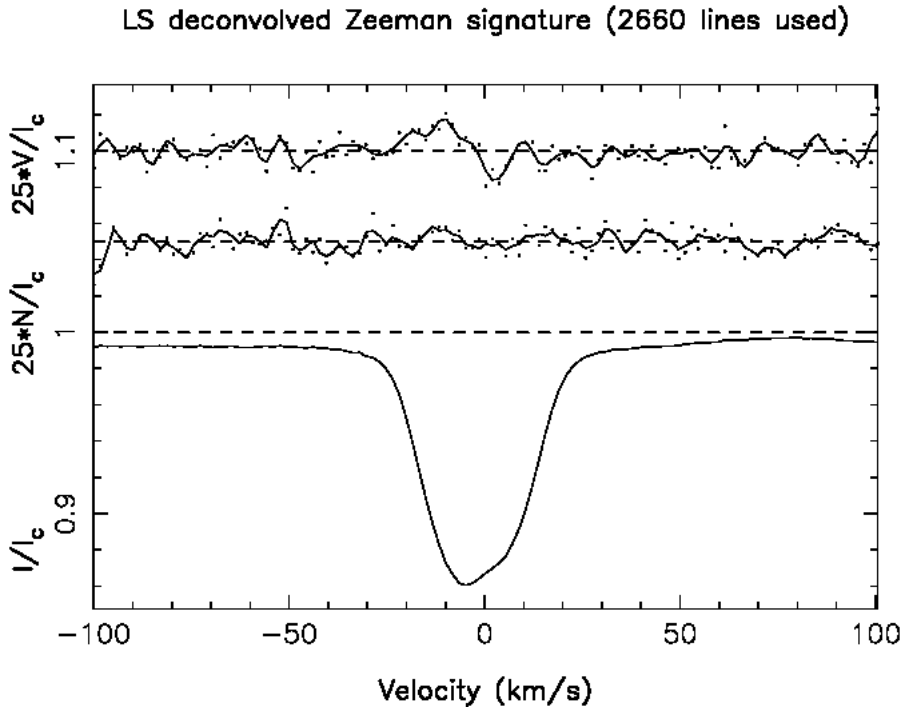

Figure B.11: The various LSD profiles, as explained in Figure B.3, for HIP 90899.

B.4.1.9 HIP 105388

HIP 105388 is a G7V pre-main-sequence star (Torres et al., 2006). This star has a $v\sin i$ of 17 km s^{-1}. This compares with the measurement of Torres et al. (2006) of 15.4 km s^{-1}. The value of this star's radial velocity was determined to be -1.8 ± 1.0 km s^{-1}. This value is consistent with those measured by Torres et al. (2006) of -0.9 km s^{-1} and Bobylev et al. (2006) $^{-}$1.6 ± 0.2 km s^{-1}, to within the respective errors. This star has an emission equivalent width for the Hα line of 520 mÅ; yet there is little core emission in either the magnesium triplet or sodium doublet. Zuckerman and Song (2004) proposed that HIP 105388 was a member of the Tucana/Horologium Association and an age estimate for this moving group, hence this star, is 30 Myr. Further indication of the youthful nature of this star is the very strong Li I line, as shown in Figure B.1. Tetzlaff et al. (2011) estimate that this is a 1.0 ± 0.1 M$_\odot$ star. Whereas the $v\sin i$ is at the lower limit for ZDI at the AAT, a magnetic detection on this star was secured with an S/N of only 3822. There is limited spot activity as evidenced by the smooth Stokes I profile (lower LSD profile) in Figure B.12. Recovering magnetic features from slow to moderate rotators is possible, as shown by Petit and Donati (2005) and Petit et al. (2008).

B.4.2 Ultra-Rapid Rotator: HIP 89829

HIP 89829 is a G5V star (Torres et al., 2006). With a $v\sin i$ of 114 km s^{-1}, this star has been classified as an URR. This measurement is consistent with Torres et al. (2006) measurement of 114.7 km s^{-1}. Pojmański et al. (2002a) quote a rotational period of 0.570751d with a photometric amplitude of ΔV = 0.07. This star is very active and has an emission equivalent width for the Hα line of 280 ± 52 mÅ yet little if any emission in the magnesium triplet or the sodium doublet is seen. It has a very deep, albeit broadened, lithium line with an equivalent width of 211 ± 13 mÅ. This indicates, in the absence of a companion star, a youthful star. This is consistent with that found by Torres et al. (2006). When placed on the theoretical isochrones of Siess et al. (2000), this star is approximately 25-30 Myr and has a mass of between 1.0 and 1.2 M$_\odot$. The magnetic detection is shown in Figure B.13. This is one of the most rapidly rotating stars that has had its magnetic field detected at the AAT.

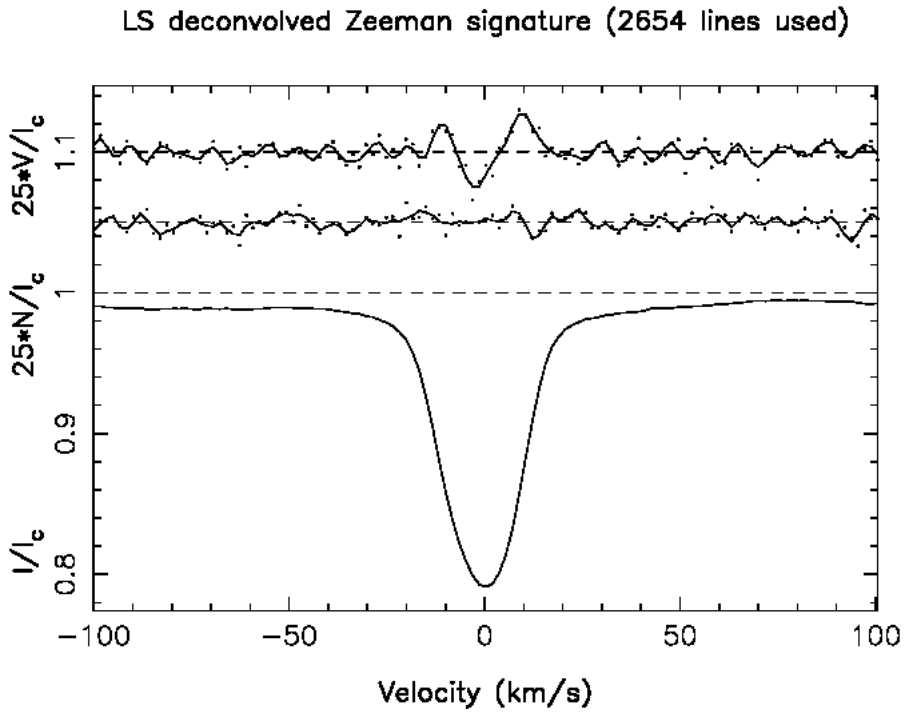

Figure B.12: The various LSD profiles, as explained in Figure B.3, for HIP 105388. The Stokes I LSD profile shows limited spot activity on the star yet there is a definite magnetic detection in the Stokes V profile. This is supported by the absence of signal in the null profile.

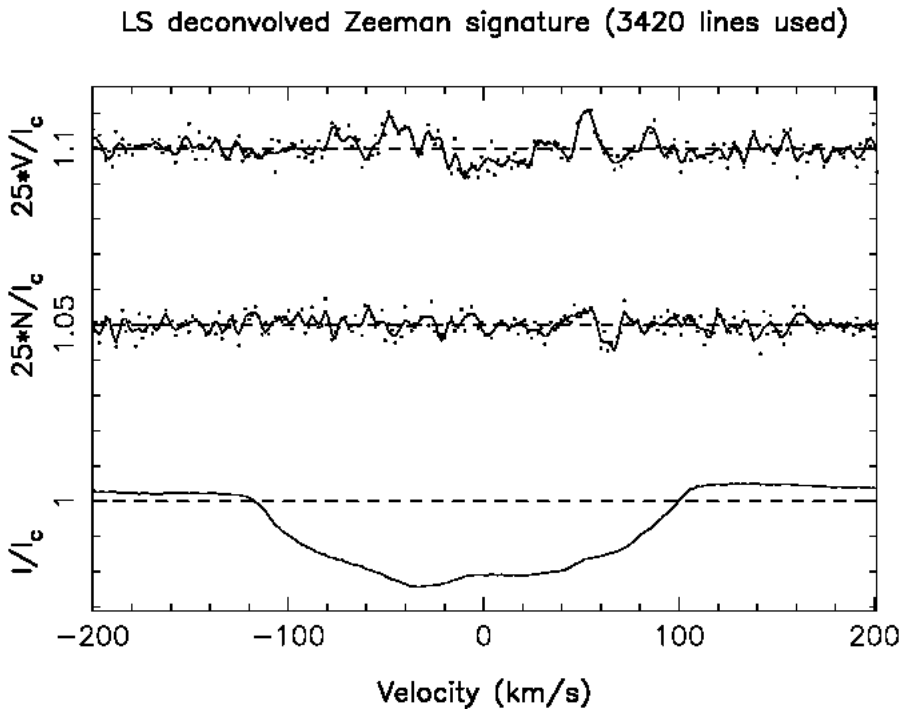

Figure B.13: The various LSD profiles, as explained in Figure B.3, for HIP 89829.

As mentioned in Section B.3.2, the large variation seen in the radial velocity measurements for HIP 89829 could be a result of this star being a binary star. However, after carefully considering the resulting LSD profiles from both the normal UCLES setup (R∼50000) and SEMPOL setup (R∼70 000), this star is **probably** single.

B.4.3 Hyper-Rapid Rotator: HIP 93378

HIP 93378 is a pre-main-sequence, G5V star (Torres et al., 2006). According to *HIPPARCOS* database, this star has a parallax of 9.14 ± 0.92 mas (van Leeuwen, 2007), giving a distance of 357^{+40}_{-33} ly. It is a HRR with a $v \sin i$ of 226 km s^{-1}, which is consistent with the 230 km s^{-1} value measured by Torres et al. (2006) within the large uncertainty created by such a rapid rotation. This star's Hα profile, when matched against a rotationally broadened solar profile, exhibited no emission in the core. Thus it appears that there is limited chromospheric activity occurring on this star. However, as mentioned previously, this lack of chromospheric emission may be due to the extreme broadening of the spectral lines thereby "washing out" the emission component.

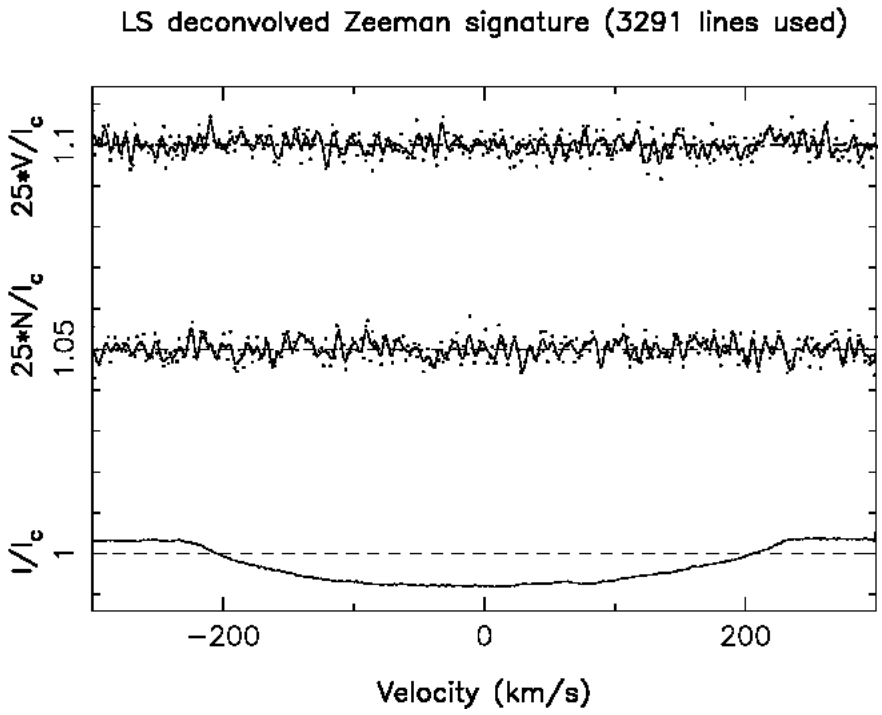

Figure B.14: The various LSD profiles, as explained in Figure B.3, for HIP 93378.

Another reason for this decreased Hα emission may be due to supersaturation or even a modification of the chromospheric structure by the extremely strong shear forces as a result of such rapid rotation.

No magnetic detection was observed on this star, even when the data were binned to increase the relative signal-to-noise in excess of 9000. Again this extreme rotation may have simply washed out any magnetic signature. The resulting LSD profile is shown in Figure B.14. Although this star is an extremely difficult target for ZDI at the AAT, its extreme rotation makes it an interesting target for Doppler imaging.

B.4.4 Active, young, slowly rotating stars.

This survey also found a number of slower rotating stars that are very young. Due to time constraints spectropolarimetric observations were not taken of these stars. However, the CFHT and TBL have been able to recover magnetic fields on slow rotators (Petit et al., 2008). One such star is the early G0 (Sartori et al., 2003) star HIP 68328. It has a relatively slow rotation of $\sim$6 km s^{-1}. It has a parallax of 8.34 $\pm$ 1.56 mas

(van Leeuwen, 2007) giving a distance of 391^{+90}_{-61} ly. Using the bolometric corrections of Bessell et al. (1998), the temperature of HIP 68328 was estimated to be 5420^{+114}_{-107} K. This is lower than the most recent estimate by Bailer-Jones (2011) of 5871 K. This project estimates that this star has a radius of $1.4^{+0.26}_{-0.17}$ $R_{\odot}$, giving a luminosity of $1.49^{+0.78}_{-0.44}$ $L_{\odot}$. This value is similar, within the relative error bars, to that estimated by Sartori et al. (2003) of 1.66 $L_{\odot}$. de Zeeuw et al. (1999) identified this star as a possible member of the Scorpius-Centaurus OB association. This is a young star-forming region with stars less than 20 Myr old. When placing this star on the theoretical isochrones of Siess et al. (2000), as shown in Figure B.5, the star has an age of $\sim$20 $\pm$ 10 Myr and a mass of $\sim$1.2 $\pm$ 0.1 $M_{\odot}$. This age is consistent with the observation of a very deep Li I line with an equivalent width of 263 $\pm$ 4 mÅ. It has a emission equivalent width for the Hα of 850 $\pm$ 45 mÅ, the most active star in this sample by this measure. These observations of youth and activity are shown in Figure B.15. Other slow rotators with substantial lithium lines include HIP 23316, HIP 41688, HIP 63734 and HIP 11241. All have indicators of having an active chromosphere with core emission in the Hα line. Another interesting target is the slow rotator is HIP 5617. It has very prominent emission in the wings of the Hα line, extending above the continuum, indicating the presence of circumstellar material. However, the lithium line is very weak. This is perhaps a T-Tauri star.

B.4.5 Binary and Multiple Stellar Systems

The LSD profile is an excellent way of identifying a binary star (Waite et al., 2005), as the LSD profiles often show both stars, except if the star is undergoing an eclipse or is a faint star such as an M-dwarf. Where stars that appear to be rapidly rotating, more than one spectra (often two, three or more) were taken to make sure that the star was indeed single. HIP 31021, HIP 64732 and HIP 73780 were identified as binary stars based on their individual LSD profiles. HIP 64732 may have a giant polar spot on one of the components as one of the LSD profiles exhibited a "flat bottom", indicating the likely presence of a giant polar spot or high latitude features. This is shown in top left panel of Figure B.16. HIP 19072, HIP 67651 and HIP 75636 are likely to be spectroscopic binary stars while HIP 33111 could be a triple system. The associated LSD profiles are shown in Figure B.16. There is a slight deformation of the LSD profile of HIP 75636 on the blue side that could be due to a companion star just moving into

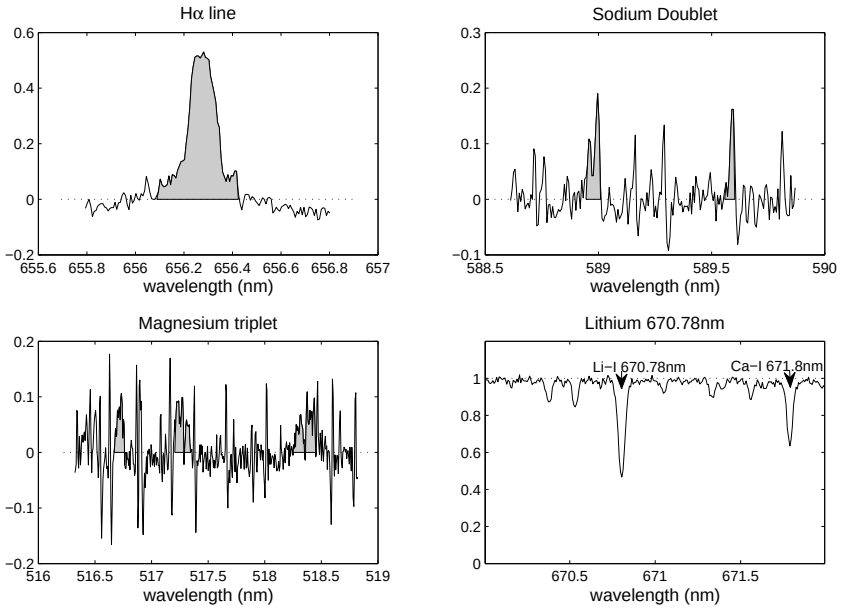

Figure B.15: The activity indicators for HIP 68328. This star has a very strong emission component of the Hα line with some moderate filling in of the sodium doublet and magnesium triplet. Also shown in this figure is the strong Li I 670.78 nm line.

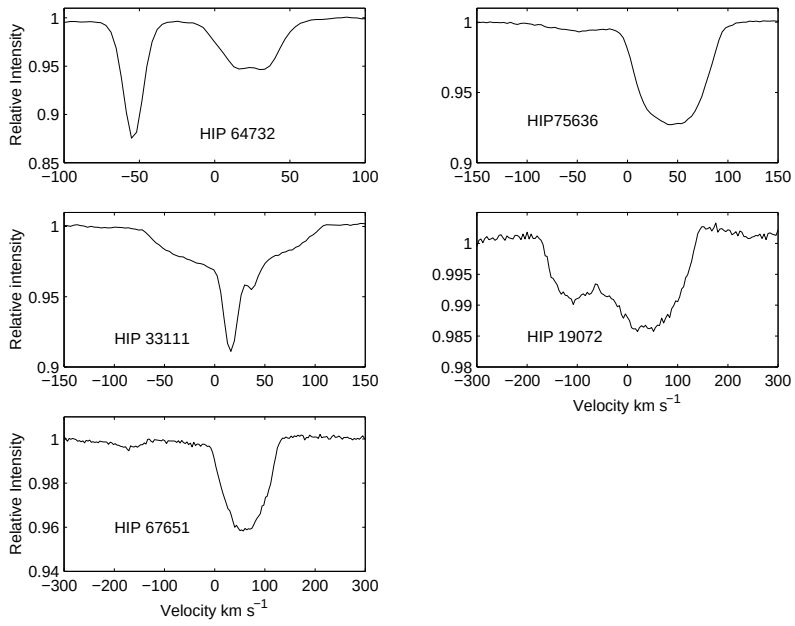

Figure B.16: LSD profiles of some likely binary stars.

an eclipse of the second star. Also, the radial velocity of this star was measured to be 43.7 ± 1 km s^{-1} whereas Torres et al. (2006) measured the radial velocity to be 5.9 km s^{-1}. While some of the stars in this survey exhibit slight shifts in the radial velocity when compared with the work of Torres et al. (2006), this difference is far too great to conclude anything else except that it is a binary star.

Table B.6 gives a summary of the likely targets for follow-up magnetic studies.

B.5 Conclusion

This survey aimed to determine the nature of a number of some unresolved variable stars from the *HIPPARCOS* database and to identify a number of targets for follow-up spectropolarimetric studies at the AAT. Of the 38 stars observed, three stars (HIP 31021, HIP 64732, HIP 73780) were spectroscopic binary stars while further three stars, (HIP 19072, HIP 67651 and HIP 75636) are likely to be a spectroscopic binary stars while HIP 33111 could be a triple system. Two stars rotate with speeds in excess of 100 km s^{-1}: HIP 93378 ($v \sin i \sim 226$ km s^{-1}) and HIP 89829 ($v \sin i \sim 114$ km s^{-1}). Magnetic fields were detected on a number of the survey stars: HIP 21632,

Table B.6: New solar-type targets for Zeeman Doppler imaging.

Confirmed targets	HIP number
MR	21632, 90899, 105388
RR	43720, 48770, 62517, 71933, 77144
URR	89829
Potential targets [1]	
SR & MR	5617, 10699, 11241, 23316, 25848, 63734, 68328
HRR	93378 (DI target)
Binary Stars	
Binary Stars	31021, 64732, 73780
Probable Binary Stars	19072, 33111[2], 67651, 75636

See Table B.5 for definitions used in this table.

[1] Based solely on activity (if SR or MR) or rapid rotation.

[2] This star may even well be a triple system.

HIP 43720, HIP 48770, HIP 62517, HIP 71933, HIP 77144, HIP 89829, HIP 90899 and HIP 105388. All of these stars would be suitable for follow-up spectropolarimetric studies using SEMPOL at the AAT.

Appendix C

Deriving error estimates on differential rotation

C.1 Deriving error estimates on differential rotation.

Error estimation for the differential rotation measurements was done by individually varying stellar parameters such as inclination, spot occupancy and global magnetic field across a physically reasonable range. The resulting "variation bars" are thus analogous to conventional error bars but indicate errors resulting from varying input parameters within certain predetermined limits (Waite et al., 2011b). To determine the magnitude of this variation, the results of each individual differential rotation measurement were graphed onto the $\Omega_{\rm eq}$ and $\delta\Omega$ parameter space, and an ellipse generated to encompass all the results. Figure 6.5 is an example on how the error estimate is made. The paraboloid fit to each individual differential rotation measurement with the error bar on each being 1-σ errors in the paraboloid fit. The grid of χ^2 values for each $\Omega_{\rm eq}$ and $\delta\Omega$ are shown in the following tables. The appropriate variation ellipses are shown in the respective chapters of this thesis.

C.2 HD 106506

Table C.1 shows the values obtained for HD 106506.

Table C.1: The determination of the error ellipse for HD 106506 for Stokes I and Stokes V

Variable	Aim	Ω_{eq}	$\delta\Omega$
Stokes I: Aim is the spot coverage			
Solid body rotation[1]	0.063	4.537286 ± 0.002888	0.211039 ± 0.007201
Inclination=75^o	0.088	4.535293 ± 0.002668	0.207136 ± 0.007001
Inclination=55^o	0.050	4.535944 ± 0.002470	0.213590 ± 0.006637
Spot = 0.069	0.069	4.532461 ± 0.002470	0.210993 ± 0.006068
Spot = 0.057	0.057	4.541968 ± 0.004258	0.208997 ± 0.010576
Stokes V: Aim is the Magnetic Field Strength, G			
Solid body rotation[1]	92	4.50778 ± 0.00476	0.23900 ± 0.02188
Inclination = 55^o	75	4.50763 ± 0.00505	0.22647 ± 0.01796
Inclination = 75^o	116	4.50763 ± 0.00505	0.22647 ± 0.01796
$\chi^2 = 0.9$	112	4.50756 ± 0.00494	0.23644 ± 0.01805
$\chi^2 = 1.1$	78	4.50772 ± 0.00493	0.23876 ± 0.02015

[1] This assumes the "best" set of parameters were used to determine the differential rotation. Assumes an inclination angle = 65^o and $v\sin i = 79.5$ km s^{-1}.

C.3 HD 76298

Table C.2 shows the values obtained for HD 76298 using Stokes I and V data.

C.4 HD 35296

Table C.3 shows the values obtained for HD 35296 Stokes V.

C.5 HD 29615

Table C.4 shows the values obtained for HD 29615.

C.6 EK Draconis

Table C.5 shows the values obtained for EK Draconis Stokes V and I error determination for differential rotation using the January 2007 data only. Table C.6 shows the differential rotation parameters using the full TBL dataset, January and February

Table C.2: The determination of the error ellipse for HD 76298, using the Stokes I and V data.

Variable	Aim	Ω_{eq}	$\delta\Omega$
Stokes I: Aim is the spot coverage			
Solid body rotation	0.067	2.005673 ± 0.017624	0.092537 ± 0.024139
Inclination = 50^o	0.057	1.991747 ± 0.003385	0.072023 ± 0.006107
Inclination = 60^o	0.081	2.001790 ± 0.005754	0.087423 ± 0.011107
$v\sin i$= 39 km s^{-1}	0.086	1.991292 ± 0.004199	0.079242 ± 0.006870
$v\sin i$= 40 km s^{-1}	0.050	2.001644 ± 0.025457	0.078194 ± 0.035995
spot 6.0%	0.060	1.983305 ± 0.005163	0.052213 ± 0.009435
spot 7.4%	0.074	2.000530 ± 0.002607	0.088011 ± 0.004602
Stokes V: Aim is the Magnetic Field Strength, G			
Solid body rotation	47	2.13339 ± 0.01560	0.31063 ± 0.02245
Inclination = 65^o	60.8	2.14400 ± 0.01196	0.32638 ± 0.02135
Inclination = 45^o	38.5	2.06468 ± 0.01529	0.21031 ± 0.02731
$v\sin i$= 39 km s^{-1}	47	2.13346 ± 0.01351	0.31384 ± 0.02194
$v\sin i$= 40 km s^{-1}	47	2.13487 ± 0.00916	0.30923 ± 0.01910
Field Strength = 52G	52	2.05347 ± 0.01117	0.20062 ± 0.02262
Field Strength = 42G	42	2.12955 ± 0.01610	0.31610 ± 0.02366

Table C.3: The determination of the error ellipse for HD 35296 Stokes V only

I_{max}	Variable	Aim	Ω_{eq}	$\delta\Omega$
Stokes V: Aim is the Magnetic Field Strength, G				
30	Solid-body[1]	20	1.805401 ± 0.003584	0.315883 ± 0.026755
20	Solid-body[1]	20	1.804117 ± 0.003308	0.291084 ± 0.022685
20	$v\sin i$15.5 km s^{-1}		1.802147 ± 0.006838	0.300817 ± 0.027040
20	$v\sin i$16.5 km s^{-1}		1.805987 ± 0.003390	0.265763 ± 0.039433
20	inclination = 70^o		1.805050 ± 0.004933	0.321051 ± 0.037338
20	inclination = 60^o		1.807604 ± 0.003058	0.232205 ± 0.018935
20	inclination = 55^o		1.804220 ± 0.003448	0.223605 ± 0.019204
20	Field Strength = 15.0 G	15.0	1.809581 ± 0.002486	0.227887 ± 0.019080
20	Field Strength = 15.5 G	15.5	1.809196 ± 0.002717	0.234347 ± 0.019933
20	Field Strength = 18.6 G	18.6	1.805717 ± 0.003491	0.276548 ± 0.039491
30	Field Strength = 16.8 G	16.8	1.807317 ± 0.002948	0.263287 ± 0.040684

[1]: This assumes the "best" set of parameters were used to determine the differential rotation.

2007. Only the Stokes I data provided meaningful results whereas the Stokes V did not produce any believable results.

Table C.4: The determination of the error ellipse for HD 29615 for Stokes I and Stokes V

Variable	Aim	Ω_{eq}	$\delta\Omega$
Stokes I: Aim is the spot coverage			
Solid Body[1]	0.021	2.690853 ± 0.014742	0.103979 ± 0.019811
Inclination = 65^o	0.021	2.673292 ± 0.009773	0.086302 ± 0.015452
Inclination = 55^o	0.021	2.686910 ± 0.02	0.097456 ± 0.031378
$v\sin i$ = 20 km s^{-1}	0.021	2.736349 ± 0.015623	0.283481 ± 0.072313
$v\sin i$ = 19 km s^{-12}	—	—	—
Spot = 0.019	0.019	2.678184 ± 0.015734	0.090038 ± 0.021571
Spot = 0.023	0.023	2.684325 ± 0.013028	0.092986 ± 0.020597
Stokes V: Aim is the Magnetic Field Strength, G			
Solid body rotation[1]	62	2.754673 ± 0.031113	0.480560 ± 0.049093
Inclination = 65^o	79	2.747907 ± 0.032004	0.517613 ± 0.073166
Inclination = 55^o	66	2.757925 ± 0.035414	0.504184 ± 0.068869
$v\sin i$ = 19 km s^{-1}	66	2.752190 ± 0.026141	0.493573 ± 0.059596
$v\sin i$ = 20 km s^{-1}	66	2.756855 ± 0.035917	0.486302 ± 0.062850
Field Strength = 68G	68	2.754842 ± 0.033087	0.494980 ± 0.057980
Field Strength = 56G	56	2.755402 ± 0.032435	0.490458 ± 0.054861

[1] This assumes the "best" set of parameters were used to determine the differential rotation.

[2] The differential rotation parameters when the $v\sin i$ was 19 km s^{-1} were not able to be determined.

Table C.5: The determination of the error ellipse for EK Draconis for the Stokes I and Stokes V, 2007

Variable	Aim	Ω_{eq}	$\delta\Omega$
Stokes I: Aim is the spot coverage			
Solid body rotation[1]	0.048	2.505971 ± 0.012696	0.342527 ± 0.012696
Inclination = 65^o	0.051	2.502778 ± 0.006711	0.336284 ± 0.020983
Inclination = 55^o	0.048	2.508280 ± 0.011568	0.328246 ± 0.038219
$v\sin i$ = 16.6 km s^{-1}	0.056	2.519742 ± 0.007948	0.333112 ± 0.019941
$v\sin i$ = 17.0 km s^{-12}	–	– ± –	– ± –
Spot Size = 5.3%	0.053	2.499034 ± 0.005502	0.335593 ± 0.019341
Spot Size = 4.3%	0.043	2.514181 ± 0.009628	0.351754 ± 0.025507
Stokes V: Aim is the Magnetic Field Strength, G			
Solid body rotation[1]	77	2.528219 ± 0.016900	0.440258 ± 0.080925
Inclination = 65^o	73	2.525892 ± 0.049792	0.493533 ± 0.163413
Inclination = 55^o[2]	–	– ± –	– ± –
$v\sin i$ = 16.5 km s^{-1}	75	2.523583 ± 0.024242	0.437086 ± 0.080162
$v\sin i$ = 17.0 km s^{-12}	–	– ± –	– ± –
Field Strength = 85G	85	2.523910 ± 0.011863	0.450572 ± 0.073113
Field Strength = 69G	69	2.521203 ± 0.024013	0.428184 ± 0.064844

[1] This assumes the "best" set of parameters were used to determine the differential rotation. The best set of parameters were: $v\sin i$ = 16.8 km s^{-1}, inclination = 60^o, Magnetic Field Strength = 77G

[2] The differential rotation parameters were not determined for these parameter variation.

Table C.6: The determination of the error ellipse for EK Draconis for the Stokes I and Stokes V, 2007

Variable	Aim	Ω_{eq}	$\delta\Omega$
Stokes I: Aim is the spot coverage			
Solid body rotation[1]	0.030	2.501363 ± 0.012068	0.353506 ± 0.029245
Inclination = 65^o[2]	–	– ± –	– ± –
Inclination = 55^o	0.026	2.514535 ± 0.005642	0.351781 ± 0.016520
$v\sin i$ = 16.65 km s^{-1}	0.028	2.476450 ± 0.024133	0.266916 ± 0.039283
$v\sin i$ = 17.0 km s^{-1}[2]	–	– ± –	– ± –
Spot Size = 3.3%	–	– ± –	– ± –
Spot Size = 2.7%	0.027	2.498011 ± 0.011877	0.340130 ± 0.027366

[1] This assumes the "best" set of parameters were used to determine the differential rotation. The best set of parameters were: $v\sin i$ = 16.8 km s^{-1}, inclination = 60^o, Magnetic Field Strength = 77 G

[2] The differential rotation parameters were not determined for these parameter variation.

Appendix D

List of Solar-type stars with DR

D.1 Lists of Solar-type stars that have had their differential rotation parameters measured using DI and ZDI.

Tables D.1 and D.2 gives the basic details of the single, solar-type stars that have had their differential rotational measured using χ^2 minimisation techniques. Tables D.3, D.4 and D.5 give the differential rotation measurements for these solar-type stars.

Table D.1: Properties of stars that have had their differential rotation parameters measured using DI and ZDI.

Star	Other Names	SpT	Type	B-V	Period (d)	vsini	inclination	Teff
HD 106506		G1V[1]	PMS	0.605[10]	1.416±0.133[a]	79.5	65±5	5900
HD 35296	V1119 Tau	F8V[2]	BY Dra	0.544[11]	3.500	16	65±5	6170
HD 29615	HIP 21632	G3V[1]	PMS	0.611[11]	2.34±0.02[a]	19.5	75±5	5820
LQ LUP		G8IVe[1]	T Tau	0.690[12]	0.31[15]	115	35±5	5750
R58	HD 307938	G2V[3]	BY Dra	0.610[13]	0.5641±0.0004[3]	92±0.5	60±10	5800
HD 171488	V889 Her	G2V[2]	BY Dra	0.620[14]	1.313±0.004[16]	37.5±0.5	60±10	5800
HD 141943	NZ Lup	G2V[1]	BY Dra	0.650[14]	2.182[17]	35±0.5	70±10	5850
τ Boo	HD120136	F6IV+M2	VS[b]	0.508[11]	3.312[18]	15.9	40	6387
HD 76298	HIP 43720	G1V[1]	PMS(?)	0.647[11]	3.14±0.1[a]	39.5[a]	55±5[a]	6000[a]
EK Dra	HD 129333	G1.5V[2]	BYDra	0.626[11]	2.603±0.0003[19]	16.8	60±10	5870
PZ Tel	HD 174429	G9IV[1]	BYDra	0.784[11]	0.945[20]	69	60±10	5169
AB Dor	HD 36705A	K0V[1]	RVS[c]	0.820	0.510[21]	89[21]	70[21]	5386
LQ Hya	HD 82558	K0V[2]	BY Dra	0.920	1.614	26	60±10	5019
HD 197890	Speedy Mic	K3V[1]	BY Dra	0.930	0.380	156.3	70±10	4989
LO Peg	HIP 106231	K5-7V[4]	BY Dra	1.080	0.4231[21]	66	–	4577
EY Dra		dM1.5[5]	BY Dra	1.450	0.459[22]	–	–	3489
HK Aqr	HIP 114252	M0V[1]	BY Dra	1.420	0.431[22]	69	–	3697
HD 190771	–	M4III[6]	–	1.574[10]	8.800	4.3	50±10	5834
HD 73350	V401 Hya	G5V[7]	BY Dra	0.655[11]	12.300	4±0.5	75^{15}_{22}	5802
HD 179949	HR 7291	F8V[2]	–	0.530[11]	7.600	7.02±0.05	60±10	6168
ξ Boo	HD 131156	G8V[8]	By Dra	0.725	6.430	3	28	5600
HR 1817	AF Lep	F8V	RS CVn ?	0.553	0.980[10]	50	50±10	6131
RX J0850.1-7554	–	G9V[1]	T Tau	0.9[11]	1.1679	42.5±0.5	70	5700

[a]: This work, [b]: Variable Star, [c]: Rotationally Variable Star,
[1]Torres et al. (2006),[2]Montes et al. (2001),[3]Marsden et al. (2005),[4]Strassmeier (2009),[5]Jeffries et al. (1994),[6]Houk and Cowley (1975),[7]Koen et al. (2010),[8]Ruck and Smith (1995),[9]Gray et al. (2006),[10]ESA (1997),[11]van Leeuwen (2007),[12]Wichmann et al. (1997),[13]Randich (2001),[14]Cutispoto et al. (2002),[15]R. et al. (1998),[16]Marsden et al. (2006),[17]Marsden et al. (2011a),[18]Catala et al. (2007),[19]Strassmeier and Rice (1998),[20]Innis et al. (1990),[21]Donati and Collier Cameron (1997),[21]Pojmański et al. (2002b),[22]Messina et al. (2003)

Table D.2: Properties of stars that have had their differential rotation parameters measured using DI and ZDI cont.

Star	Other Names	SpT	Type	B-V	Period (d)	vsini	inclination	Teff
HD 197890	Speedy Mic	K3V[1]	BY Dra	0.930	0.380	156.3	70±10	4989
LO Peg	HIP 106231	K5-7V[4]	BY Dra	1.080	0.4231[21]	66	–	4577
EY Dra		dM1.5[5]	BY Dra	1.450	0.459[22]	–	–	3489
HK Aqr	HIP 114252	M0V[1]	BY Dra	1.420	0.431[22]	69	–	3697
HD 190771	–	M4III[6]	–	1.574[10]	8.800	4.3	50±10	5834
HD 73350	V401 Hya	G5V[7]	BY Dra	0.655[11]	12.300	4±0.5	75^{15}_{22}	5802
HD 179949	HR 7291	F8V[2]	–	0.530[11]	7.600	7.02±0.05	60±10	6168
ξ Boo	HD 131156	G8V[8]	By Dra	0.725	6.430	3	28	5600
HR 1817	AF Lep	F8V	RS CVn ?	0.553	0.980[10]	50	50±10	6131
RX J0850.1-7554	–	G9V[1]	T Tau	0.9[11]	1.1679	42.5±0.5	70	5700

[a]: This work, [b]: Variable Star, [c]: Rotationally Variable Star,
[1]Torres et al. (2006),[2]Montes et al. (2001),[3]Marsden et al. (2005),[4]Strassmeier (2009),[5]Jeffries et al. (1994),[6]Houk and Cowley (1975),[7]Koen et al. (2010),[8]Ruck and Smith (1995),[9]Gray et al. (2006),[10]ESA (1997),[11]van Leeuwen (2007),[12]Wichmann et al. (1997),[13]Randich (2001),[14]Cutispoto et al. (2002),[15]R. et al. (1998),[16]Marsden et al. (2006),[17]Marsden et al. (2011a),[18]Catala et al. (2007),[19]Strassmeier and Rice (1998),[20]Innis et al. (1990),[21]Donati and Collier Cameron (1997),[21]Pojmański et al. (2002b),[22]Messina et al. (2003)

Table D.3: Differential rotation parameters for some solar-types stars found using the principles of DI and ZDI

Name	Age (Myr)	Mass	Radius	CZD	Ω_{eq}	$\delta\Omega$	Ω_{eq}	$\delta\Omega$	B_{mean}	epoch
HD 106506[1]	$\leq\sim$10	1.5	2.15	$0.240^{0.060}_{0.050}$	4.540±0.010	0.210±0.025	4.510±0.010	0.240±0.030	69	2007.257
HD 35296[1]	20-50[1]	1.1[2]	1.13	$0.190^{0.003}_{0.006}$	–	–	1.800±0.010	0.280±0.080	15.8	2008.08
HD 29615[1]	20-30	0.95	1.0	$0.390^{0.030}_{0.030}$	$2.670^{+0.09}_{-0.01}$	$0.090^{+0.04}_{-0.02}$	$2.750^{0.07}_{0.04}$	$0.580^{+0.14}_{-0.12}$	72.000	2009.910
LQ LUP[2]	25	1.16	1.22	$0.265^{0.022}_{0.129}$	20.280±0.040	0.120±0.020	–	–	–	1998.35
LQ LUP[3]				$0.265^{0.022}_{0.129}$	20.268±0.002	0.094±0.004	–	–	–	2002.33
R58[4]	35	1.15	1.18	$0.239^{0.001}_{0.001}$	11.160±0.040	0.080±0.070	–	–	–	2000.05
R58[3]				$0.239^{0.001}_{0.001}$	11.182±0.008	0.109±0.014	–	–	–	2003.21
R58[3]				$0.239^{0.001}_{0.001}$	11.240±0.013	0.195±0.024	–	–	–	2005.12
HD 171488[5]	30-50	1.2	1.13	$0.200^{0.010}_{0.010}$	4.786±0.013	0.402±0.044	–	–	–	2004.650
HD 171488[6]				$0.200^{0.010}_{0.010}$	4.930±0.050	0.520±0.040	4.850±0.050	0.470±0.040	68	2005.420
HD 171488[7]				$0.200^{0.010}_{0.010}$	4.790±0.090	0.400±0.150	4.780±0.027	0.450±0.053	70	2007.390
HD 171488[7]				$0.200^{0.010}_{0.010}$	4.860±0.030	0.410±0.020	4.790±0.080	0.415±0.016	75	2007.770
HD 141943[8]	17	1.3	1.6	$0.160^{0.030}_{0.040}$	–	–	2.880±0.020	0.360±0.090	91.3	2007.257
HD 141943[8]				$0.160^{0.030}_{0.040}$	2.860±0.020	0.240±0.030	2.890±0.050	0.450±0.080	70.9	2010.244
τ Boo[9]		1.34[7]	1.46[7]	$0.100^{0.020}_{0.010}$	–	–	–	–	–	–
HD 76298[1]	$\sim$10 (?)	1.6	2.2	$0.195^{0.175}_{0.145}$	$2.010^{+0.1}_{-0.03}$	$0.090^{+0.03}_{-0.04}$	$2.150^{+0.10}_{-0.11}$	$0.340^{+0.01}_{-0.16}$	79.500	2010.245
EK Dra[1]	30-50[3]	1.06[2]	0.99[2]	$0.280^{0.040}_{0.040}$	2.510±0.017	0.340 ±0.050	2.530±0.050	0.440±0.200	98.78	2007.082

The source of each differential rotation measurement: [1] This work, [2]Donati et al. (2000),[3]Brown (2011),[4]Marsden et al. (2005),[5]Marsden et al. (2006)[6]Jeffers and Donati (2008),[7]Jeffers et al. (2011),[8]Marsden et al. (2011b),[9]Mason et al. (2001),[1]0Barnes et al. (2000),[11]Donati and Collier Cameron (1997),[12]Collier Cameron and Donati (2002),[13]Donati et al. (2003a).

Table D.4: Differential rotation parameters for some solar-types stars found using the principles of DI and ZDI cont.

Name	Age (Myr)	Mass	Radius	CZD	Ω_{eq}	$\delta\Omega$	Ω_{eq}	$\delta\Omega$	B_{mean}	epoch
PZ Tel[10]	70	0.76	1.1	$0.361^{0.006}_{0.019}$	–	0.101 ±0.007	–	–	–	–
AB Dor[11]				$0.334^{0.019}_{0.001}$	–	0.04620±0.00578	–	–	–	–
AB Dor[12]				$0.334^{0.019}_{0.001}$	–	0.09106±0.01188	–	–	–	–
AB Dor[12]				$0.334^{0.019}_{0.001}$	–	0.08850±0.00748	–	–	–	–
AB Dor[12]				$0.334^{0.019}_{0.001}$	–	0.06684±0.02027	–	–	–	–
AB Dor[12]				$0.334^{0.019}_{0.001}$	–	0.07140±0.00568	–	–	–	–
AB Dor[12]				$0.334^{0.019}_{0.001}$	–	0.05764±0.00476	–	–	–	–
AB Dor[13]				$0.334^{0.019}_{0.001}$	12.2421±0.0008	0.05340±0.00250	12.25380±0.00310	0.0967±0.0081	110	1995.940
AB Dor[13]				$0.334^{0.019}_{0.001}$	12.2359±0.0008	0.0471±0.0025	12.24280±0.00110	0.0596±0.0031	110	1996.99
AB Dor[13]				$0.334^{0.019}_{0.001}$	12.2391±0.0004	0.0584±0.0015	12.25130±0.00320	0.0765±0.0074	125	1999.00
AB Dor[13]				$0.334^{0.019}_{0.001}$	12.2351±0.0009	0.0461±0.0028	12.24260±0.00210	0.07410±0.0060	125	2000.93
AB Dor[13]				$0.334^{0.019}_{0.001}$	12.2366±0.0004	0.0540±0.0013	12.24010±0.00080	0.0682±0.0024	175	2001.99
LQ Hya[13]	51±17.5[4]	0.753[7]	0.71[7]	$0.335^{0.012}_{0.008}$	–	–	3.89230±0.00960	-0.0487±0.0235	30	1999.97
LQ Hya[13]				$0.335^{0.012}_{0.008}$	3.98240±0.00910	0.19420±0.0216	3.96930±0.00290	0.2009±0.0724	80	1995.94
LQ Hya[13]				$0.335^{0.012}_{0.008}$	2.92230±0.00100	0.01440±0.0029	3.94460±0.00230	0.00867±0.0087	50	1996.99

The source of each differential rotation measurement: [1] This work, [2]Donati et al. (2000),[3]Brown (2011),[4]Marsden et al. (2005),[5]Marsden et al. (2006)[6]Jeffers and Donati (2008),[7]Jeffers et al. (2011),[8]Marsden et al. (2011b),[9]Mason et al. (2001),[10]Barnes et al. (2000),[11]Donati and Collier Cameron (1997),[12]Collier Cameron and Donati (2002),[13]Donati et al. (2003a).

Table D.5: Differential rotation parameters for some solar-types stars found using the principles of DI and ZDI cont.

Name	Age (Myr)	Mass	Radius	CZD	Ω_{eq}	$\delta\Omega$	Ω_{eq}	$\delta\Omega$	B_{mean}	epoch
HD 197890[14]	24.1	1	1.2	$0.365^{0.011}_{0.014}$	–	0.03157±0.00206	–	–	–	–
LO Peg[15]	30-50[5]	0.65	0.7	$0.415^{0.108}_{0.012}$	–	0.03550±0.00682	–	–	–	–
EY Dra[16]		0.8	0.6	$0.527^{0.038}_{0.083}$	–	0.00030±0.00333	–	–	–	–
HK Aqr[17]		0.56	0.6	$0.527^{0.038}_{0.083}$	–	0.00496±0.00917	–	–	–	–
HD 190771[18]	2.7 Gyr	0.96[6]	1.01[7]	$0.287^{0.001}_{0.001}$	–	–	0.71±0.01	0.12±0.03	51	2007.59
HD 190771[19]				$0.287^{0.001}_{0.001}$	–	–	0.71±0.01	0.12±0.03	59	2008.67
HD 190771[19]				$0.287^{0.001}_{0.001}$	–	–	0.66±0.01	0.12±0.02	58	2009.47
HD 73350[18]	1.88 Gyr[7]	1.038[7]	0.98[7]	$0.287^{0.001}_{0.001}$	–	–	0.511±0.04	0.200±0.200	42	2007.088
HD 179949[20]	2.1±0.8 Gyr[6]	1.038[7]	0.98[7]	$0.209^{0.015}_{0.036}$	–	–	0.825±0.008	0.216±0.061	2.6	2009.755
ξ Boo[21]	5.3±1 Gyr[6]	0.931[7]	0.84[7]	$0.330^{0.020}_{0.035}$	–	–	1.13±0.01	0.380±0.020	30±8	2008.088
ξ Boo[21]				$0.330^{0.020}_{0.035}$	–	–	1.27±0.01	0.570±0.030	47±11	2009.475
ξ Boo[21]				$0.330^{0.020}_{0.035}$	–	–	1.055±0.005	0.670±0.010	36±12	2010.498
ξ Boo[21]				$0.330^{0.020}_{0.035}$	–	–	1.09±0.03	0.270±0.050	46±17	2010.595
HR 1817	12	1.268[7]	1.22[7]	$0.447^{0.030}_{0.030}$	–	–	6.494 ±0.010	0.256±0.017	–	–
RX J0850.17554[3]	17	1.2	1.09	$0.240^{0.065}_{0.065}$	5.475±0.018	0.034±0.056	–	–	–	2006.35

The source of each differential rotation measurement: [3]Brown (2011),[13]Donati et al. (2003a),[14]Barnes (2005),[15]Barnes et al. (2005b),[16]Barnes et al. (2005a),[17]Barnes et al. (2004),[18]Petit et al. (2008),[19]Petit et al. (2009),[20]Fares et al. (2012),[21]Morgenthaler et al. (2012).

Appendix E

Magnetic components for Solar-type stars

E.1 Magnetic components determined for solar-type stars

This appendix shows the magnetic parameters for a number of selected ZDI targets.

Table E.1: Magnetic parameters for a number of selected ZDI targets.

Star	epoch	B_{mean} (G)	Pol Ener[1] % total	dipole[2] (%)	quad.[2] (%)	oct.[2] (%)	Axi.[1] (%)	reference
HD 106506	2007.257	69	30±3	10±2	11±1.5	10±1	35±2	Waite et al, 2011
HD 35296	2007.080	13.2	82±4	19±5	5±1	15±3	7±4	this work
HD 35296	2008.080	15.8	52±6	8±2	13±1	7±4	10±5	this work
HD 29615	2009.910	72	73±4	35±16	11±8	12±4	35±10	this work
HD 76298	2010.245	33	76±4	20±9	8±8	7±2	76±4	this work
HIP 141943	2007.257	91^{+26}_{-11}	47^{+8}_{-9}	16^{+1}_{-5}	10^{+4}_{-3}	15^{+2}_{-4}	28^{+2}_{-5}	Marsden et al, 2011a
HIP 141943	2009.273	37^{+4}_{-4}	82^{+2}_{-2}	29^{+2}_{-9}	20^{+5}_{-6}	6^{+3}_{-2}	22^{+10}_{-2}	Marsden et al, 2011a
HIP 141943	2010.244	71^{+19}_{-10}	50^{+5}_{-3}	6^{+3}_{-2}	9^{+1}_{-2}	21^{+7}_{-6}	30^{+7}_{-10}	Marsden et al, 2011a
HD 146233		3.6±1	99.3±0.2	34±6	56±6	10±10		Petit et al, 2008
HD 76151		5.6±2	99±6	79±13	18±8	3±3		Petit et al, 2008
HD 73350		42±7	52±3	24±5	29±8	33±5		Petit et al, 2008
HD 190711	2007.590	51±6	34±1	43±8	20±2	23±4	73±3	Petit et al, 2008
HD 190711	2008.670	59±3	39±3	36±8	18±2	19±4	61±3	Petit et al, 2009
HD 190711	2009.470	58±8	81±2	23±7	40±2	21±2	36±12	Petit et al, 2009
τ Boo	June 2007	3.7	83	52[3]			60	Fares et al, 2009
τ Boo	Jan 2008	3.1	38	50[3]			20	Fares et al, 2009
τ Boo	June 2008	2.3	87	36[3]			36	Fares et al, 2009
τ Boo	July 2008	1.7	91	47[3]			62	Fares et al, 2009
HD 179949	Sept 2009	3.7	90				35	Fares et al. 2012
HD 179949	June 2007	2.6	80				54	Fares et al, 2012
ξ Boo	2007.587	69±27	17±3	71±2	13±1	9±1	83±3	Morgenthaler et al, 2011
ξ Boo	2008.088	30±8	58±6	41±7	15±1	15±2	56±1	Morgenthaler et al, 2011
ξ Boo	2009.457	47±11	35±9	41±7	20±1	19±3	69±3	Morgenthaler et al, 2011
ξ Boo	2010.040	38±9	32±9	29±20	9±1	8±1	29±6	Morgenthaler et al, 2011
ξ Boo	2010.480	36±12	62±2	50±6	13±3	7±2	43±8	Morgenthaler et al, 2011
ξ Boo	2010.595	46±17	13±6	48±14	18±4	13±4	95±1	Morgenthaler et al, 2011
ξ Boo	2011.066	43±20	18±4	77±3	14±1	4±3	85±2	Morgenthaler et al, 2011

[1]: % of the total magnetic energy available.

[2]: % of the poloidal field geometry.

Listed also is the fraction of the poloidal magnetic energy in the dipolar ($\ell = 1$), quadrupolar ($\ell = 2$) and octupolar ($\ell = 3$) components as well as the fraction of energy stored in the axisymmetric component (m = 0).

[3]: % of the poloidal energy ($\ell \leq 2$).